GL-TR-89-0143

Investigations of Eurasian Seismic Sources
and Upper Mantle Structure

Thomas H. Jordan
Justin S. Revenaugh
Lind S. Gee

Massachusetts Institute of Technology
Earth, Atmospheric & Planetary Sciences
77 Massachusetts Avenue
Cambridge, MA 02139

25 May 1989

DTIC
ELECTE
S AUG 2 8 1989 **D**
D

Final Report
9 June 1987-8 November 1988

GEOPHYSICS LABORATORY
AIR FORCE SYSTEMS COMMAND
UNITED STATES AIR FORCE
HANSCOM AIR FORCE BASE, MASSACHUSETTS 01731-5000

AD-A211 806

89 8 29 038
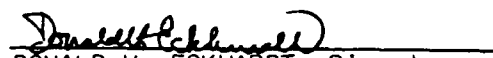
The views and conclusions contained in this document are those of the authors and should not be interpreted as representing the official policies, either expressed or implied, of the Defense Advanced Research Projects Agency or the U.S. Government.

This technical report has been reviewed and is approved for publication.

JAMES F. LEWKOWICZ
Contract Manager
Solid Earth Geophysics Branch
Earth Sciences Division

JAMES F. LEWKOWICZ
Branch Chief
Solid Earth Geophysics Branch
Earth Sciences Division

FOR THE COMMANDER

DONALD H. ECKHARDT, Director
Earth Sciences Division

This report has been reviewed by the ESD Public Affairs Office (PA) and is releasable to the National Technical Information Service (NTIS).

Qualified requestors may obtain additional copies from the Defense Technical Information Center. All others should apply to the National Technical Information Service.

If your address has changed, or if you wish to be removed from the mailing list, or if the addressee is no longer employed by your organization, please notify AFGL/DAA, Hanscom AFB, MA 01731-5000. This will assist us in maintaining a current mailing list.

Do not return copies of this report unless contractual obligations or notices on a specific document requires that it be returned.

REPORT DOCUMENTATION PAGE	Form Approved OMB No. 0704-0188

1a. REPORT SECURITY CLASSIFICATION UNCLASSIFIED	1b. RESTRICTIVE MARKINGS

2a. SECURITY CLASSIFICATION AUTHORITY	3. DISTRIBUTION/AVAILABILITY OF REPORT APPROVED FOR PUBLIC RELEASE;
2b. DECLASSIFICATION/DOWNGRADING SCHEDULE	DISTRIBUTION UNLIMITED

4. PERFORMING ORGANIZATION REPORT NUMBER(S)	5. MONITORING ORGANIZATION REPORT NUMBER(S) GL-TR-89-0143

6a. NAME OF PERFORMING ORGANIZATION MASSACHUSETTS INSTITUTE OF TECHNOLOGY	6b. OFFICE SYMBOL (If applicable)	7a. NAME OF MONITORING ORGANIZATION GEOPHYSICS LABORATORY
6c. ADDRESS (City, State, and ZIP Code) EARTH, ATMOSPHERIC AND PLANETARY SCIENCES 77 MASSACHUSETTS AVENUE CAMBRIDGE, MA 02139		7b. ADDRESS (City, State, and ZIP Code) HANSCOM AFB MASSACHUSETTS 01731-5000

8a. NAME OF FUNDING/SPONSORING ORGANIZATION DEFENCE ADVANCED RESEARCH PROCTS AGENCY	8b. OFFICE SYMBOL (If applicable) NMRO	9. PROCUREMENT INSTRUMENT IDENTIFICATION NUMBER F19628-87-K-0040

8c. ADDRESS (City, State, and ZIP Code) 1400 WILSON BLVD ARLINGTON, VA 22209-2308	10. SOURCE OF FUNDING NUMBERS			
	PROGRAM ELEMENT NO. 61101E	PROJECT NO. 7A10	TASK NO. DA	WORK UNIT ACCESSION NO. CH

11. TITLE (Include Security Classification)
UNCLASSIFIED: INVESTIGATIONS OF EURASIAN SEISMIC SOURCES AND UPPER MANTLE STRUCTURE

12. PERSONAL AUTHOR(S)
JORDAN, THOMAS H.; REVENAUGH, JUSTIN S.; GEE, LIND S.

13a. TYPE OF REPORT FINAL TECHNICAL	13b. TIME COVERED FROM 6/9/87 TO 11/8/88	14. DATE OF REPORT (Year, Month, Day) 1989 MAY 25	15. PAGE COUNT 310

16. SUPPLEMENTARY NOTATION

17. COSATI CODES			18. SUBJECT TERMS (Continue on reverse if necessary and identify by block number)
FIELD	GROUP	SUB-GROUP	anisotropy, body waves, Eurasia, reverberations, surface waves, upper mantle structure, Western Pacific

19. ABSTRACT (Continue on reverse if necessary and identify by block number)

SEE REVERSE SIDE

20. DISTRIBUTION/AVAILABILITY OF ABSTRACT ☒ UNCLASSIFIED/UNLIMITED ☒ SAME AS RPT. ☐ DTIC USERS	21. ABSTRACT SECURITY CLASSIFICATION UNCLASSIFIED	
22a. NAME OF RESPONSIBLE INDIVIDUAL JAMES LEWKOWICZ	22b. TELEPHONE (Include Area Code) (617) 377-3028	22c. OFFICE SYMBOL GL/LWH

DD Form 1473, JUN 86   Previous editions are obsolete.

19. ABSTRACT

We have formulated a new set of waveform-analysis procedures to recover phase and amplitude information from seismograms. The new procedures have a number of advantages over existing techniques, and they appear to be capable of making fundamentally new observations about the structure of the earth's interior. We have used them to measure the travel times and quality factors of body waves, including those imbedded in the complex wavetrains, as well as the dispersion and attenuation of surface waves, including higher modes. In particular, we have applied these techniques to three-component seismograms to investigate the structure of the Eurasian upper mantle. Specifically, we have made observations of shear-wave splitting on long-period records of multiply reflected S waves bottoming in the upper mantle beneath the Russian and Siberian platforms. The dispersion of Love and Rayleigh waves over these paths shows discrepancies of comparable or larger magnitude with respect to smooth isotropic structures, consistent with a model of the uppermost mantle having significant apparent vertical anisotropy. Although the splitting and dispersion data can be fit by smooth anisotropic models, we have investigated the apparent anisotropy associated with fine-scale ("rough") structure beneath stable Eurasia. We fit the data with a rough isotropic model having an rms shear velocity fluctuation that varies from 14% in the uppermost mantle to zero at 400-km depth. The fluctuations are larger than the variation expected for even a diverse assemblage of upper-mantle ultrabasic rocks, which we take as evidence for some sort of intrinsic (local) anisotropy.

We have also developed signal enhancement and waveform inversion schemes to progressively extract information pertaining to mantle layering from the waveforms of zeroth- and first-order reverberations. The reverberative interval of the seismogram, defined as the portion following the surface wave train propagating along the minor arc and ending with the first body-wave arrivals from the major arc, provides an excellent window in which to observe subcritical reflections from mantle discontinuities. On an SH polarized seismogram the intervals between ScS and $sScS_n$ wave groups (zeroth-order reverberations) are approximately 15 minutes long and consist almost entirely of waves reflected one or more times from mantle discontinuities (first- and higher-order reverberations). We have applied our techniques to a data set of long-period, digital seismograms drawn from a number of tectonic regions in the western and central Pacific, the adjoining marginal basins, Indonesia, and Australia - a study area which includes the majority of deep subduction zones. The results place important constraints on the nature of the transition-zone discontinuities.

INVESTIGATIONS OF EURASIAN SEISMIC SOURCES AND UPPER MANTLE STRUCTURE

TABLE OF CONTENTS

Accesion For

NTIS CRA&I	☑
DTIC TAB	☐
Unannounced	☐
Justification	

By ....

Distribution /

| Availability Codes |
| Dist | Avail and / or Special |
| A-1 | |

iii

LIST OF CONTRIBUTING SCIENTISTS

Thomas H. Jordan, Professor of Geophysics, Massachusetts Institute of Technology

Justin S. Revenaugh, Graduate Research Assistant, Massachusetts Institute of Technology

Lind S. Gee, Graduate Research Assistant, Massachusetts Institute of Technology

LIST OF ALL PREVIOUS RELATED CONTRACTS

DARPA/AFGL Contract #F19628-85-K-0024, "Investigations of Eurasian Seismic Sources and Upper Mantle Structure," December 1984 - March 1987.

BIBLIOGRAPHY OF THE TITLE AND AUTHORS OF ALL PUBLICATIONS

OR ARTICLES RESULTING FROM

TOTAL OR PARTIAL SPONSORSHIP OF THE CONTRACT

L. S. Gee and T. H. Jordan, The *Sn* discrepancy in Eurasia, 9th Annual AFGL/DARPA Seismic Research Symposium, 1987.

L. S. Gee and T. H. Jordan, How can synthetic seismograms be used in structural inverse problems?, 19th General Assembly of the International Union of Geodesy and Geophysics (IUGG), 1987.

J. S. Revenaugh and T. H. Jordan, Application of first-order reverberations to the study of mantle layering, *Eos, Trans. Am. Geophys. Union, 68*, 1376, 1987.

L. S. Gee and T. H. Jordan, Polarization anisotropy and fine-scale layering of the Eurasian upper mantle, *Eos, Trans. Am. Geophys. Union, 69*, 397, 1988.

J. S. Revenaugh and T. H. Jordan, The nature of the 400-km and 650-km discontinuities from mantle reverberations, *Eos, Trans. Am. Geophys. Union, 69*, 398, 1988.

L. S. Gee and T. H. Jordan, Polarization anisotropy and fine-scale layering of the Eurasian upper mantle, 10th Annual AFGL/DARPA Seismic Research Symposium, 1988.

L. S. Gee and T. H. Jordan, Polarization anisotropy and fine-scale layering of the Eurasian upper mantle, *Geophys. Res. Lett., 15,* 824-827, 1988.

J. S. Revenaugh and T. H. Jordan, A study of mantle layering beneath the western Pacific, *J. Geophys. Res., 94,* 5787-5813, 1988.

L. S. Gee and T. H. Jordan, The measurement of travel times for tomography, *Eos, Trans. Am. Geophys. Union, 69,* 1308, 1988.

J. S. Revenaugh and T. H. Jordan, Constraints on mantle discontinuities, composition and heterogeneity from first-order reverberations, *Eos, Trans. Am. Geophys. Union, 69,* 1333, 1988.

T. H. Jordan and J. S. Revenaugh, Structure of the lower mantle and D" from first-order reverberations, *Eos, Trans. Am. Geophys. Union, 69,* 1409, 1988.

L. S. Gee and T. H. Jordan, On the measurement of travel time, manuscript in preparation, 1989.

L. S. Gee and T. H. Jordan, Eurasian upper mantle structure from three-component seismograms, manuscript in preparation, 1989.

DISTRIBUTION LIST

Distribution:	AFGL/LWH
	ESD/PKR
	AFGL/SULR
	DCASMA (ACO)
	DARPA/PM
	DARPA/STO/GSD

INVESTIGATIONS OF EURASIAN SEISMIC SOURCES AND UPPER MANTLE STRUCTURE

I: NEW DATA PROCESSING TECHNIQUES FOR SEISMOLOGICAL STUDIES OF EARTH STRUCTURE

LIND S. GEE AND THOMAS H. JORDAN

Department of Earth, Atmospheric and Planetary Sciences
Massachusetts Institute of Technology
Cambridge, MA 02139

ABSTRACT

We have formulated a new set of waveform-analysis procedures to recover phase and amplitude information from seismograms. The new procedures have a number of advantages over existing techniques, and they appear to be capable of making fundamentally new observations about the structure of the earth's interior. We have used them to measure the travel times and quality factors of body waves, including those imbedded in the complex wavetrains, as well as the dispersion and attenuation of surface waves, including higher modes. In particular, we have applied these techniques to three-component seismograms to investigate the structure of the Eurasian upper mantle.

TABLE OF CONTENTS

INTRODUCTION

Seismograms recorded by global networks following large earthquakes contain a vast quantity of information about the details of earth structure. A major focus of seismological research concerns methods for extracting this information, understanding its implications, and using it to refine structural models. By employing a series of techniques developed over the last decade, seismologists have made spectacular progress in elucidating the three-dimensional structural variations associated with boundary layers and internal dynamics of the mantle and core [e.g., Dziewonski *et al.*, 1977; Masters *et al.*, 1982; Clayton and Comer, 1983; Dziewonski, 1984; Woodhouse and Dziewonski, 1984; Nataf *et al.*, 1984, 1986; Hager *et al.*, 1985; Creager and Jordan, 1986a,b; Ritzwoller et al., 1986; Dziewonski and Woodhouse, 1987; Jordan *et al.*, 1988]. Only a small fraction of the information available from existing data has been used for this purpose, however, and many important geophysical questions related to the details of earth structure remain unanswered. What is the fine structure of the inner core-outer core transition, the core-mantle boundary, and the mid-mantle transition zone? What are the spectra of lateral heterogeneity at these interfaces, how are they correlated, and how do they differ from the spectra at other levels? What seismological structures are diagnostic of the modulation of mantle convection by chemical, phase and/or viscosity variations within the transition zone? To what degree are the deep-seated thermal and chemical structures of the surficial boundary layers correlated with shallow crustal structures? What aspects of seismic-wave anisotropy are related to present-day mantle flow? Does the near-surface anisotropy of the sub-continental mantle reflect structures frozen into the plates during deformation events in the distant geological past? Is inner-core anisotropy associated with frozen-in structure or active convection?

The continued application of existing techniques to an ever growing catalog of digitally recorded seismograms will no doubt allow seismologists to make further progress on these problems. However, we believe this progress can be greatly accelerated by the introduction of techniques that take advantage of improving capabilities, especially the ever-increasing speed with which large machines can perform signal processing, seismogram synthesis, and inversion calculations. As part of the DARPA-sponsored program in test-ban treaty verification, we have developed an approach to extracting structural information from the seismogram that is novel and promises to deliver fundamentally new constraints on earth structure.

We have formulated a new set of waveform-analysis procedures to recover phase and amplitude information from seismograms. These procedures have a number of advantages over existing methods. Like waveform-inversion techniques, they make use of our ability to compute synthetic seismograms from realistic earth models, and they provide a uniform methodology for inverting body-wave, surface-wave, and other types of wave groups from three-component data. Unlike waveform-inversion techniques, whose "black-box" character can make interpretation

difficult, they isolate from the seismogram time-like quantities that correspond to well-defined scalar-valued functionals of earth structure: phase delays, group delays, attenuation times, and their generalizations. An inversion of these quantities for earth structure (1-D, 2-D or 3-D) can thus be accomplished in a separate step using standard perturbation techniques. By separating the measurement of data functionals from the inversion of the data for earth structure, we facilitate the assessment of the significance and robustness of the measurements, and we allow a variety of model parameterizations and inversion schemes to be compared.

We have implemented these waveform-analysis procedures on the Geophysical Computing System at MIT and have demonstrated that they are capable of making fundamentally new observations about the structure of the earth's deep interior. We have used them to measure the travel times and quality factors of body waves, including those imbedded in the complex wavetrains, as well as the dispersion and attenuation of surface waves, including higher modes. In particular, we have made observations of large-magnitude ($\sim$10 s) shear-wave splitting in multiply reflected S waves propagating across the stable continental platforms of Eurasia.

4

TECHNICAL DISCUSSION

A seismogram $s(t)$ can be represented as a sum over waveforms $\{u_n(t) : n = 1, 2, ...\}$:

$$s(t) = \sum_{n=0}^{\infty} u_n(t) \qquad (1)$$

The seismologist may choose a particular element $u_n(t)$ to be a body-wave pulse, a surface-wave group, or any other convenient representation of the seismic wavetrain [Aki and Richards, 1980]. The classical approach is to separate the process of measuring waveform properties from the process of inverting for earth structure. Discrete body-wave arrivals are identified and their travel times and attenuation factors are determined; surface-wave groups are isolated and their dispersion and attenuation properties are measured. These data are then inverted for an earth model whose parameterization is sufficiently complete to explain the observed variations. If a sufficiently good starting model is available, the latter step can be accomplished using a perturbation theory based on the variational principles of Fermat and Rayleigh (Figure 1).
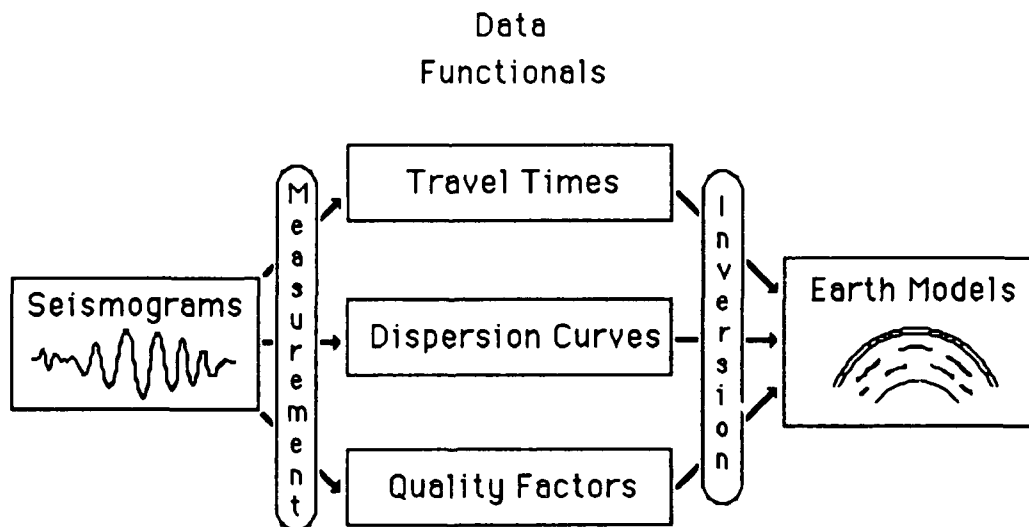
Data
Functionals

Figure 1. "Classical" seismological methodology breaks the problem of determining earth structure into two parts: (1) the measurement of well-defined data functionals--e.g., the travel times of body phases; phase and group velocities of surface waves--and (2) the inversion of these data for earth models.

A problem with this approach concerns the various wave effects that complicate the measurement of individual wave groups. In the case of body-wave travel times, these include

caustic phase shifts, diffraction effects, and the physical dispersion associated with attenuation. In the case of surface-wave dispersion, they involve source-related phase shifts and the problems associated with isolating individual modes. Indeed, for portions of the seismogram where many wave groups arrive simultaneously, the waveforms cannot generally be resolved into either individual body waves or surface waves, and the classical measurement schemes that rely on waveform isolation can fail to produce reliable results. Techniques based on frequency-wavenumber filtering have been used to separate interfering surface waves [Nolet, 1975, 1977; Cara, 1979; Cara et al., 1980], but they generally require large-aperture arrays of seismometers not common in global studies of earth structure.

Many of these difficulties can be avoided by inverting the complete seismogram directly for earth structure. In the ideal situation where the entire wavefield is recorded by a spatially dense set of receivers from a spatially dense set of sources, powerful nonlinear inversion techniques can be applied to recover an image of the three-dimensional structure [A. Tarantola, personal communication, 1988]. Although the collection of these sorts of ideal data sets can be approached in exploration seismology, where the effort and resources concentrated on imaging small volumes of the earth are high, the data sets available to global seismology are limited by the distribution of large-magnitude sources, primarily earthquakes, and the sparse distribution of stations, especially those with high-quality, digitally recording seismometers. In this situation, fully nonlinear methods cannot be applied because the solution manifolds have multiple minima, and we are forced to linearize the problem by assuming the solution to the waveform-inversion problem is in some sense close to a chosen reference earth structure.

Theoretical and computational advances over the last two decades now permit the routine calculation of synthetic seismograms $\tilde{s}(t)$ using a variety of waveform representations. As in the case of equation (1), a seismogram computed from a reference earth model $\mathbf{m}_0$ can be written as a sum over synthetic waveforms $\{ \tilde{u}_n(t) \}$:

$$\tilde{s}(t) = \sum_{n=0}^{N} \tilde{u}_n(t) \qquad (2)$$

although the number of elements in the sum, N, must necessarily be finite. Synthetic seismograms accurately model wave propagation through realistic earth structures, as well as source excitation effects. Most waveform-inversion algorithms [e.g., Lerner-Lam and Jordan, 1983, 1987; Dziewonski ar ' Steim, 1983; Woodhouse and Dziewonski, 1984] subtract synthetic seismograms computed for the reference structure from the observed time series to form differential seismogram... that are then inverted for a structural perturbation using first-order perturbation theory (Figure 2). This " 'arized inverse problem thus takes the form

$$G \, \delta m = \delta s \qquad (3)$$

6

where δs is a vector containing the differential time series, δm is the model perturbation, and G is a matrix of partial derivatives.
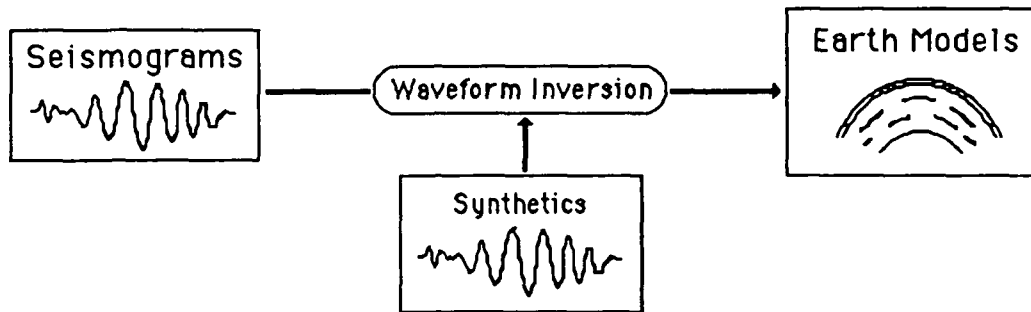

Figure 2. The more modern methodology of waveform inversion computes the differences between the observed seismograms and synthetic seismograms and inverts these differential seismograms directly for earth structure.

The primary problem with waveform inversion is its "black-box" character: it is difficult to evaluate exactly what features on the seismograms are being used to determine what features of the earth model. Waveform inversion allows more information on the seismogram to be used in constraining earth structure, but the information is of uneven quality. Amplitude and phase information gets all mixed up, so understanding the robustness of the solution to departures from the modeling assumptions (which are usually incomplete with respect to first-order amplitude perturbations) is often impossible. Moreover, the results can be very sensitive to how the data are weighted, and the resolving power of any particular data set is hard to assess. For example, it is not easy for a seismologist to know how much of the residual contained in a differential seismogram is ascribable to a one-dimensional path-averaged perturbation, as opposed to two- or three-dimensional along-path and off-path perturbations.

For the last several years, one goal of our research program has been to improve automated techniques for recovering information from seismograms. Our first efforts were directed at developing waveform-inversion algorithms [Lerner-Lam and Jordan, 1983, 1987]. In particular, we introduced matched-filtering techniques that isolated higher-mode information prior to inversion and thus facilitated the understanding of what information on the seismograms is most significant in constraining the solution. We used our ability to manipulate this information to set up various weighting schemes and investigated how they affected the resolving power of the waveform data [Gee et al., 1985]. By applying these techniques to a series of paths crossing the western Pacific Ocean and the Eurasian continent, we were able to demonstrate that the higher-mode data are inconsistent with models that confine continent-ocean heterogeneity to depths less than about 220 km [Lerner-Lam and Jordan, 1987].

7

We have recently developed a new set of techniques for extracting information from the seismogram, which are as yet unpublished although several papers are in the final stages of preparation. Like the waveform-inversion method of Lerner-Lam and Jordan [1983], they make use of the cross-correlation between waveform synthetics and the observed seismograms to isolate structural information. However, the way this information is recovered from the seismogram and then inverted for earth models is very different (Figure 3).
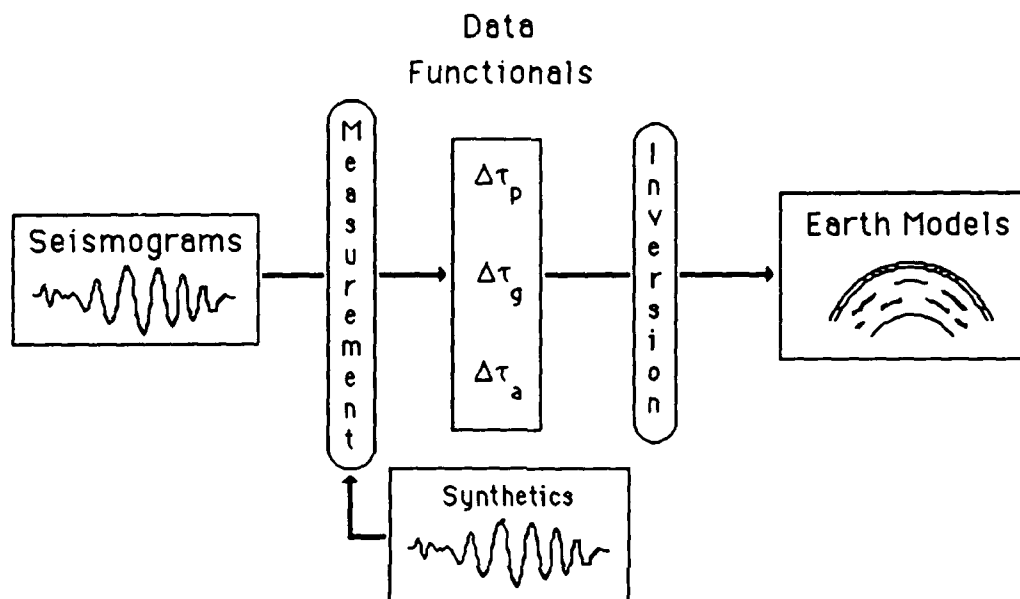

Figure 3. The methodology discussed in this proposal combines the advantages of the classical approach with those of waveform inversion. Measurements of time-like data functionals are made using synthetic seismograms to account for wave effects; e.g., caustic phase shifts, dispersion, and diffraction. These data are subsequently inverted for earth models. By separating the measurement process from the inversion process, the significance of the data and the robustness of the modeling can be more easily assessed than in a one-step, "black-box" waveform inversion scheme. The technique provides a uniform methodology for inverting body-wave, surface-wave, and other types of wave groups from three-component data. For the definitions of the data functionals $\Delta\tau_p$, $\Delta\tau_g$, and$\Delta\tau_a$, see equation (13).

Our technique is best described in the context of a simple numerical experiment. Consider the two continental structures illustrated in Figure 4: SNA, a model of stable North America which Grand and Helmberger [1984] derived by fitting SH-polarized waveforms of multiply reflected shear waves, and EU2, a model of northern Eurasia which Lerner-Lam and Jordan [1987] derived by waveform inversion of fundamental Rayleigh waves and PSV-polarized higher modes. The average upper-mantle shear velocity in SNA is significantly greater than in EU2, evidently due in part to genuine path differences and in part to strong polarization anisotropy in the upper mantle [Lerner-Lam and Jordan, 1987; Gee and Jordan, 1988]. These hypotheses are discussed in the Appendix; here we simply consider the two models to be representative of differences in regional upper-mantle structure that a seismologist might seek to determine by waveform measurements.

8

The specific problem we pose is to estimate the Love-wave dispersion of SNA using EU2 as a reference model.
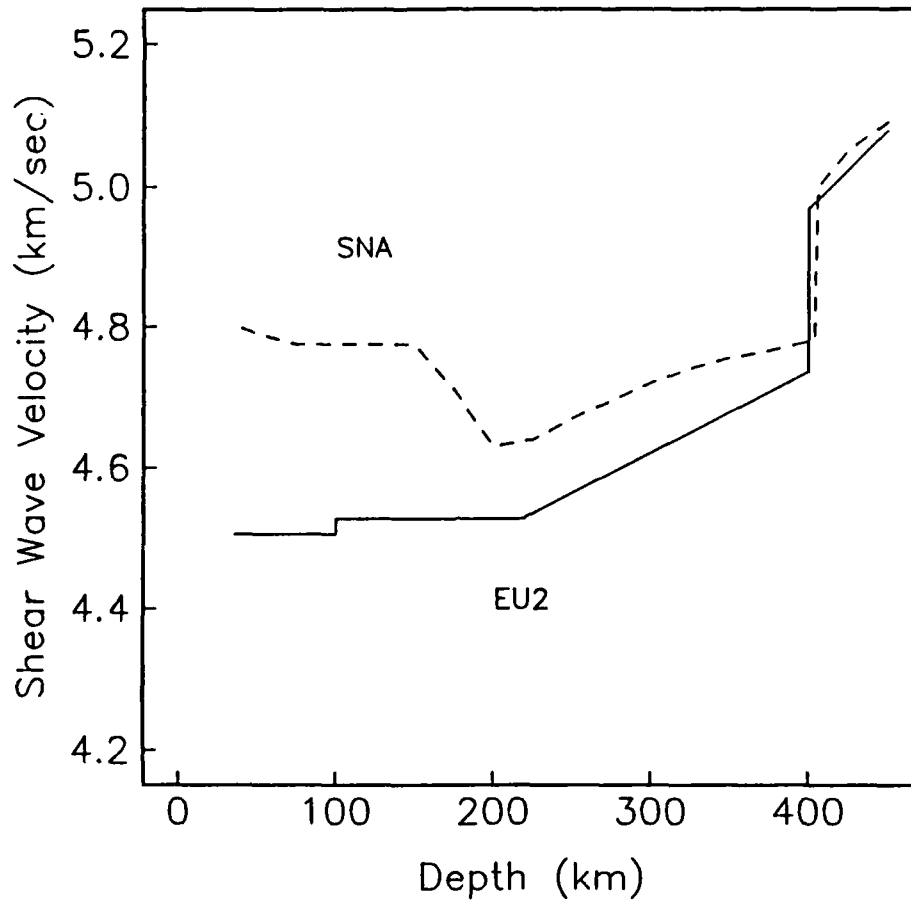

Figure 4. Shear velocity as a function of depth for continental upper mantle models EU2 [Lerner-Lam and Jordan, 1987] and SNA [Grand and Helmberger, 1984]. SNA (dashed line) was derived from fitting multiply reflected SH-polarized waveforms for stable North America paths; EU2 (solid line) was derived from waveform inversion of fundamental Rayleigh waves and *PSV*-polarized higher modes for northern Eurasia. SNA has significantly higher velocities than EU2 in the upper 400 km; the discrepancy between these models is due in part to path differences and in part to strong polarization anisotropy in the upper mantle [Lerner-Lam and Jordan, 1987; Gee and Jordan, 1988].

The basis for our waveform-analysis method is the construction of an "isolation filter" $\tilde{f}(t)$, which we define as a weighted sum over synthetic waveforms:

$$\tilde{f}(t) = \sum_{n=0}^{N} \alpha_n \, \tilde{u}_n(t) \tag{4}$$

For standard measurements of surface-wave dispersion and body-wave travel times, we usually take the coefficients α_n to be zero for all but one value of n; i.e., we choose the isolation filter to be the waveform of interest. In the case of the problem posed above, therefore, $\tilde{f}(t)$ is simply the fundamental-mode Love wave, which we calculate from the reference model EU2. Examples of transverse-component synthetics corresponding to an earthquake in Kamchatka ($83/08/17$, $h = 77$ km) recorded at the ASRO station KONO in Norway ($\Delta = 63°$) are plotted in Figure 5a.

The autocorrelation function of $\tilde{f}(t)$ is defined by

$$C_{\tilde{f}\tilde{f}}(t) = \tilde{f}(t) \otimes \tilde{f}(t) \equiv \int_{-}^{-} \tilde{f}(\tau) \, \tilde{f}(\tau + t) \, d\tau \tag{5}$$

$C_{\tilde{f}\tilde{f}}(t)$ is a symmetric function peaked at zero lag (Figure 5b) whose real-valued Fourier spectrum $C_{\tilde{f}\tilde{f}}(\omega)$ is the squared modulus of the complex Fourier spectrum $\tilde{f}(\omega)$. Before proceeding further, it will be useful to develop the properties of this autocorrelation function in terms of a set of special functions known as Hermite functions, which are defined to be the product of an unnormalized Gaussian, $G(x) \equiv \exp(-x^2/2)$, and a Hermite polynomial of degree k, $He_k(x)$ [Szegö, 1959]. These functions play an important role in the theory that underlies our method. We expand the spectrum on the positive ω-axis in terms of Hermite functions:

$$C_{\tilde{f}\tilde{f}}(\omega) \, H(\omega) = G(\frac{\omega - \omega_f}{\sigma_f}) \sum_{k=0}^{\infty} f_k \, He_k(\frac{\omega - \omega_f}{\sigma_f}) \tag{6}$$

In this expression, $H(\omega)$ is the Heaviside step function. Hermite polynomials are defined by the expression

$$He_k(x) = k! \sum_{j=0}^{[k/2]} \frac{(-1)^j \, x^{k-2j}}{2^j \, j! \, (k-2j)!} \tag{7}$$

Sansone [1959] and Szegö [1959] give further definitions and properties; in particular, on the interval $(-\infty, \infty)$ the functions $\{He_k(x) : k = 0, 1, 2, ...\}$ are complete and orthogonal with respect to the Gaussian weight $G(x)$. The coefficients in (6) are given by

10

$$f_k = \frac{1}{k!\,\sqrt{2\pi}\,\sigma_f} \int_0^\infty C_{\tilde{f}\tilde{f}}(\omega)\,He_k\left(\frac{\omega-\omega_f}{\sigma_f}\right) d\omega \qquad (8)$$

An expansion of $C_{\tilde{f}\tilde{f}}(\omega)$ in terms of Hermite functions has two advantages. First, the convenient Fourier-transform properties of Hermite functions [Szegö, 1959] yield a simple series expression for its time-domain image:

$$C_{\tilde{f}\tilde{f}}(t) = \sqrt{2/\pi}\,\sigma_f\,G(\sigma_f\,t)\,[(f_0 - f_2\,\sigma_f^2\,t^2 + f_4\,\sigma_f^4\,t^4 - \ldots)\cos\omega_f t$$
$$- (f_1\,\sigma_f t - f_3\,\sigma_f^3\,t^3 + f_5\,\sigma_f^5\,t^5 - \ldots)\sin\omega_f t\,] \qquad (9)$$

Second, because $C_{\tilde{f}\tilde{f}}(\omega)$ is expected to be peaked in the pass-band of the instrument response, (9) can usually be approximated by its first few terms. We can always choose the location parameter ω_f such that $f_1 = 0$, and the scale parameter σ_f such that $f_2 = 0$. Therefore, if terms of third and higher order can be neglected, then we obtain the standard "wave-packet" approximation [e.g., Bracewell, 1978]:

$$C_{\tilde{f}\tilde{f}}(t) = E(t)\cos\Phi(t) \qquad (10)$$

where $E(t) = \sqrt{2/\pi f_0}\,\sigma_f\,G(\sigma_f t)$ and $\Phi(t) = \omega_f t$. In other words, the autocorrelation function of the isolation filter can be represented as a cosinusoidal "carrier" modulated by a Gaussian "envelope". The carrier frequency is the center frequency of the response, ω_f, and the half-width of the envelope is the inverse of the half-bandwidth, σ_f. Because equation (10) corresponds to taking the spectrum $C_{\tilde{f}\tilde{f}}(\omega)$ to be a Gaussian with $\sigma_f \ll \omega_f$, we refer to it as the "Gaussian narrow-band approximation".

Figure 5b shows the good agreement between the actual autocorrelation function computed for the ASRO response to the Love wave (solid line) and that obtained from the narrow-band approximation (dotted line). In this comparison, the parameters of the Gaussian were computed from the first three polynomial moments of the spectrum.

Now consider the cross-correlation between the isolation filter and the complete synthetic seismogram, $C_{\tilde{f}\tilde{s}}(t) = \tilde{f}(t) \otimes \tilde{s}(t)$, and the cross-correlation between the isolation filter and the observed seismogram, $C_{\tilde{f}s}(t) = \tilde{f}(t) \otimes s(t)$. If the isolation filter corresponds to a single waveform that is reasonably well separated from other energy on the seismogram, then $C_{\tilde{f}\tilde{s}}(t)$ will closely approximate $C_{\tilde{f}\tilde{f}}(t)$ near zero lag. Figure 5b shows that this is indeed the case for our Love-wave example. $C_{\tilde{f}s}(t)$, on the other hand, will not be the same as $C_{\tilde{f}\tilde{f}}(t)$ because of differences in propagation, which we hope to measure, as well as differences between the actual

11

and assumed source mechanisms, which we ignore, at least for the present discussion. (In practice, we have generally found the Harvard CMT solutions to be adequate for the sorts of modeling we propose here; when they are not, we have the capability to determine our own moment-tensor solutions.) We suppose the actual waveform f has a spectrum that is related to the synthetic $\tilde{f}$ by a differential response operator D:

$$f(\omega) = D(\omega)\tilde{f}(\omega) \tag{11}$$

We write the differential response in the form $D(\omega) = D_0 e^{i\Delta k(\omega)x}$, where D_0 is a real-valued constant, x is the propagation distance, and $\Delta k(\omega) \equiv k(\omega) - \tilde{k}(\omega)$ is the complex-valued differential wavenumber. We expand the latter in a Taylor series about the center frequency ω_f:

$$\Delta k(\omega) = \Delta k(\omega_f) + (\omega - \omega_f)\,\Delta k'(\omega_f) + \frac{(\omega - \omega_f)^2}{2}\,\Delta k''(\omega_f) + \cdots \tag{12}$$

If the differential dispersion is sufficiently weak across the band $\omega_f \pm \sigma_f$, then we can neglect terms of order higher than the first, and (12) becomes

$$\Delta k(\omega) = x^{-1}\,[\,\omega_f\,\Delta\tau_p(\omega_f) + (\omega - \omega_f)\,\Delta\tau_g(\omega_f) + i\,(\omega - \omega_f)\,\Delta\tau_a\,] \tag{13}$$

$\Delta\tau_p(\omega_f)$ is the differential phase delay at the center frequency ω_f; $\Delta\tau_g(\omega_f)$ is the differential group delay; and $\Delta\tau_a(\omega_f)$ is a differential amplitude factor. In the case where the differential amplitude is due solely to attenuation, $\Delta\tau_a(\omega_f)$ is the difference between the actual and reference values of t^*, defined to be the travel time divided by twice the quality factor Q.

Under the linear dispersion approximation (13) we can obtain closed-form expressions for the coefficients of a complete Hermite-function expansion of $C_{\tilde{f}f}(t)$. Since the expressions are fairly complicated, we do not reproduce them here. Instead, we give explicit formulae for the Gaussian narrow-band approximation, $C_{\tilde{f}f}(t) = E(t)\cos\Phi(t)$:

$$E(t) = \sqrt{2/\pi}\,f_0\,\sigma_f D_0\,e^{\sigma_f^2\,\Delta\tau_a^2/2}\,G(\sigma_f\,(t - \Delta\tau_g)) \tag{14a}$$

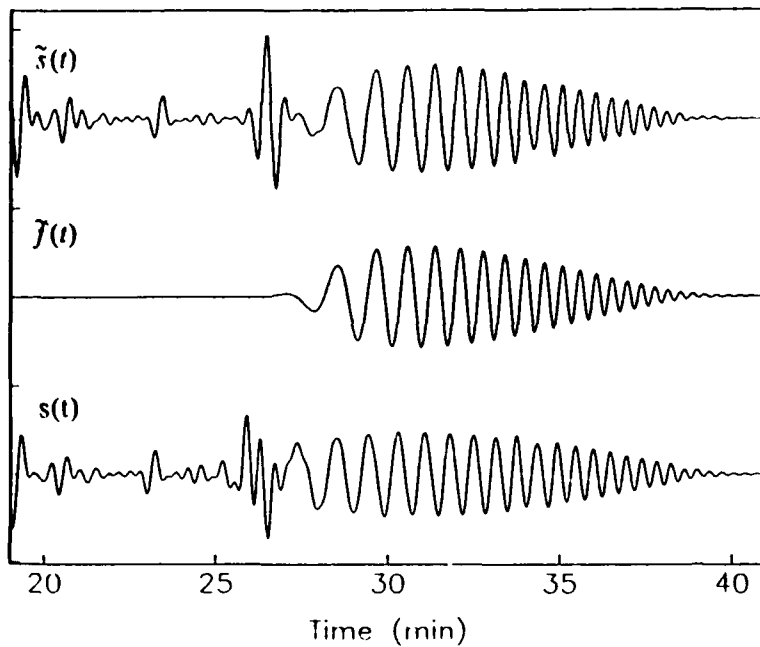$$\Phi(t) = \omega_f\,(\Delta\tau_p - t) - \sigma_f^2\,\Delta\tau_a\,(\Delta\tau_g - t) \tag{14b}$$

Figure 5a. Transverse component synthetic seismograms calculated from models EU2 and SNA for a Kamchatka event (83/08/18, h=77km) recorded at the ASRO station KONO. $\tilde{s}(t)$ is the seismogram calculated from EU2; $s(t)$ is the seismogram calculated from SNA. $\tilde{f}(t)$ is the isolation filter for the Love wave, calculated from EU2. All three synthetic seismograms were calculated by normal mode summation and are complete to 50 mHz. For $\tilde{s}(t)$ and $s(t)$, this represents a sum of over 16000 modes; for $\tilde{f}(t)$ a sum over 500 modes.
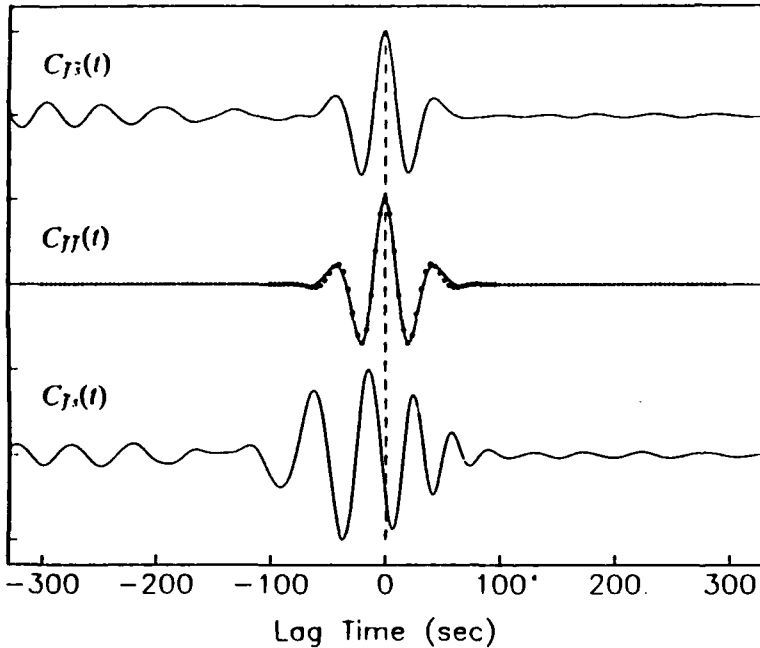

Figure 5b. $C_{\tilde{f}\tilde{s}}(t)$, $C_{\tilde{f}\tilde{f}}(t)$, and $C_{\tilde{f}s}(t)$ calculated from the seismograms in Figure 5a. $C_{\tilde{f}\tilde{f}}(t)$ is a symmetric function, peaked at zero lag. The dotted line is the Gaussian narrow-band approximation to $C_{\tilde{f}\tilde{f}}(t) = E(t) \cos\omega_f t$ (equation 10); in this example, ω_f is 23 mHz and σ_f is 6.2 mHz. The Gaussian narrow-band approximation is valid near zero lag. If the waveform of interest is isolated in the time domain, then $C_{\tilde{f}\tilde{s}}(t) \approx C_{\tilde{f}\tilde{f}}(t)$ near zero lag, which is the case in this example. However, $C_{\tilde{f}s}(t)$ will not in general be the same as $C_{\tilde{f}\tilde{s}}(t)$ due to differences in propagation, which we hope to measure, as well as differences in actual and assumed source mechanisms, which we presently ignore.
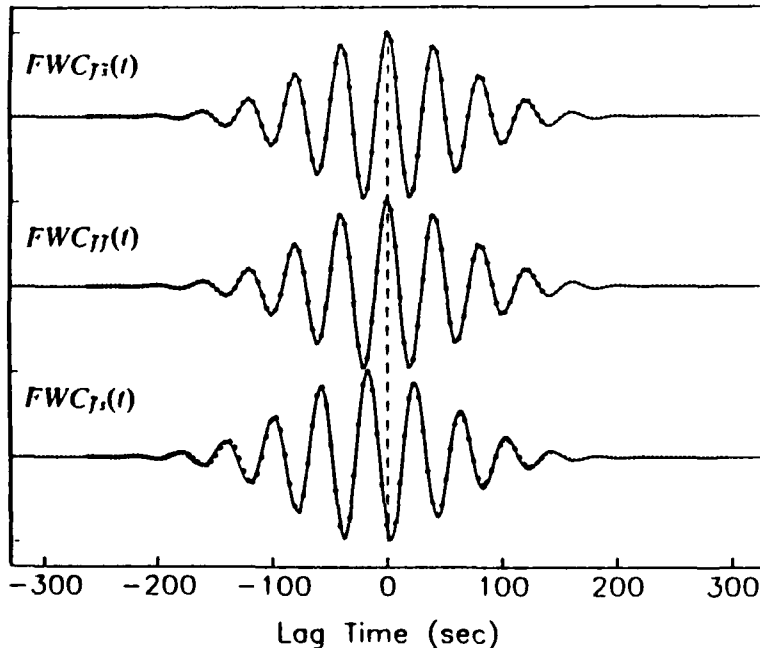

Figure 5c. Comparisons between the calculated filtered windowed cross-correlation functions $F_i WC_{\tilde{f}\tilde{s}}(t)$, $F_i WC_{\tilde{f}\tilde{f}}(t)$, and $F_i WC_{\tilde{f}s}(t)$, given by the solid line, and the functions obtained by fitting the analytic expressions for the Gaussian approximation for a filter with a center frequency of 25mHz and bandwidth of 2.5 mHz, given by the dotted line. The fit of the Gaussian approximation to the observed values, which is excellent, determines the values of $\Delta\tau_p$, $\Delta\tau_g$, and $\Delta\tau_a$ (equation 13).

13

It is possible to fit the narrow-band expression to the observed function $C\tilde{\jmath}s(t)$ and thereby determine the values of $\Delta\tau_p(\omega_f)$, $\Delta\tau_g(\omega_f)$, and $\Delta\tau_a(\omega_f)$. For the case at hand, however, the results are poor, primarily because the differential dispersion is sufficiently strong that equation (13) does not provide an adequate approximation across the entire bandwidth of the ASRO instrument response.

We could, of course, pre-filter the seismograms in narrow bands of our choosing and thus enforce the weak-dispersion approximation, but this spreads the energy over the time series and increases the interference with other waveforms. For this reason, we include two additional steps in our processing: (1) We first apply a Hanning taper of half-width σ_w^{-1} centered at a reference time t_w to the cross-correlation function, yielding a windowed cross-correlation function $WC\tilde{\jmath}s(t)$. (2) We then apply to $WC\tilde{\jmath}s(t)$ a series of narrow-band filters $\{F_i : i = 1, \dots , I\}$ with varying center frequencies ω_i and half-bandwidths $\sigma_i << \omega_i$, yielding the filtered, windowed cross-correlation functions $F_i WC\tilde{\jmath}s(t)$. Windowing the broad-band correlation function prior to narrow-band filtering allows the full bandwidth to be used to separate the waveform of interest from other interfering arrivals. This procedure has been previously employed in residual-dispersion and phase-matched filtering analysis [Dziewonski *et al.*, 1972; Herrin and Goforth, 1977, 1986], to which our techniques are closely related.

We have obtained closed-form formulae for the Hermite-function coefficients that allow each $F_i WC\tilde{\jmath}s(t)$ to be computed to arbitrary accuracy, but even the equations for the Gaussian approximation are sufficiently complicated that we do not give them here. These expressions depend upon a number of quantities that are either known (the four parameters t_w, σ_w, ω_i, and σ_i) or can be determined by fitting the Gaussian expressions to the synthetic autocorrelation function (the parameters ω_f and σ_f), and three quantities that depend on the differential response (the observables $\Delta\tau_p(\omega'_i)$, $\Delta\tau_g(\omega'_i)$, and $\Delta\tau_a(\omega'_i)$). The latter are functions of the effective center frequency

$$\omega'_i = \frac{\omega_f \sigma_i^2 + \omega_i (\sigma_f^2 + \sigma_w^2)}{\sigma_f^2 + \sigma_w^2 + \sigma_i^2} \qquad (15)$$

and can be estimated by fitting the Gaussian approximation to the observed time series $F_i WC\tilde{\jmath}s(t)$.

Figure 5c displays the results of this waveform-analysis procedure to our Love-wave example. The fit obtained is excellent, and the phase and group delays recovered from it are close to the theoretical values (the attenuation structure was not perturbed). The results for center frequencies varying from 13 to 42 mHz for both Love and Rayleigh waves from this single station are plotted against the theoretical values in Figure 6. Additional synthetic tests have been done to assess the performance of the method in recovering body-wave travel times, including times from triplicated

14

branches, and quality factors (see Figure 7). Formal errors in the observed times are easily derived from the waveform fits, and we will include this uncertainty analysis into our automated procedures.

The observables $\Delta\tau_p$, $\Delta\tau_g$, and $\Delta\tau_a$ are functionals of earth structure. In the case where the isolation filter $\hat{f}(t)$ is a single waveform, the Fréchet kernels are known [Aki and Richards, 1980]. Hence, once they have been measured and their uncertainties determined as a function of frequency (and source-receiver position) by fitting the Gaussian narrow-band expressions to $F_i WC_{\hat{f}s}(t)$, they are easily inverted for structural models using standard linearized methods. If the interference by other waveforms is not severe, this inversion can be accomplished independently of the measurement. If the interference is significant, so that $C_{\hat{f}f}(t)$ is not a good approximation to $C_{\hat{f}s}(t)$ near zero lag, then we can correct the measurements by the values of the parameters determined from $F_i WC_{\hat{f}s}(t)$. If it is really severe, so that these corrections are themselves inaccurate, then it may be necessary to proceed by iterating between the data analysis and the data inversion. We have thus far not encountered examples where this is required.

It is important to note that we do not require that the isolation filters $\hat{f}(t)$ accurately model the waveforms they are intended to represent, so long as we have available a complete synthetic seismogram $\tilde{s}(t)$ that does. In our applications, we generally compute $\tilde{s}(t)$ by complete normal-mode summation (regularly up to 50 mHz for *PSV* components and 100 mHz for *SH*), whereas we use approximate ray-theoretic methods (e.g., WKBJ) to calculate the isolation filters for body waves. We then employ the differential phase and group delays computed from $FWC_{\hat{f}s}(t)$ to correct the observations for inaccuracies in the ray-theoretic approximations. Using this hybrid capability, we can thus combine the computational efficiency and theoretical insight offered by asymptotic traveling-wave representations with the computational accuracy and uniform methodology afforded by normal-mode summation.

We have applied these techniques to the study of upper-mantle structure beneath the Eurasian and North American continents. Some highlights of the Eurasian results have been recently published in a short note to *Geophysical Research Letters* [Gee and Jordan, 1988], which is reproduced here as an appendix. In particular, by treating waveforms of differing polarizations using a uniform methodology we have been able to observe shear-wave splitting as large as 10 s on *S* waves multiply reflected beneath the Siberian and Russian platforms (see Figures 8 and 9).
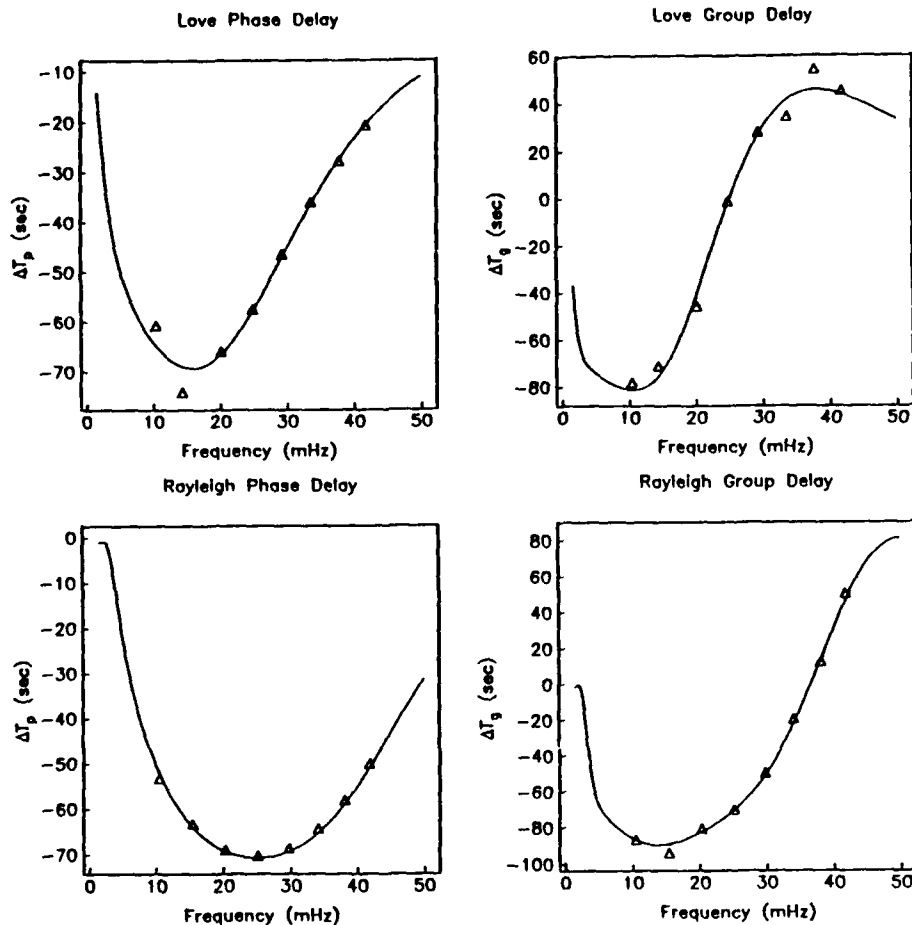
Figure 6. Estimates of $\Delta\tau_p(\omega_i')$ and $\Delta\tau_g(\omega_i')$ (attenuation structure was not perturbed) recovered using this waveform analysis procedure for fundamental Love and Rayleigh waves (triangles) compared to the theoretical values for SNA-EU2 (solid lines). In general, the agreement between the actual and estimated values are very good, although there is more scatter in the Love wave dispersion due to the greater interference from higher modes (see Figure 5a).
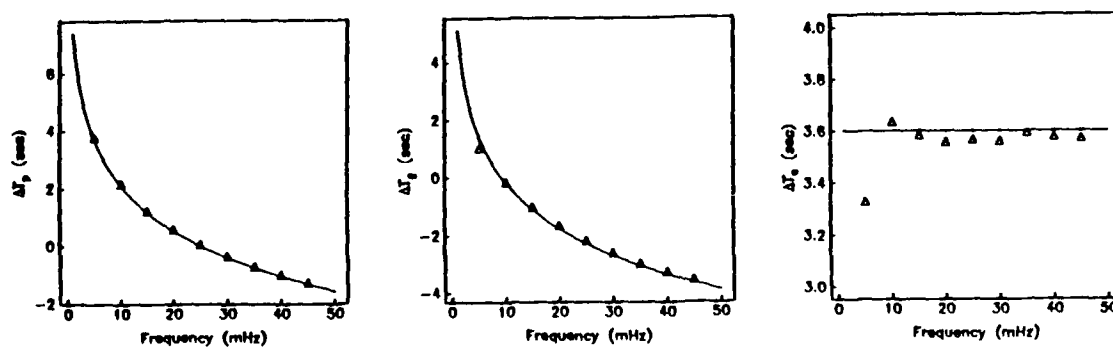

Figure 7. Estimates of $\Delta\tau_p(\omega_i')$, $\Delta\tau_g(\omega_i')$, and $\Delta\tau_a(\omega_i')$ recovered from a numerical experiment in which the "observed seismograms" were calculated from a model having a linear, causal, constant Q and the isolation filter was calculated from a reference model having no intrinsic attenuation. Estimates of $\Delta\tau_p(\omega_i')$, $\Delta\tau_g(\omega_i')$, and $\Delta\tau_a(\omega_i')$ (triangles) compare favorably with the theoretical values (solid line).
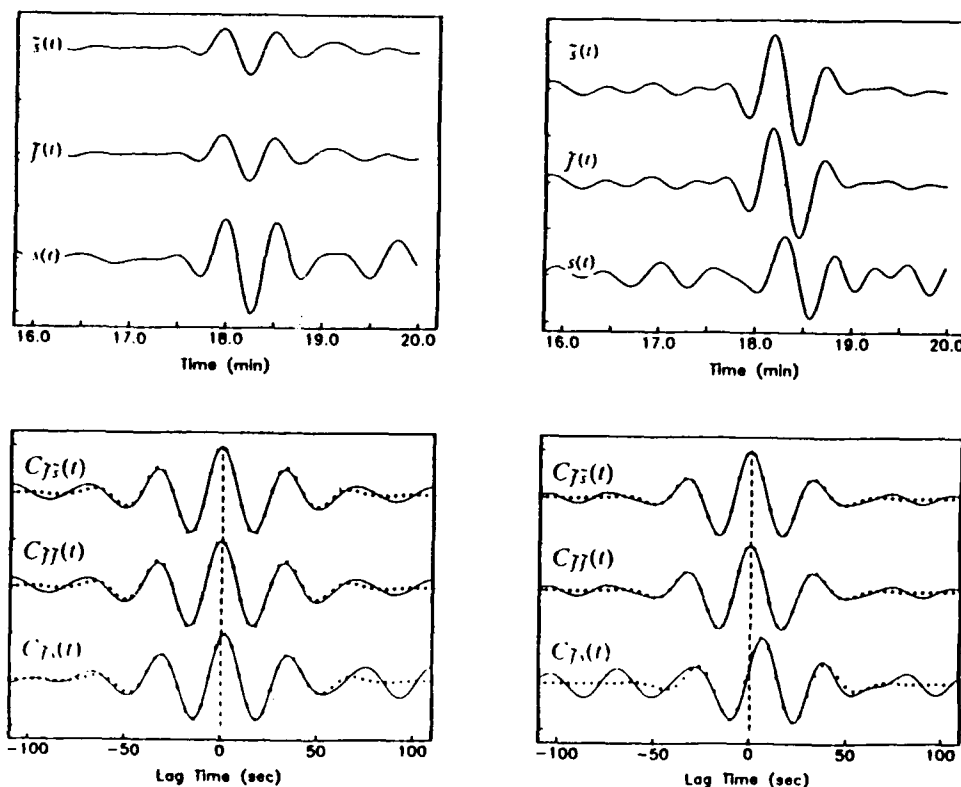
16

Figure 8. Application of the waveform analysis procedures to shear-wave splitting in Eurasia. a) contains the observed transverse component seismogram recorded at KONO for a Hindu Kush earthquake (84/07/01, h = 199 km); the complete synthetic seismogram and the isolation filter for SS, calculated from SNA. b) contains the observed vertical component and the appropriate synthetic seismograms. c) and d) display the correlation functions for the transverse and vertical seismograms. We have estimated $\Delta\tau_p^{SH}(30 \text{ mHz}) = 2.1 \pm 1.0$ s and $\Delta\tau_p^{SV}(30 \text{ mHz}) = 6.3 \pm 1.0$ s. Thus, the total apparent splitting time for SS is $\Delta\tau_{SS} = \Delta\tau_p^{SH} - \Delta\tau_p^{SV}$ is 4.2 ± 1.4 s.
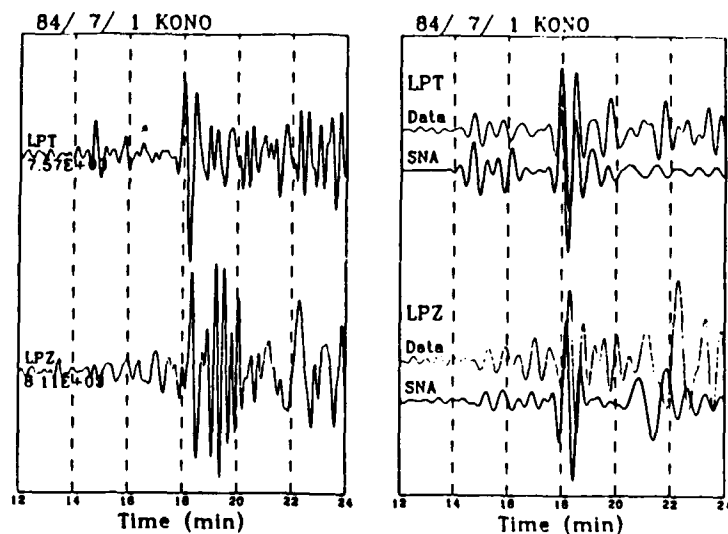

Figure 9. Raw observed vertical and transverse component seismograms (left panel) and filtered synthetic and data (right panel). The apparent shear-wave splitting is dramatically shown by the data-synthetic comparisons, but is also striking in the unfiltered data. For further discussion of these and other observations of shear-wave splitting in Eurasia, see the Appendix.

17

REFERENCES

Aki, K., and P. Richards, Quantative Seismology, vol 1., Freeman and Co., San Francisco, 557p., 1980.

Cara, M., Lateral variations of S velocity in the upper mantle from higher Rayleigh modes, *Geophys. J. R. Astr. Soc.*, *57*, 649-670, 1979.

Cara, M., A. Nercessian, and G. Nolet, New inferences from higher mode data in western Europe and northern Eurasia, *Geophys. J. R. Astr. Soc.*, *61*, 459-478, 1980.

Clayton, R. W., and R. P. Comer, A tomographic analysis of mantle heterogeneities from body wave travel times (abstract), *EOS. Trans. AGU*, *62*, 776, 1983.

Creager, K. C., and T. H. Jordan, Slab penetration into the lower mantle beneath the Mariana and other Island Arcs of the Northwest Pacific, *J. Geophys. Res.*, *91*, 3573-3589, 1986a.

Creager, K.C., and T.H. Jordan, Aspherical structure of the core-mantle boundary from PKP travel times, *Geophys. Res. Lett.*, *13*, 1497-1500, 1986b.

Dziewonski, A. M., Mapping the lower mantle: Determination of lateral heterogeneity in *P*-velocity up to degree and order 6, *J. Geophys. Res.*, *89*, 5929-5952, 1984.

Dziewonski, A. M., and D. L. Anderson, Preliminary reference Earth model, *Phys. Earth Planet. Inter.*, *25*, 297-356, 1981.

Dziewonski, A. M., and F. Gilbert, Observations of normal modes for 84 recordings of the Alaskan earthquake of 1964 March 28. Part II: Further remarks based on new spheroidal overtone data, *Geophys. J. R. Astr. Soc.*, *35*, 401-437, 1973.

Dziewonski, A. M., and J. M. Steim, Dispersion and attenuation of mantle waves through waveform inversion, *Geophys. J. R. Astr. Soc.*, *70*, 503-527, 1982.

Dziewonski, A. M., and J. H. Woodhouse, Global images of the Earth's interior, *Science*, *236*, 37-48, 1987.

Dziewonski, A. M., J. Mills, and S. Bloch, Residual dispersion measurement - a new method of surface-wave analysis, *Bull. Seis Soc. Am.*, *62*, 129-139, 1972.

Dziewonski, A. M., B. H. Hager, and R. J. O'Connell, Large-scale heterogeneities in the lower mantle, *J. Geophys. Res.*, *82*, 239-255, 1977.

Gee, L. S., A. L. Lerner-Lam, and T. H. Jordan, Resolving power of higher-mode waveform inversion for Eurasian upper-mantle structure, *AFGL Technical Report 85-0206*, Air Force Geophysical Laboratory, Cambridge, pp. 11-36, 1985. ADA165228

Gee, L. S., and T. H. Jordan, Polarization anisotropy and fine-scale structure of the Eurasian upper mantle, *Geophys. Res. Lett.*, *15*, 824-827, 1988.

Giardini, D., X.-D. Li, and J. H. Woodhouse, Three-dimensional structure of the Earth from splitting in free-oscillation spectra, *Nature*, *325*, 405-411, 1987.

Grand, S. P., and D. V. Helmberger, Upper mantle shear structure of North America, *Geophys. J. R. Astr. Soc.*, *76*, 399-438, 1984.

Hager, B. H., R. W. Clayton, M. A. Richards, R. P. Comer, and A. M. Dziewonski, Lower mantle heterogeneity, dynamic topography and the geoid, *Nature, 313*, 541-545, 1985.

Herrin, E., and T. Goforth, Phase-matched filters: application to the study of Rayleigh waves, *Bull. Seis Soc. Am., 67*, 1259-1275, 1977.

Herrin, E., and T. Goforth, Phase analysis of Rayleigh waves from the Shagan River test site in the USSR, *Bull. Seis Soc. Am., 76*, 1739-1754, 1977.

Julian, B. R., D. Davies, and R. M. Sheppard, PKJKP, *Nature, 235*, 317-318, 1972.

Jordan, T. H., A. L. Lerner-Lam, and K. C. Creager, Seismic imaging of boundary layers and deep mantle convection, in Mantle Convection, ed. W. R. Peltier, in press, 1988.

Lerner-Lam, A. L., and T. H. Jordan, Earth structure from fundamental and higher-mode waveform analysis, *Geophys. J. R. Astr. Soc., 75*, 759-797, 1983.

Lerner-Lam, A. L., and T. H. Jordan, How thick are the continents?, *J. Geophys. Res., 92*, 14007-14026, 1987.

Leveque, J. J., and M. Cara, Long-period Love wave overtone data in North America and the Pacific Ocean: new evidence for upper mantle anisotropy, *Phys. Earth Planet. Inter., 33*, 164-179, 1983.

Masters, G., and F. Gilbert, Structure of the inner core inferred from observations of its spheroidal shear modes, *Geophys. Res. Lett., 8*, 569-571, 1981.

Masters, G., T. H. Jordan, P. G. Silver, and F. Gilbert, Aspherical earth structure from fundamental spheroidal-mode data, *Nature, 298*, 609-613, 1982.

Nataf, H.-C., I. Nakanishi, and D. L. Anderson, Anisotropy and shear-velocity heterogeneities in the upper mantle, *Geophys. Res. Lett., 11*, 109-112, 1984.

Nataf, H.-C., I. Nakanishi, and D. L. Anderson, Measurements of mantle wave velocities and inversion for lateral heterogeneities and anisotropy, 3, Inversion, *J. Geophys. Res., 91*, 7261-7307, 1986.

Nolet, G., Higher Rayleigh modes in wester Europe, *Geophys. Res. Lett., 2*, 60-62, 1975.

Nolet, G., The upper mantle structure under western Europe inferred from the dispersion of Rayleigh modes, *J. Geophys., 43*, 265-285, 1977.

Revenaugh, J., and T. H. Jordan, Observations of first-order mantle reverberations, *Bull. Seis Soc. Am., 77*, 1704-1717, 1987.

Revenaugh, J., and T. H. Jordan, A study of mantle layering beneath the western Pacific, *J. Geophys. Res., in press*, 1989.

Ritzwoller, M., G. Masters, and F. Gilbert, Observations of anomalous splitting and their interpretation in terms of aspherical structure, *J. Geophys. Res., 91*, 10203-10228, 1986.

Sansone, G., Orthogonal functions, Pure and Applied Mathematics, vol. IX, Intersciences Publishers, New York, 411p, 1959.

Szegö, G., Orthogonal Polynomials, American Mathematical Society Colloquim Publications, vol. 23, American Mathematical Society, Providence, 421p., 1959.

Widmer, R., G. Masters, and F. Gilbert, The spherically symmetric earth: observational aspects and constraints on new models (abstract), *EOS Trans. AGU , 69*, 1310, 1988.

Woodhouse, J. H., and A. M. Dziewonski, Mapping the upper mantle: three-dimensional modeling of earth structure by inversion of seismic waveforms, *J. Geophys. Res.*, *89*, 5953-5986, 1984.

POLARIZATION ANISOTROPY AND FINE-SCALE STRUCTURE OF THE EURASIAN UPPER MANTLE

LIND S. GEE AND THOMAS H. JORDAN

Department of Earth, Atmospheric, and Planetary Sciences, Massachusetts Institute of Technology

Abstract. We have observed shear-wave splitting, with $(t_{SH}-t_{SV})/t_{SV}$ up to 1.5%, on long-period records of multiply reflected S waves bottoming in the upper mantle beneath the Russian and Siberian platforms. The dispersion of Love and Rayleigh waves over these paths shows discrepancies of comparable or larger magnitude with respect to smooth, isotropic (SI) structures, consistent with a model of the uppermost mantle having significant apparent vertical anisotropy. Although the splitting and dispersion data can be fit by smooth, anisotropic (SA) models, we have investigated the apparent anisotropy associated with fine-scale ("rough") structure beneath stable Eurasia. We fit the data with a rough, isotropic (RI) model having an rms shear velocity fluctuation that varies from 14% in the uppermost mantle to zero at 400-km depth. These fluctuations are larger than the variation in isotropically averaged parameters expected for even a diverse assemblage of upper-mantle ultrabasic rocks, which we take to be evidence for some sort of intrinsic (local) anisotropy.

Introduction

Although seismological studies have begun to illuminate the fine structure of the upper mantle, very little can yet be said to quantify the spatial distribution of wave-speed heterogeneity and anisotropy. A particularly interesting region for the study of small-scale structure is the continental upper mantle, where comparisons between data and the predictions of smooth, isotropic (SI) earth models reveal several discrepancies:

Love-Rayleigh (LR) discrepancy. The problems of satisfying the dispersion of Love and Rayleigh waves by SI structures is well documented [McEvilly, 1964; Cara et al., 1980; Lévêque and Cara, 1983]. The discrepancy appears to be global in nature, and some form of radial anisotropy (our preferred term for the type of anisotropy whose contrapositive is transverse isotropy) is usually invoked to explain it [e.g., Anderson and Dziewonski, 1982]. The significance of the LR discrepancy for the continents has been debated [James, 1971; Mitchell, 1984].

SNA-EU2 discrepancy. Structures of the upper mantle beneath stable cratons derived from waveform matches to SH-polarized waves, specifically the SNA model of Grand and Helmberger [1984], have consistently higher v_s values in the upper 400 km than structures derived from PSV-polarized waves, specifically the EU2 model of Lerner-Lam and Jordan [1987]. Lerner-Lam and Jordan argue that the SNA-EU2 discrepancy cannot be entirely explained by path differences and must involve polarization anisotropy in the continental upper mantle.

Sn discrepancy. The apparent velocities of high-frequency (~1 Hz) Sn waves on both horizontal and vertical components are typically 100–300 m/s higher than the average shear velocity v_s of the uppermost mantle inferred from low-frequency (~.01 Hz) Rayleigh waves. Although not systematically treated in the literature, this problem is evident in the comparison of the Sn velocities of Heustis et al. [1973] with Rayleigh-wave models such as EU2 (Figure 1).

In this paper, we report some new observations of shear-wave splitting for multiple-S waves bottoming beneath Eurasia that are relevant to these discrepancies, and we attempt to explain them in terms of a stochastic model of fine-scale upper-mantle structure.

Observations

We have measured the travel times (both phase and group delays) of direct and multiply reflected S waves and
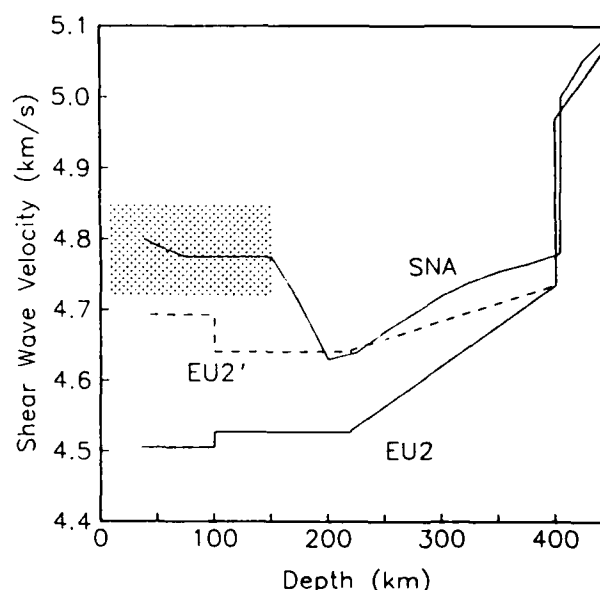
Fig. 1. Shear velocity as a function of depth for continental models EU2 and SNA. Stippling indicates the range of regional Sn velocities typical of continental cratons [Heustis et al., 1973]. The dashed line labeled EU2' is the SH velocity structure corresponding to the RI model in Table 1.

fundamental-mode surface waves on 40 three-component records from the Global Digital Seismic Network (GDSN) stations KONO and GRFO for two corridors across Eurasia (Figure 2). The northern Eurasia corridor is nearly identical to that used in deriving EU2; it includes the marginal basins and active foldbelts east of the Verkhoyansk suture, as well as the stable cratons of the Siberian and Russian platforms. The southwestern Eurasia corridor includes two paths, one crossing the central part of the Russian platform from Hindu Kush events to KONO, and one traversing the southwestern margin of the platform along the Alpine-Himalayan front to GRFO. Large variations in SS travel times are observed across the transition from the Russian platform to the Alpine-Himalayan orogenic belt, the latter yielding times delayed by as much as 20-30 s [Rial et al., 1984]. Grand and Helmberger [1985] find that SNA satisfies the data from SH body waves propagating across the central Russian platform.

Our technique for measuring travel times is based the ability to synthesize complete seismograms by normal-mode summation [Gee and Jordan, 1986]. A narrow-band isolation filter for a particular wave group, such as a body-wave pulse or a fundamental-mode surface wave, is computed by a convenient method (we use both ray and mode theoretic algorithms) and cross-correlated with both the observed seismogram and the complete normal-mode synthetic for an appropriate source location and mechanism. The difference between the peak times of the observed and synthetic cross-correlation functions is measured and corrected for differential dispersion and attenuation to obtain the differential phase-delay time Δt at the center frequency f_0 of the isolation filter. Δt thus measures the difference between the true arrival time and the model-predicted time at f_0. This phase-isolation technique provides a self-consistent methodology for measuring the travel times of complex wave groups on three-component seismograms. The complications handled by the technique include caustic phase shifts, interference among multiple arrivals, dispersion, attenuation, and differences in polarization.
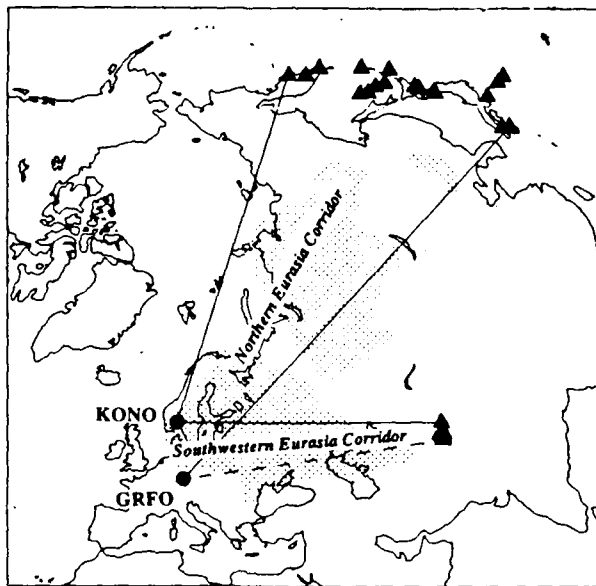
824

Fig. 2. Azimuthal equidistant projection centered on KONO, illustrating the source-receiver geometry. Triangles are earthquake locations; octagons are receiver locations. Shields and stable platforms (shaded) are from Jordan [1981].

For the body-wave data presented in this paper, the center frequencies of the isolation filters range from 25-30 mHz, and their bandwidths from 8-10 mHz; the standard errors of measurement are typically 1-2 s, excluding the bias due to unmodeled interference. The surface waves were measured in the band $10 \leq f_0 \leq 25$ mHz using isolation filters with bandwidths of $0.15 f_0$, yielding an experimental precision of $\sim 0.1 f_0^{-1}$, or about 5 s for a 20-mHz observation.

Examples of seismograms on which these measurements have been made are presented in Figures 3 and 4. The best match between data and synthetics is obtained by using EU2 as the reference model for computing the isolation filters and complete synthetics for the northern Eurasia corridor and SNA for the southwestern Eurasia corridor (although the results of the data
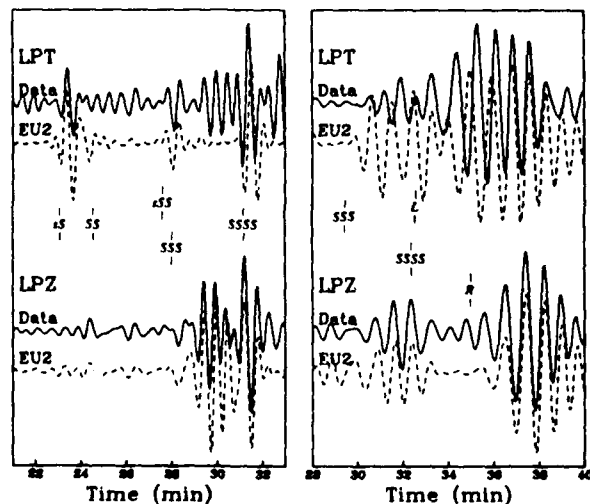

Fig. 3. Comparison of transverse and vertical component seismograms from northern Eurasian paths with EU2 synthetics. (a) Shear-wave splitting in $SSSS$ at GRFO for the 01 Feb 84 Sea of Okhotsk event. Observed seismograms shifted by +2.5 s to align the $SSSS$ pulse on the vertical component; $\Delta\tau_{SSSS}$ is 6 s. (b) LR discrepancy at KONO for the 25 Aug 83 Kyushu event. Observed seismograms shifted by +3.2 s to align the Rayleigh wave; $\Delta\tau_{LR}$ is 39 s for $f_0 = 20$ mHz.
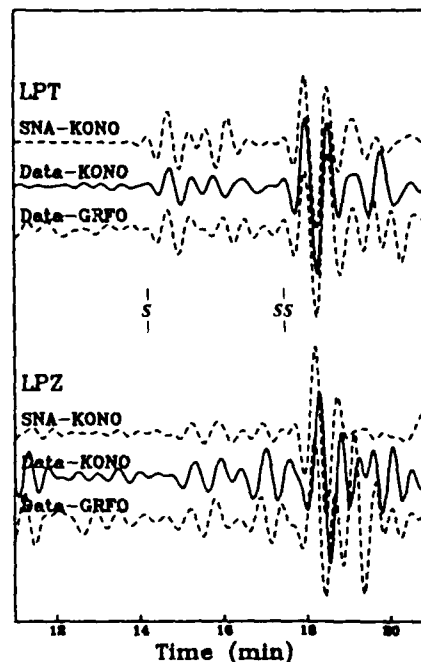

Fig. 4. Example of shear-wave splitting in SS for a path crossing the Russian platform from the 01 Jul 84 Hindu Kush event. The traces for GRFO have been shifted by +2.5 s and the traces for KONO have been shifted by +1.5 s to align the SS pulses with the SNA synthetic on the transverse component. $\Delta\tau_{SS}$ is 5 s for KONO, but less than 1 s for GRFO.

analysis are essentially independent of this choice). EU2 provides a good fit to the Rayleigh waves and PSV-polarized waveforms of multiply reflected S phases for the northern Eurasia corridor, but is too slow for the Love waves and SH-polarized phases with turning points in the upper mantle (Figure 3). SNA is generally consistent with the waveforms and travel times of SH-polarized body phases for paths to KONO across the Russian platform, but is too fast for the PSV-polarized SS phases with turning points in the upper mantle (Figure 4).

On the other hand, the path to GRFO along the southwestern margin of the Russian platform does not show this polarization difference; the observed travel times exceed those predicted by SNA by about 15 s on both components, consistent with the SH observations of Rial et al. [1984]. Shifting the synthetics by this amount aligns the SH and PSV waveforms equally well. Therefore, the data-synthetic comparisons indicate strong shear-wave splitting for the northern Eurasia and central Russian platform paths, but not for paths along the Alpine-Himalayan front.

To quantify the polarization difference in the data-model residual for a specific source-receiver pair, we define an "apparent splitting time" by

$$\Delta\tau = \Delta t_{SH} - \Delta t_{PSV} \qquad (1)$$

where Δt_{SH} is the phase-delay time measured for a particular wave group on the transverse component and Δt_{PSV} is the phase-delay time for the corresponding wave group on the vertical component. In the case of body waves, we employ the standard phase notation as a subscript; e.g., $\Delta\tau_{SS}$ is the difference between the travel-time residual for an SS arrival on the transverse component and its residual on the vertical component. For surface waves, however, we choose Δt_{SH} to be the Love-wave phase delay and Δt_{PSV} to be the Rayleigh-wave phase delay at the same f_0 and let $\Delta\tau_{LR}$ denote the difference. Hence, the values of $\Delta\tau$ for body waves are essentially independent of the reference model (to the extent that it correctly predicts the interference effects), while the values of $\Delta\tau_{LR}$ depend on the differential dispersion between Love and Rayleigh waves of the reference model.

Figure 5 summarizes the data for northern Eurasia (circles) and the Russian platform (crosses). The apparent splitting time, expressed as a percentage of the total PSV travel time, is plotted
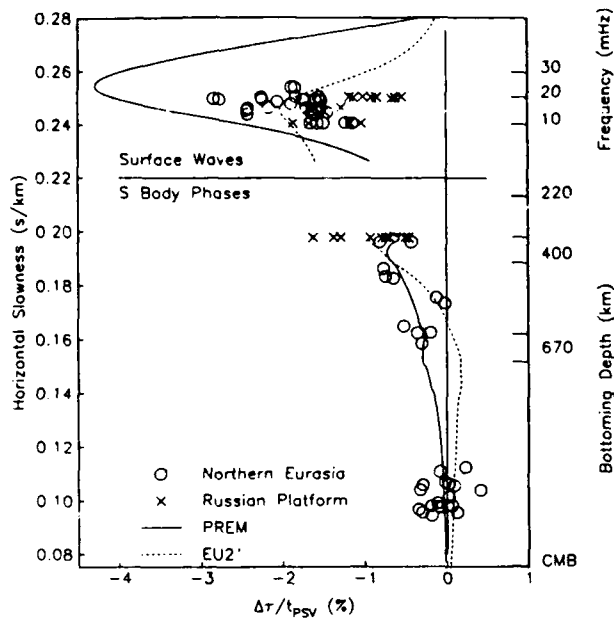
Fig. 5. The ratio $\Delta\tau/t_{PSV}$ as a function of horizontal slowness for the data and models discussed in this study. Circles are measurements from the northern Eurasia corridor, and crosses from the Russian platform path. The zero line corresponds to the isotropic reference model EU2. Calculated values from PREM, modified to have an EU2 crust, are indicated by solid lines. Short dashed lines labeled EU2' are calculated from the RI model in Table 1. Body-wave travel times for the radially anisotropic models calculated using the algorithm of Cormier [1986].

against the horizontal slowness of the wavegroup computed from the EU2 reference model. The northern Eurasia body wave data include observations of S, SSS, $SSSS$, and $SSSSS$ between 60° and 90°. The cluster of points with ray parameters between .09 and .12 s/km are S waves that bottom in the lower mantle and do not exhibit any significant splitting. However, the multiply reflected S waves which turn in the upper mantle and transition zone, such as SSS from 65° to 75° and $SSSS$ from 75° to 85°, are split with values of $\Delta\tau$ up to 12 s. For the body waves, the largest values of the ratio $\Delta\tau/t_{PSV}$ are the Russian platform observations of SS in the range 43° to 46°. The LR discrepancy for northern Eurasia, which has a mean value of −1.8% ± .08%, is somewhat larger in magnitude than that for the Russian platform (−1.1% ± .09%). There is an indication of systematic variations in $\Delta\tau_{LR}$ with frequency, but the present data set is inadequate to quantify the effect.

As shown in Figure 5, the apparent splitting times for the northern Eurasia and Russian platform paths vary systematically with horizontal slowness: phases most sensitive to velocity perturbations in the uppermost mantle display the greatest apparent splitting. For comparison, we also plot the apparent splitting times computed from two models: (1) Dziewonski and Anderson's [1981] radially anisotropic earth model PREM, modified to have an EU2 crust, and (2) an isotropic, finely layered stochastic model which we now describe.

Interpretation

The body-wave measurements are very consistent with the *shear-wave splitting computed from PREM*. However, the surface-wave observations show a smaller LR discrepancy than predicted by this radially anisotropic structure. It is certainly possible to derive a smooth, anisotropic (SA) structure that fits the data by relatively small perturbations to the five elastic moduli profiles that characterize PREM. We defer this exercise to a later, more detailed report. However, we find it interesting to note that most aspects of the data can be fit by a rough, isotropic (RI) model whose deviations from an SI structure are given by a single function of depth.

We consider a stochastic model of the upper mantle $m = \{\lambda, \mu, \rho\}$ in which the variation of isotropic elastic constants and density with vector position $x = [x_1, x_2, x_3]$ is a small perturbation to a

horizontally layered structure $m(x_3)$, where x_3 is depth. In any particular layer, we write this small perturbation as the product of a constant triplet $\{\delta\lambda, \delta\mu, \delta\rho\}$ and a homogeneous, scalar-valued, Gaussian random field $f(x)$ with zero mean and autocovariance function

$$C_{ff}(x) = \langle f(x+x') f(x') \rangle = e^{-\sqrt{k_1^2 x_1^2 + k_2^2 x_2^2 + k_3^2 x_3^2}} \quad (2)$$

Such a random field is fractal with Hausdorff dimension 7/2; the two-dimensional version of (2) has proven useful in the study of seafloor morphology, where the parameters $\{k_i\}$ are the characteristic wavenumbers of the abyssal hills [Goff and Jordan, submitted to *J. Geophys. Res.*, 1988].

We assume the characteristic vertical wavenumber is large compared to the two horizontal wavenumbers: $k_1 \sim k_2 \ll k_3$; i.e., the depth variations have much shorter scale lengths than the lateral variations. Then, for waves of length $l \gg k_3^{-1}$, a theoretical argument due to Backus [1962] may be extended to show that the medium responds like a homogeneous, radially anisotropic solid. In the special case where the root-mean-square (rms) perturbations are described by a single, small fluctuation parameter $\varepsilon = \delta\lambda/\bar{\lambda} = \delta\mu/\bar{\mu} \ll 1$, Backus's averaging procedure yields to $O(\varepsilon^2)$,

$$v_{PV}^2 = \bar{v}_P^2 (1 - \varepsilon^2), \quad v_{PH}^2 = \bar{v}_P^2 (1 - \bar{\lambda}^2/\bar{\sigma}^2 \varepsilon^2)$$

$$v_{SV}^2 = \bar{v}_S^2 (1 - \varepsilon^2), \quad v_{SH}^2 = \bar{v}_S^2 \quad (3)$$

$$\eta = 1 - (\bar{\sigma}/\bar{\lambda} - \bar{\lambda}/\bar{\sigma})\varepsilon^2$$

where $\bar{\sigma} = \bar{\lambda} + 2\bar{\mu}$.

These equations allow us to calculate an SA model $\{v_{PH}, v_{PV}, v_{SH}, v_{SV}, \eta\}$ that is equivalent to the RI model $\{v_P, v_S, \varepsilon\}$ in the long-wavelength limit. An example is given in Table 1. In deriving this structure, we took v_{PV} and v_{SV} from EU2 and computed v_{PH}, v_{SH} and η from the values of ε listed in the table. We found that the LR discrepancy could be satisfied by an uppermost mantle with $\varepsilon = .28$. This yields a long-wavelength SH-SV velocity difference of 4.2% for a ray angle of 90°(horizontal path), which accounts for most of the SNA-EU2 discrepancy (Figure 1). The SH-SV difference described by (3) is a strong function of ray angle, becoming negative for angles steeper than about 52°. Consequently, to explain the magnitude of the shear-wave splitting observed for rays with bottoming depths in the transition zone, it was necessary to maintain a relatively large value of ε to depths greater than 200 km. In our example structure, ε decreases linearly from .22 at 220 km to zero at 400 km. Given the scatter, the model is consistent with most of the observations, although it predicts a somewhat smaller amount of splitting than is observed for rays bottoming near the 670-km discontinuity for the northern Eurasian paths.

This modeling exercise establishes the magnitude of the velocity heterogeneity needed to explain the splitting data by an RI mechanism. It is large: a value of $\varepsilon = .28$ corresponds to a 14% rms fluctuation in the isotropic wave speeds. This exceeds the variation in isotropically averaged parameters expected for even a diverse assemblage of upper-mantle ultrabasic rocks, which we interpret as evidence for intrinsic (local) anisotropy. This interpretation is consistent with investigations of the azimuthal variation in Pn velocity [Fuchs, 1983] and shear-wave splitting in SKS [Silver and Chan, 1988] in Western Europe, which provide additional evidence for intrinsic anisotropy within the continental lithosphere.

In future modeling work, we intend to generalize the Gaussian stochastic description represented by (2) to include the tensor

Table 1. RI and equivalent SA models for Eurasian paths.

Depth (km)	ε	v_{PH} (km/s)	v_{PV} (km/s)	v_{SH} (km/s)	v_{SV} (km/s)	η
40-100	.28	8.48	8.19	4.69	4.51	0.85
100-200	.22	8.36	8.19	4.64	4.53	0.90
220	.22	8.32	8.14	4.64	4.53	0.90
400	0	8.65	8.65	4.74	4.74	1.00

All values linearly interpolated between 220 and 400 km.

properties of local anisotropy; i.e., we will consider rough, anisotropic (RA) structures. These structures may be divided into two classes based on the organization of the anisotropy: models where the elasticity tensor averaged over some volume is isotropic, and models which contain a smooth component of anisotropy. Preliminary calculations indicate that the former are inconsistent with petrologic constraints and that a smooth component of anisotropy is required.

In terms of (2) and its generalizations, the qualitative difference between smooth and rough structures is represented as a quantitative difference in the characteristic wavenumbers $\{k_i\}$. The long-wavelength splitting data presented in this paper do not constrain these wavenumbers. However, the fact that the first arrival times from short-period Sn waves on both horizontal and vertical components yield high apparent velocities is evidence that the characteristic vertical scale of the heterogeneity, k_3^{-1}, lies between the lengths of the long-period and short-period waves, say between 100 km and 10 km. In addition to giving apparent anisotropy at long wavelengths, characteristic scale lengths in this intermediate range provide high-velocity "micropaths" at short wavelengths [cf. Flatté, 1979], which could account for the Sn discrepancy. This hypothesis is consistent with the thinking of Fuchs and Schulz [1976], who have suggested that an RA structure is needed to account for the "shingling" of P arrivals observed on long refraction profiles in Europe.

In conclusion, although RA models of the upper mantle may be constructed which satisfy the splitting data, they are inconsistent with petrologic constraints, and a smooth component of intrinsic anisotropy is indicated. Nevertheless, fine-scale heterogeneity in the elastic parameters is likely to play a role in explaining the LR, Sn, and SNA-EU2 discrepancies, as well as other aspects of wave propagation in the continental upper mantle. Our observation that the shear-wave splitting is significantly smaller for paths along the Alpine-Himalayan front than for cratonic paths suggests that the large scale variations in anisotropic properties may be related to continental deep structure.

References

Anderson, D. L., and A. M. Dziewonski, Upper mantle anisotropy: evidence from free oscillations, *Geophys. J. R. astr. Soc.*, *69*, 383-404, 1982.

Backus, G. E., Long-wave elastic anisotropy produced by horizontal layering, *J. Geophys. Res.*, *67*, 4427-4440, 1962.

Dziewonski, A. M., and D. L. Anderson, Preliminary reference earth model, *Phys. Earth Planet. Int.*, *25*, 297-356, 1981.

Cara, M., A. Nercessian, and G. Nolet, New inferences from higher mode data in western Europe and northern Eurasia, *Geophys. J. R. astr. Soc.*, *61*, 459-478, 1980.

Cormier, V. F., Synthesis of body waves in transversely isotropic earth models, *Bull. Seis. Soc. Am.*, *76*, 231-240, 1986.

Flatté, S. M. (ed.), *Sound Transmission through a Fluctuating Ocean*, Cambridge University Press, New York, 299 pp., 1979.

Fuchs, K., Recently formed elastic anisotropy and petrological models for the continental subcrustal lithosphere in southern Germany, *Phys. Earth Planet. Int.*, *31*, 93-118, 1983.

Fuchs, K., and K. Schulz, Tunneling of low-frequency waves through the subcrustal lithosphere, *J. Geophys.*, *42*, 175-190, 1976.

Gee, L. S., and T. H. Jordan, Parameter retrieval using three-component seismograms and hybrid synthetics: an application to seismic anisotropy, *Eos Trans. AGU*, *67*, 1113, 1986.

Grand, S. P., and D. V. Helmberger, Upper mantle shear structure of North America, *Geophys. J. R. astr. Soc.*, *76*, 399-438, 1984.

Grand, S. P., and D. V. Helmberger, Uppermantle shear structure beneath Asia from multi-bounce S waves, *Phys. Earth Planet. Int.*, *41*, 154-169, 1985.

Heustis, S., P. Molnar, and J. Oliver, Regional Sn velocities and shear velocity in the upper mantle, *Bull. Seis. Soc. Am.*, *63*, 469-475, 1973.

James, D. E., Anomalous Love wave phase velocities, *J. Geophys. Res.*, *76*, 2077-2083, 1971.

Jordan, T. H., Global tectonic regionalization for seismological data analysis, *Bull. Seis. Soc. Am.*, *71*, 1131-1141, 1981.

Lerner-Lam, A. L., and T. H. Jordan, How thick are the continents?, *J. Geophys. Res.*, *92*, 14007-14026, 1987.

Lévêque, J.-J., and M. Cara, Long-period Love wave overtone data in North America and the Pacific Ocean: new evidence for upper mantle anisotropy, *Phys. Earth Planet. Int.*, *33*, 164-179, 1983.

McEvilly, T. V., Central US crust-upper mantle structure from Love and Rayleigh wave phase velocity inversion, *Bull. Seis. Soc. Am.*, *54*, 1997-2015, 1964.

Mitchell, B. J., On the inversion of Love and Rayleigh-wave dispersion and implications for earth structure and anisotropy, *Geophys. J. R. astr. Soc.*, *76*, 233-241, 1984.

Rial, J. A., S. P. Grand, and D. V. Helmberger, A note on lateral variation in upper mantle shear-wave velocity across the Alpine front, *Geophys. J. R. astr. Soc.*, *77*, 639-654, 1984.

Silver, P. G., and W. Chan, Constraints on early continental evolution from observations of seismic anisotropy, *Eos Trans. AGU*, *69*, 483, 1988.

L. S. Gee and T. H. Jordan, Department of Earth, Atmospheric, and Planetary Sciences, MIT, Cambridge, MA 02139.

24

ACKNOWLEDGMENTS

25

INVESTIGATIONS OF EURASIAN SEISMIC SOURCES AND UPPER MANTLE STRUCTURE

II: THE NATURE OF MANTLE LAYERING FROM FIRST-ORDER REVERBERATIONS

by
J. S. REVENAUGH
Submitted to the Department of Earth, Atmospheric and Planetary Sciences,
Massachusetts Institute of Technology
on April 21, 1989 in Partial Fulfillment of the Requirements for the
Degree of Doctor of Philosophy.

ABSTRACT

The reverberative interval of the seismogram, defined as the portion following the surface wave train propagating along the minor arc and ending with the first body-wave arrivals from the major arc, provides an excellent window in which to observe subcritical reflections from mantle discontinuities. On an SH-polarized seismogram the intervals between ScS_n and $sScS_n$ wave groups (zeroth-order reverberations) are approximately 15 minutes long and consist almost entirely of waves reflected one or more times from mantle discontinuities (first- and higher-order reverberations). We have developed signal enhancement and waveform inversion schemes to progressively extract information pertaining to mantle layering from the waveforms of zeroth- and first-order reverberations and have applied them to a data set of long-period, digital seismograms drawn from a number of tectonic regions in the western and central Pacific, the adjoining marginal basins, Indonesia, and Australia—a study area which includes the majority of deep subduction zones. The results place important constraints on the nature of the transition-zone discontinuities.

Measurements of the two-way, vertical shear-wave travel time from the free surface to the 400-km and 650-km discontinuities (τ_{400} and τ_{650}, respectively) yield estimates of transition-zone travel time, τ_{TZ}, largely uncontaminated by outside heterogeneity. Variations in the path-averaged estimates of τ_{TZ} are of the order of 10 s, indicating significant lateral heterogeneity in the transition zone. Correlations of τ_{TZ} with τ_{400} and τ_{LM} (travel time through the lower mantle) are consistent with, but do not require, the thermal deflection of an exothermic phase transition near 400 km and an endothermic transition at 650 km, with ~25 km of long-wavelength (500–5000 km) topography on each. The amount of topography estimated for the 650-km discontinuity is significantly less than expected for a rigorously-stratified mantle (>100 km), where, in regions of subduction, the interface between the upper and lower mantle is predicted to be deflected to compensate the mass excess of downgoing slab material.

Apart from the apparently ubiquitous transition-zone discontinuities, we find evidence for a number of smaller discontinuities throughout the mantle. An abrupt 5–8% increase in

shear-wave impedance at an average depth of 67 km is interpreted as the spinel → garnet lherzolite (or peridotite) transition. Seismic corridors sampling primarily oceanic, back-arc, and tectonically-active continental regimes feature a prominent impedance decrease in the upper 100 km, marking the onset of the low-velocity zone (LVZ). The reflector is significantly brighter on the back-arc side of subduction zones, perhaps requiring a small degree of partial melting in these regions. Anisotropy associated with strong corner flow above the subducting slab may play an accessary role. The bottom boundary of the LVZ typically appears to be a gradual transition (greater than 50 km in vertical extent) rather than an abrupt velocity increase. A third discontinuity, at an average depth of 232 km, is observed for paths crossing the western and central portions of the Australian continent and northern margin, and marks a small (~4%) increase in shear-wave impedance. Observations of this discontinuity and the LVZ reflector do not overlap. Correlation of depth to the 220-km discontinuity with Q_{ScS}, and sampling of surface tectonic regimes, follow the same trends as the LVZ reflector, suggesting that the 220-km discontinuity delimits the base of the subcontinental lithosphere, perhaps marking an anisotropic, high-velocity cap over a subcontinental LVZ, similar to the structure believed to exist at shallower depths beneath the oceans. In regions of subduction, an abrupt 3.6% increase in shear-wave impedance occurs at an average depth of 318 km. This reflector may be the seismic signature of the high-pressure bound of the LVZ, made locally bright by the reaction of H_2O and forsterite driving the mantle solidus upward, a reaction facilitated by greater water pressure due to advection of hydrous phases in the downgoing oceanic crust.

Additional impedance increases occur at average depths of 530 km, 730 km, and 915 km, and may persist throughout the data set. The shallowest is attributed to the β-spinel → γ-spinel phase transition, although the experimentally determined two-phase region may be too broad to explain the observations. The 730-km discontinuity may mark the seismic signature of the ilmenite → perovskite transition, a change in silicate perovskite symmetry, or the γ-spinel → perovskite + magnesiowüstite phase transition locally depressed to greater depths by a cold chemical boundary layer trapped upon it. Identification of the 915-km discontinuity is more speculative, but could mark a symmetry change in silicate perovskite. Complex upper-mantle and transition-zone structures previously proposed for the northern continental margin and interior of the Australian continent predict the fine-scale structure of our data set remarkably well, providing strong independent support of these observations.

Beneath the regions sampled, the depth interval of 1000 km to 2500 km appears free of any distinct layering, in agreement with most recent seismic models depicting adiabatic compression of an homogeneous mantle. Any discontinuities occurring in this depth interval must be either small (SH-polarized reflection coefficient <1.0%) or intermittent or have lateral depth variations in excess of 50 km. At greater depths, we find evidence for a reflector of long-period seismic energy located approximately 325 km above the core-mantle boundary (CMB), which likely corresponds to the discontinuity proposed by T. Lay and associates. It is characterized by normal-incidence, SH reflection coefficient R =

0.022, implying a 1.7% increase in density for the 2.75% increase in shear velocity proposed by Lay and Helmberger (1983). The discontinuity does not appear to be a ubiquitous feature of the lower mantle, occurring beneath roughly one-third of the seismic corridors examined. This and the observed correlation of discontinuity depth and lower mantle heterogeneity favor a compositional origin. Strong, mantle-side layering near the CMB boundary–perhaps associated with a thin chemical boundary layer not unlike the crust–is not required by the data, but could be present if it is a fluid or accompanied by little impedance contrast or thin (<10 km).

TABLE OF CONTENTS

31

CHAPTER 1

INTRODUCTION

"The interior of the Earth is a problem at once fascinating and baffling as one may easily judge from the vast literature, and the few established facts, concerning it. There is no dearth of information–astronomical, geochemical, petrological, geological, geophysical–but the relationship of most of this material to the Earth's interior is vague. The only information about definite levels of the interior, derived from seismology, has an abstract character and requires deciphering."

Francis Birch
Elasticity and Constitution of the Earth's Interior, 1952

Although written in 1952, the introduction to Birch's seminal paper on the constitution of the Earth's interior still rings true today. Despite tremendous strides made in all fields connected with the study of the Earth's deep structure, the accumulation of nearly forty years worth of seismological and laboratory data has often raised as many questions as it has answered. This is especially true of the Earth's mantle, the largest of the four major seismological layers (crust, mantle, inner and outer core), which alone comprises greater than 80% of the Earth's total volume, and nearly 65% of its mass. While is resides just scant kilometers beneath the oceans, the mantle is (today) every bit as inaccessible as the core. Direct samples of the mantle are rare–occurring as the odd xenolith in kimberlites and other igneous intrusions, or exposed in mountain peridotites and ophiolite sequences–and carry with them a number of attendant questions concerning their rather unusual origins. As a result, study of the mantle has relied primarily on seismology. However, as Birch so succinctly put it: "(seismological results) have an abstract character and need deciphering." The process of deciphering is still in progress, and despite constant bombardment from the combined arsenals of geology, petrology, and geochemistry, no true consensus has emerged on many of the most fundamental and consequential questions regarding the composition and state of the Earth's mantle.

As a case in point, let us consider one of the most oft-asked questions, namely: What is the nature of the 650-km discontinuity? Does this discontinuity, the largest in the mantle, represent a phase transition in an compositionally homogeneous mantle, a change in composition (such as an increase in Fe content), or a combination of both? The answer to this question has grave implications for a number of geodynamically important processes, including the depth extent of mantle flow, mixing of mantle reservoirs, and the bulk composition of the Earth. Seismology tells us much about the 650-km discontinuity, for example: the average depth and contrast in velocity across the discontinuity are known from the study of body-wave travel times and amplitudes in the triplication range [e.g., *King and Calcagnile*, 1976; *Given and Helmberger*, 1980; *Grand and Helmberger*, 1984], tomography [e.g., *Dziewonski and Woodhouse*, 1987; *Tanimoto*, 1987, 1988] and residual-sphere analysis [e.g., *Creager and Jordan*, 1986; *Fischer et al.*, 1986] suggest that velocity anomalies, especially in regions of subduction, are coherent across the discontinuity, while reflections of high-frequency $P'P'$ phases point to a sharp increase in compressional-wave impedance [e.g., *Engdahl and Flinn*, 1969; *Whitcomb and Anderson*, 1970; *Richards*, 1972]. Of these observations, the last is perhaps the most telling. Studies of the phase change of $(Mg,Fe)_2SiO_4$ (γ-spinel) $\rightarrow$ $(Mg,Fe)SiO_3$ (perovskite) + $(Mg,Fe)O$ (magnesiowüstite), the most likely candidate reaction for the 650-km discontinuity, reveal a broad two-phase region [e.g., *Ito and Yamada*, 1982] incapable of supporting high-frequency body-wave reflections [*Lees et al.*, 1983]. But here we run into a conundrum. If the discontinuity is primarily compositional in origin, we would expect to observe a great deal of topography on it, likely in excess of 100 km [e.g., *Hager and Raefsky*, 1981; *Christensen and Yuen*, 1984], as it deflects to support the mass excess of downgoing slabs in regions of subduction. It is a major conclusion of this thesis that topography of this magnitude does not occur, and that the observed topography is consistent with the thermal deflection of an endothermic phase transition.

A more precise knowledge of the composition and state of the mantle will undoubtedly contribute to our understanding of its contribution to the complex dynamics and evolution of the Earth. Because of its great size and slow characteristic time scales, the mantle is the major player in many important and ongoing geodynamic processes. For instance, flow in the mantle ultimately provides the driving force of plate tectonics, while its coupling to core convection may exert a profound influence on the geodynamo and the resultant magnetic field [e.g., *Bloxham and Gubbins*, 1987].

Recently a number of attempts have been made to model the radial variations of density and elastic moduli in the upper mantle and transition zone using results of high-pressure petrology [e.g., *Bass and Anderson*, 1984; *Weidner*, 1985; *Irifune*, 1987; *Duffy and Anderson*, 1989]. A major outcome of this research is the realization that the radial variation of velocity and density in the upper mantle, away from discontinuities, does not strongly constrain the candidate modal phase assemblages, admitting a wide range of olivine, pyroxene and garnet mineralogies. This problem is further aggravated by severe thermal heterogeneity in the upper mantle, whose effects on velocities are not well calibrated. Rather, it is found that the seismologically determined depth and variation in material properties associated with mantle discontinuities are the most diagnostic indicators of composition and state [*Duffy and Anderson*, 1989]. This thesis presents a number of fundamentally new observations pertinent to mantle layering obtained from a recently recognized class of body waves known as mantle reverberations. The observations provide constraints that would be difficult–if not impossible–to obtain from other seismic phases.

Mantle reverberations form the class of body waves which repeatedly traverse the mantle along steeply-dipping ray paths, alternately reflecting from the free surface (FS) and core-mantle boundary (CMB), and including such phases as PcP and ScS_n (where n is the number of core reflections). The latter are examples of what we term zeroth-order reverberations, denoting that they have not been reflected from any discontinuities internal

to the mantle. While these phases are perhaps the most familiar mantle reverberations, the overwhelming majority of mantle reverberations are of higher order, having suffered one or more reflections from mantle discontinuities. Unlike their zeroth-order counterparts, higher-order reverberations are uniquely sensitive to layering of the mantle. Unfortunately the small contrasts in material properties typically associated with mantle discontinuities ensures that most higher-order reverberations will go unnoticed. Crucial to this study is the existence of a window on the seismogram, located between the surface wave train propagating along the minor arc and the first body-wave arrivals from the major arc, in which it is possible to observe first- and higher-order reverberations. Known as the reverberative interval, on an SH-polarized seismogram it consists almost entirely of mantle reverberations, and is dominated by ScS_n and $sScS_n$. In the gaps between ScS_n and $sScS_n$ wave groups, each approximately 15 minutes long, we have observed first-order reverberations generated by the major mantle discontinuities–apparently the first time that these phases have been observed as distinct, isolated arrivals.

First-order reverberations have a number of properties which make them ideally suited to the study of mantle layering. Perhaps the singlemost important asset is the ability to image the entire depth extent of the mantle with a single data set, and being able to do so almost irrespective of the horizontal path length. It is this property that distinguishes mantle reverberations from the majority of seismological tools; one which we exploit to produce an internally consistent description of mantle layering.

Organization

Like the Earth's mantle, this thesis is broken into three sections: In the first, we document observations of first-order mantle reverberations drawn from a data set of more than 200 recordings of 130 intermediate- and deep-focus earthquakes in the western Pacific, the adjoining marginal basins and Indonesia. Sampling of the mantle and surface tectonic regimes are discussed, and found to run the gamut of tectonic types, including

intermediate to older aged ocean, back-arc marginal basins, continental margins, platforms and shields, as well as the majority of deep subduction zones. As an preliminary example of the power of first-order reverberations, we employ the phase equalization and stacking algorithm of *Jordan and Sipkin* [1977] to simultaneously estimate the path-averaged, shear-wave quality factor of the upper and lower mantle and the reflection coefficient of the 650-km discontinuity.

Part two develops specifically tailored algorithms capable of extracting parameters describing mantle layering from the waveforms of zeroth- and first-order reverberations. The inversion of zeroth-order reverberations tells us much about the regional variation of whole-mantle attenuation and travel time, while also providing estimates of source parameters and crustal structure needed to describe the waveforms of higher-order reverberative interval arrivals. Inversion of first-order reverberations then adds information describing the gross properties of mantle layering. The analysis resembles the methods of migration common to exploration seismology and offers a powerful alternative to traditional travel-time studies. Once developed, these techniques are applied to data. By repeating the experiments on synthetic data sets we address the non-uniqueness, resolution, and robustness of the algorithms. Synthetic modeling also serves as an aid to interpretation, the success of which has enabled us to identify a number of low-magnitude reflectors in both the upper and lower mantle. Because of its importance to this study, much attention is paid to the process of synthetic forward modeling, results of which are documented on a path-by-path basis. The results of section two are numerous; of greatest importance, however, is a map of the path-averaged depths and magnitudes of the major mantle reflectors.

The third section analyzes and expands upon these results in the context of the transition zone, the upper mantle and, lastly, the lower mantle—an ordering which follows the most straightforward decomposition of the data. Important new constraints on mantle layering, especially as regards the lateral variability of structure in the upper mantle and the possible existence of a chemical boundary layer in the D" region, are obtained. Measurements of

topography on the 400-km and 650-km discontinuity are discussed in terms of transition-zone thermal structure and composition. As alluded to previously, we do not find the degree of topography expected for a rigorously stratified mantle. There does exist, however, preliminary evidence for the accumulation of a chemical boundary layer on the 650-km discontinuity. Whether formation of this feature is associated with subduction is unknown, but the observations can be explained the thermal equilibration of an initially cold layer residing on the discontinuity.

By drawing heavily from the allied fields of mantle petrology and geochemistry throughout, we attempt to interpret and tie together these observations into a coherent, mantle-wide reference frame–hopefully making the seismological results a little less "abstract" in the process.

Related Publications

The bulk of this thesis has either been published or is in press. Much of chapters 2, 3 and 4 appear in *Revenaugh and Jordan* [1987, 1989]. The remaining chapters are to be published as a series of four papers.

Revenaugh, J., and T.H. Jordan, Observations of first-order mantle reverberations, *Bull. Seismol. Soc. Am.*, 77, 1704–1717, 1987.

Revenaugh, J., and T.H. Jordan, A study of mantle layering beneath the western Pacific, *J. Geophys. Res.*, in press, 1989.

CHAPTER 2

MANTLE REVERBERATIONS

INTRODUCTION

Direct arrivals and fundamental-mode surface waves have long been the mainstays of seismology. Besides offering the greatest signal-to-noise ratios (SNRs), study of these phases has in large part been motivated by the ease of interpretation. However, with the advent of powerful, accurate and efficient algorithms for computing complete synthetic seismograms, seismologists have recently begun to look more closely at the seismogram—discovering a wealth of untapped information in the process. Studies of higher-mode surface waves, variously interpreted as the superposition of overtone branches [e.g., *Lerner-Lam and Jordan*, 1987; *Tanimoto*, 1988] or as multiple *P* and *S* waves [e.g., *Given and Helmberger*, 1980; *Grand and Helmberger*, 1984] have contributed greatly to our knowledge of the upper mantle and transition zone, while studies such as those of *Dziewonski and Woodhouse* [1987] and *Tanimoto* [1987], treating the entire low-frequency seismic wave train, have succeeded in mapping the low-wavenumber velocity heterogeneity of both the upper and lower mantles.

Study of discontinuity phases (by which we refer to reflected and mode-converted body waves) has been slower to succumb to synthetic modeling, not for a lack of creativity on the part of seismology, but rather due to their generally poor SNR. Although the vast majority of seismic body waves an be classified as discontinuity phases, only a very few, such as *PcP* and certain post-critical reflections, have SNRs comparable to direct arrivals. Studies of other discontinuity phases, in particular those interacting with discontinuities internal to the mantle, have traditionally relied on fortuitous experimental geometries to isolate the low-magnitude phases. Examples include precursors to *P'P'* [e.g., *Engdahl and Flinn*, 1969; *Whitcomb and Anderson*, 1970; *Nakanishi*, 1988] and *PP* [e.g., *Bolt*, 1970; *Ward*, 1978; *Souriau*, 1986; *Wajeman*, 1988], and mode-converted *P* and *S* waves

[*Paulssen*, 1985; 1988; *Vinnik*, 1977; *Vinnik et al.*, 1983; *Faber and Müller*, 1980, 1984], to name but a few. However, even with station array data, the usefulness of these phases is in general severely curtailed by their low amplitudes–an unfortunate fact given the information they contain.

The Reverberative Interval

Perhaps the best window in which to view subcritical angle reflections from mantle discontinuities is the reverberative interval, defined as the portion of the seismogram between the surface wave train propagating along the minor arc and the first body-wave arrivals from the major arc. This interval is dominated by core-reflected phases such as ScS_n and other reverberations from internal discontinuities (Figure 2.1). On a transversely-polarized (*SH*) seismogram, free from mode conversions and core-penetrating phases, these reverberations can be conveniently classified by the number of internal mantle reflections they experience; ScS_n and $sScS_n$ phases suffer no such reflections and are therefore termed zeroth-order reverberations, those experiencing one reflection are first-order reverberations, and so forth. (Hereafter, the term "mantle reverberations" will be used to designate these *SH*-polarized shear waves.)

The properties of zeroth-order reverberations have been investigated in a number of attenuation experiments [e.g., *Kovach and Anderson*, 1964; *Jordan and Sipkin*, 1977; *Sipkin and Jordan*, 1979, 1980*b*; *Nakanishi*, 1980; *Lay and Wallace*, 1983, 1988; *Chan and Der*, 1988] and studies of lateral velocity heterogeneity [e.g., *Okal and Anderson*, 1975; *Sipkin and Jordan*, 1976, 1980*a*; *Stark and Forsyth*, 1983]. ScS_n phases sample the entire mantle, have short horizontal path lengths, and are free of many of the complications associated with turning rays. On the same seismogram, ScS_n phases of different core-bounce number n have similar propagation paths near their endpoints, so that their differential properties are insensitive to instrument response, source structure, and heterogeneity beneath the receivers. Experimental geometries can therefore be devised that

39

selectively sample the upper mantle beneath regions well removed from either seismic sources or receivers. Unfortunately, zeroth-order reverberations alone can resolve only whole-mantle averages. First- and higher-order reverberations, by virtue of the reflections they experience, preferentially sample certain mantle regions and can be combined with lower-order reverberations to resolve vertically-averaged properties of mantle regions delineated by major discontinuities, as well as the impedance contrasts across the interfaces.

We have observed first-order reverberations--specifically SH-polarized ScS_n and $sScS_n$ phases reflected at near normal incidence from upper mantle discontinuities--on long period, digital seismograms of the HGLP and SRO networks. Such arrivals are the primary contributors to the "background" signal level between the multiple-ScS waves in Figure 2.1. They correspond to a dynamic family of rays which we shall denote by $\{ScS_n, Sd^{\pm}S\}$, where n is the multiple number of the parent (zeroth-order) phase, "d^+" signifies a reflection from the top of an internal discontinuity at depth d, and "d^-" signifies a reflection from the bottom. Each $\{ScS_n, Sd^{\pm}S\}$ arrival is comprised of either n or $n+1$ dynamic analogs, depending on the depths of the source and reflector and on whether the reflection is topside or bottomside. In a spherically symmetric Earth, these analogs arrive at exactly the same time with the same amplitude and phase to build up an observable arrival; this multiplicity offsets attenuation and helps maintain the amplitude of the ray family as the ScS_n reflection number n increases, allowing observations over a range of n. (In the real Earth, we expect some small degree of destructive interference owing to the splitting of the reverberation by ellipticity and aspherical structure encountered along its various component rays.) Figure 2.2 illustrates ray paths for the families $\{ScS_2, S650^+S\}$ and $\{ScS_2, S650^-S\}$, the topside and bottomside reflections from the 650-km discontinuity, respectively.

OBSERVATIONS

Although we have assembled a large and geographically extensive database of mantle reverberations, in this section we will concentrate our efforts on paths within the Tonga-Hawaii corridor, which has a favorable geometry for the observation of mantle reverberations. The properties of multiple ScS phases along this relatively uniform swath of old oceanic lithosphere have been investigated extensively by *Jordan and Sipkin* [1977] and *Sipkin and Jordan* [1979, 1980a, b]. Seismograms from the High-Gain, Long-Period (HGLP) instruments at station KIP, on the island of Oahu, were provided to the author by S. Sipkin of the U.S. Geological Survey. Eleven Tonga-Fiji events with focal depths ranging from 229 km to 602 km were selected for detailed analysis. As was typical of the data set in general, records for these events had apparently simple time functions (characterized by impulsive, short duration P and S waveforms), good SH signal-to-noise ratios at KIP, and depths of focus large enough to separate the ScS_n and $sScS_n$ phases. At the epicentral distances typical of this path (40°–51°), the reverberative interval is about 50 minutes long and includes reverberations with reflection numbers n between two and four (Figure 2.1).

Synthetic seismograms of the reverberative interval have been generated by both normal-mode summation and geometrical-optics ray theory. Source mechanisms were taken from *Richter* [1979], *Billington* [1980], and *Giardini* [1984], and the HGLP instrument response was adapted from *Berg and Chesley* [1976]. To compute the synthetics, we superposed *Lerner-Lam and Jordan's* [1987] PA2 model of the western-Pacific upper mantle on the PEM lower mantle of *Dziewonski et al.* [1975]. Anelastic structure was specified by *Sipkin and Jordan's* [1980b, Table 4] Oceanic Model B, a two-layer model constructed to satisfy ScS_n attenuation data. The ray synthetics include all first-order and second-order reverberations from the two transition-zone discontinuities, located at 400 km and 670 km in the PA2 model.

In the ray synthetics, third- and higher-order reverberations from the transition-zone interfaces are ignored, as are all reflections from the first-order discontinuities at the lid-

LVZ boundary (98 km in PA2), and the base of the LVZ (180 km). The mode synthetics, computed by summing all toroidal free oscillations with frequencies up to 50 mHz, necessarily include all reverberations. As discussed by *Anderson and Cleary* [1974] and *Kennett and Nolet* [1979], the reverberation structure associated with internal mantle discontinuities is manifested by harmonic variations in the asymptotic spacing of toroidal-mode eigenfrequencies.

Figure 2.3 compares the mode and ray synthetics with data for the deep-focus ($h = 373$ km) event of Feb. 22, 1975. The good agreement validates the approximations made in the ray summation. Some minor differences can be discerned just prior to the arrival of the ScS_n and $sScS_n$ phases, owing primarily to reflections from shallow discontinuities not included in the ray sum, but the reflections from the free surface, CMB, and transition-zone discontinuities clearly dominate the theoretical seismogram. The comparison shows that geometrical optics provides an excellent description of reflections from sharp discontinuities at center frequencies on the order of 30 mHz.

One advantage of the ray method is that it is easily modified to account for aspherical heterogeneity along the ray paths. *Sipkin and Jordan* [1980b] have obtained evidence for the existence of small-scale lateral variations along the Tonga-KIP path which perturb the ScS_n travel times by about 0.5%. In this study, we ignore this heterogeneity and deal exclusively with path-averaged radial structure. However, we do correct our ray synthetics by modifying the travel time of each wavelet according to the average ellipticity along the minor arc. Since the reverberations are primarily sensitive to the average thicknesses of the mantle layers, especially for large multiple number n, this approximation is justified. For the predominantly equatorial paths used in this study, the two-way whole-mantle travel time is typically increased by ≤ 2.5 s. Although not very obvious in Figure 2.3, this ellipticity correction improves the agreement between the observed and computed travel times of the ScS_n and $sScS_n$ phases.

At frequencies below about 40 mHz, the theoretical seismograms do a reasonably good job of predicting the signal amplitude in the reverberative interval observed along the Tonga-KIP path, indicating that most of the energy between the ScS_n-$sScS_n$ wave groups results from coherent reflections off the transition-zone discontinuities. However, the observed seismograms tend to be richer in higher frequency energy than the synthetics. Although some of this discrepancy may result from errors in the HGLP instrument response or complications in the source structure, incoherent scattering by small-scale heterogeneities undoubtably plays a role. Because the primary wave field is concentrated at such high horizontal phase velocities, and back-scattered as well as forward-scattered energy can be observed, the study of broad-band signals within the reverberative interval can potentially provide unique constraints on the statistics of scattering at nearly vertical angles of incidence. The detailed investigation of this problem would likely require data from an array of three-component, broad-band seismometers of the sort proposed by the PASSCAL program [*Incorporated Research Institutions for Seismology*, 1984].

Figure 2.4 compares the observed seismogram with the synthetic for the event of March 23, 1974, a deep-focus Fiji earthquake ($h = 515$ km) located 50° from KIP. To facilitate the identification of individual phases, the synthetic has been broken up into families of dynamic analogs corresponding to the first-order topside and bottomside reflections from the two transition-zone discontinuities. We also show separately the contributions from the zeroth-order and all second-order reverberations. Since the latter are small compared to the primary internal reflections, we can safely ignore higher-order reverberations. Figure 2.5 is a similar comparison for the intermediate-focus event of Dec. 19, 1973 ($h = 229$ km). Figure 2.6 compares observed and theoretical seismograms of the reverberative interval for a suite of focal depths.

Particularly prominent in both the data and synthetics are the topside and bottomside reflections from the 650-km (or 670-km) discontinuity. A close look at the differences between the observed and synthetic seismograms reveals that the topside reflections from

43

this interface are consistently earlier and the bottomside reflections consistently later than predicted by PA2, indicating that the shallower depth is more appropriate to the Tonga-KIP corridor; we have therefore employed $d = 650$ km in our phase designations. On a corridor-by-corridor basis, these sorts of offsets provide evidence for topography on the 650-km and other mantle discontinuities, and are discussed in later chapters. The topside reflections $\{ScS_n, S650^+S\}$ and $\{sScS_n, S650^+S\}$ follow their respective parent phases, ScS_n and $sScS_n$, by the two-way, vertical travel time from the free surface to the 650-km discontinuity, $\tau_{650} \approx 280$ s (4.65 min). For events with intermediate hypocentral depths, this time difference is sufficient to isolate $\{ScS_n, S650^+S\}$ from the zeroth-order reverberations, but for deep-focus events, these arrivals appear as an extra swing at the end of $sScS_n$; this waveform complexity can be observed on the seismograms of the deepest four events of Figure 2.6. The $\{sScS_n, S650^+S\}$ phases are isolated from the zeroth-order reverberations at all focal depths and can be observed for $n = 2, 3,$ and 4 on most of the seismograms in Figure 2.6. The corresponding bottomside reflections $\{ScS_n, S650^-S\}$ and $\{sScS_n, S650^-S\}$ precede ScS_{n+1} and $sScS_{n+1}$, respectively, by τ_{650}. Good examples of the former can be seen for $n = 2$ on the observed seismograms for the deep-focus earthquakes in Figure 2.6. On the same seismograms, the latter are evident as precursors to ScS_{n+1}, although their signal-to-noise levels are generally lower than the other first-order reverberations from the 650-km interface. As mentioned in our discussion of Figure 2.3, some of the energy in this precursory interval is due to reflections from shallow discontinuities not included in these preliminary synthetics.

The first-order reverberations for the 400-km discontinuity are predicted to have only 60% of the amplitude of the 650-km reflections, making them more difficult to identify as individual arrivals. The two-way, vertical travel time from the free surface to the 400-km discontinuity, τ_{400} is only about 180 s, so that $\{ScS_n, S400^+S\}$ and $\{sScS_n, S400^-S\}$ are obscured by $sScS_n$ and ScS_{n+1} for deep-focus events. However, these two phases can be seen on seismograms of intermediate-focus earthquakes; e.g., $n = 2$ in Figure 2.5.

44

Although $\{sScS_n, S400^+S\}$ and $\{ScS_n, S400^-S\}$ interfere with $\{ScS_n, S650^+S\}$ and $\{sScS_n, S650^-S\}$ for intermediate foci, they can be observed as isolated pulses on the deep-event seismograms in Figure 2.6.

Although we have concentrated our discussion on the transition zone discontinuities, first-order reverberations from discontinuities at depths other than 400 and 650 km also contribute to the signal levels observed in Figure 2.6. Chapter 3 presents a matched-filtering technique specifically designed to isolate such reflections.

DATA

A total of 18 seismic corridors (source region/receiver pairs) have been chosen for further study, a data set comprising over 200 recordings of 130 intermediate- and deep-focus earthquakes in the western and southern Pacific and Indonesia (Table 2.1). Together these corridors sample a variety of tectonic regimes, including: intermediate to older age oceans, back-arc marginal basins, continental margins, platforms and shields, as well as the majority of active deep subduction zones. Details of the individual corridors are compiled in Table 2.2. Included is the distribution of tectonic sampling amongst the six provinces of the *Jordan* [1981] GTR1 regionalization, expressed as the proportion of total horizontal path length within each region. The experimental geometries employed were dictated largely by the positions of digital, low-frequency seismic instruments (both Global Digital Seismic Network (GDSN) and High-Gain, Long-Period (HGLP) network instruments were utilized) and regions of frequent intermediate- and deep-focus seismicity (Figure 2.7). Unfortunately, with the present distribution of seismic installations, it is difficult to study young oceanic regions, precluding the possibility of sampling active ridge segments. As compared to global areal fraction, our sampling of the GTR1 tectonic provinces is biased towards regions B (25 Myr $\leq$ age $\leq$ 100 Myr ocean) and Q (phanerozoic orogenic zones, regions of submerged continental or transitional crust, and

subduction zones), but does include significant path lengths through all regions other than A (young oceans).

For each seismic corridor, all available records of events of body-wave magnitude 5.7 or greater occurring at depths greater than 75 km were examined. Data were kept on the combined criteria of high observed signal-to-noise ratios (SNRs) and apparent source simplicity; i.e., the presence of simple and impulsive P and S waveforms. The preprocessing of data involved forming the SH component by rotation of the N-S and E-W instruments assuming the great-circle back-azimuth. Records which displayed significant P wave energy following rotation were discarded. Rotation was followed by damped least-squares deconvolution, low-pass filtering employing a Hanning taper with corner frequency of 40 mHz and maximum pass of 60 mHz, and decimation onto a 3-s digitization interval. The former two steps combined resulted in a flat Fourier spectrum throughout most of the effective passband, centered on the dominant frequency of ScS_n (~30 mHz) and approximately 30 mHz wide. Loss of very low frequencies, owing to the small amount of damping employed in deconvolution, is considered unimportant, in that these frequencies undergo very little attenuation and contribute little additional phase information. After filtering, the reverberative interval of the seismogram was extracted by selective muting of unwanted portions of the time series. This sequence of steps produced records of optimal SNR and pulse simplicity, and facilitated comparison of parameter estimates between corridors by standardizing the effective frequency response of an otherwise heterogeneous network of instruments. Unless stated otherwise, all data can be assumed to have been filtered in this fashion. Other examples of data, drawn from corridors 6 and 9 in Table 2.2 can be found in Figures 2.8 and 2.9.

A SIMPLE EXPERIMENT

The similarity of ray paths for first-order reverberations and their parent phases allows us to study the path-averaged properties along the differential path element in a manner

analogous to multiple ScS studies of whole-mantle quality factors (Q_{ScS}). In this section we describe the results of a simple experiment which demonstrates the utility of first-order reverberations in the study of mantle layering by exploiting the differential sampling of the mantle by zeroth- and first-order reverberations. Although primarily tutorial in nature-- intended to acquaint the reader with some of the more salient features of first-order reverberations--the results of this experiment are not without interest.

Attenuation in the Mantle

For the phase pair $\{sScS_n, S650^+S\}$-$sScS_n$, the differential element consists of a "pegleg" reflection in the upper mantle, so we can estimate the path-averaged attenuation of the upper mantle independently of either the lower-mantle or whole-mantle values. The average attenuation of the upper mantle is defined by the depth integral

$$Q_{UM}^{-1} = \frac{2}{\tau_{650}} \int_0^{650} dz \, v_s^{-1}(z) \, Q_{\beta}^{-1}(z) \tag{2.1}$$

where τ_{650} is the two-way travel time through the upper 650 km of the mantle. We have applied the phase-equalization and stacking algorithm of *Jordan and Sipkin* [1977] to twenty $\{sScS_n, S650^+S\}$-$sScS_n$ phase pairs observed along the Tonga-KIP corridor (number 8 in Table 2.2) to obtain a least-squares estimate of the upper-mantle attenuation operator. The moduli and phases at eight frequencies from 13 to 33 mHz are plotted in Figure 2.10. Although the individual amplitude estimates have a large uncertainty, the frequency variation of amplitude and phase is consistent with the linear, causal, constant-Q assumption. Attributing all the differential attenuation to the upper mantle and using PA2 to calculate propagation corrections and reflection coefficients, we obtain $Q_{UM} = 70 \pm 15$ for the average upper-mantle quality factor. This result is consistent with *Nakanishi's* [1980]

47

estimate of 70 for the Sea of Japan above 552 km depth, derived from $sScS_n/ScS_n$ spectral ratios, and with *Sipkin and Jordan's* [1980*b*] Oceanic Model B, which has $Q_{UM} = 84$.

By a similar procedure, we obtained an average lower-mantle quality factor of $Q_{LM} = 190 \pm 60$ from eighteen $\{ScS_n, S650^-S\}$-ScS_n phase pairs. As seen in Figure 2.11, the moduli and phases estimated for this differential response operator are more uncertain, a consequence of the fact that the amplitude and attenuation of the bottomside reflections from 650 km are smaller than the topside reflections.

As a consistency check, we have also estimated the whole-mantle attenuation operator by phase-equalizing and stacking ScS_n phases from the same set of seismograms. Twenty six phase pairs yielded $Q_{ScS} = 150 \pm 10$. (In their comprehensive study, *Sipkin and Jordan* [1980*b*] found $Q_{ScS} = 141 \pm 16$ along the Tonga-KIP corridor and 155 ± 11 for all paths crossing the western Pacific.) Energy losses due to scattering of $sScS_n$ are small (occurring primarily as loss of energy to higher-order reverberations) [*Revenaugh et al.*, 1985], and will affect both zeroth- and first-order reverberations in a similar fashion, thus we can calculate a whole-mantle attenuation factor from the first-order reverberations using the relation

$$Q_{ScS}^{-1} = \frac{1}{\tau_{ScS}} \left[\tau_{650} \, Q_{UM}^{-1} + \tau_{LM} \, Q_{LM}^{-1} \right] \qquad (2.2)$$

Combining the Q_{LM} and Q_{UM} estimates from Figures 2.10 and 2.11 in this manner gives $Q_{ScS} = 125 \pm 35$, which is less than the direct measurement, though not significantly so. In other words, there is a slight inconsistency between the whole-mantle quality factors obtained from the first-order and zeroth-order reverberations.

The estimates of Q_{UM} and Q_{LM} quoted above are only apparent values, however, since they depend strongly on the reflection coefficient $R(650)$, whose magnitude was set at the PA2 value of 0.0835 (all reflection coefficients are stated at normal incidence and apply to SH-polarized waves unless stated otherwise). In principle, the three apparent Q

observations can be used to solve for the reflection coefficient of the 650-km discontinuity, as well as the integrated attenuation factors in the two mantle layers. To perform this refinement, we linearized the relation between Q^{-1} and $R(650)$ about a reference frequency of 20 mHz and an angle of incidence of 7°, judged to be the average for the reverberations employed. We sought perturbations to apparent values of Q_{UM}^{-1} and Q_{LM}^{-1} and the PA2 value of $R(650)$ that matched the attenuation data for both the first-order and zeroth-order reverberations. The perturbations were thus required to satisfy the system of equations

$$\begin{bmatrix} 1 & 0 & \dfrac{-2}{\omega \tau_{UM}} \\ 0 & 1 & \dfrac{-2}{\omega \tau_{LM}} \\ \dfrac{\tau_{UM}}{\tau_{ScS}} & \dfrac{\tau_{LM}}{\tau_{ScS}} & 0 \end{bmatrix} \begin{bmatrix} \delta Q_{UM}^{-1} \\ \delta Q_{LM}^{-1} \\ \delta R(650) \end{bmatrix} = \begin{bmatrix} 0 \\ 0 \\ \Delta Q_{ScS}^{-1} \end{bmatrix} \qquad (2.3)$$

here ΔQ_{ScS}^{-1} is the difference between the ScS attenuation factors estimated from zeroth-order and first-order reverberations. Evaluating the weighted-least–squares solution of this system at $\omega = 20$ mHz, we obtained the revised values: $Q_{UM} = 82 \pm 18$, $Q_{LM} = 231 \pm 60$, and $R(650) = 0.080 \pm 0.004$.

The uncertainties in the average quality factors are fairly large and strongly correlated with the uncertainty in the reflection coefficient (Figure 2.12), but the values are consistent with *Sipkin and Jordan's* [1980b] Oceanic Model B, for which $Q_{UM} = 84$ and $Q_{LM} = 225$. Recent free-oscillation solutions give lower-mantle Q_β values of 304 [*Masters and Gilbert*, 1982], 350 (model QMU of *Sailor and Dziewonski* [1978]) and 360 (model SL8 of *Anderson and Hart* [1978]) over the mode band 3–10 mHz. These are substantially greater than our 10–30-mHz estimate of 231 ± 60, suggesting Q_β is frequency dependent in the lower mantle. Therefore, the low Q_{LM} obtained from this experiment corroborates *Sipkin*

49

and Jordan's [1979, 1980*b*] arguments that the average attenuation of the lower mantle decreases with frequency between 3 and 30 Mhz.

Reflection Coefficient of the 650-Km Discontinuity

We note that our reflection-coefficient estimate is relatively insensitive to errors in Q (Figures 2.12*a* and 2.12*b*), indicating that first-order reverberations can be used to measure $R(650)$ very stably. The result for this path differs only slightly from the starting model PA2, which satisfies the higher-mode Rayleigh-wave data for the western Pacific, and is consistent with the velocity structures constrained by both body waves and normal modes. For example, model ATL of *Grand and Helmberger* [1984] gives $R(650) = 0.080$ and PREM [*Dziewonski and Anderson*, 1981] gives 0.077. Hence, within the Tonga-KIP corridor, the impedance contrast across the 650-km discontinuity is similar to these models. In Chapter 3 we develop a robust inversion scheme, capable of accurately estimating the reflection coefficients of lower magnitude mantle discontinuities, a task which cannot generally be accomplished by the simple technique outlined above.

SUMMARY

In this section, we have documented (evidently for the first time) that first-order mantle reverberations can be observed as discrete phases on the seismogram. The existence of the reverberative interval, especially as manifested on *SH*-polarized seismograms, allows us to profitably employ these low-amplitude phases to study the properties of mantle layering over relatively short horizontal path lengths. It is the last property, the ability to sample the entire mantle over short epicentral distances, that distinguishes mantle reverberations from the majority of tools available to seismology. The agreement obtained between data and ray-theory seismograms implies that most of the low-frequency energy arriving within the reverberative interval is directly attributable to these reverberations, and as such can be

parameterized in relatively simple terms, namely the vertical travel times, path-averaged Qs and reflection coefficients of the major mantle layers.

TABLE 2.1. Source Parameters of the Events Used in This Study

Time, UTC			Latitude deg	Longitude deg	Depth km	m_b
July 21, 1973	04	19:13.7	24.83S	179.19W	419	5.9
Dec. 19, 1973	12	55:51.1	20.60S	176.32W	229	5.8
Dec. 28, 1973	05	31:03.8	23.88S	180.00W	526	6.4
March 23, 1974	14	28:33.0	23.92S	179.88E	515	6.1
June 4, 1974	04	14:13.8	15.89S	175.04W	275	6.0
Oct. 21, 1974	04	12:28.7	17.97S	178.49W	596	6.0
Feb. 22, 1975	22	04:33.5	24.98S	178.88W	373	6.2
Feb. 3, 1976	12	77:30.1	25.14S	179.69E	477	5.8
Jan. 21, 1977	06	11:05.3	18.06S	178.37W	602	5.8
April 19, 1977	21	46:40.7	05.62S	125.62E	555	5.7
June 29, 1977	07	24:36.7	07.85S	127.99E	98	6.0
July 6, 1977	11	28:31.5	21.00S	178.58W	597	5.8
Aug. 11, 1977	01	43:05.2	17.77S	174.14W	106	6.3
Sept. 10, 1977	13	39:07.7	07.03S	106.90E	138	5.9
Oct. 29, 1977	20	15:47.7	06.45S	146.70E	111	5.9
Nov. 21, 1977	11	39:46.4	06.92N	123.64E	599	5.8
Nov. 22, 1977	15	56:50.5	10.00S	161.04E	96	5.9
Dec. 30, 1977	10	38:25.0	05.45S	151.63E	78	5.9
Jan. 28, 1978	19	36:45.6	25.95S	177.35W	97	6.0
Feb. 3, 1978	14	33:42.2	04.73N	125.59E	179	5.7
Feb. 12, 1978	03	34:35.2	08.82S	124.12E	112	5.8
Feb. 19, 1978	12	19:40.4	0\390S	128.95E	11	5.8
March 7, 1978	02	48:55.3	31.90N	137.44E	434	6.9
April 18, 1978	17	27:33.0	05.01N	127.28E	114	6.0
May 23, 1978	07	50:39.6	31.00N	130.45E	176	6.3
June 15, 1978	13	30:52.0	07.43S	129.07E	172	5.8
Aug. 5, 1978	15	46:42.8	03.67S	151.93E	249	5.7
Aug. 14, 1978	23	45:09.9	08.08S	146.83E	139	5.8
Sept. 6, 1978	11	07:53.1	13.46S	166.82E	202	6.0
Oct. 15, 1978	05	36:19.8	05.76S	147.96E	162	5.8
Dec. 11, 1978	03	33:59.6	07.07S	118.13E	488	5.9
Feb. 7, 1979	21	02:09.5	05.13N	147.96E	129	6.2
Feb 11, 1979	22	22:24.9	06.13N	126.24E	143	6.1
April 15, 1979	22	14:57.3	05.56N	12.366E	536	5.9
April 24, 1979	01	45:16.6	20.81S	178.90W	604	6.0
May 13, 1979	17	31:01.4	04.09S	122.96E	613	5.7
Aug. 5, 1979	00	53:55.0	22.95S	177.10W	229	6.4
Aug. 16, 1979	21	31:31.2	41.97N	131.74N	604	6.1
Jan. 8, 1980	10	08:49.0	05.73N	126.29E	100	5.7
Jan. 20, 1980	07	28:49.7	02.72N	128.16E	208	5.8
Feb. 29, 1980	11	13:30.6	06.13N	127.17E	79	6.1
March 29, 1980	04	07:50.8	04.44S	154.82E	480	5.8
April 13, 1980	18	04:52.8	23.74S	176.70W	166	6.7
May 23, 1980	10	33:08.5	07.10S	129.70E	149	5.8
June 4, 1980	09	31:56.6	05.45S	151.11E	91	5.7
June 11, 1980	08	10:15.1	06.98S	125.46E	540	5.8
July 8, 1980	04	39:31.7	06.63N	125.95E	165	5.9
July 16, 1980	19	56:52.5	04.68S	143.18E	82	6.5
Oct. 19, 1980	15	03:39.8	06.12S	145.28W	132	5.8
Jan. 2, 1981	15	39:65.5	29.03N	128.38E	217	6.1
Jan 23, 1981	04	58:35.8	42.20N	142.07E	121	6.3
March 21, 1981	22	52:45.1	05.48S	146.88E	233	6.0

TABLE 2.1. Continued.

Time, UTC			Latitude deg	Longitude deg	Depth km	m_b
April 5, 1981	03	17:58.4	06.12S	154.34E	417	5.8
April 28, 1981	21	14:56.7	23.62S	179.93W	553	6.0
May 28, 1981	16	10:14.2	14.48S	166.96E	138	5.9
Sept. 3, 1981	04	29:55.8	0.644N	126.33E	84	5.8
Sept. 4, 1981	11	15:19.5	09.87N	124.17E	636	5.9
Sept 28, 1981	17	56:28.1	29.27S	178.65W	309	5.9
Oct. 7, 1981	03	02:20.2	20.52S	179.00W	625	5.9
Oct. 17, 1981	06	44:57.6	07.22S	128.78E	186	6.1
Nov. 25, 1981	23	51:23.3	20.68S	179.07W	615	5.9
March 29, 1982	21	33:55.8	00.01N	123.29E	165	6.0
May 12, 1982	10	03:41.9	24.64S	179.08E	560	5.6
June 4, 1982	15	21:40.6	04.11N	124.50E	332	5.8
June 11, 1982	00	38:22.7	17.40S	174.09W	113	6.3
June 22, 1982	04	18:55.3	07.28S	125.99E	473	6.2
July 4, 1982	01	20:13.1	27.92N	136.48E	552	6.3
July 5, 1982	08	57:01.1	30.77N	130.47W	119	5.7
Sept. 17, 1982	13	28:33.3	23.15S	179.83E	562	5.9
Oct. 7, 1982	07	16:01.9	06.97S	125.88E	521	6.2
Jan. 16, 1983	22	10:18.4	05.37S	147.07E	230	6.0
Jan. 26, 1983	16	02:28.6	30.52S	179.21W	224	6.1
May 10, 1983	11	02:40.1	05.42S	150.94E	101	6.0
May 11, 1983	00	17:16.9	02.61N	128.35E	133	5.8
June 1, 1983	02	00:01.9	16.93S	174.39W	186	6.1
June 20, 1983	05	43:41.8	23.68S	179.23E	562	5.6
June 21, 1983	17	06:56.6	29.69N	129.45E	155	5.9
Aug. 6, 1983	22	37:57.7	06.52S	130.02E	173	5.8
Sept. 16, 1983	08	09:33.0	23.61S	179.78W	517	5.9
Oct. 31, 1983	17	37:59.9	09.00S	119.05E	98	6.0
Nov. 6, 1983	09	38:44.1	20.02S	177.86W	394	5.5
Nov. 20, 1983	20	32:24.3	07.31S	130.72E	79	5.9
Nov. 24, 1983	05	30:42.8	07.44S	128.32E	157	6.2
Dec. 12, 1983	09	26:12.8	07.72S	127.25E	165	6.2
Dec. 18, 1983	17	28:36.0	08.84S	119.51E	75	5.7
Jan. 1, 1984	09	03:46.8	33.38N	136.81N	384	6.5
Feb. 1, 1984	07	28:31.7	49.10N	146.31E	581	6.0
Feb. 17, 1984	16	32:25.6	06.49S	130.14E	172	6.1
March 5, 1984	03	33:58.2	08.26N	123.86E	644	6.7
March 6, 1984	02	17:30.6	29.60N	139.11E	446	6.3
April 13, 1984	22	05:14.6	05.69S	148.44E	170	5.8
April 20, 1984	06	31:13.6	50.19N	148.77E	593	6.0
April 24, 1984	04	11:35.2	30.81N	138.46E	395	6.2
May 30, 1984	07	49:55.1	05.02S	151.64E	157	6.2
July 9, 1984	23	19:08.1	05.97S	111.37E	531	5.9
Aug. 6, 1984	12	02:06.9	00.29S	122.38E	253	6.2
Sept. 5, 1984	09	32:15.4	08.33S	121.58E	197	5.9
Oct. 15, 1984	10	21:17.5	15.81S	173.40W	120	6.5
Oct. 29, 1984	23	18:06.6	05.66N	125.72E	136	6.0
Oct. 30, 1984	01	05:58.8	17.07S	173.75W	150	6.0
Nov. 21, 1984	08	15:24.4	05.02N	125.56E	181	6.4
Jan. 11, 1985	14	41:56.0	00.21S	123.79E	145	6.0
March 25, 1985	11	07:23.8	06.83S	128.92E	290	5.7
March 28, 1985	16	07:11.2	40.42N	140.17E	169	6.1
April 3, 1985	20	21:41.2	28.40N	139.61E	455	5.9
June 4, 1985	03	56:29.1	04.79N	127.38E	117	6.0

TABLE 2.1. Continued.

Time, UTC			Latitude deg	Longitude deg	Depth km	m_b
Sept. 3, 1985	23	32:49.7	01.44N	128.29E	103	5.7
Sept. 10, 1985	09	39:06.3	27.14N	139.91E	497	5.8
Oct. 12, 1985	02	13:05.1	21.79S	176.08W	170	5.8
Oct. 25, 1985	18	12:22.7	07.24S	124.15E	596	5.9
Dec. 30, 1985	11	13:18.3	05.82S	150.64E	77	5.7
Feb. 7, 1986	02	46:58.4	05.19S	151.91E	101	5.8
May 8, 1986	14	37:37.5	04.60N	125.47E	144	5.8
May 11, 1986	01	24:32.7	26.37N	125.21E	204	5.9
June 16, 1986	10	48:35.6	21.86S	178.87W	565	6.1
June 24, 1986	03	11:43.2	04.42S	143.64E	100	6.7
July 19, 1986	05	59:42.1	47.05N	151.32E	153	5.9
Aug. 10, 1986	04	40:54.0	01.95N	128.11E	110	6.1
Oct. 4, 1986	02	00:12.3	03.09N	127.79E	128	5.9
Oct. 22, 1986	08	59:36.2	10.72S	165.99E	183	5.8
Oct. 23, 1986	03	54:27.1	06.21S	146.11E	118	5.8
April 3, 1987	17	54:30.4	04.82S	144.12E	95	5.7
June 18, 1987	14	03:23.0	10.59S	162.38E	86	6.0

TABLE 2.2. Sampling of Surface-Tectonic Regions

#	Source Region	Recv.	Num Records	Tectonic Regime[1]					
				A	B	C	Q	P	S
1	Sumba-Phil.	CHTO	17	0.00	0.25	0.00	0.60	0.15	0.00
2	New Britain	CTAO	9	0.00	0.47	0.00	0.53	0.00	0.00
3	Sumba		11	0.00	0.00	0.01	0.85	0.03	0.11
4	Philippines		11	0.00	0.03	0.00	0.97	0.00	0.00
5	Tonga-Fiji		10	0.00	0.66	0.00	0.34	0.00	0.00
6	Sumba-Phil.	GUMO	20	0.00	0.52	0.00	0.48	0.00	0.00
7	Izu-Bonin		5	0.00	0.45	0.10	0.45	0.00	0.00
8	Tonga-Fiji	KIP	9	0.08	0.14	0.68	0.10	0.00	0.00
9	Sumba-Phil.	MAJO	14	0.00	0.77	0.00	0.23	0.00	0.00
10	Japan-Izu		9	0.00	0.36	0.00	0.64	0.00	0.00
11	Philippines	NWAO	14	0.00	0.04	0.00	0.49	0.11	0.36
12	New Britain		15	0.00	0.15	0.00	0.29	0.17	0.39
13	Sumba		16	0.00	0.00	0.02	0.31	0.13	0.54
14	Tonga-Fiji		13	0.01	0.42	0.00	0.40	0.00	0.16
15	Tonga-Fiji	SNZO	13	0.00	0.42	0.00	0.58	0.00	0.00
16	Philippines	TATO	8	0.00	0.09	0.00	0.91	0.00	0.00
17	New Britain		9	0.00	0.77	0.01	0.22	0.00	0.00
18	Japan-Izu		10	0.00	0.25	0.00	0.75	0.00	0.00
Total			203	0.01	0.32	0.05	0.51	0.03	0.09
Global Areal Fraction				0.13	0.35	0.13	0.22	0.10	0.07

[1]Fraction of horizontal path length spent in *Jordan's* [1981] GTR1 tectonic regionalization: A (young ocean; <25 Myr), B (intermediate ocean; <100 Myr), C (old ocean; >100 Myr), Q (Phanerozoic orogenic zones, transitional and subduction zones), P (Phanerozoic platforms), S (stable shields).

Fig. 2.1. (Left) SH-polarized seismogram of an intermediate-focus event in the Tonga-Fiji seismic zone (Dec. 19, 1973) recorded by the HGLP station KIP on the island of Oahu. Time is minutes after origin time. The reverberative interval is defined as the portion of the seismogram between the fundamental-mode surface wave and the first arrivals propagating along the major arc (SSS_2). (Right) Portions of seismogram located between ScS_n-$sScS_n$ wave groups (zeroth-order reverberations) shown on an expanded scale. These portions consist almost entirely of higher-order energy, and are dominated by first-order reverberations from the transition zone. Two important first-order reverberations are aligned and labeled: $\{sScS_n, S650^+S\}$ and $\{ScS_n, S650^-S\}$, corresponding to topside and bottomside reflections from the 650-km discontinuity, respectively.

Fig. 2.2. (Top) Schematic ray paths for the three members of the family $\{ScS_2, S650^+S\}$, the first-order reverberation from the topside of the 650-km discontinuity. For a spherically symmetric Earth, the three phases shown here are dynamic analogs; i.e., they have the same travel time, amplitude and phase at the receiver and thus constructively interfere to produce an observable arrival. (Bottom) Schematic ray paths for the two members of the family $\{ScS_2, S650^-S\}$, the first-order reverberation from the bottomside of the 650-km discontinuity. In general there are either n or $n+1$ members of a first-order reverberation family depending on the depth of the source and whether the reflection is topside or bottomside, where n is the number of core bounces of the parent zeroth-order reverberation.

Fig. 2.3. SH-polarized seismograms showing the reverberative interval at KIP for the Feb. 22, 1975 event ($h = 373$ km, $\Delta = 50.4°$). Top three traces are synthetic seismograms generated by normal-mode summation, geometrical-optics ray summation, and ray summation with an approximate ellipticity correction. Bottom trace is data from the HGLP

instruments at KIP. Ray summation includes only zeroth-order reverberations and first- and second-order reverberations from the 400-km and 650-km discontinuities; they do not include direct arrivals along the minor and major arcs, nor any reverberations from other mantle discontinuities. Normal-mode summation is complete to 50 mHz. Time is minutes after origin time.

Fig. 2.4. SH-polarized seismograms showing the reverberative interval for the March 23, 1974 event ($h = 515$ km, $\Delta = 49.9°$). Bottom trace is data; all others are synthetics computed by geometrical-optics ray theory. The trace labeled "zeroth" comprises the ScS_n and $sScS_n$ phases, beginning with ScS_2 and $sScS_2$. The traces labelled "650+," "400+," "650−," and "400−" are the first-order reverberations reflecting from the top and bottom of the 650-km and 400-km discontinuities, respectively. The trace labelled "2nd" contains all the second-order reverberations from the 400-km and 650-km discontinuities. The first-order reverberations decay slowly with increasing multiple number n, owing to the constructive interference among members of each dynamic ray family. Time is minutes after origin time.

Fig. 2.5. SH-polarized seismograms showing the reverberative interval for the Dec. 19, 1973 event ($h = 229$ km, $\Delta = 45.4°$). Bottom trace is data; all others are synthetics computed by geometrical-optics ray theory. Conventions are the same as in Figure 2.4.

Fig. 2.6. SH-polarized seismograms of the reverberative interval at KIP for six earthquakes in the Tonga seismic zone arrayed according to focal depth. The bottom trace for each event is data; the top trace is the ray-summation synthetic containing zeroth-order reverberations and first- and second-order reverberations from the 400-km and 650-km discontinuities. Time is minutes after origin time. Large-amplitude phases seen in the data

beyond ~76 min are the first arrivals along the major arc and are not included in the synthetics.

Fig. 2.7. Mercator projections of the study area depicting the geographic distribution of earthquake sources (triangles) and receivers (squares). Stippled region depicts the surface sampling offered by zeroth- and first-order reverberations along the 18 individual seismic corridors detailed in Table 2.2.

Fig. 2.8. SH-polarized seismograms of the reverberative interval at GUMO for 5 earthquakes in the Sumba and Philippines seismic zones (corridor 6 in Table 2.2) arrayed according to focal depth. The bottom trace for each event is data; the top trace is the ray-summation synthetic containing zeroth-order reverberations and first- and second-order reverberations from the 400-km and 650-km discontinuities, as well as a number of smaller discontinuities in the upper mantle and transition zone. Time is minutes after origin time. Data and synthetic seismograms are filtered as described in the text..

Fig. 2.9. SH-polarized seismograms of the reverberative interval at MAJO for 5 earthquakes in the Sumba and Philippines seismic zones (corridor 9 in Table 2.2) arrayed according to focal depth. Conventions the same as Figure 2.8.

Fig. 2.10. Modulus and phase of the upper-mantle differential response operator for corridor 8 in Table 2.2, showing estimates derived from twenty $\{sScS_n,S650^+S\}$-$sScS_n$ phase pairs using the phase-equalization and stacking algorithm of *Jordan and Sipkin* [1977]. Lines represent predicted differential response for a linear, causal, constant-Q model with $Q_{UM} = 70$. Error bars are 2σ.

Fig. 2.11. Modulus and phase of the lower-mantle differential response operator, showing estimates derived from eighteen $\{sScS_n, S650^-S\}$-$sScS_n$ phase pairs using the phase-equalization and stacking algorithm of *Jordan and Sipkin* [1977]. Lines represent predicted differential response for a linear, causal, constant-Q model with $Q_{LM} = 190$. Error bars are 2σ.

Fig. 2.12. Estimates and 1σ error ellipses obtained by inverting the apparent Qs from zeroth-order and first-order reverberations for self-consistent estimates of Q_{UM}, Q_{LM}, and $R(650)$. (*a*) Correlation between $R(650)$ and Q_{UM}^{-1}. (*b*) Correlation between $R(650)$ and Q_{LM}^{-1}. (*c*) Correlation between Q_{UM}^{-1} and Q_{LM}^{-1}.
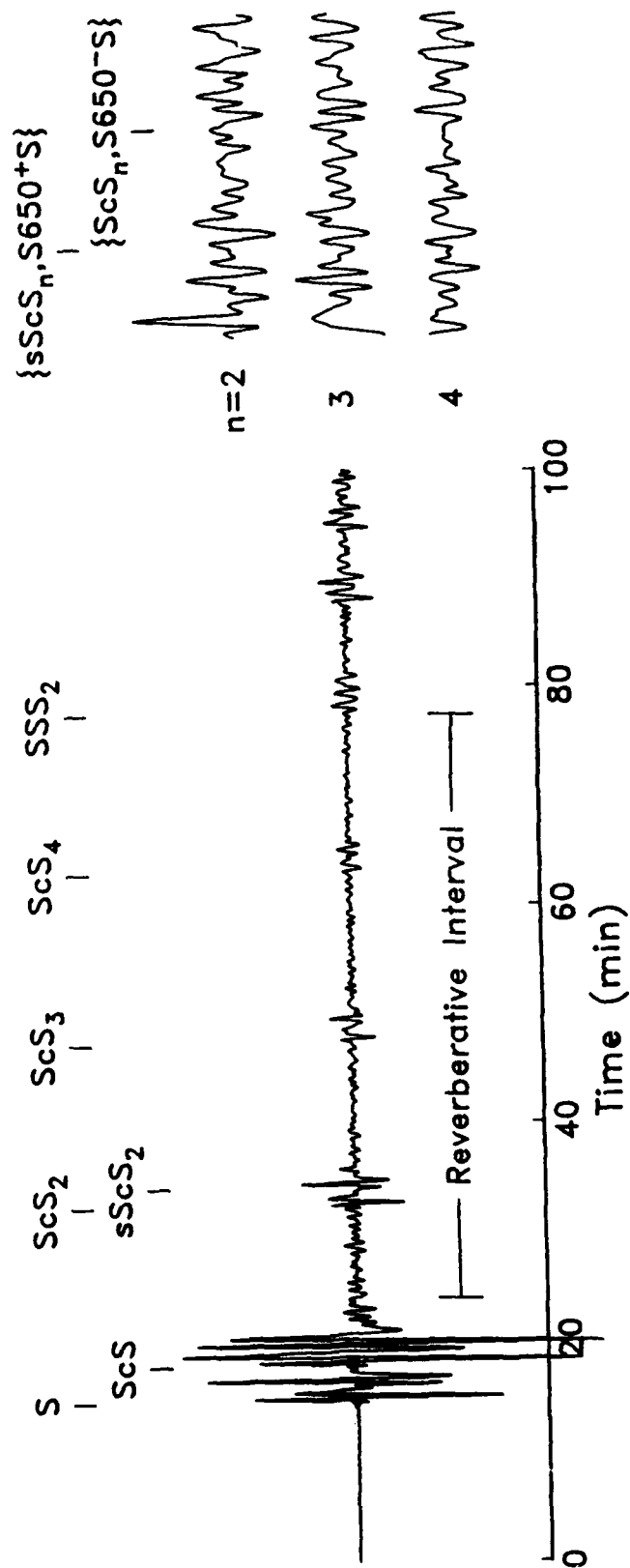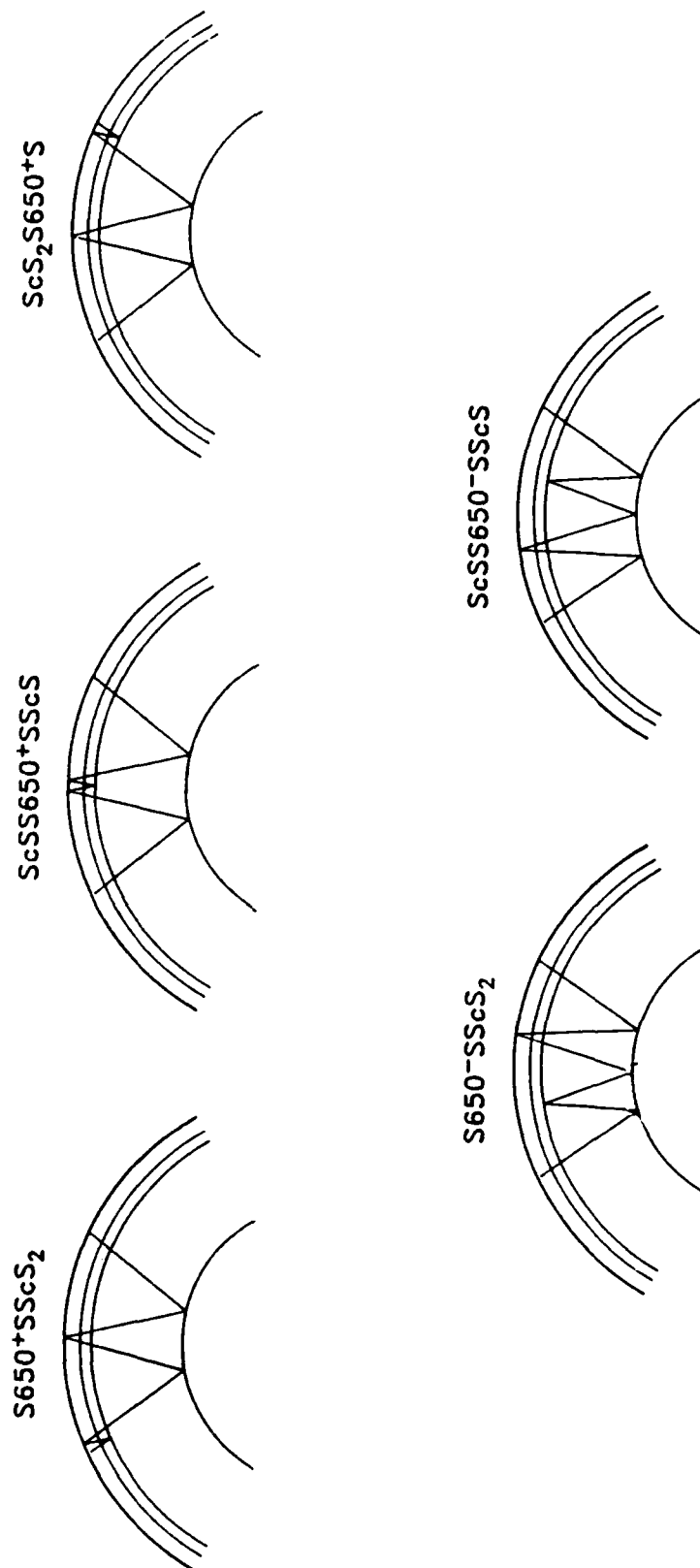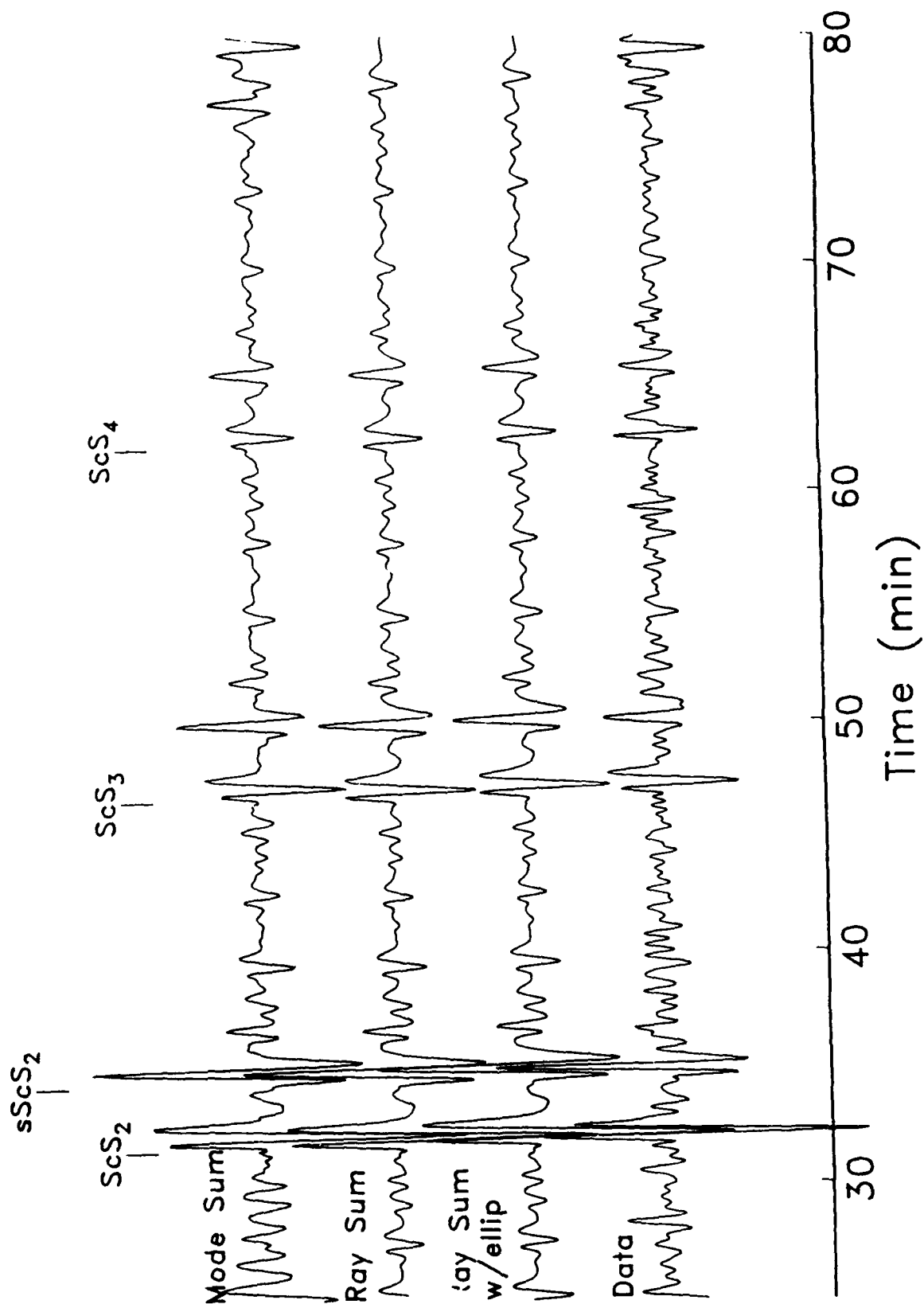
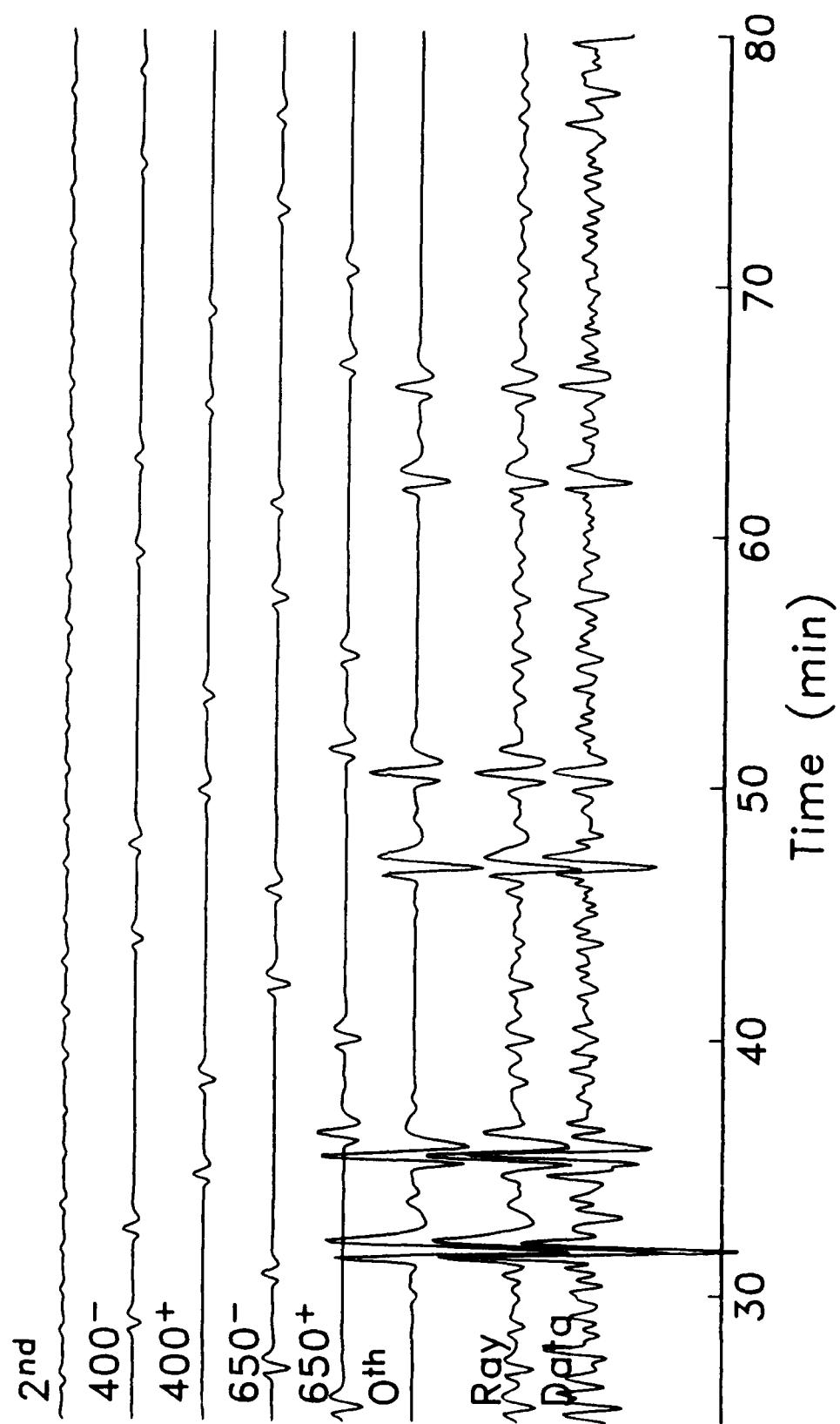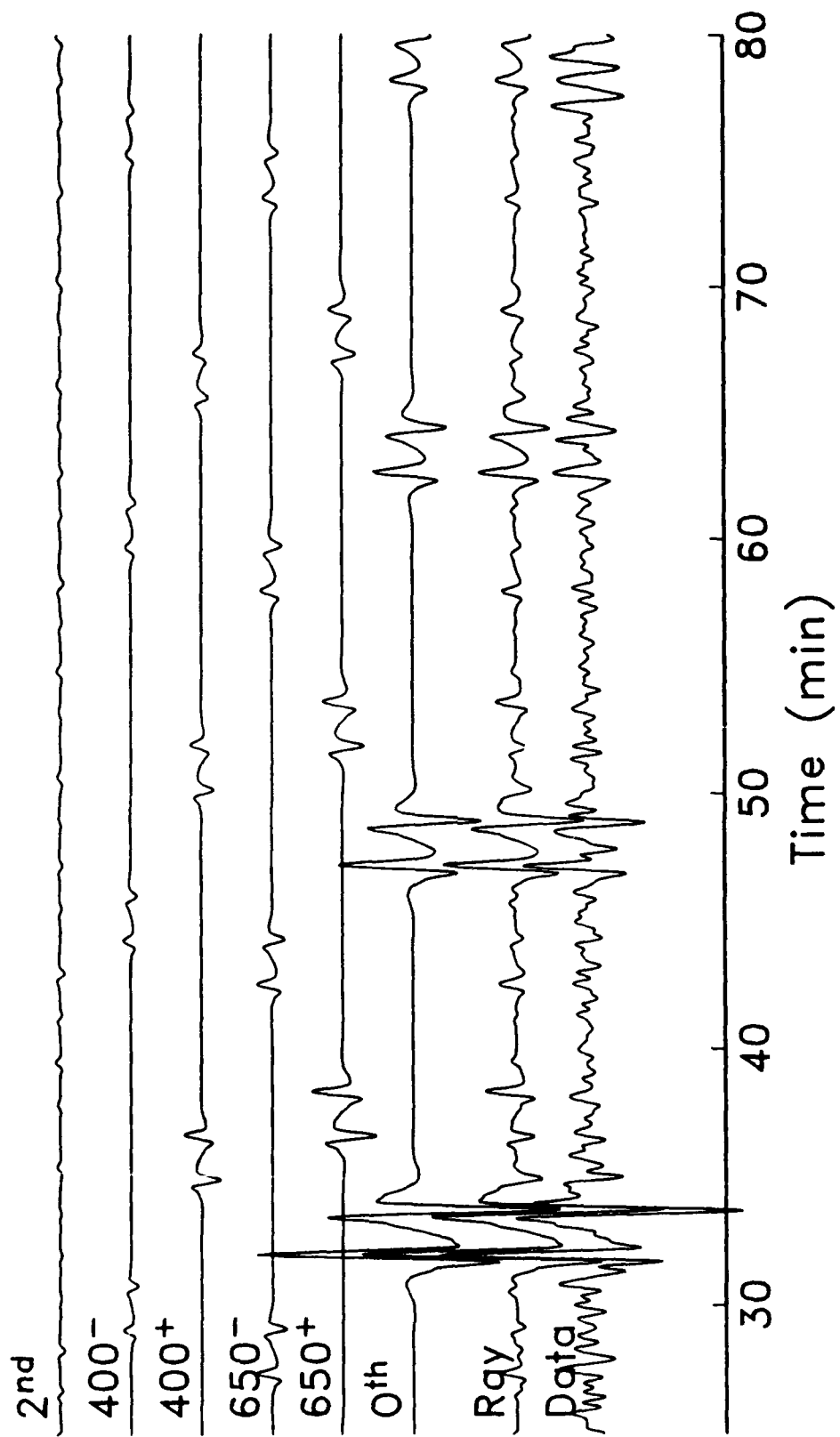Figure 2.1

60

Figure 2.2

61

Figure 2.3

62

Figure 2.4

Figure 2.5

64

Figure 2.6

65

Figure 2.7

Figure 2.8

h=613

h=536

h=165

h=149

h=144

Time (min)

Figure 2.9

68

Figure 2.10

69

Figure 2.11

70

Figure 2.12

71
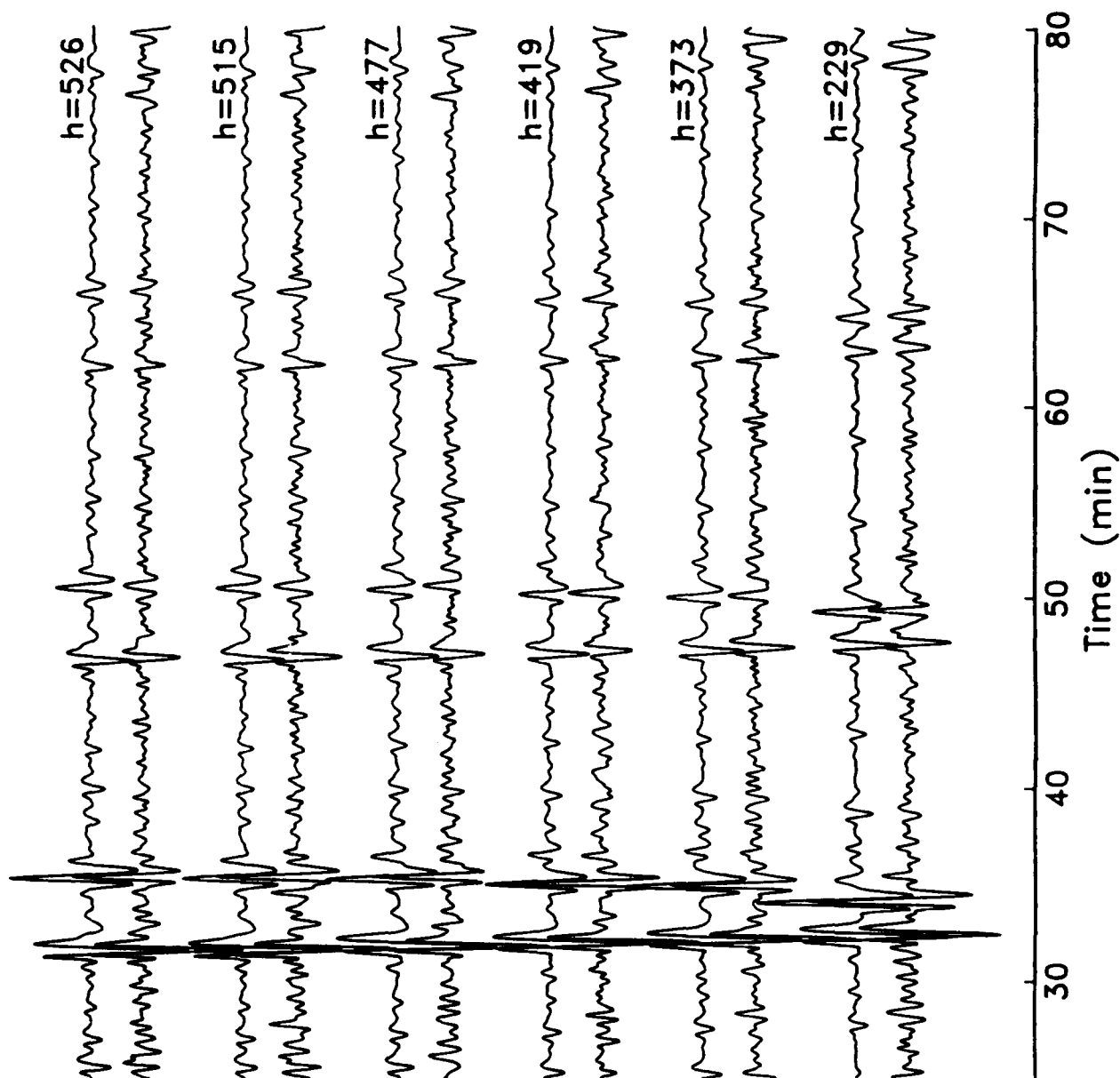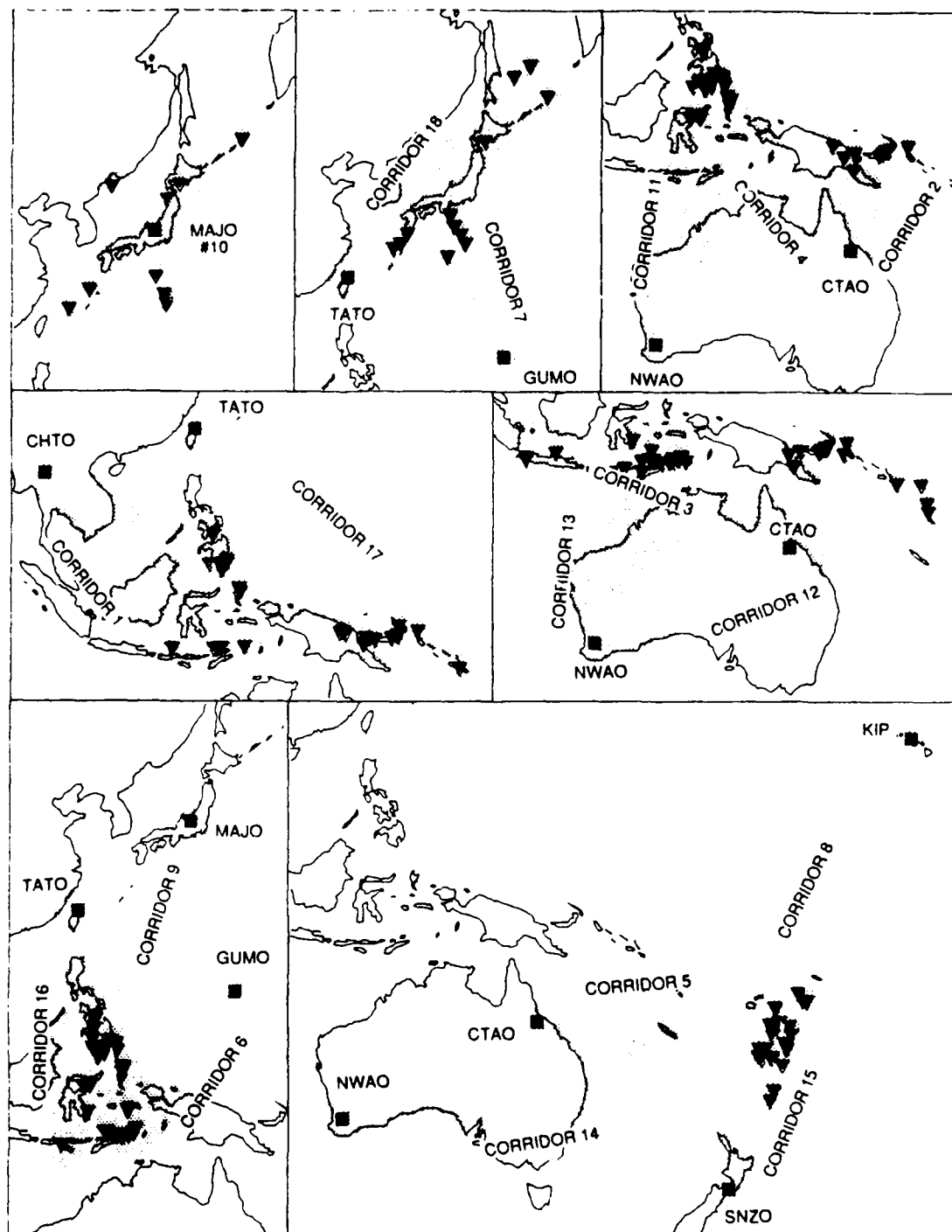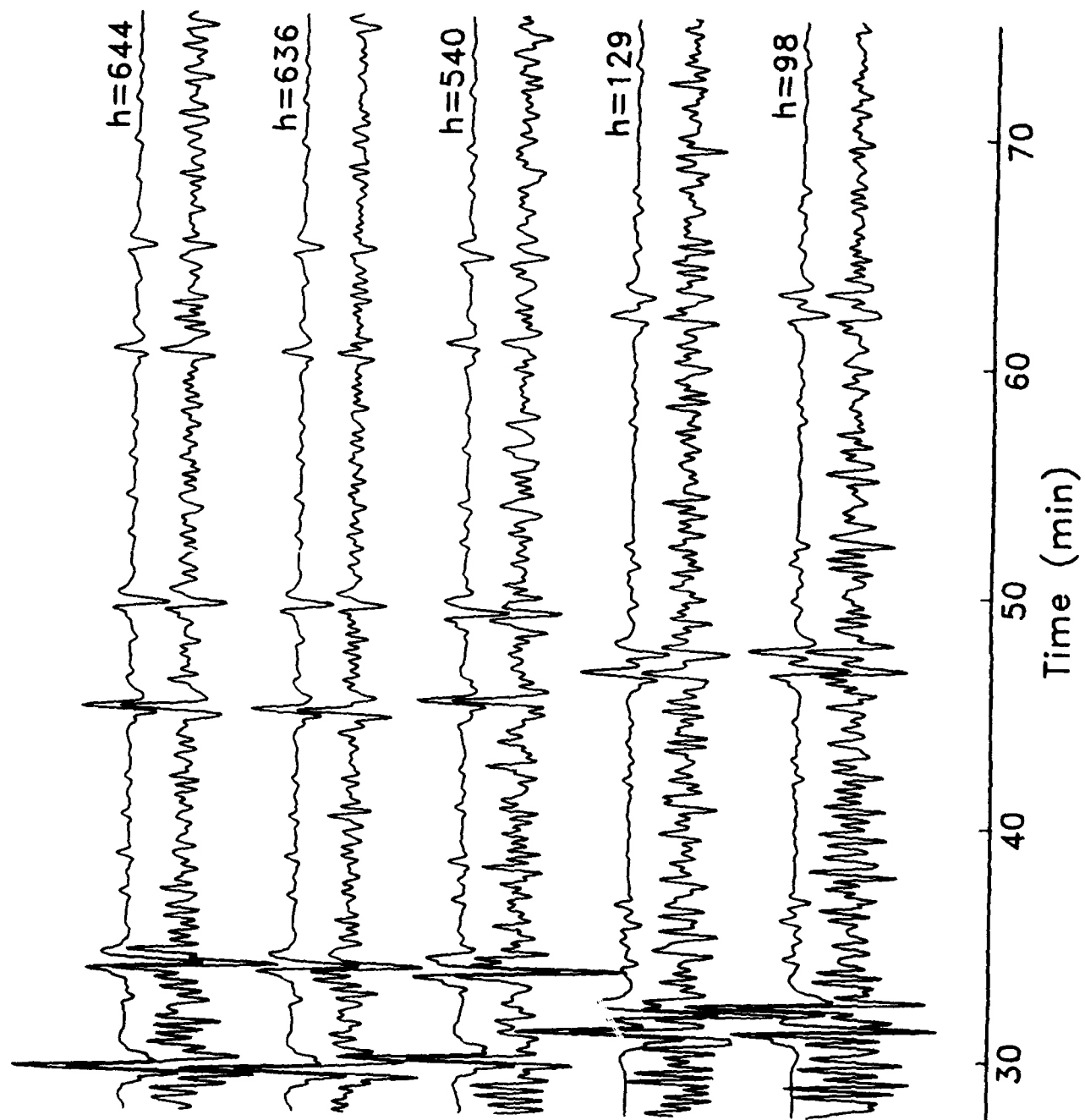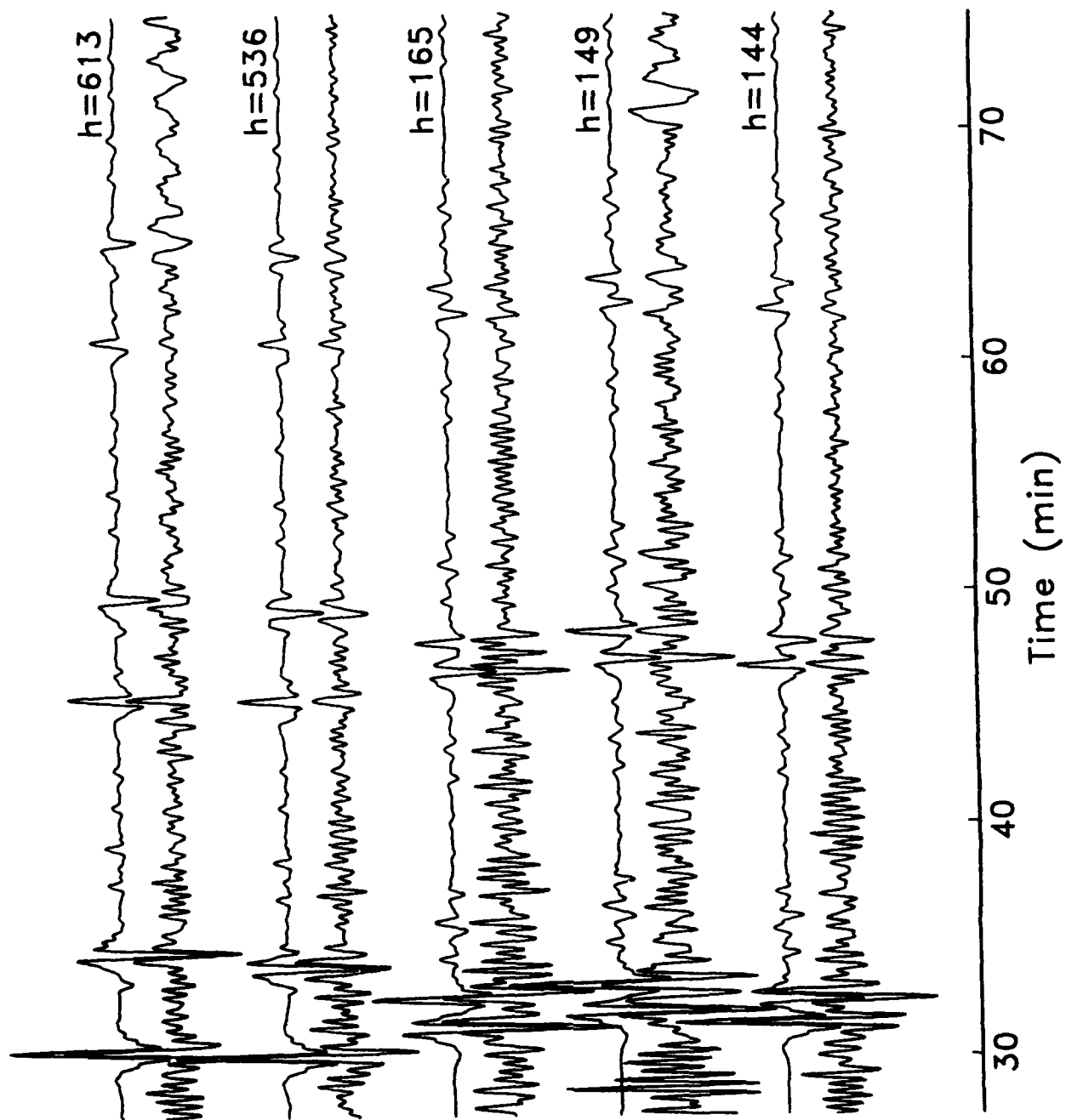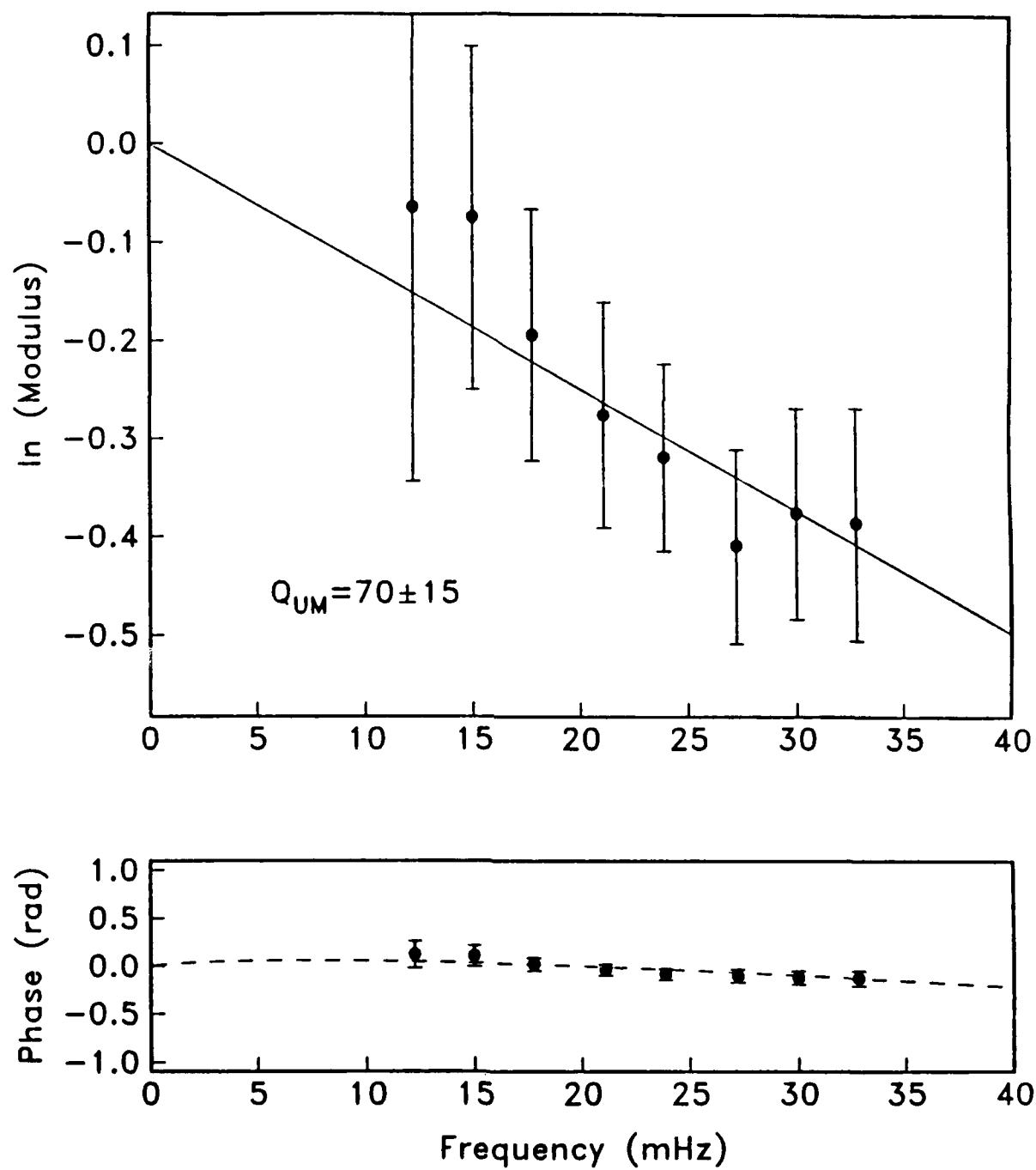
CHAPTER 3

REVERBERATION WAVEFORM INVERSION: FORMULATION

INTRODUCTION

In seismology, the Earth's structure can usually be parameterized as an n-tuple of

material properties $\mathbf{m} = \{\rho, \kappa, \mu, ...\}$, which include density, complex elastic moduli, etc.

Functions in this n-tuple are assumed to vary smoothly with spherical coordinates r, θ, ϕ,

except at a discrete set of interfaces $\{r = a_k (\theta, \phi): k = 1, K\}$, where some or all of the

functions in $\mathbf{m}$ may be discontinuous. The interfaces in classical Earth models include the

free surface, the Mohorovicic (M) discontinuity, the core-mantle boundary (CMB), and the

inner core-outer core boundary (ICB). Each of these interfaces is sharp enough to reflect

seismic body waves. By measuring the travel times and amplitudes of the reflected waves,

seismologists have learned much about the location of these interfaces and the contrast in
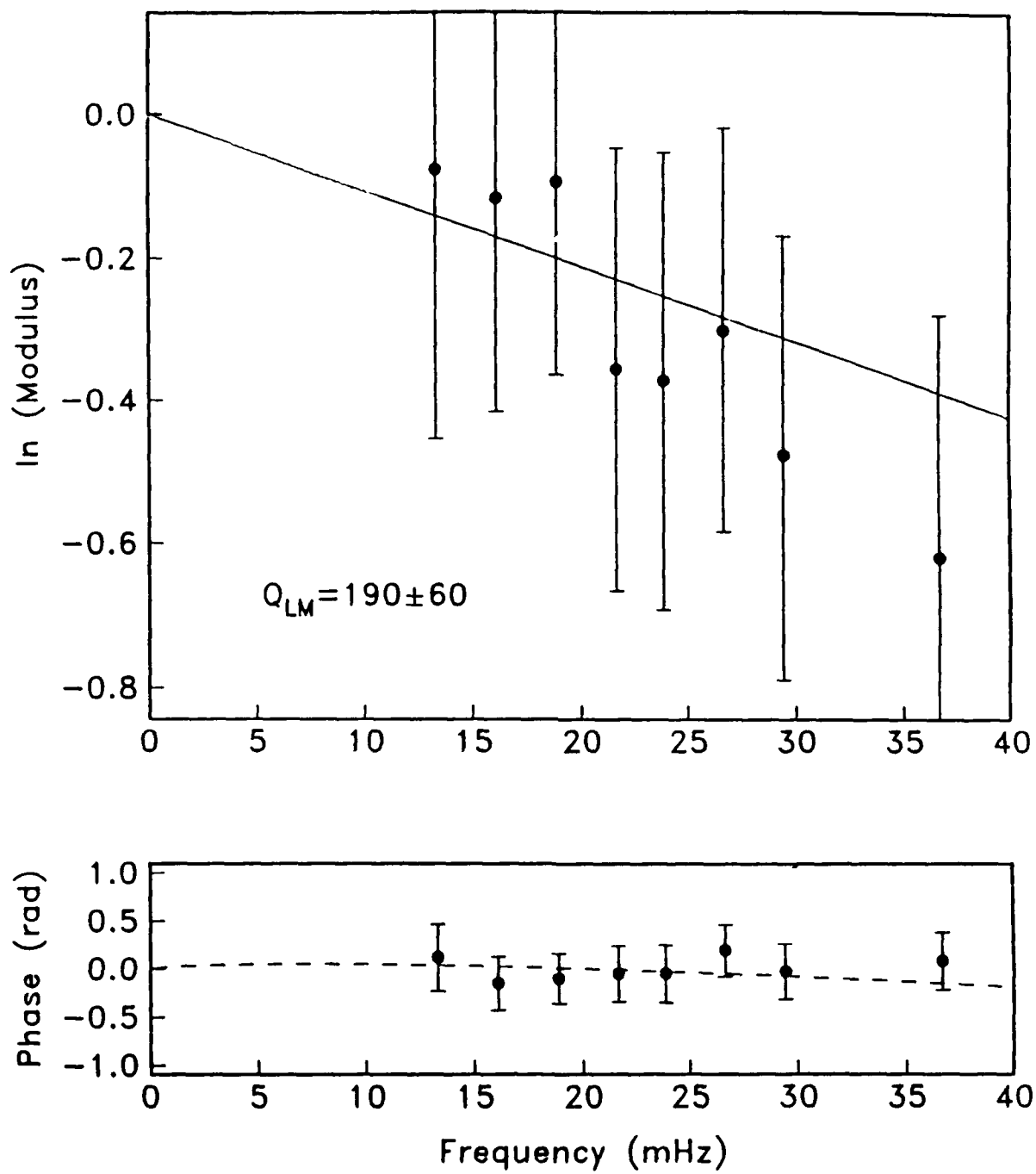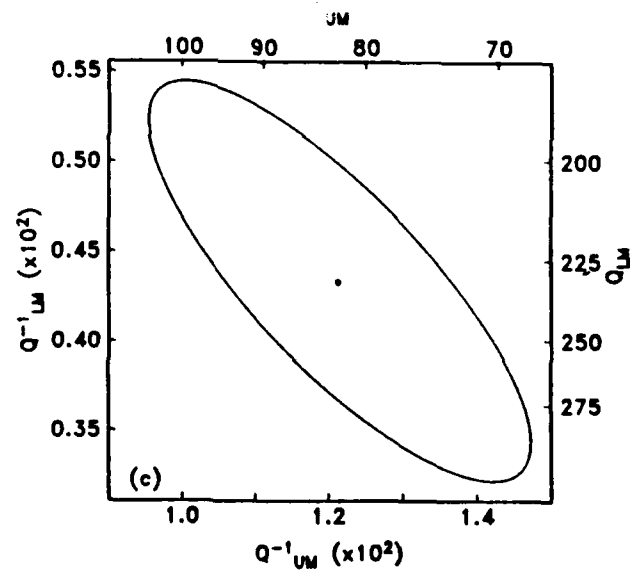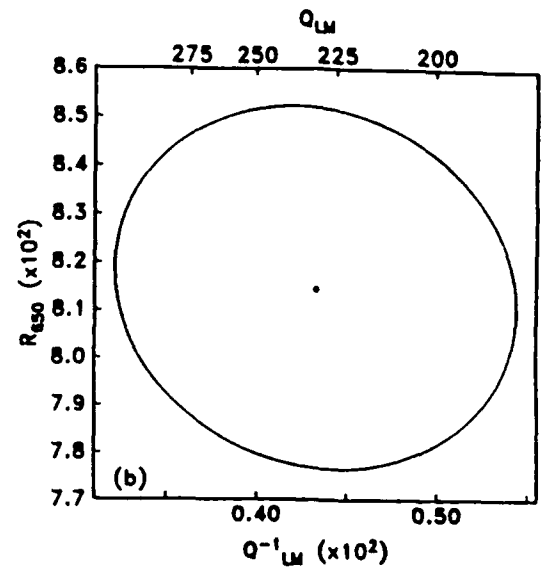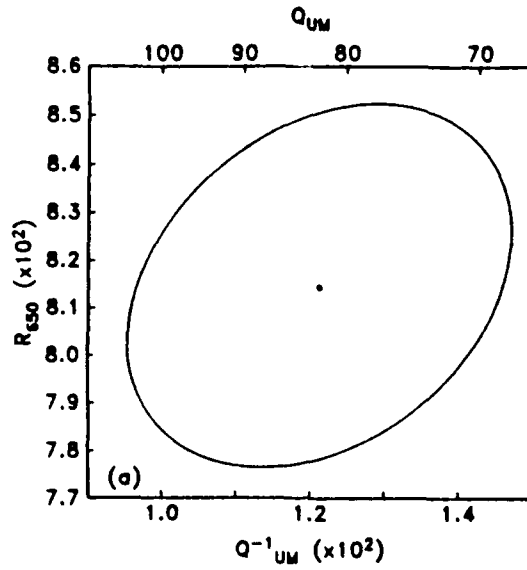
material properties across them.

The Earth's mantle is itself internally layered. Abrupt increases in seismic wave speeds

are known to occur at depths near 400 km and 650 km [e.g., *Niazi and Anderson*, 1965;

Johnson, 1967; *Burdick and Helmberger*, 1978; *Given and Helmberger*, 1980; *Walck*,

1984], and various other discontinuities have been identified in both the upper mantle [e.g.,

Hales, 1969; *Kanamori and Press*, 1970; *Anderson*, 1979a; *Hales et al.*, 1980] and the

lower mantle [e.g., *Johnson*, 1969; *Muirhead and Hales*, 1980; *Lay and Helmberger*,

1983; *Wright et al.*, 1985]. Understanding the nature of these discontinuities will

undoubtedly contribute substantially to understanding the dynamics of mantle convection

and its coupling to core convection.

There are a number of questions a more detailed knowledge of discontinuities could

begin to answer: (1) Does the 650-km discontinuity represent a change in mineral phase, a

change in composition, or both? (2) Is the 400-km discontinuity adequately explained by

standard models of mantle composition? (3) Is the aspherical structure of the mantle,

anelastic as well as elastic, coherent across the 650-km discontinuity, and what does this imply about convective flow at that depth? (4) Is there a sharp increase or decrease in wave speeds associated with the top of region D"? What does the structure of this interface say about chemical stratification in the vicinity of the CMB and the heat transfer from the core to the mantle?

The advent of tomography has enabled seismologists to generate three-dimensional maps of lateral velocity heterogeneity in the upper mantle [e.g., *Woodhouse and Dziewonski*, 1984; *Tanimoto and Anderson*, 1985; *Nataf et al.*, 1986], the transition zone [e.g., *Masters et al.*, 1982; *Romanowicz et al.*, 1987], the lower mantle [e.g. *Sengupta and Toksöz*, 1976; *Dziewonski*, 1984; *Grand*, 1987], and the core-mantle boundary [e.g., *Creager and Jordan*, 1986; *Morelli and Dziewonski*, 1987]. Unfortunately, the vertical resolution of the presently available data sets is inadequate to detect discontinuities internal to the mantle or to separate the structural contrasts across them. Instead, an appeal must be made to seismic signals whose interaction with discontinuity structure is much stronger. Reflected [e.g., *Engdahl and Flinn*, 1969; *Whitcomb and Anderson*, 1970] and mode-converted arrivals [e.g., *Jordan and Frazer*, 1975; *Vinnik*, 1977; *Faber and Müller*, 1980; *Barley et al.*, 1982; *Bock and Ha*, 1984; *Paulssen*, 1985, 1988] provide seismology with its most direct link to mantle discontinuities. Unfortunately they commonly suffer from low signal-to-noise ratios, curtailing their utility.

The reverberative interval of the seismogram, encapsulating the portion of time series between the passage of the fundamental surface wave train and the first body-wave arrivals from the major arc, provides an excellent window in which to observe subcritical-angle reflections from mantle discontinuities. The intervals between ScS_n and $sScS_n$ wave groups (zeroth-order reverberations) on an SH-polarized seismogram are approximately 15 minutes long and populated almost entirely of waves reflected one or more times from mantle and crustal discontinuities (first- and higher-order reverberations). A remarkable feature of higher-order reverberations is that they comprise families of dynamic analogs

73

(i.e., rays which travel by different paths but arrive at the receiver with the same amplitude, travel time and phase) whose membership increases with the number of core reflections n of the parent ScS_n or $sScS_n$ wave. As discussed in Chapter 2, there are either n or $n+1$ members depending on the geometry of the ray and the discontinuity depth. This increasing multiplicity helps offset the amplitude losses owing to geometrical spreading and anelastic dissipation, facilitating observation of several multiples on a single seismogram. The availability of multiples, topside and bottomside reflections, and their depth-phase equivalents, all on a single seismogram, make it possible to profitably employ first-order reverberations without access to, or need for, station array data.

We have developed techniques to extract information pertaining to mantle layering from the waveforms of zeroth- and first-order reverberations, techniques which make full use of the simplicity of structure and redundancy of information indigenous to the reverberative interval. Zeroth-order reverberations, by virtue of their greater SNRs and insensitivity to internal mantle discontinuities, are used to constrain source parameters and whole-mantle elastic and anelastic properties. Using these quantities, the method proceeds to first-order reverberations, whose waveforms are inverted for parameters describing gross mantle layering. The layering parameters that we can reasonably expect to extract are limited by the finite SNR and narrow-band frequency content. At a minimum, however, we can obtain path-averaged estimates of the whole-mantle travel time τ_{ScS} and quality factor Q_{ScS}, and the depths and reflection coefficients of the 400-km, 650-km, and M discontinuities. A major advantage of the method is the lack of a priori information necessary for the successful application to data–the method will image any and all prominent reflectors. Using this method we have observed a number of discontinuities outside of the transition zone.

In Chapter 2 we discussed observations of first-order reverberations sampling the Tonga-KIP corridor (corridor 8 in Table 2.2). For that path strong reflections from the 650-km discontinuity could easily be seen in the data, and it was possible to apply standard

74

estimators of travel time and attenuation to obtain path-averaged mantle properties from the waveforms of first-order reverberations. That particular source region/receiver geometry was chosen primarily for its unusually high SNR; SNRs typical of the data set in general are lower (compare Figure 2.6 with Figures 2.8 and 2.9). Combined with bandwidth limitations, the analysis of individual phases within the reverberative interval is fraught with difficulties. For example, the tendency of the seismologist to pick the arrivals of highest amplitude can introduce strong bias into estimates of amplitude dependent quantities. By applying consistent analysis methods to all phases in the reverberative interval, we hope to avoid these difficulties.

ZEROTH-ORDER REVERBERATIONS

On an SH-polarized seismogram, free from mode conversions and core-penetrating phases, ScS_n and $sScS_n$ are the only zeroth-order reverberations supported by the Earth's mantle. For the epicentral distances encountered in this study (less than a radian), the reverberative interval includes ScS_n for $2 \leq n \leq 4$ and up to $n = 5$ at regional distances. These arrivals dominate the reverberative interval, and on a long-period instrument it is not unusual to observe strong ScS_5 phases. Significant regional variations in the travel time (τ_{ScS}) and quality factor (Q_{ScS}) of ScS_n are well documented in the literature [e.g., *Jordan and Sipkin, 1977; Nakanishi, 1980; Lay and Wallace, 1983; Chan and Der, 1988*] and have been used to argue that the seismic structures beneath continents and oceans differ to depths as great as 400 km in the mantle [*Sipkin and Jordan, 1976, 1980b*]. Although our purpose is not to recreate or confirm these experimental results, we must obtain accurate estimates of the parameters controlling the waveforms of zeroth-order reverberations in order to study the internal layering of the mantle: whole-mantle travel times and quality factors place important constraints on the properties of the first-order reverberations that we use to investigate individual mantle layers. Nonlinear waveform inversion, operating

directly on the time-domain expression of zeroth-order reverberations, is used to estimate these parameters.

Model Parameterization

Attenuation of zeroth-order reverberations is parameterized as a single value, Q_{ScS}, defined as

$$Q_{ScS}^{-1} = \frac{2}{\tau_{ScS}} \int_0^{z_c} dz \, v_s^{-1}(z) \, Q_\beta^{-1}(z)$$

where $z_c \approx 2885$ km is the depth of the core-mantle boundary. This parameterization ignores variations in attenuation with frequency, along different paths within the same corridor, and between different multiples along a single path. Because of the low frequencies employed in this study (5–60 mHz), the attenuation of seismic energy is not strong, and attempts at modeling variations in attenuation on a pulse-by-pulse and event-by-event basis showed insufficient additional variance reduction to be justifiable. Our results agree with those of *Sipkin and Jordan* [1979], who noted no significant departure from a constant-Q mechanism of attenuation for long-period body waves. That Q in the lower mantle may increase at very low (<10 mHz) and very high (>100 mHz) frequencies (Chapter 2; *Sipkin and Jordan* [1979, 1980b]) is not of direct importance to the remainder of this study, since our passband largely excludes these extremes.

The travel time of each individual zeroth-order reverberation is parameterized as a small perturbation $\delta\tau_i$ to the theoretically-predicted travel time of each reverberation. This phase equalization reduces the bias in attenuation estimates owing to misalignment of synthetic and data waveforms. Perturbations away from the arrival time calculated from a radial reference model can arise through a variety of mechanisms, including errors in the earthquake origin time and focal depth, inaccuracies in the reference model, and lateral velocity heterogeneity. Once measured, the perturbations are used to refine estimates of

event origin time, depth, and τ_{ScS}, quantities more useful in the synthesis of first-order reverberations.

Two simple, source-amplitude correction terms are included for each seismogram: e_u and e_d, the average upward and downward scalar excitation, respectively. Ray parameters for ScS_n vary little with increasing n, and therefore in the vicinity of the source or receiver the various multiples all have similar ray paths; hence, for a given event and receiver pair, the effects of near-source and receiver structure, and the time history of the shock itself, will be nearly constant for all ScS_n waves. The same is also true for $sScS_n$ waves, which exit the source through the upper focal hemisphere. The model parameters e_u and e_d are included to account for frequency- and time-independent amplitude effects, and act as a rotation of the a priori double-couple focal mechanism. Frequency- and time-dependent effects are not modeled; however, detailed comparison of theoretical and data seismograms shows excellent agreement, suggesting that these effects are small and can be ignored, a not unreasonable result considering the low-frequency, band-limited spectrum of the data.

Much more important is the contamination of zeroth-order reverberation waveforms by first- and higher-order reverberations generated at the M discontinuity. Like all first- and higher-order reverberations, crustal reverberations comprise families of dynamic analogs whose membership increases with the multiple number n. For large n (≥ 3), the waveforms of ScS_n and superposed crustal reverberations can appear considerably different than ScS_n alone (Figure 3.1). Ignoring crustal reverberations can lead to significant bias in estimated Q_{ScS} and strongly reduce the amount of signal variance explained by the model. Crustal reverberations also affect first- and higher-order reverberations in a similar fashion. Unfortunately, the crustal structures beneath many of the reverberation bounce points are either poorly known or unknown–especially as regards the strength of the M discontinuity–forcing us to include a model of the crust as additional free parameters in the inversion of zeroth-order reverberations. Experiments with synthetic data show that at the low frequencies of interest in this study, a simple, one-layer crust parameterized by its

thickness, z_M, and the *SH* reflection coefficient of the M discontinuity, $R(z_M)$, is adequate. In particular, theoretical seismograms generated for crustal models containing multiple reflectors, most notably the layer 2-layer 3 interface, are little different than those for which midcrustal reflectors are ignored. Furthermore, the multiple bounce points of ScS_n waves tend to average crustal structure along the path, resulting in a composite pulse whose shape closely resembles that predicted for a uniform crust of average thickness and impedance contrast. Of course, small phase and amplitude errors can be introduced by crustal variation within a corridor. Whenever possible we have attempted to minimize this bias by choosing seismic sources which are tightly grouped in epicentral location.

Inversion Formulation

To derive the dozen or so phase and amplitude parameters describing the zeroth-order reverberations on each seismogram, we employ an iterative waveform inversion algorithm. Besides automating the modeling, error analysis, and assessment of various weighting schemes (a necessity given the large volume of data involved), this time-domain technique avoids the problems of window carpentry common to spectral-domain methods [e.g., *Jordan and Sipkin*, 1977; *Chan and Der*, 1988].

Given a collection of model parameters $\mathbf{m}_k$, we can calculate the synthetic model response $\mathbf{s}_k = \mathbf{g}(\mathbf{m}_k)$, where $\mathbf{g}$ is in general a nonlinear function over the elements of $\mathbf{m}_k$. We assume that the response to a slightly perturbed model can be approximated as the first term in the Taylor series expansion of $\mathbf{g}$ about $\mathbf{m}_k$

$$\mathbf{s}_{k+1} \approx \mathbf{s}_k + \mathbf{A}\,\delta\mathbf{m}, \quad k = 0, 1, \ldots \tag{3.1}$$

where k is an index enumerating iterations and

$$A_{ij} = \frac{\partial g_i(\mathbf{m}_k)}{\partial m_j} \tag{3.2}$$

78

The model perturbations, δm, are chosen to minimize the squared misfit between data, d, and perturbed synthetic, s_{k+1}, waveforms, defined by

$$F_{k+1} = (d - s_{k+1})^T C_{nn}^{-1} (d - s_{k+1}) \qquad (3.3)$$

where C_{nn} is the matrix of noise covariance. In optimization problems of this sort, it is often helpful to include a constraint on the length of the model perturbation, which we write as

$$\varepsilon^2 = \delta m^T B \, \delta m \qquad (3.4)$$

where B is a positive-semidefinite, but otherwise general, matrix. Minimizing $F_{k+1} + \beta \varepsilon^2$ with respect to δm gives

$$\delta m = (A^T C_{nn}^{-1} A + \beta B)^{-1} A^T C_{nn}^{-1} (d - s_k) \qquad (3.5)$$

which completes the $k+1$ iteration

$$m_{k+1} = m_k + \delta m \qquad (3.6)$$

B is generally taken to be the identity matrix I, corresponding to the damped least-squares method of *Levenberg* [1944] and *Marquardt* [1963], although more general forms can be defined to accelerate convergence or avoid numerical singularities [*Smith and Shanno*, 1971]. We adopt the form $B_{ij} = \gamma_i \, \delta_{ij}$, so that by allowing γ_i to vary over the index i, we are able to selectively damp some model perturbations more strongly than others. Increasing γ_i decreases the step length of the ith parameter, inhibiting progress from the starting model. In our application, the primary use of selective damping is to limit the perturbation to amplitude dependent quantities while varying perturbations to arrival time to better align the waveforms when k is small. aligned, damping of all perturbations is reduced to a constant, near-zero level. Although both damped and undamped inversions eventually converge to the same model, application of this small amount of damping often reduces the number of intermediate iterations by a factor of 2. A

more general discussion of how variable damping can be used to improve convergence is given by *Smith and Shanno* [1971].

From the viewpoint of zeroth-order reverberations as signal, noise in the reverberative interval is composed of first- and higher-order reverberations, incoherent scattering of zeroth-order reverberations, and environmental noise such as ocean-wave reverberations and microseisms. By examining the portions of seismograms between ScS_n and $sScS_n$ wave groups it is possible to estimate the spectral characteristics of the noise contribution. Noise panels taken prior to or just after the passage of a zeroth-order reverberation wave train are used to construct C_{nn} for the signal window.

Model responses and columns of the Jacobian matrix A are computed at each iteration step via a hybrid ray theory scheme where the reverberative response of the crust is synthesized by matrix propagators [*Haskell*, 1960] and waves are propagated through the mantle by geometrical optics. Although one might question the use of geometrical optics at such low frequencies, comparisons of theoretical seismograms computed by normal-mode summation and ray theory display excellent agreement in the reverberative interval at frequencies less than 50 mHz (Figure 2.3). Since waves within the reverberative interval propagate nearly parallel to the (radial) gradient of velocity and do not involve critical phenomena such as caustics, frequency-dependent effects are small [e.g., *Richards*, 1976].

Tests on synthetic data demonstrate a marked inability of the linearized inversion scheme to converge to accurate estimates of known crustal models, owing to what we believe to be strong trade-offs between perturbations to arrival time $\delta\tau_i$ and crustal thickness z_M (crustal velocities were held fixed) and, to a lesser extent, between Q_{ScS} and $R(z_M)$. To avoid these trade-offs, a grid-searching algorithm is employed, incrementally stepping through the crustal parameters z_M and $R(z_M)$. At each node of the grid search, the remaining model parameters (Q_{ScS}, arrival time perturbations, and source terms) are estimated by the waveform inversion algorithm detailed above, with a final model chosen on the basis of least residual data variance defined by F_{k+1}.

Tests on Synthetic Data

To evaluate the algorithm's response to imperfect data, a number of synthetic test cases were run. Of specific interest were the effects of finite data SNR and along-path variations in both the depth and impedance contrast of the M discontinuity.

To model actual noise processes as closely as possible, synthetic noise panels were generated by assigning a random phase to the components of the noise amplitude spectra as estimated from data seismograms. Nonstationary processes, such as the time rate of decay of the average noise power, were modeled using multiple noise panels. To provide a more stringent test of the robustness of the algorithm, noise powers for the synthetic seismograms used in the inversion were raised by a factor of 1.5 over that estimated for data. To simulate along-path variations in the depth of the M discontinuity, perturbations to the mean depth of 20 km were drawn from a Gaussian distribution with a standard deviation of 10 km. Resulting crustal thicknesses in excess of 35 km or less than 5 km were not allowed. Along-path variations in $R(z_M)$ were assigned in a similar fashion, with mean and standard deviation of 0.18 and 0.03, respectively.

In this way, 20 synthetic data sets, modeled after the Tonga-CTAO experimental geometry (corridor 5 in Table 2.2), were generated (Figure 3.2) and subsequently inverted. Results of one such inversion are displayed in Figure 3.3. Shown are contours of the variance reduction (defined as the ratio of F_{k+1} to total covariance-weighted data power) and the associated estimate of Q_{ScS} for the portion of crustal model space sampled. For the specific example of Figure 3.3, the synthetic data were best fit by $z_M = 22$ km, $R(z_M) = 0.16$, and $Q_{ScS} = 155$, as compared to the actual mean values of 20 km, 0.18, and 155, respectively. The mean and standard deviations for the entire suite of twenty individual experiments were $z_M = 21 \pm 3$ km, $R(z_M) = 0.16 \pm 0.03$, and $Q_{ScS} = 145 \pm 10$. Thus, while the improvement in variance reduction over the whole of sampled model space is small, and associated variations in the whole mantle quality factor are large, the method

81

proves to be robust, displaying relatively little bias and good repeatability for synthetic data sets containing many realistic imperfections. The corresponding data inversion for this corridor is shown in Figure 3.4. As is apparent from the figure, the "topography" of the variance reduction and Q_{ScS} surfaces is quite similar to the synthetic data example of Figure 3.3. The good correspondence, especially in portions of model space well removed from the best estimates, will later be used to argue against strong mantleside layering of the CMB.

Although detailed discussion of the results of data inversion are postponed to Chapter 4, a few comments are in order here: (1) Variance reduction, defined relative to a null starting model, was typically on the order of 80%–a value close to the maximum expectable given reasonable SNR estimates. Besides justifying the parameterization, this also stands as testimony to the simplicity of reverberation waveforms. Paths realizing lower variance reductions are typically found to have zeroth-order reverberation waveforms that are contaminated by first-order reverberations from shallow discontinuities, such as the lid/low-velocity zone. Although not attempted in this study, it should be possible to incorporate the effects of shallow structure in an iterative estimation scheme using estimates obtained by the methods discussed in the next section. (2) Estimates of the uncertainties in whole-mantle travel time and travel-time perturbations are obtained by a posteriori rescaling of marginal uncertainties assuming a value of reduced χ^2 equal to the asymptotically expected value of 1. Uncertainties in Q_{ScS}, z_M, and $R(z_M)$ are obtained by a Monte Carlo method based on the standard deviation of estimates obtained from suites of noisy synthetic data inversions. Although the results depend on the quantity and quality of data, as well as the particular experimental geometry, uncertainties in travel time terms are on the order of 0.3 s (1σ); for Q_{ScS} uncertainties are larger, typically of order 40, compared to an average value of 210. Uncertainty estimates for the crustal parameters are more variable, however typical levels of uncertainty are 5 km and 0.04 for crustal thickness and reflection coefficient of the M discontinuity, respectively.

By accurately modeling the waveforms of zeroth-order reverberations, we are able to strip (subtract) them from the reverberative interval of the seismogram (Figure 3.5). The deterministic energy that remains after this step consists entirely of first- and higher-order reverberations, with first-order reverberations from the transition-zone discontinuities contributing most significantly. The next section deals with the extraction of information pertaining to the internally layered structure of the mantle from the waveforms of these first-order reverberations.

FIRST-ORDER REVERBERATIONS

The structural interactions of first-order reverberations differ from their zeroth-order parent reverberations in two important ways: (1) addition of a single reflection from an internal mantle discontinuity and (2) preferential sampling of one or more mantle layers (Figure 2.2). By combining observations of both orders of reverberations, it is possible to exploit these interactions in estimating the elastic and anelastic properties of the major mantle layers and the reflection coefficients of the interfaces. For example, in Chapter 2 we combined observations of topside and bottomside reflections from the 650-km discontinuity with zeroth-order reverberations to simultaneously estimate the path-averaged, upper-mantle and lower-mantle quality factors, and the reflection coefficient of the discontinuity at 20 mHz. However, the methods used in that section required picking individual first-order reverberations, something which can be done only in cases of unusually clean signals. Typical first-order reverberations do not fulfill this criterion, and their analysis requires the use of more robust methods.

The Earth's mantle supports a number of different first-order reverberations. Arriving upon a suitable starting model for the mantle capable of predicting the travel times and waveforms of these reverberations is a difficult task. Considering that every discontinuity in the mantle generates two first-order reverberation families for each ScS_n or $sScS_n$ wave passing through it (topside and bottomside reflections), the number of first-order

83

reverberations to be found in the reverberative interval is potentially very large. Sorting out the individual arrivals and estimating their depth of origin can be a difficult task. Major discontinuities are known to exist near depths of 400 km and 650 km in the mantle, but it is possible that other discontinuities contribute significantly to the sum of first-order reverberations. Candidates include the seismic lid and the 220-km, or Lehmann, discontinuity. The success or failure of waveform inversion is very much dependent upon the model parameterization. If an important discontinuity is not included in the model, no information about it can be recovered. On the other hand, including parameters to describe a nonexistent reflector can doom an inversion. In the following sections we describe an inversion algorithm capable of detecting, locating, and describing discontinuities in the mantle. The primary advantage of the method is the lack of a priori information needed for successful application to real data.

Parameterization of Waveforms

In parameterizing the waveforms of first-order reverberations we are guided by several basic, but crucial, questions regarding the layering of the mantle: at what depths are the major mantle interfaces, do these depths have significant lateral variations, and do these variations correlate with surface tectonics and/or tomographic maps of the mantle and core? Unfortunately, the finite SNR, low-frequency content, and limited range of ray parameters of our data set impose fundamental constraints on the mantle layering parameters that we can hope to retrieve. Since the characteristic wavelengths for the reverberations employed in this study are of the order of 150 km, it is not possible to resolve the fine structure of mantle layer interfaces. Indeed, even a extended transition width of 15–25 km would appear essentially discontinuous [*Ingate et al.*, 1986]. For this reason, the transitions between mantle layers are modeled as first-order discontinuities, characterized by a frequency-independent reflection coefficient R. Although the ability to detect fine structure is lost by restricting our observations to low frequencies, we do gain two important

benefits: (1) Modeling the effects of crustal reverberations is greatly simplified. Had we looked at higher frequencies, the need for more complex crustal modeling would have arisen. Of course, this simplification extends to other mantle discontinuities as well. (2) Wide transition layers, which are nearly transparent to higher-frequency body waves, are detectable at low frequencies. Although there is reason to believe that both the 400-km [e.g., *Leven*, 1985] and 650-km [e.g., *Engdahl and Flinn*, 1969; *Whitcomb and Anderson*, 1970; *Paulssen*, 1988] discontinuities are locally "sharp," i.e., that they represent transitions localized to within 10 km or so, other discontinuities may not be. For example, the velocity increase at the top of layer D" proposed by *Lay and Helmberger* [1983] to explain observations of a lower mantle, S-wave triplication may be modeled as an extended transition of up to 40 km width without seriously degrading the level of fit obtained between synthetic and data waveforms (see also *Young and Lay* [1987]).

The reflection points of individual dynamic analogs, which together form a single first-order reverberation, will be spread out along the great-circle path connecting source and receiver. Topographic relief on the discontinuity being sampled will thus lead to travel-time variations among analogs, "splitting" the reverberative "multiplet" into its constituent "singlets" (individual phases). However, in the absence of extreme lateral variations in discontinuity depth, the splitting will not be great enough to allow us to resolve the analogs individually. If a number of singlets arrive at times differing by only a small portion of their characteristic period, we expect a slightly broadened composite waveform whose centroid time is a measure of the average travel time of the individual singlets. As the terminology might suggest, this phenomena has an analog in the splitting of free oscillations by aspherical structure; in both cases, the singlets typically cannot be resolved on a single seismogram. Theoretically, it should be possible to reconstruct the topography of a discontinuity sampled in this way through tomographic reconstruction. Unfortunately, to be viable, such an experiment would require considerably more data than presently available. Instead, we estimate only the path-averaged discontinuity depth z_i. Similarly,

85

we assume that along-path variations in the strength of the reflector are averaged out and that $R(z_i)$ represents the true mean value. Phase misalignments due to discontinuity topography and lateral heterogeneity elsewhere in the mantle will bias our $R(z_i)$ estimates toward lower values and introduce an apparent frequency dependence. By examining this phenomena, we able to place important constraints on the magnitude of discontinuity topography and obtain an unbiased estimate of $R(z_i)$.

Since the ray parameters of mantle reverberations do not vary greatly, first- and higher-order reverberations illuminate discontinuities over a small range of incidence angles, concentrated close to normal incidence ($\leq 15°$ from vertical). For plausible contrasts in material properties, the reflection coefficient of a discontinuity will be near constant for these angles, prompting us to ignore the angular dependence of $R(z_i)$. A discontinuity in this idealized model of the mantle is therefore completely characterized by its path-averaged depth z_i, and vertical-incidence reflection coefficient $R(z_i)$.

Because first-order reverberations preferentially sample certain mantle layers relative to their parent zeroth-order reverberations, their attenuation can in theory be used to estimate the vertically-averaged quality factors of the major mantle layers. Unfortunately, the interference between singlets of a split reverberative family is usually too great to permit reliable estimates of attenuation to be made. Although this problem can be avoided by selecting only those reverberations that appear not to be split, i.e., those whose waveforms most closely match the parent, as in Chapter 2, we have chosen not to estimate quality factors on a layer-by-layer basis. Instead, we will use as the quality factor of first-order reverberations the whole-mantle estimate, Q_{ScS}, derived from the inversion of zeroth-order reverberation waveforms. This is not expected to generate any significant bias in our results, owing to the similarity of the path-averaged quality factors of zeroth- and first-order reverberations. For example, using the Q model obtained in Chapter 2 ($Q_{UM} = 81$; $Q_{LM} = 231$), the path-averaged quality factors of ScS_3 and $\{ScS_3; S650^+S\}$ at zero ray parameter are 150 and 139, respectively.

Other propagation effects, such as crustal reverberations and delays due to source and receiver structure, have already been estimated from zeroth-order reverberations and are included in the modeling of first-order reverberations. Thus the only additional parameters necessary to adequately characterize the low-frequency wave train of first-order reverberations are those describing the location and magnitude of the major mantle interfaces, specifically: z_i, and $R(z_i)$.

Inversion Formulation

In the absence of noise and lateral heterogeneity, the reverberative interval of the seismogram is comprised entirely of a sum of zeroth- and higher-order reverberations, which we write

$$\mathbf{d} = \sum_{l=0}^{\infty} \mathbf{d}^{(l)} \tag{3.7}$$

where $\mathbf{d}$ is a column vector representing samples of the discrete data time series and $\mathbf{d}^{(l)}$ is the sum of reverberations of order l. By studying the waveforms of zeroth-order reverberations we have arrived at an accurate approximation to $\mathbf{d}^{(0)}$, call it $\overline{\mathbf{d}}^{(0)}$, which we strip from the data, leaving

$$\mathbf{d} - \overline{\mathbf{d}}^{(0)} \approx \mathbf{d}^{scat} = \sum_{l=1}^{\infty} \mathbf{d}^{(l)} \tag{3.8}$$

where $\mathbf{d}^{scat}$ denotes the sum of first- and higher-order reverberations, all of which have been scattered from at least one internal mantle discontinuity. With the notable exception of the M discontinuity, whose effects are explicitly included in modeling of the $\mathbf{d}^{(l)}$, discontinuities in the mantle are characterized by only small increases or decreases in velocity and density ($\leq 8\%$). As a result, near-normal incidence reflection coefficients for these discontinuities are small, even at low frequencies. Thus in considering the scattered wave field, $\mathbf{d}^{scat}$, we feel justified in ignoring the contributions of second- and higher-order

reverberations, in effect invoking the Born approximation: $\mathbf{d}^{scat} \approx \mathbf{d}^{(1)}$ (more formally, this assumption is justified for $R \ll 1/n$, where n is the core-bounce number). Given the adopted parameterization of discontinuities, we can write

$$\mathbf{d}^{scat} = \sum_{i=1}^{N} R(z_i)\, \mathbf{g}(z_i) + \mathbf{n} \qquad (3.9)$$

where $\mathbf{g}(z_i)$ is the seismogram of first-order reverberations that would be generated by a discontinuity at depth z_i with unit reflection coefficient ("discontinuity response functions," or DRFs), $R(z_i)$ is the unknown reflection coefficient at z_i, and $\mathbf{n}$ is noise. Equation (3.9) can be expressed in matrix notation

$$\mathbf{d}^{scat} = \mathbf{G}\,\mathbf{R} + \mathbf{n} \qquad (3.10)$$

Using the hybrid geometrical-optics, Haskell-propagator scheme, it is a simple task to generate the $\mathbf{g}(z_i)$ for a given Earth model; see Figure 3.6. The standard least-squares values of the reflection coefficients are then

$$\mathbf{R} = (\mathbf{G}^T \mathbf{C}_{nn}^{-1} \mathbf{G})^{-1} \mathbf{G}^T \mathbf{C}_{nn}^{-1} \mathbf{d}^{scat} \qquad (3.11)$$

where $\mathbf{C}_{nn}$ is the matrix of noise covariance. Because the estimator is linear with respect to $\mathbf{d}^{scat}$, extension to multiple data seismograms is trivial.

Since, in general, we do not know the depths of the mantle discontinuities a priori, we have chosen to place hypothetical discontinuities at regularly spaced intervals in the mantle, so that the solution (3.11) represents a profile of mantle "reflectivity." Ideally, depths marked by significant discontinuities should appear as high amplitudes (bright spots) in this profile, and only at these depths should $R(z_i)$ rise above the background level predicted for noise alone. Thus, for a sufficiently fine mesh of model radii, this technique should be able to estimate both the depth and strength of reflectors in the mantle. In form, our algorithm is a specific and simple application of Tarantola's [1984b] inversion scheme for

acoustic reflection data and is also similar to *Middleton and Whittlesey's* [1968] water reverberation inversion.

In order to precisely locate the depths of mantle discontinuities it is necessary to sample the mantle reflectivity profile at finely spaced depth intervals. However, the low-frequency, limited-bandwidth nature of the data set ensures that DRFs for closely spaced discontinuities will be similar in form, since travel time differences among the various first-order reverberations will be small compared to the characteristic periods of the waveforms. In fact, even for a depth sampling increment as modest as 25 km, response functions for adjacent depths are sufficiently similar in form to drive $G^T C_{nn}^{-1} G$ toward unworkably high condition numbers. Experiments with noisy synthetic zeroth- and first-order reverberation records suggest that the mean travel time of suites of low-frequency reverberations can be measured to better than 1.5 s, implying a 5–7 km depth resolution of mantle discontinuities. This figure is considerably better than that implied by the direct application of (3.11), which is severely hampered by finite computing precision. Various means exist by which the inverse in (3.11) can be regularized, allowing for finer sampling intervals. However, we have chosen to adopt a different approach, obtained as a simplification of (3.11) motivated by traditional seismic migration algorithms.

If the matrix product $G^T C_{nn}^{-1} G$ were diagonal, i.e., if the covariance-weighted DRFs for different discontinuity depths were orthogonal, then the least-squares solution of (3.10) could be simplified to

$$R(z_i) = \frac{g^T(z_i)\, C_{nn}^{-1}\, d^{scat}}{g^T(z_i)\, C_{nn}^{-1}\, g(z_i)} \tag{3.12}$$

This estimate admits several interesting interpretations which bear further examination. If we restrict our attention to the numerator alone, we see that it corresponds to the zero-lag term of the cross correlation of $C_{nn}^{-1} g(z_i)$ with d^{scat}, an operation known as matched filtering [*Robinson and Treitel*, 1980], a commonly used SNR enhancement technique that

89

has found frequent use in both classical [e.g., *Dziewonski and Hales*, 1972] and exploration seismology (e.g., *White* [1980] and VIBROSEIS™). The design goal of a matched filter is to maximize the ratio of instantaneous energy of filtered signal to average noise energy by folding the energy of the unfiltered signal into a single sample (generally taken to be zero lag). The success of the method is due largely to the degree to which a priori knowledge is incorporated, assuming that both the form of the signal, in this case $g(z_i)$, and noise autocorrelation, C_{nn}, are known in advance. Matched filtering also plays an important role in signal detection theory [e.g., *Helstrom* 1960; *Selim*, 1965], from which it can be shown that (3.12) is an optimal detector, tuned to the first-order reverberations expected for a discontinuity at a depth z_i, should that discontinuity exist.

Equation (3.12) can also be interpreted as a migration operator. To demonstrate this, however, we must first expand the ith discontinuity response function into a sum of r individual ray-theoretical arrivals, each characterized by an arrival time τ_{ij} and waveform s_{ij}, such that

$$g(z_i, t) = \sum_{j=1}^{r} s_{ij}(t) * \delta(t - \tau_{ij}) \tag{3.13}$$

where the asterisk operator denotes convolution, and we have assumed that the DRF is sampled continuously in time for notational convenience. It is also convenient to assume that $C_{nn} = I$ (although in practice we always employ the full noise covariance). Substituting (3.13) into (3.12) and rearranging gives

$$R(z_i) = \frac{\displaystyle\sum_{j=1}^{r} \int_{t_{min}}^{t_{max}} \left[s_{ij}(-t) * d^{scat}(t) \right] \delta(t - \tau_{ij})\, dt}{\displaystyle\sum_{j=1}^{r} \int_{t_{min}}^{t_{max}} s_{ij}^2(t)\, dt} \tag{3.14}$$

where $t_{min} \leq t \leq t_{max}$ is the window of time series considered. That this is a migration operator now becomes clear. The bracketed term of the numerator is the cross correlation of pulse waveform with data. This step concentrates the energy of the jth arrival into a single time sample, specifically $t = \tau_{ij}$. Integrating the r individual cross correlograms against $\delta(t - \tau_{ij})$ then sifts out and sums the wave field at times when energy from a potential discontinuity at z_i should arrive. In this way the method closely resembles classical diffraction-stack migration [e.g., *Hagedoorn*, 1954; *French*, 1974], where the observed wave field, given as a function of receiver position and time, is summed along curves of equal travel time between shot, scatterer, and receiver. However, since the mapping of the wave field into reflector strength is consistent with the wave equation, the method is better described as a variant of Kirchoff migration [e.g., *Schneider*, 1978] and could have been derived as an extension of *Tarantola's* [1984a] linearized acoustic waveform inversion scheme to *SH*-polarized, elastic-wave propagation.

Tests on Synthetic Data

To arrive at equation (3.12), we assumed that the covariance-weighted DRFs are orthogonal. This is not true. However, the ramifications of this assumption are easily predicted and can be demonstrated in a simple experiment on synthetic data with known discontinuities. A noise-free synthetic data set was generated to mimic the Tonga-KIP experimental geometry (corridor 8 in Table 2.2) using PA2 [*Lerner-Lam and Jordan*, 1987] as an upper mantle model and PEM [*Dziewonski et al.*, 1975] as a lower mantle model. In subsequent discussions we will refer to this composite model as PA2'. In generating the synthetic data we allowed first-order reverberations from the 400-km and 650-km discontinuities only (see Figure 2.6). Other discontinuities present in model PA2', such as the lid and 220-km discontinuity, were ignored for simplicity. DRFs were computed by ray tracing through a modified form of the PA2' model, where the first-order discontinuities present in PA2' were smoothed using a quartic interpolation scheme

designed to match both the velocity and its first derivative at the endpoints, as well as the vertical travel time through the interpolated region. Model smoothing is performed to minimize errors in the predicted travel times of topside and bottomside reflections when the true depth of the reflector is unknown. Employing equation (3.12), the reflectivity profile of the mantle was computed; the results are depicted in Figure 3.7. For this synthetic test case, and for all subsequent experiments, the mantle reflectivity profile was sampled on a 5-km interval starting at the base of the crust and extending to 10 km above the CMB. The 5-km depth spacing corresponds to our estimate of depth resolution obtained from experiments on noisy synthetic data.

Ideally, the estimated reflectivity profile should be composed of two nonzero values, occurring at depths of 400 and 670 km, the depths of the 400-km and 650-km discontinuities in model PA2'. Obviously, the reflectivity profile depicted in Figure 3.7 has considerably more structure than this. Perhaps the most dramatic departure from the ideal are the strong negative reflectivity peaks near 1900 km and 2200 km depth in the lower mantle. These features arise from an ambiguity in apparent discontinuity depth peculiar to first- and higher-order reverberations. To understand the source of this ambiguity, consider an experiment with a coincident shot and receiver. For this geometry it is always possible to pick two mantle depths, one deep, one shallow, such that the topside reflections from one have the same travel time as bottomside reflections from the other, and vice versa. Because the moveout of travel times with increasing distance (or core bounce number n) for higher-order reverberations is only a weak function of the discontinuity depth, the ambiguity persists to finite ray parameters. An example can be found in Figure 3.6 where the DRFs computed for 650 km and 1900 km are similar in appearance, but of opposite sign, a result of mapping topside to bottomside reflections. The final product is a reflectivity profile with nearly odd symmetry about the midpoint of the mantle with respect to travel time (~1260 km) and slightly elongated in the lower mantle owing to the greater velocities. For the profile in Figure 3.7, the reflectivity peaks near 1900 km and 2200 km

92

depth are the alternative interpretations, or false images, of the 650-km and 400-km discontinuities, respectively. Although ambiguity does not present a problem in the interpretation of the transition-zone discontinuities (apart from lowering resolution in the depth range populated by their false images), it becomes more profound at both shallow and great depths where structure is more uncertain, and introduces the possibility of mistaking structure in D" for upper mantle structure and vice versa. Resolution of this ambiguity is important for the successful application of first-order reverberations to the study of mantle layering, and is treated in depth in subsequent chapters.

Other, typically smaller, oscillations in the reflectivity profiles result from the occasional correlation of a subset of data and DRFs, which persist in the stack due to hypocenter clustering and the limited number of records available. In the analysis of data it has proven helpful to model these features with synthetic profiles.

Also apparent in Figure 3.7 is the nonzero width and side lobes of reflectivity profile peaks. This is a result of the finite bandwidth of the data set, in fact the peaks have the form of the signal autocorrelation where depth replaces time as the lag variable. This phenomena can be easily understood by examining equation (3.14). The bracketed term of the numerator consists of the cross correlation of pulse shape $s_{ij}(t)$ and data. In the vicinity of τ_{ij}, the filtered data will resemble the autocorrelation of $s_{ij}(t)$, with some discrepancies owing to noise and interference between reverberations. Now consider a DRF computed for a depth which varies by an amount δz from the depth of the actual discontinuity. If δz is small, the synthetic waveforms, $s_{ij}(t)$, will be largely unaffected. However, the travel times of the individual first-order reverberations will be perturbed by an amount $\delta \tau_{ij}$, given by

$$\delta \tau_{ij} = \pm \frac{2\,\delta z}{v_s(z_i)} \cos \theta_{ij} \tag{3.15}$$

93

for a (topside, bottomside) reflection, where θ_{ij} is the departure of the ray from the vertical at the discontinuity. Substituting $\tau_{ij} + \delta\tau_{ij}$ for τ_{ij} in (3.14) and varying δz maps the autocorrelation of s_{ij} from the lag time domain to δz.

In the following chapter we apply the algorithm embodied by equation (3.12) to data for the 18 seismic corridors sampled in this study.

SUMMARY

In this chapter we have developed powerful, yet simple, techniques to extract information describing the internal layering of the mantle from the waveforms of mantle reverberations, techniques which make full use of the simplicity of structure and level of redundancy of information indigenous to the reverberative interval. Inversion of zeroth-order reverberation waveforms provides accurate estimates of whole-mantle travel time, attenuation, source parameters and path-averaged crustal structure. Apart from their intrinsic interest, accurate estimates of these quantities are crucial for the subsequent evaluation of higher-order reverberations. The inversion scheme applied to first-order reverberations bears a strong resemblance to techniques of migration common in the exploration literature, and offers a powerful alternative to the traditional travel-time methods common in earthquake seismology. Together these methods are capable of providing a wealth of information regarding mantle layering averaged over relatively short path lengths–yet imaging the entire 2900 km depth extent of the mantle. In the following chapter we discuss results obtained by applying these methods to the data set of Chapter 2, results which form the observational basis of this thesis.

FIGURE CAPTIONS

Fig. 3.1. Comparison of synthetic SH-polarized pulses computed using a hybrid geometrical-optics, Haskell propagator scheme and low-passed filtered as described in Chapter 2. The effect of multiple transits through a 25-km-thick crust is dramatic, even at these low frequencies (< 60 mHz). Ignoring the contribution of crustal reverberations introduces considerable bias into estimates of Q_{ScS}.

Fig. 3.2. Comparison of SH-polarized seismograms showing the reverberative interval for several deep- and intermediate-focus events in the Tonga-Fiji seismic zone recorded by station CTAO in northeastern Australia (corridor 5 in Table 2.2). For each pair, the bottom trace is data; top trace is a synthetic which includes random additive noise, based on a nonstationary model whose spectral characteristics are that of real data. Large-amplitude arrivals in the data beginning at ~76 minutes are major arc phases not modeled in the synthetics. Experiments on synthetic data sets such as these were used to assess the reliability and robustness of the waveform inversion scheme.

Fig. 3.3. Results of the combined grid search-inversion scheme for a synthetic data set modeled after the Tonga-CTAO geometry (corridor 5 in Table 2.2). (Left) A contour map of variance reduction as a function of assumed crustal thickness z_M, and M-discontinuity reflection coefficient $R(z_M)$. At each grid point, Q_{ScS} and other model parameters were inverted for using a nonlinear, Levenberg-Marquardt inversion formulation. (Right) The resulting estimates of Q_{ScS}. Solid circles mark the best estimate based on variance reduction, actual parameter values are $z_M = 20$ km, $R(z_M) = 0.18$, and $Q_{ScS} = 155$. Tests on synthetic data sets were performed to evaluate the sensitivity of the method and to estimate the covariance between the parameters of the crustal model and attenuation.

Fig. 3.4. Results of the combined grid search-inversion scheme for the Tonga-CTAO seismic corridor. (Left) A contour map of variance reduction as a function of assumed crustal thickness z_M, and M-discontinuity reflection coefficient $R(z_M)$. At each grid point, Q_{ScS} and other model parameters were inverted for using a nonlinear Levenberg-Marquardt inversion formulation. (Right) The resulting estimates of Q_{ScS}. The data are best fit by z_M = 24 ± 8 km, $R(z_M)$ = 0.11 ± 0.08, and Q_{ScS} = 210 ± 40 (solid circles).

Fig. 3.5. Two examples of stripping of zeroth-order reverberations taken from the data inversion of Figure 3.4 . For each triplet, the top seismogram is data, the middle is the model of zeroth-order reverberations obtained by waveform inversion, and the bottom is data minus synthetic. The latter are used as input to the processing of first-order reverberations for mantle reflectivity profiles.

Fig. 3.6. *SH*-polarized seismograms showing the reverberative interval for a deep-focus Tonga event recorded at KIP. Bottom trace is data. Top traces are synthetic discontinuity response functions (DRFs), i.e., the seismogram of first-order reverberations generated by a unit discontinuity at the labeled depth (km). These seismograms are used in the inversion of first-order reverberations for mantle layering. Properly normalized, the cross correlation of data and DRF evaluated at zero lag is a maximum-likelihood estimate of reflection coefficient R. By sweeping through the mantle, and stacking over many seismograms, a profile of reflectivity, $R(z)$, is generated. Generally, the large-amplitude ScS_n and $sScS_n$ phases are stripped from data prior to this step (see Figure 3.5); here they have been left in for consistency with previous figures.

Fig. 3.7. (Left) Reflectivity profile obtained for a synthetic data set modeled after the Tonga-KIP geometry (corridor 8 in Table 2.2). $R(z)$ is a low-passed filtered version of the normal-incidence, *SH*-polarized reflection coefficient of the mantle. Positive $R(z)$ implies

an increase in impedance with depth across the discontinuity. (Right) Although the PA2' Earth model used to generate this data set contains a number of upper mantle discontinuities, for the sack of simplicity only reverberations from the 400-km and 650-km discontinuities were included in the synthetics. The large-amplitude peaks near 400 km and 670 km in the reflectivity profile are the registrations of these discontinuities, and their amplitudes are estimates of the reflection coefficients. The slight offset from the model predicted depth is due to the smoothing applied to the Earth model used to generate DRFs. Large-magnitude features in the lower mantle are false images of transition-zone discontinuities–artifacts which arise due to poor ray-parameter coverage, resulting in a near mirror image profile. Stippled region denotes the 5% false-alarm probability level estimated on a Monte Carlo basis from synthetic noise panels modeled after data (not shown). Gap in the mid-mantle is due to interference between topside and bottomside reflections, leading to instability in the inversion.
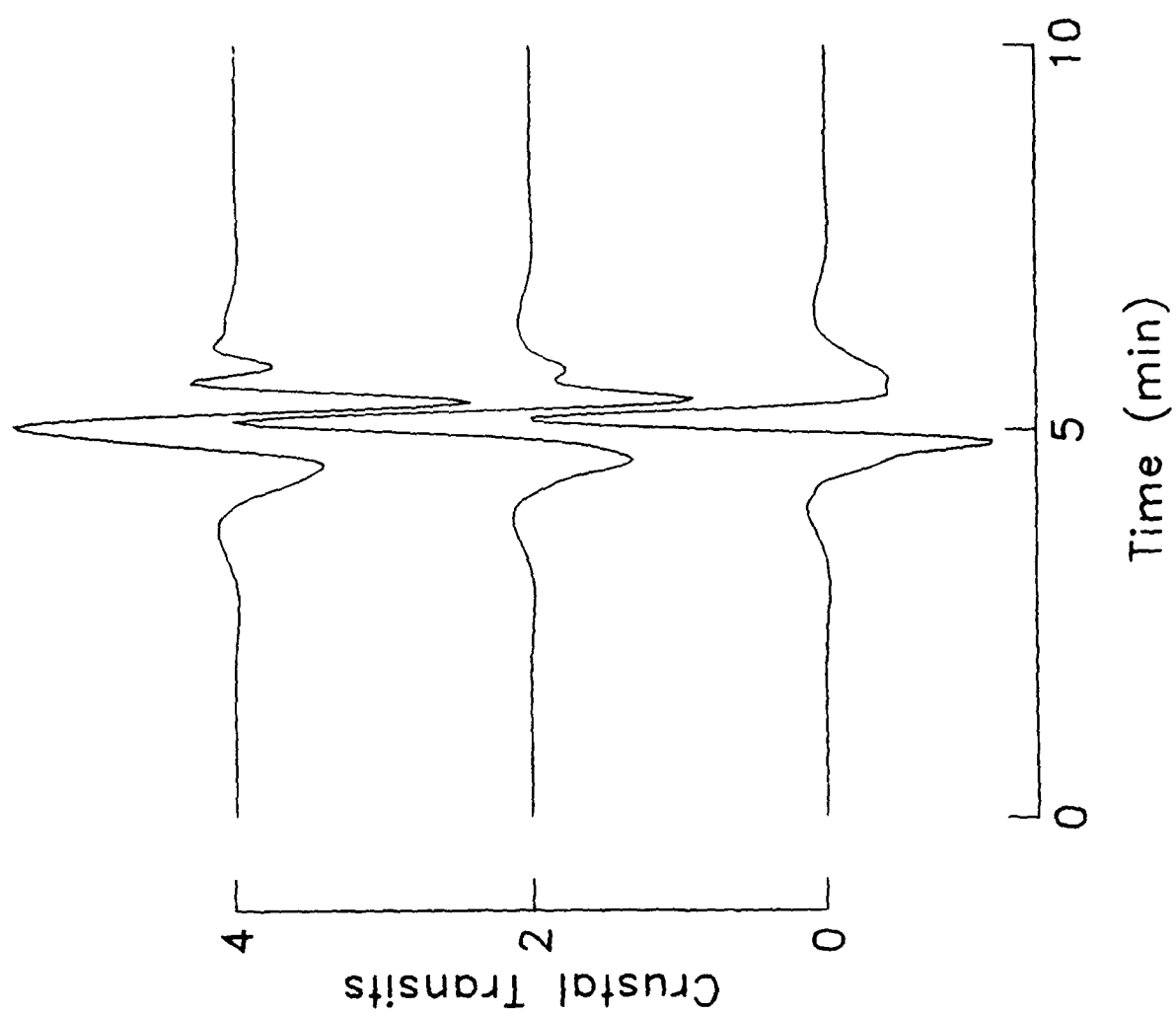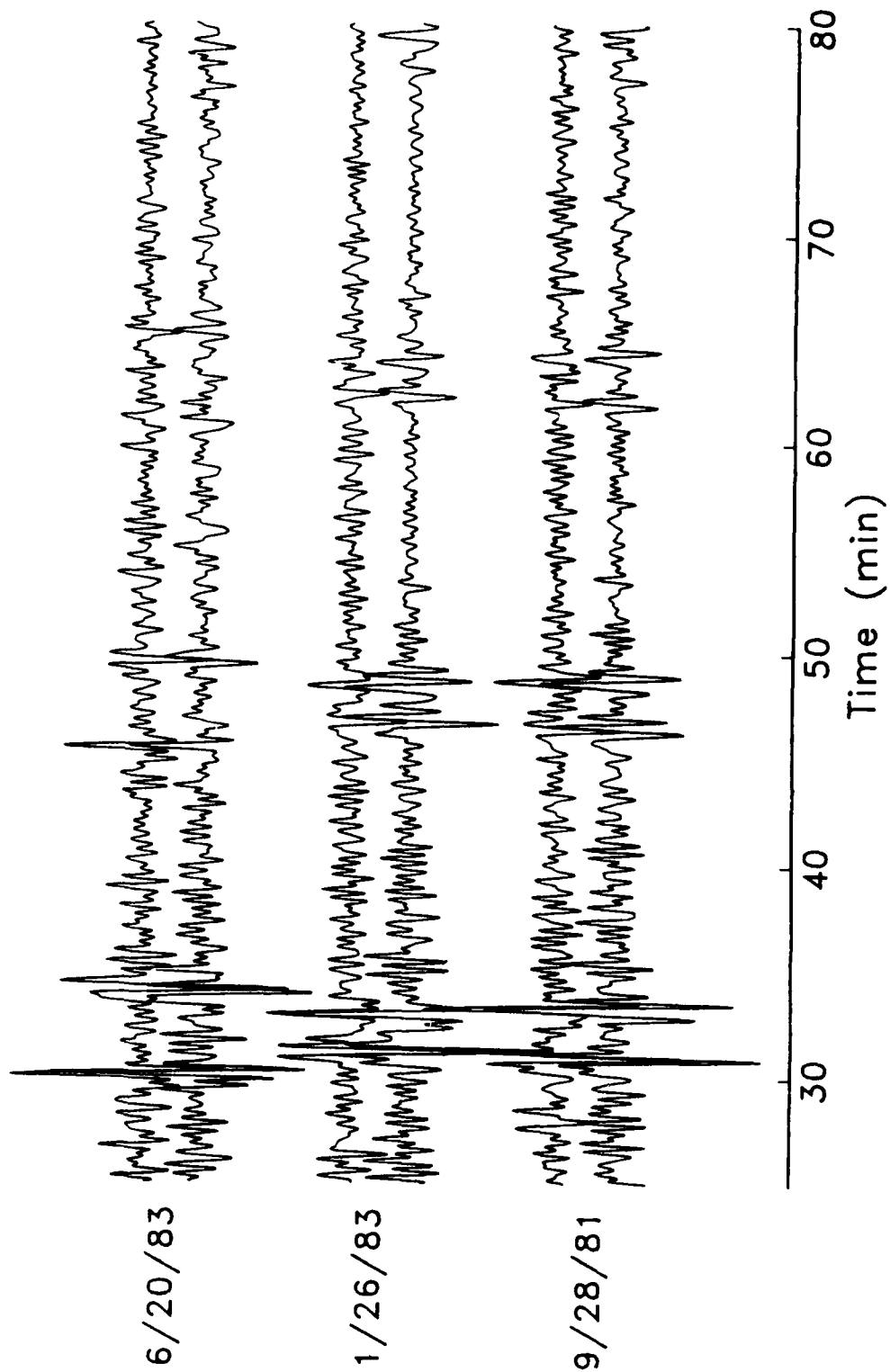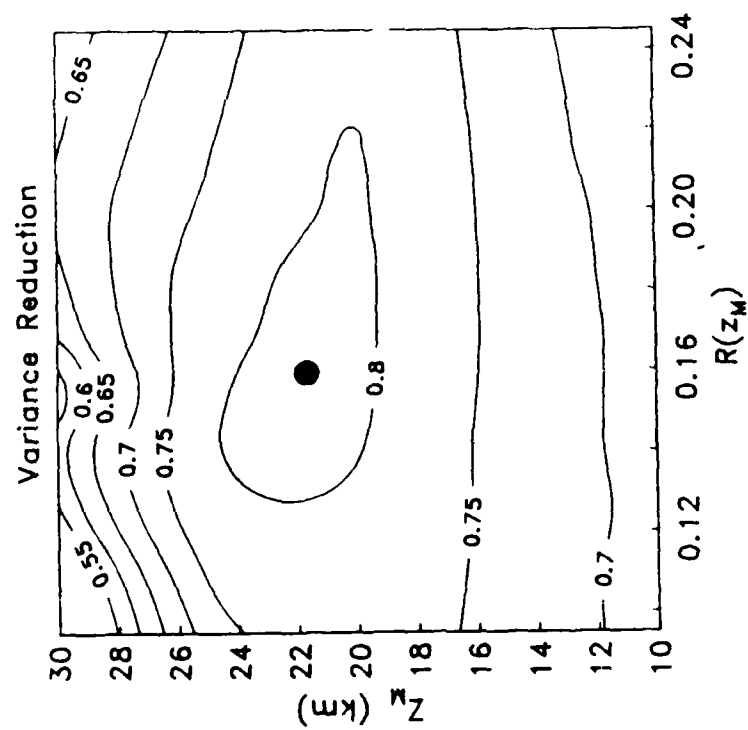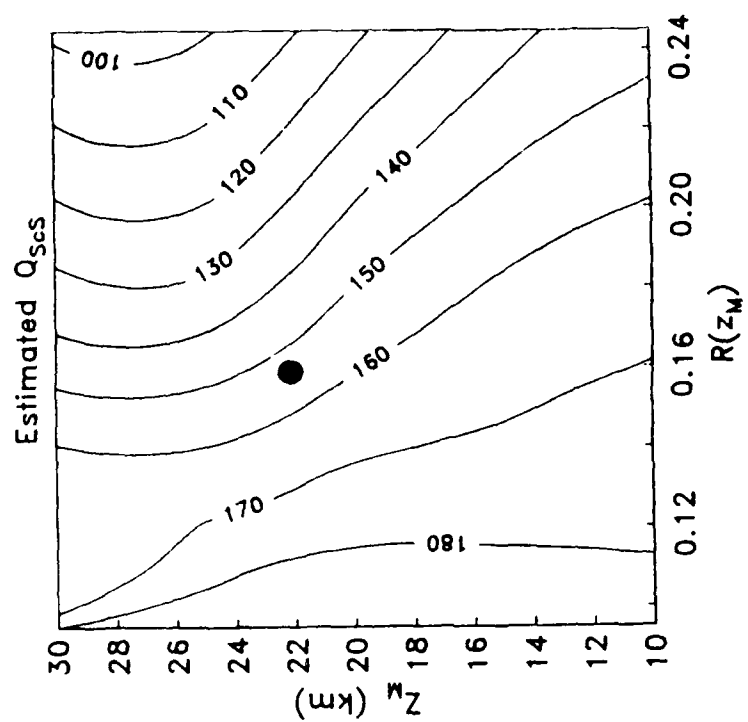
Figure 3.1

98

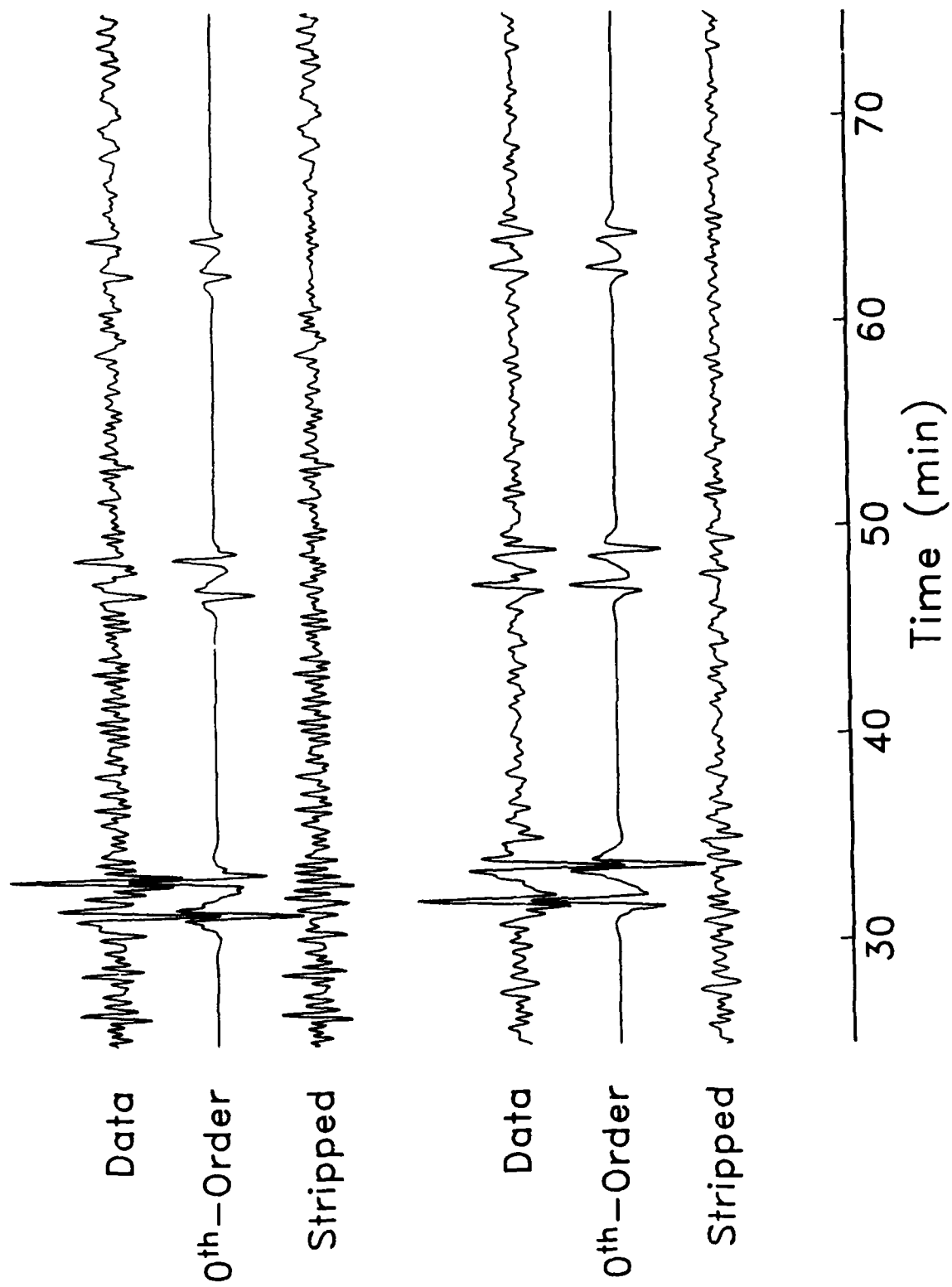Figure 3.2

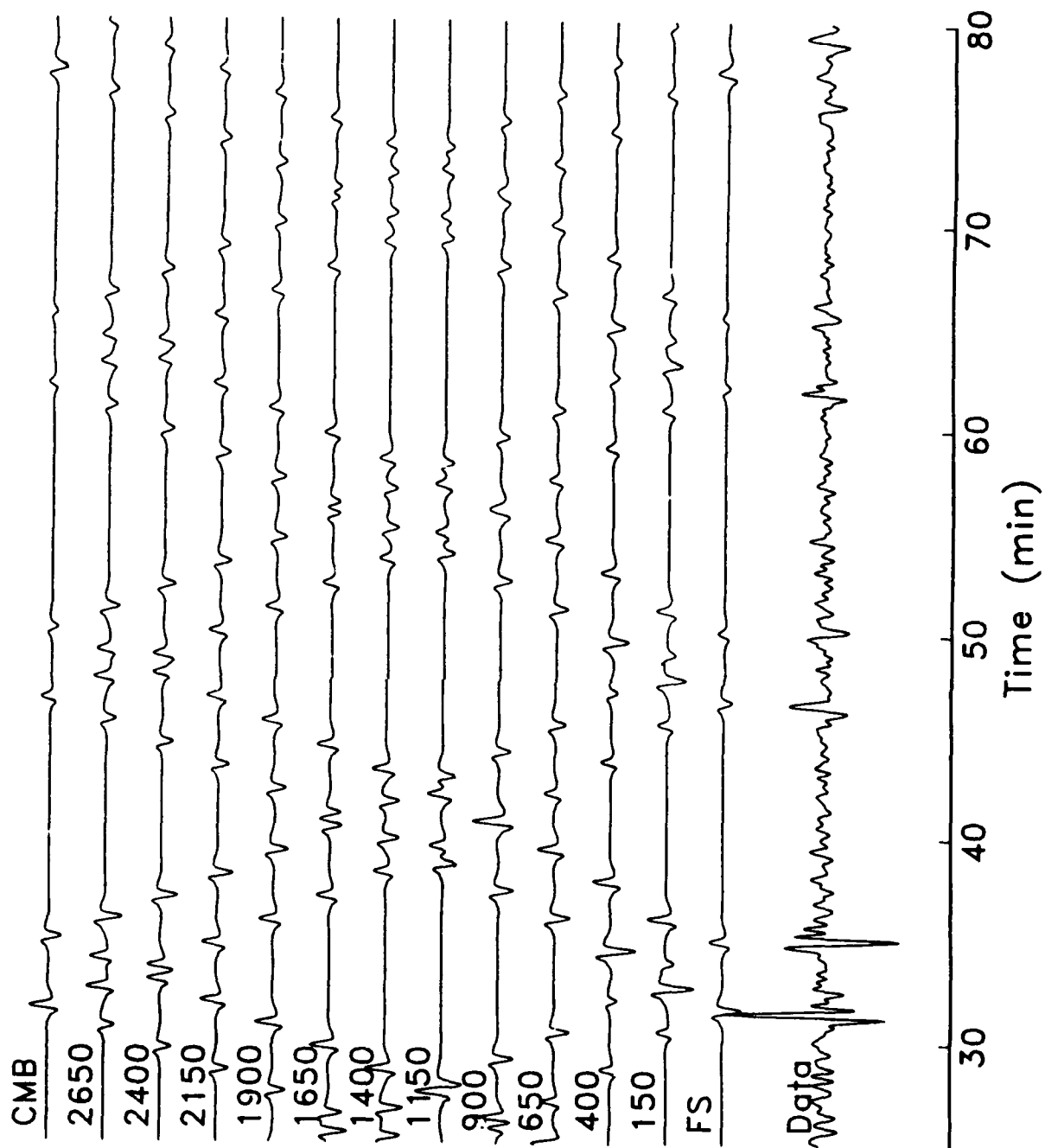99

Figure 3.3
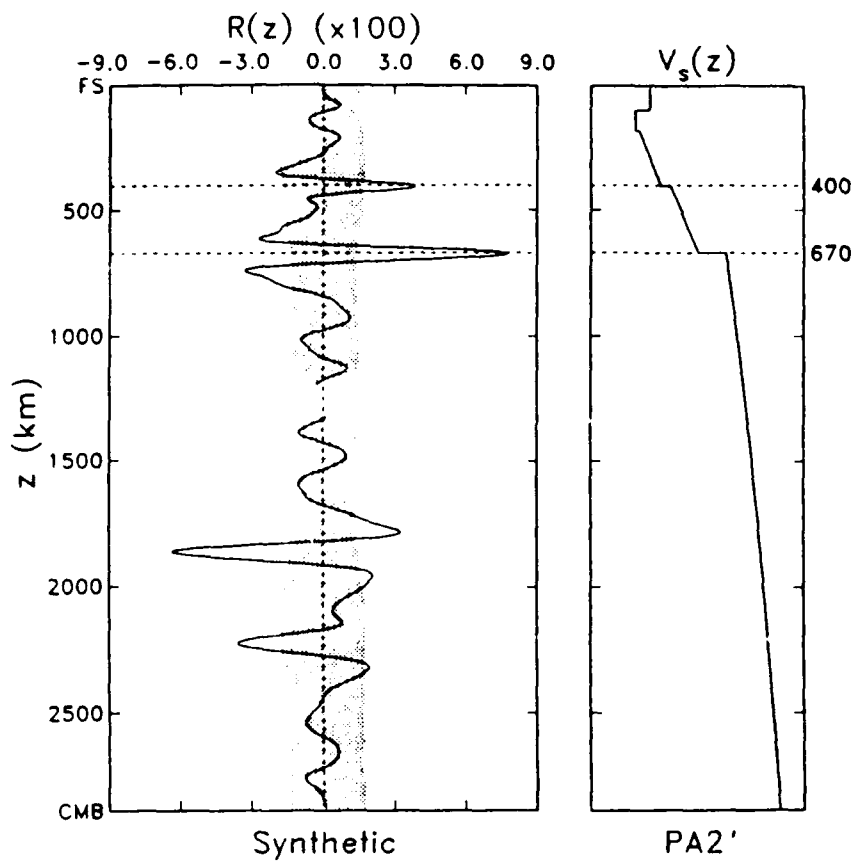
100

Figure 3.4

101

Figure 3.5

102

Figure 3.6

103

Figure 3.7

104
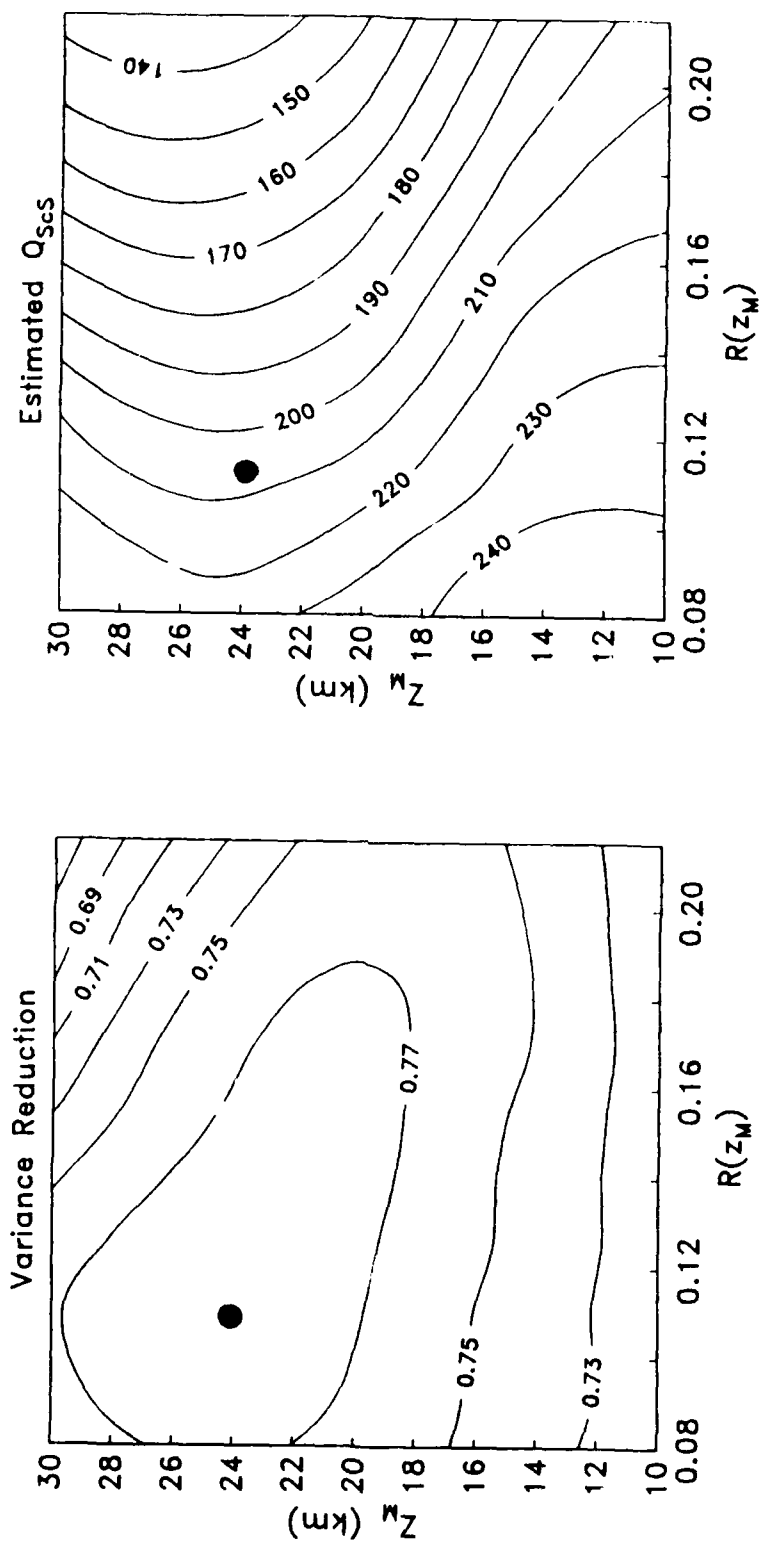
CHAPTER 4

REVERBERATION WAVEFORM INVERSION: RESULTS

INTRODUCTION

In this chapter, we apply the methods developed in Chapter 3 to invert zeroth-order reverberation waveforms for path-averaged estimates of whole-mantle travel time, Q_{ScS}, and crustal structure. While our primary interest in these quantities arises from a need to accurately model the waveforms of higher-order reverberations, they are nonetheless important in and of themselves. Measurements of multiple-ScS travel-time residuals and attenuation have been an important source of information regarding the lateral heterogeneity of the upper mantle [*Sipkin and Jordan*, 1979, 1980*a, b*; *Chan and Der*, 1988; *Lay and Wallace* 1983, 1988]. Although these phases sample the entire mantle, the correlation of travel-time residuals and variations in attenuation with surface tectonics argue for the predominance of upper mantle heterogeneity. Results presented in this chapter add significantly to the geographical coverage of multiple ScS observations, and reinforce the conclusion of previous studies, requiring a significant dichotomy between old oceans and continents, with variations in velocity and attenuation structure persisting to depths as great as 400 km in the upper mantle [e.g., *Sipkin and Jordan*, 1979; 1980*a, b*].

The accurate model of zeroth-order reverberations obtained by waveform inversion is stripped from the seismogram. In the reverberative interval, the residual is dominated by first-order reverberations, with contributions from the transition-zone discontinuities figuring most heavily. "Migration" of the stripped seismograms produces a map of mantle reflectivity, but, as discussed in Chapter 3, this map will contain artifacts arising from data limitations, impeding straightforward interpretation. Through migration of synthetic data sets we are able to model these artifacts. By progressively adding complexity to the mantle models used to construct the synthetic data, we are able to produce excellent fits to data profiles, obtaining in the process accurate estimates of the apparent depths and reflection

105

coefficients of the both the major and minor reflectors of seismic energy in the mantle. The discontinuity structures obtained in this way provide the bulk of the observational basis of this thesis. The remaining chapters are devoted to extracting and expounding upon the rich stores of information they contain.

RESULTS OF ZEROTH-ORDER REVERBERATION INVERSION

The grid search-inversion algorithm of Chapter 3 has been applied to 18 seismic corridors in the western and central Pacific, Indonesia and Australia. An example of output produced by this method, obtained for the corridor linking shocks in the Tonga-Fiji seismic zone with the ASRO station CTAO (corridor 5 in Table 2.2), can be found in Figure 3.4 (a second example can be found in Chapter 7). Results from the entire suite of experiments are compiled in Table 4.1. Several aspects of this work have implications for upper mantle layering, and the subsequent analysis of first-order reverberations, and bear further scrutiny.

Tectonic Correlation of τ_{ScS}

Previous studies of the geographic variation of multiple-*ScS* travel times have documented significant lateral heterogeneity [e.g., *Okal and Anderson*, 1975; *Sipkin and Jordan*, 1980a; *Stark and Forsyth*, 1983]. As expected from plate-cooling arguments there is a systematic decrease in travel time with increasing age in the oceans, and with increasing age since the last orogenic disturbance for continents. More important, however, is the identification of a 5.2-s decrease from τ_{ScS} estimates for old oceanic regions to estimates for stable continental platforms and shields [e.g. *Sipkin and Jordan*, 1980a]–regions predicted to be essentially similar in the plate-cooling model..

Using the GTR1 tectonic regionalization [*Jordan*, 1981] we have computed regionalized estimates of τ_{ScS} via a weighted least-squares decomposition of the individual corridor estimates (Table 4.1). Because our sampling of the GTR1 regions is not uniform, we have

repartitioned the GTR1 provinces into three groups, namely: oceans (regions A, B, and C), phanerozoic orogenic zones (region Q), and stable continental blocks (regions P and S). To eliminate the contribution due to shallow-seated heterogeneity, the times presented in Table 4.1 have been corrected for variations in crustal thickness and bounce-point bathymetry. Crustal corrections were computed by adjusting all times to a canonical crustal thickness of 33 km, assuming a crustal velocity of 3.6 km/s, and upper mantle velocity of 4.5 km/s (values similar to the Jeffrey's Earth model). Bounce point bathymetry was reduced to sea level using the same crustal velocity, with bathymetry estimated from the DBDB5 digital database averaged over the first Fresnel zone of the bounce point with a Gaussian weighting function. The magnitude of both of corrections is of order 2 s. The resulting regionalized estimates of τ_{ScS} are: 943.2 ± 0.2 s (oceans), 936.3 ± 0.2 s (phanerozoic orogenic zones), and 935.5 ± 0.3 s (stable continental blocks), consistent with a 7.7-s decrease in two-way travel time going from oceanic regions (primarily of intermediate age; 24–100 Myr), to stable continental blocks. Weighting the regional estimates of τ_{ScS} by their global areal fractions (Table 2.2) results in an average value of 940.4 ± 0.2 s. By way of comparison, the PREM predicts τ_{ScS} = 940.5 s.

The ability of this simple, three-parameter model to reconstruct τ_{ScS} on a corridor-by-corridor basis is remarkable (Figure 4.1), implying that variations in τ_{ScS} are strongly correlated with surface tectonics. As discussed by *Sipkin and Jordan* [1980a] it is difficult to explain the large discrepancy in oceanic and continental travel times by shallow-seated heterogeneity alone, requiring tectonically-correlated differences in velocity structure perhaps as deep as 400 km.

Tectonic Correlation of Q_{ScS}

Following the analysis of τ_{ScS} we have obtained regionalized estimates of Q_{ScS} from the 18 path averages of Table 4.1. As is typically the case with attenuation measurements, the uncertainties in these quantities are larger, and the ability of the three parameter model to

reconstruct the corridor estimates poorer (Figure 4.2), than for travel times. However, the results are consistent with τ_{ScS}, displaying a systematic increase in quality factor from oceanic to stable continental blocks: 189 ± 16 (oceans), 200 ± 16 (phanerozoic orogenic zones), and 280 ± 30 (continental platforms and shields), with an inferred global average value of 207 ± 25 (likely to be biased high by the lack of estimates for young oceanic regions). While there is considerable scatter in the observations, the data display a positive correlation between τ_{ScS} and Q_{ScS}^{-1} which is nominally significant at the 95% confidence level (Figure 4.3). A similar correlation was noted by *Sipkin and Jordan* [1980*b*] in a data set with little overlap with the present, suggesting that it may be true of the Earth in general. Given the observed tectonic correlations of both τ_{ScS} and Q_{ScS}^{-1}, it seems reasonable to assign their mutual correlation to thermal heterogeneity largely confined to the upper mantle, although other heterogeneities, such as large-scale compositional variations may also contribute.

For the seismic corridor connecting shocks in the Izu-Bonin seismic zone with station GUMO on the island of Guam (corridor 6 in Table 2.2), our data is best fit by Q_{ScS} = 97 ± 30, an extremely low value indicative of severe attenuation. Bounce points for the zeroth-order reverberations entering into this estimate lie in, or near, the Mariana and Bonin ridges–sites of active inter-arc spreading [*Karig*, 1971]. The presence of high temperatures and a small amount of partial melt beneath these features may explain the anomalous attenuation of multiple *ScS*. Measurements of ScS_n attenuation in the Basin and Range and northern South America yield similarly low values of Q_{ScS}. [*Lay and Wallace*, 1983; 1988].

Crustal Modeling

Detailed crustal structures were not available for many of the regions sampled in this study (especially with regards to the strength of the M discontinuity), a fact which motivated us to solve for the parameters of a simple crustal model in the inversion process.

Nevertheless, by searching the gravity, heat flow and seismic-survey literature (see *Soller et al.* [1982], and references therein), it was possible to infer the depth of the M discontinuity beneath many of the zeroth-order reverberation surface bounce points. Where unavailable, estimates often could be obtained by extrapolation from nearby points or by comparison with similar tectonic regions where the crust had been studied. In this way the average depth of the M discontinuity sampled by the various zeroth-order reverberations was obtained on a path-by-path basis. Although the uncertainties in these values are high, the agreement with our estimates, derived solely from the low-frequency waveforms of multiple *ScS*, is remarkable (Figure 4.4). A small bias in our estimates toward thicker crustal values can be seen, which could be explained by one or more of several effects. By ignoring the possibility of extended source time functions we may have consistently underestimated pulse duration. If so, broader composite synthetic waveforms, resulting from a thicker crust, may offer a better fit to data. The use of constant-velocity layers in the interpretation of seismic refraction surveys leads to estimated layer thicknesses that are consistently too small (P. Spudich, personal communication, 1987). Most of the older literature was based on this methodology, implying that the depths inferred from some of these studies may be too shallow.

Another potential source of bias of particular interest to this study is distortion of zeroth-order reverberation waveforms owing to boundary-layer structure near the CMB. Because the core is a near-perfect reflector of *SH*-polarized waves, mantle-side layering near the CMB will produce first- and higher-order reverberations analogously to the crust. To be hydrodynamically stable, any such layering must be associated with appreciable contrasts in density. Assuming that velocity variations are commensurate with those of density, deep mantle structure, if present, could have a profound influence on composite ScS_n waveforms. The very good agreement of our estimates of crustal thickness and published estimates documented in Figure 4.4 imposes important upper limits on the magnitude of

CMB structure beneath the sampled regions. This subject will be treated in greater detail in Chapter 7.

We note that our estimates of the reflection coefficient of the M discontinuity also display a tectonic correlation which, albeit not strong, tend towards larger values beneath continents, yielding regionalized estimates of: 0.13 ± 0.04 (oceans), 0.18 ± 0.04 (phanerozoic orogenic zones), and 0.22 ± 0.07 (stable continental blocks). At the low frequencies of interest to this study it is difficult to determine the exact nature of crustal sampling, however the sense of correlation is consistent with the notion of a slower and less-dense granitic continental crust. A second possibility is that this trend reflects the presence of a basal low-velocity layer in the continental crust, acting to increase the effective impedance contrast of the M discontinuity [e.g., *Landisman et al.*, 1971; *Jordan and Frazer*, 1975].

INVERSION OF FIRST-ORDER REVERBERATIONS

The migration algorithm developed in the previous chapter, embodied by equation (3.12), was applied to data from the 18 seismic corridors sampled in this study. Prior to processing, the data were stripped of zeroth-order reverberations as in Figure 3.5, and the results of the inversion of zeroth-order reverberation waveforms, namely, revised source parameters, Q_{ScS}, τ_{ScS}, z_M, and $R(z_M)$, were used in the construction of DRFs. To model the moveout in time and distance of first-order reverberations, ray tracing through the smoothed mantle model, PA2', was performed. However, since τ_{ScS} varied from region to region, that velocity model had to be adjusted. The ScS_n and $sScS_n$ phases employed to estimate τ_{ScS} sample the entire mantle uniformly and therefore provide no control over velocity as a function of depth. Thus in order to match model-predicted and observed τ_{ScS} values, we decided to uniformly increase or decrease the upper mantle velocities of PA2' as appropriate for each path.

Results of the experiments are shown in Figures 4.6 through 4.23. However, before discussing specific results, several general comments regarding these experiments need to be made: (1) To avoid contamination by unmodeled, nonreverberative arrivals, the time window considered usually consists of the portion of seismogram starting with the passage of $sScS_2$ and ending with the first major arc arrivals. In some cases, typical of paths with the lowest SNRs and greatest epicentral distances, the window is further abbreviated, to begin with the passage of $sScS_3$. (2) The noise covariance matrix C_{nn} is estimated from the autocorrelation of the entire reverberative interval after stripping of zeroth-order reverberations. Since signal from any single discontinuity represents only a small portion of the energy of the reverberative interval this approach is justifiable. For simplicity we also assumed that C_{nn} was stationary over the duration of the reverberative interval. Amplitude losses due to attenuation and geometric spreading are largely compensated by the increasing number of dynamic analogs found for later arrivals, resulting in time-averaged energy levels which do not change drastically (Figure 3.5). Pulse broadening, while noticeable, should not be a significant source of nonstationarity in the noise covariance. Operationally, use of the noise covariance matrix is equivalent to prewhitening of the data. (3) Estimates of the reflectivity profile variance are obtained by Monte Carlo simulation on synthetic noise panels whose spectral characteristics are that of actual data. As shown, they are referenced to zero, rather than to the estimated reflectivity. This is in accord with the interpretation of equation (3.12) as an optimal signal detector, from which it can be shown that these error bounds (2σ) also correspond to the 5% false-alarm probability level [e.g., *Helstrom*, 1960]. That is, the probability that reflectivity estimates in excess of these limits are due to noise alone is < 5%. (4) Reflectivity estimates are not made over the depth interval of 1200–1320 km, bracketing the midpoint of the mantle with respect to travel time (~1260 km). In this depth region, first-order reverberations from the topside and bottomside of a discontinuity have nearly equal travel times, but opposite polarities, destructively interfering with one another. This reduces the denominator of

(3.12) and increases the variance of the profile, with the result that little useful information can be obtained for $R(z)$ at these depths. (Note that signal energy from any discontinuity in this depth range would also be low for the same reasons.)

SYNTHETIC MODELING

Preliminary Synthetic Profiles and 'Parsimony'

From Figures 4.6 through 4.23 it is fairly obvious that the 400-km and 650-km discontinuities dominate the reflectivity signature of the mantle, so much so that synthetic profiles computed for mantle models containing just these two discontinuities provide a reasonable match to data. Also obvious, however, is the important contributions of other, albeit typically smaller, discontinuities. Here we are referring to such features as the discontinuity at 220 km depth in Figure 4.6, or at 66 km in Figure 4.16. Synthetic forward modeling of reflectivity profiles is our primary tool in identifying low-amplitude reflectors such as these, both in discriminating them from noise and experimental-design-induced artifacts, and in eliminating biases owing to interfering structures. Because there is such a heavy emphasis put on forward modeling, we must be careful to understand the assumptions we have built into the interpretative process, as well as its limitations. In this section, we document the steps taken in the analysis of a typical data profile, namely the profile obtained from 17 recordings sampling the seismic corridor connecting events in the Sumba, Philippines, New Britain and New Hebrides seismic zones with station CHTO in Thailand (corridor 1 in Table 2.2; Figure 4.6). This particular corridor was chosen because of the relatively complicated structure it displays; data quality is in no way exceptional, although the results probably suffer somewhat from the geographically extensive source region.

The approach adopted in modeling reflectivity corridors is divided into two parts. In the first, we attempt to model the primary features of data employing as parsimonious a model as possible, i.e., a model where the variations in impedance are distributed amongst the

least number of discontinuities possible. At this point we are attempting to model only the "first-order" features of the data on a corridor-by-corridor basis, and hence no reference to other paths is made, including even those adjacent to the corridor under consideration. For the specific example of corridor 1, this modeling step required placing large impedance increases at 420 and 668 km depth, corresponding to the well known 400-km and 650-km discontinuities. Smaller, but not negligible, impedance increases were also required at depths of 79 and 223 km. The interpretation of these latter two discontinuities is less straightforward than the former, and postponed to subsequent chapters. We note here that because of ambiguity, either of these two could be alternatively interpreted as impedance decreases in the lower mantle. The fact that we have chosen to model them as upper mantle discontinuities is for the sake of convenience only; had we chosen to explicitly model the lower mantle image, the estimates of reflection coefficient and depth would be little changed from what we predict having modeled the upper-mantle image instead. In other words, it makes little difference whether we choose to model the upper- or lower-mantle image of a discontinuity–ambiguity ensures that the properties we infer will not be different.

The model of mantle reflectivity obtained by this exercise is shown as the middle profile of Figure 4.6, and will be referred to as the "parsimonious" profile in what follows. This structure clearly provides a good fit to data. The magnitudes of the discontinuities have been chosen to match the amplitude of the reflectivity peaks, but even away from these peaks the "background" level predicted by the synthetic profile is by and large similar to data. Much of the energy comprising this background is due to the occasional spurious correlation of subsets of data with DRFs, correlations which persist in the stack due to hypocentral clustering and the limited number of records available along any given corridor. A typical example of spurious correlation, is the "misinterpretation" of a depth phase as a "primary" reflection, which results in a small "ghost" reflectivity peak below the actual depth of the discontinuity, separated by approximately the depth of the event. For some of the larger discontinuities, the contributions due to second-order reverberations can

113

become non-negligible (although the opposing contributions of topside and bottomside reflections acts to damp their contribution). The theoretical seismograms used to construct synthetic reflectivity profiles include all second-order reverberations; crustal reverberations of all orders are explicitly included through the Haskell propagator-matrix formalism. Our ability to accurately model these artifacts constitutes an important, although pedestrian, aspect of this study. Had we not been able to do so, much of the information content of the data reflectivity profiles would be inaccessible. However, even armed with this ability, we would be hesitant to propose additional reflectors for this corridor without some form of additional evidence. The additional line of evidence comes from comparison of estimates for nearby areas, which reveals regularities in the reflectivity profiles suggestive of additional discontinuity structure.

Higher-Order Features

The parsimonious synthetic profile of Figure 4.6, computed for a mantle model containing just four discontinuities, explains the majority of data reflectivity which differs from zero at the 95% confidence level. This analysis of resolution presupposes knowledge of the amplitude spectrum of data only, however, and does not consider any outside, and/or a priori knowledge that we may have. Because designing a formal analysis of resolution which incorporates such knowledge would be a prohibitively difficult task, and probably not of great practical utility, we have chosen instead to rely on a more intuitive measure of resolution. This measure can be summarized operationally by the following statement: We will interpret a peak or inflection in a reflectivity profile as evidence of a mantle discontinuity if and only if: (1) it can be accurately modeled by addition of a single discontinuity to the synthetic data, (2) including it does not degrade the level of profile agreement achieved away from the depth of the inferred discontinuity, and (3) it is consistently observed in a significant subset of the suite of corridor-averaged estimates.

114

For corridor 1, applying this dictum results in the synthetic reflectivity profile right of center in Figure 4.6, whose discontinuity structure is represented schematically to the right. This profile differs from the parsimonious synthetic profile by the addition of three, relatively small ($R(z) \sim$ 1–2%) reflectors, located at depths of 306, 551, and 768 km, respectively. This profile will be referred to as the "preferred" profile in what follows. Comparison with nearby seismic corridors (compare Figures 4.7, 4.9 and 4.18) show these additional discontinuities to be geographically consistent features of the data reflectivity profiles. The signatures of these discontinuities are small, and largely obscured by the stronger side-lobes of the 220-km, 400-km and 650-km discontinuities, yet they are remarkably well modeled by the preferred synthetic profiles. Addition of essentially similar discontinuities to the mantle models used to compute synthetic reflectivity profiles for the nearby corridors (corridors 2, 4, and 13 in Table 2.2) provides equally good improvements in the fit to data 9Figures 4.7, 4.9, and 4.18). While this analysis is necessarily somewhat subjective, the consistency of the observations throughout a heterogeneous data set give us confidence in our identification of these features.

R(z) Estimates

Included in each of the Figures 4.6 through 4.23 is a schematic representation of the discontinuity structure inferred from detailed synthetic modeling, wherein we plot the *SH* reflection coefficient at the apparent depth of the discontinuity (a compilation of these quantities is given in Table 4.2). We stress the use of the word "apparent"; first-order reverberations alone are incapable of providing a direct estimate of discontinuity depth, being sensitive only to the vertical travel time separating the discontinuity from either the free surface or CMB. Because the velocity structures beneath most of the sampled regions are unknown to us, we cannot uniquely determine depth. Fortunately, interval travel times differ little from model to model, with the result that depth estimates obtained from a suite of mantle models will typically vary by less than 10 km. Uncertainties in the measurement

of depth is of order 5 km for the transition-zone discontinuities (relative to the migration velocity model), increasing to ~20 km for lower-amplitude reflectors, thus this limitation of modeling is not of great significance, although it is possible to improve the estimates of discontinuity depth by appealing to global models of mantle heterogeneity obtained by seismic tomography (Chapter 5). Uncertainties in the estimates of the reflection coefficients also become proportionately greater as the inferred strength of the reflector decreases. Note that in this respect, the 5% false-alarm levels do not provide an accurate estimate of reflection coefficient variance–a measure which is better quantified by the standard deviation of estimates obtained for individual paths along a seismic corridor. Estimates obtained in this fashion suggest a relatively uniform level of measurement uncertainty, with a standard error of 0.01 (~15%) for the larger reflectors, decreasing somewhat for lower amplitude reflectors (~0.005). While this represents a significant fraction of the estimate, it is nonetheless a testimony to the unprecedented utility of first-order reverberations in retrieving these quantities.

SUMMARY

Using specifically-tailored waveform inversion and signal enhancement techniques we have accurately estimated parameters describing the gross properties of mantle discontinuity structure. On a corridor-by-corridor basis this set minimally includes the path-averaged whole-mantle travel time τ_{ScS} and quality factor Q_{ScS}, crustal thickness z_M, and M-discontinuity reflection coefficient $R(z_M)$, all of which display strong tectonic correlation, arguing for the predominance of upper mantle heterogeneity. Analysis of first-order reverberations provides estimates of the apparent depths and reflection coefficients of discontinuities internal to the mantle. Apart from the large, and apparently ubiquitous, transition-zone discontinuities, estimates of $R(z)$ for a number of other, typically much smaller, discontinuities have been obtained. These estimates represent an important new

geophysical data base--the remainder of this thesis is devoted to unraveling the wealth of information they contain.

TABLE 4.1.   Zeroth-Order Reverberation Inversion Results

#	Source Region	Recv.	τ_{ScS}[1] sec	Q_{ScS}	z_M km	$R(z_M)$
1	Sumba-Phil.	CHTO	939.6 ± 0.3	181 ± 30	23 ± 8	0.18 ± 0.04
2	New Britain	CTAO	939.1 ± 0.3	258 ± 40	30 ± 8	0.20 ± 0.06
3	Sumba		934.4 ± 0.3	262 ± 30	30 ± 8	0.18 ± 0.04
4	Philippines		935.9 ± 0.3	158 ± 30	30 ± 6	0.20 ± 0.04
5	Tonga-Fiji		941.3 ± 0.3	210 ± 40	24 ± 8	0.11 ± 0.07
6	Sumba-Phil.	GUMO	939.9 ± 0.3	181 ± 30	10 ± 5	0.18 ± 0.08
7	Izu-Bonin		938.7 ± 0.3	97 ± 30	12 ± 6	0.17 ± 0.10
8	Tonga-Fiji	KIP	945.8 ± 0.3	169 ± 30	6 ± 3	0.12 ± 0.03
9	Sumba-Phil.	MAJO	939.2 ± 0.3	181 ± 30	15 ± 4	0.20 ± 0.03
10	Japan-Izu		935.8 ± 0.3	183 ± 40	26 ± 8	0.13 ± 0.07
11	Philippines	NWAO	936.6 ± 0.3	194 ± 35	25 ± 7	0.22 ± 0.05
12	New Britain		936.8 ± 0.3	243 ± 40	27 ± 9	0.22 ± 0.07
13	Sumba		935.0 ± 0.3	289 ± 30	27 ± 5	0.18 ± 0.05
14	Tonga-Fiji		938.0 ± 0.5	191 ± 30	25 ± 7	0.12 ± 0.05
15	Tonga-Fiji	SNZO	999.9 ± 0.5	192 ± 45	15 ± 8	0.14 ± 0.09
16	Philippines	TATO	938.7 ± 0.5	210 ± 40	12 ± 7	0.20 ± 0.10
17	New Britain		940.7 ± 0.5	226 ± 30	12 ± 7	0.14 ± 0.08
18	Japan-Izu		935.9 ± 0.3	216 ± 45	28 ± 5	0.13 ± 0.08

[1]Times corrected for crustal thickness and bounce-point bathymetry variations.

118

TABLE 4.2. Estimates of $R(z)$ Obtained From First-Order Reverberations[1]

#	Source Region	Recv.	z km	R	z km	R	z km	R	z km	R	z km	R	z km	R	z km	R	z km	R
1	Sumba-Phil.	CHTO	79	0.032	223	0.023	306	0.013	420	0.041	551	0.007	668	0.073	768	0.022		
2	New Britain	CTAO	75	0.022	221	0.015	331	0.013	405	0.033	570	0.015	659	0.041			899	0.014
3	Sumba		92	0.036					406	0.042	550	0.010	658	0.053	751	0.016		
4	Philippines		56	0.037	188	0.020	341	0.029	409	0.034	505	0.016	666	0.068	746	0.030		
5	Tonga-Fiji				86	-0.025	292	0.009	411	0.032	490	0.008	663	0.049				
6	Sumba-Phil.	GUMO	63	0.037					408	0.037	530	0.010	668	0.059	768	0.009		
7	Izu-Bonin				53	-0.039							661	0.073				
8	Tonga-Fiji	KIP			59	-0.055			409	0.046	495	0.021	649	0.078				
9	Sumba-Phil.	MAJO	51	0.019	91	-0.023			408	0.042	520	0.008	661	0.058				
10	Japan-Izu		71	0.014					405	0.037	515	0.017	656	0.066				
11	Philippines	NWAO	66	0.068					413	0.052	520	0.013	651	0.069				
12	New Britain		61	0.049					405	0.044	500	0.008	654	0.041				
13	Sumba		62	0.028	251	0.021			415	0.040			647	0.067	705	0.010	861	0.019
14	Tonga-Fiji				275	0.025												
15	Tonga-Fiji	SNZO			92	-0.103	319	0.020	421	0.054	504	0.034	673	0.046	726	0.040		
16	Philippines	TATO	48	0.018	73	-0.075			414	0.040	600	0.020	653	0.057	730	0.010		
17	New Britain		48	0.016	231	0.011	321	0.021	417	0.046	510	0.008	663	0.079				
18	Japan-Izu				101	-0.023	283	0.011	413	0.028			662	0.048				

[1]Estimates of uncertainty in these measurements are discussed in the text. Discontinuities are grouped by depth and sign of the reflection coefficient.

FIGURE CAPTIONS

Fig. 4.1. Estimates of τ_{ScS} obtained by waveform inversion of zeroth-order reverberations versus reconstructed values obtained from a three-parameter model, with regionalized estimates of τ_{ScS}: 943.2 ± 0.2 (oceans), 936.3 ± 0.2 (phanerozoic orogenic zones), and 935.5 ± 0.3 (stable continental blocks). Reconstructed values are formed by averaging the regionalized estimates weighted by the percentage of path length within the region. The good agreement argues for strong tectonic correlation, implying the predominance of upper mantle heterogeneity on the travel times of mantle reverberations. Data are consistent with a 7.7-s decrease in travel times going from oceanic regions (primarily less than 100 Myr old) to stable continental blocks.

Fig. 4.2. Estimates of Q_{ScS}^{-1} obtained by waveform inversion of zeroth-order reverberations versus reconstructed values obtained from a three parameter model, with regionalized estimates of Q_{ScS}: 189 ± 16 (oceans), 200 ± 16 (phanerozoic orogenic zones), and 280 ± 30 (continental platforms and shields), with an inferred global average value of 207 ± 25. While the agreement between estimates and reconstructed values is poorer than for τ_{ScS}, the results are nonetheless indicative of significant mantle heterogeneity, with Q_{ScS} increasing by almost a factor of two from average ocean to average continental regions.

Fig. 4.3. Scatter plot of estimates of Q_{ScS}^{-1} versus τ_{ScS}. While the uncertainties in the attenuation estimates are large, they correlate with τ_{ScS} at greater than the 95% confidence interval, most likely due to thermal heterogeneity in the upper mantle. A similar correlation was observed by *Sipkin and Jordan* [1980b] in a data set with little overlap with the present, suggesting it may be a global phenomena.

Fig. 4.4. Comparison of best-fit estimates (ordinate) of the crustal thickness z_M, obtained from ScS_n and $sScS_n$ waveforms, versus estimates taken from available seismic-refraction,

reflection and gravity-survey literature (abscissa). Although the uncertainties are large, the good agreement between independent estimates argues against strong mantle-side layering of the CMB.

Fig. 4.5. Estimates of the reflection coefficient of the M discontinuity, $R(z_M)$, versus values reconstructed from a three parameter model of regionalized estimates: 0.13 ± 0.04 (oceans), 0.18 ± 0.04 (phanerozoic orogenic zones), and 0.22 ± 0.07 (stable continental blocks). While consistent with the notion of a less dense–more granitic–continental crust, this trend may also reflect the presence of a basal low-velocity layer in the continental crust, acting to increase the effective impedance contrast of the M discontinuity.

Fig. 4.6. Data (left), parsimonious synthetic (left center), and preferred synthetic (right center) reflectivity profiles for corridor 1 in Table 2.2, connecting events in the Sumba, Philippines, New Britain and New Hebrides seismic zones with station station CHTO in Thailand. $R(z)$ is a low-pass filtered estimate of the normal-incidence, SH reflection coefficient of the mantle. Synthetic profiles were computed for a mantle containing discontinuities at only the depths indicated by dashed lines. Large-magnitude features in the lower mantle are false images of upper mantle discontinuities–artifacts which arise due to poor ray-parameter coverage. Stippled region denotes the 5% false-alarm probability level. Gap in the midmantle is due to destructive interference of topside and bottomside reflections, leading to instability in the inversion. The mantle model used to construct the preferred synthetic profile is shown schematically at right, depicting the strength and depth of inferred reflectors.

Fig. 4.7. Reflectivity profiles obtained for corridor 2 in Table 2.2. Model of the mantle used to construct the preferred synthetic profile is shown schematically at right, consisting

121

of discontinuities at 75, 221, 331, 405, 570, 659, and 900 km depth. Conventions are the same as Figure 4.6.

Fig. 4.8. Reflectivity profiles obtained for corridor 3 in Table 2.2. Model of the mantle used to construct the preferred synthetic profile is shown schematically at right, consisting of discontinuities at 92, 406, 550, 658 and 751 km depth. Conventions are the same as Figure 4.5.

Fig. 4.9. Reflectivity profiles obtained for corridor 4 in Table 2.2. Model of the mantle used to construct the preferred synthetic profile is shown schematically at right, consisting of discontinuities at 56, 188, 341, 409, 505, 666, and 746 km depth. Conventions are the same as Figure 4.6.

Fig. 4.10. Reflectivity profiles obtained for corridor 5 in Table 2.2. Model of the mantle used to construct the preferred synthetic profile is shown schematically at right, consisting of discontinuities at 87, 292, 411, 490, and 663 km depth. Conventions are the same as Figure 4.6.

Fig. 4.11. Reflectivity profiles obtained for corridor 6 in Table 2.2. Model of the mantle used to construct the preferred synthetic profile is shown schematically at right, consisting of discontinuities at 63, 408, 530, 668, 768 km depth. Conventions are the same as Figure 4.6.

Fig. 4.12. Reflectivity profiles obtained for corridor 7 in Table 2.2. Model of the mantle used to construct the parsimonious synthetic profile is shown schematically at right, consisting of discontinuities at 53 and 661 km depth. Although the SNRs indicative of this corridors are amongst the lowest encountered in the data set, and the number of

seismograms employed (5) the least, the apparent lack of a 400-km discontinuity is intriguing. Parsimonious and preferred profiles coincide for this corridor. Conventions are the same as Figure 4.6.

Fig. 4.13. Reflectivity profiles obtained for corridor 8 in Table 2.2. Model of the mantle used to construct the preferred synthetic profile is shown schematically at right, consisting of discontinuities at 59, 409, 495, and 645 km depth. Conventions are the same as Figure 4.6.

Fig. 4.14. Reflectivity profiles obtained for corridor 9 in Table 2.2. Model of the mantle used to construct the preferred synthetic profile is shown schematically at right, consisting of discontinuities at 51, 91, 408, 520, and 661 km depth. Conventions are the same as Figure 4.6.

Fig. 4.15. Reflectivity profiles obtained for corridor 10 in Table 2.2. Model of the mantle used to construct the preferred synthetic profile is shown schematically at right, consisting of discontinuities at 71, 405, 515, and 656 km depth. Conventions are the same as Figure 4.6.

Fig. 4.16. Reflectivity profiles obtained for corridor 11 in Table 2.2. Model of the mantle used to construct the preferred synthetic profile is shown schematically at right, consisting of discontinuities at 66, 413, 520 and 651 km depth. Conventions are the same as Figure 4.6.

Fig. 4.17. Reflectivity profiles obtained for corridor 12 in Table 2.2. Model of the mantle used to construct the preferred synthetic profile is shown schematically at right, consisting

of discontinuities at 61, 251, 405, 500, 654, and 861 km depth. Compare the discontinuity near 900 km in Figure 4.8. Conventions are the same as Figure 4.6.

Fig. 4.18. Reflectivity profiles obtained for corridor 13 in Table 2.2. Model of the mantle used to construct the preferred synthetic profile is shown schematically at right, consisting of discontinuities at 62, 275, 415, 647, and 705 km depth. This corridor is the most nearly shield-like of the data set (Table 2.2). Conventions are the same as Figure 4.6.

Fig. 4.19. Reflectivity profiles obtained for corridor 14 in Table 2.2. Model of the mantle used to construct the preferred synthetic profile is shown schematically at right, consisting of discontinuities at 48, 89, 408, 505, and 652 km depth. Conventions are the same as Figure 4.6.

Fig. 4.20. Reflectivity profiles obtained for corridor 15 in Table 2.2. Model of the mantle used to construct the preferred synthetic profile is shown schematically at right, consisting of discontinuities at 92, 319, 421, 504, 660, and 740 km depth. The paths sampling this corridor run parallel to the strike of the Tonga slab immediately on the back-arc side. Conventions are the same as Figure 4.6.

Fig. 4.21. Reflectivity profiles obtained for corridor 16 in Table 2.2. Model of the mantle used to construct the parsimonious synthetic profile is shown schematically at right, consisting of discontinuities at 73, 414, and 653 km depth. This poor SNR corridor samples the back arc side of the Philippine subduction zone.(compare Figure 4.20). Parsimonious and preferred profiles coincide for this corridor. Conventions are the same as Figure 4.6.

Fig. 4.22. Reflectivity profiles obtained for corridor 17 in Table 2.2. Model of the mantle used to construct the preferred synthetic profile is shown schematically at right, consisting of discontinuities at 48, 231, 321, 417, 600 and 663 km depth. Conventions are the same as Figure 4.6.

Fig. 4.23. Reflectivity profiles obtained for corridor 18 in Table 2.2. Model of the mantle used to construct the preferred synthetic profile is shown schematically at right, consisting of discontinuities at 48, 101, 283, 413, 510, 662, and 730 km depth. This corridor features the deepest observed low-velocity zone. Conventions are the same as Figure 4.6.

Figure 4.1

126

Figure 4.2

Figure 4.3

128

Figure 4.4

Figure 4.5

130

Figure 4.6

131

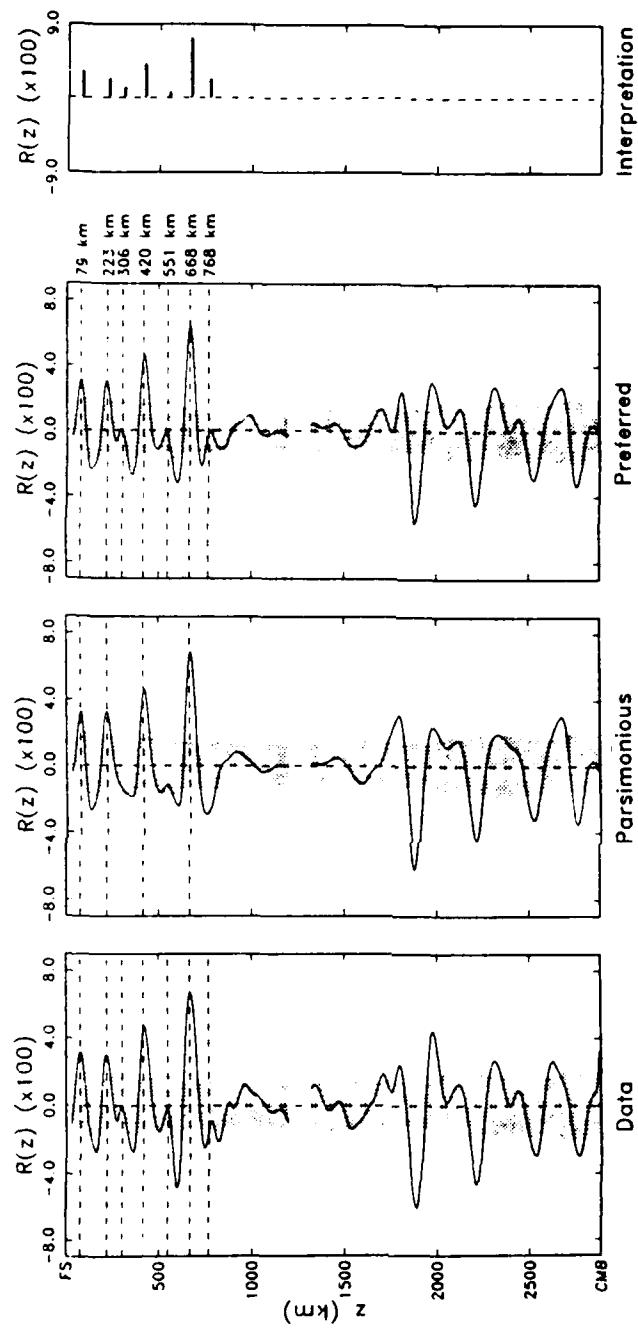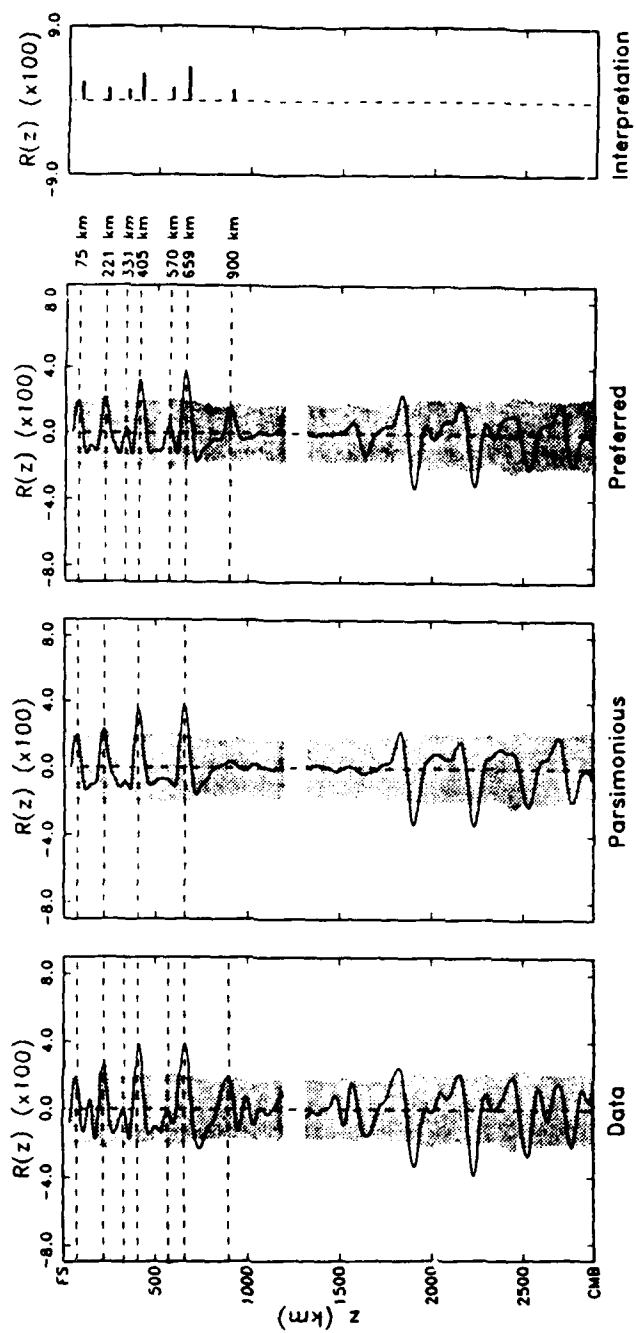**Figure 4.7**
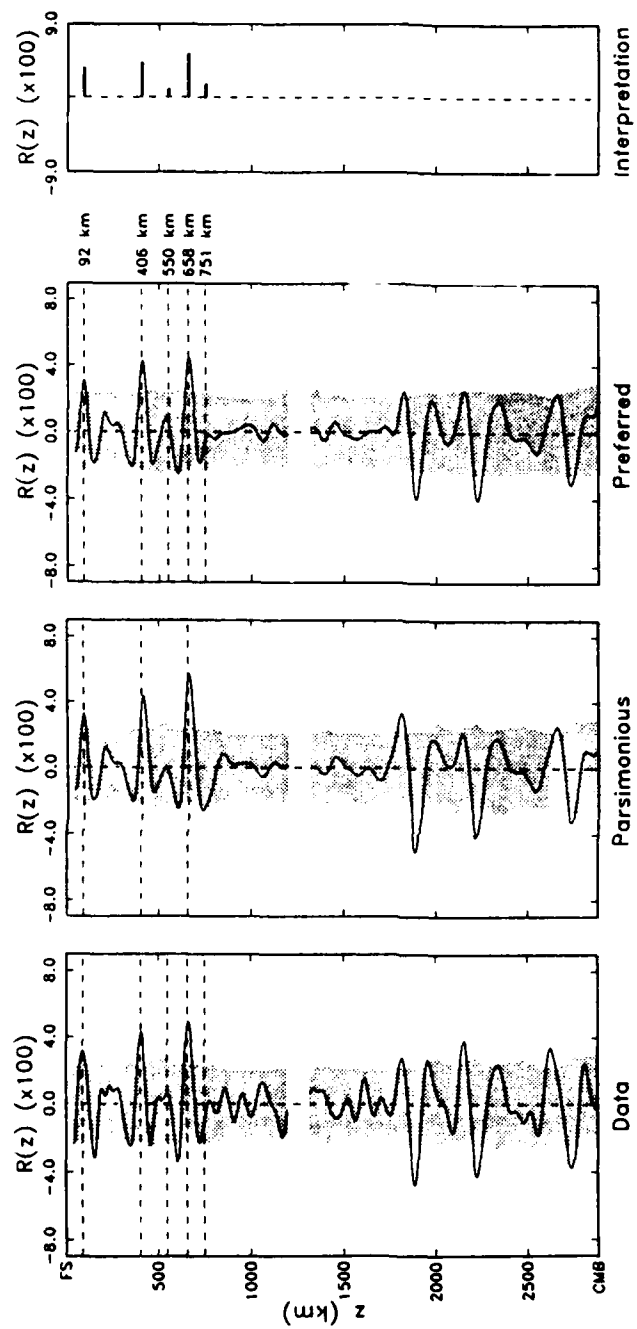
Figure 4.8

133

Figure 4.9

134

Figure 4.10

135

Source Region: Sumba, Timor, Philippines
Station: GUMO (SRO)
Low Passed Filtered (Corner at 40 mHz, truncated at 60 mHz)
Seismograms in Stack: 20
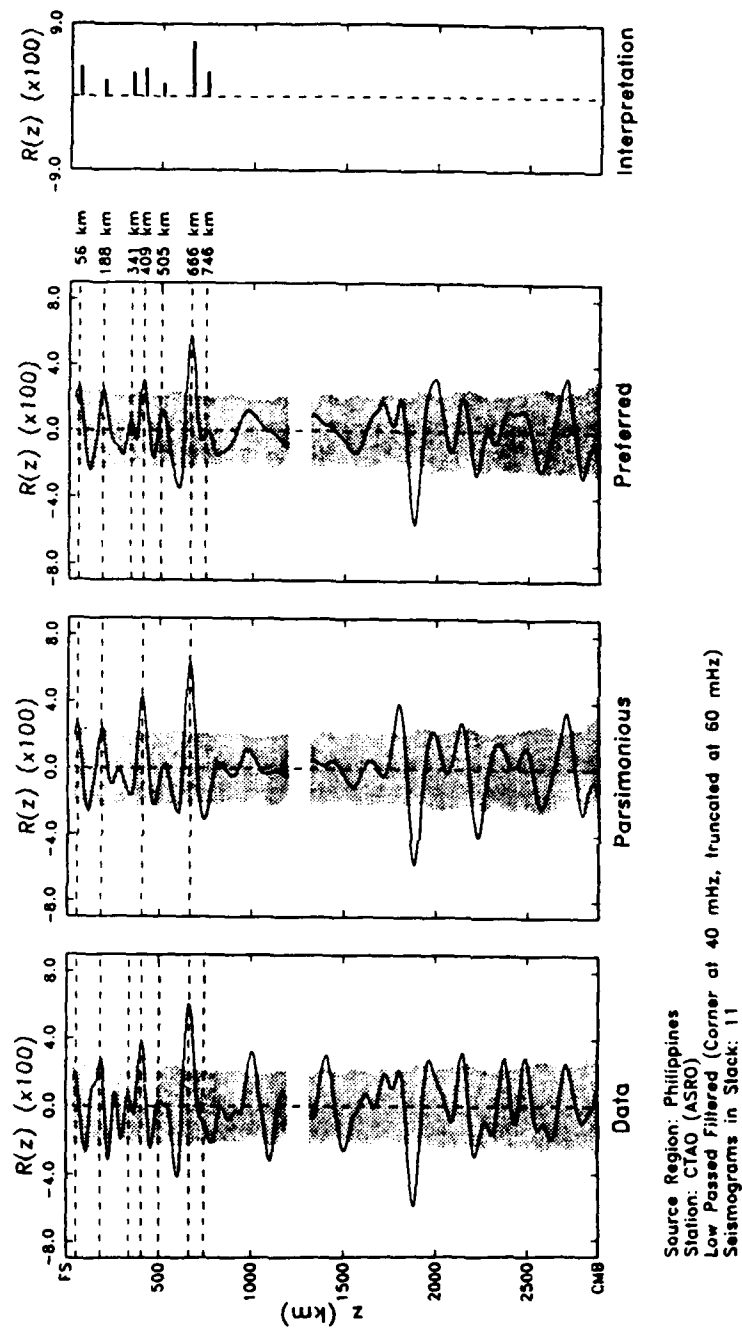
Figure 4.11

136

Figure 4.12

137

Figure 4.13

Source Region: Tonga, Fiji
Station: KIP (HGLP)
Low Passed Filtered (Corner at 40 mHz, truncated at 60 mHz)
Seismograms in Stack: 6

138

Source Region: Sumba, Timor, Philippines
Station: MAJO (ASRO)
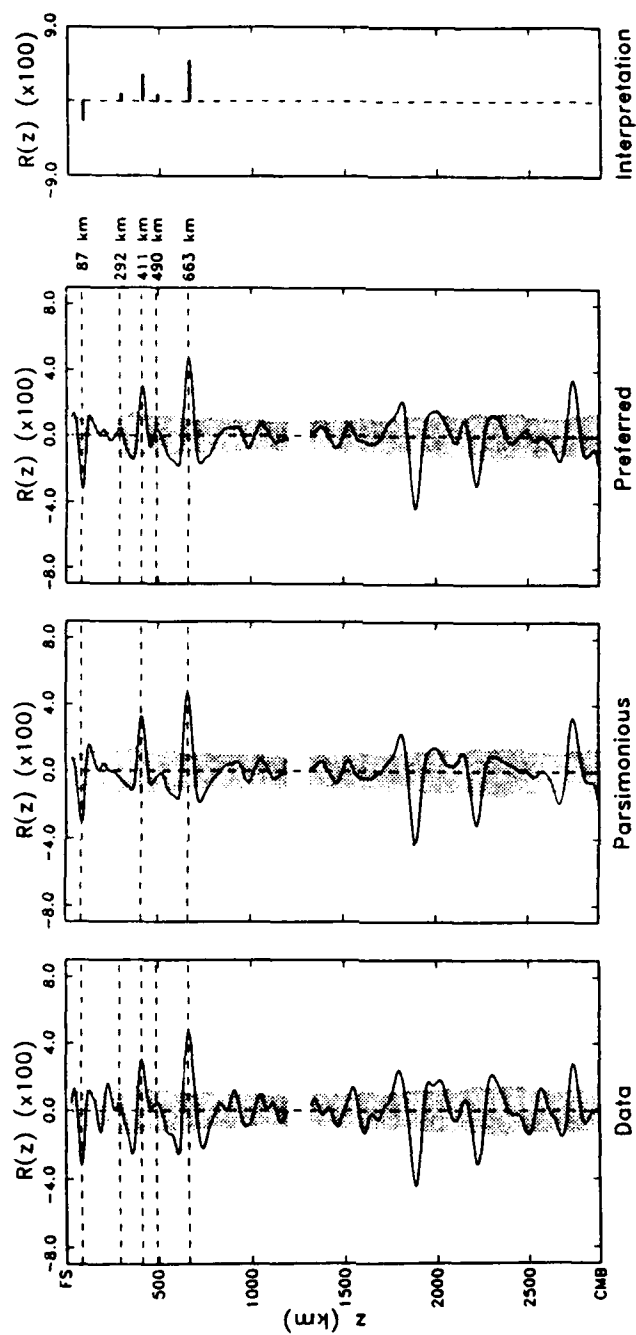Low Passed Filtered (Corner at 40 mHz, truncated at 60 mHz)
Seismograms in Stack: 14

Figure 4.14

139

R(z) (x100)

Interpretation

Preferred

Parsimonious

Data

71 km
405 km
515 km
656 km

z (km)

FS   500   1000   1500   2000   2500   CMB

Source Region: Japan, Izu Bonin
Station: MAJO (ASRO)
Low Passed Filtered (Corner at 40 mHz, truncated at 60 mHz)
Seismograms in Stack: 7

Figure 4.15

140

Figure 4.16

141

Source Region: New Britain, Solomon Islands, New Hebrides
Station: NWAO (SRO)
Low Passed Filtered (Corner at 40 mHz, truncated at 60 mHz)
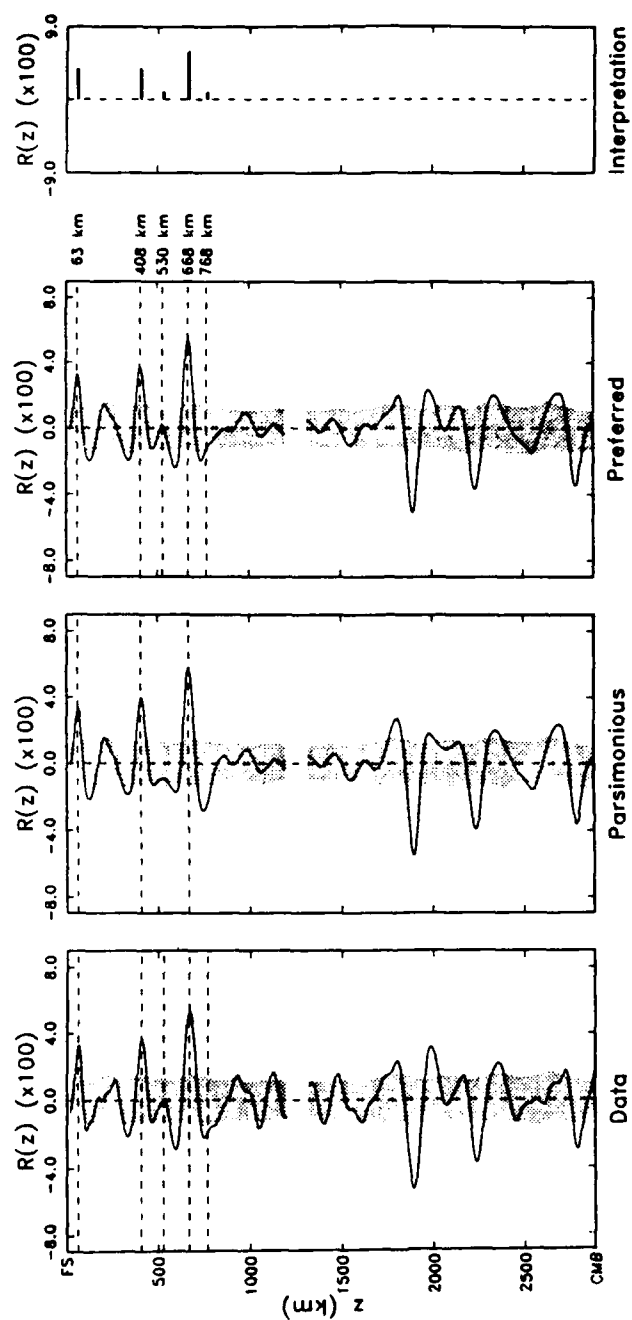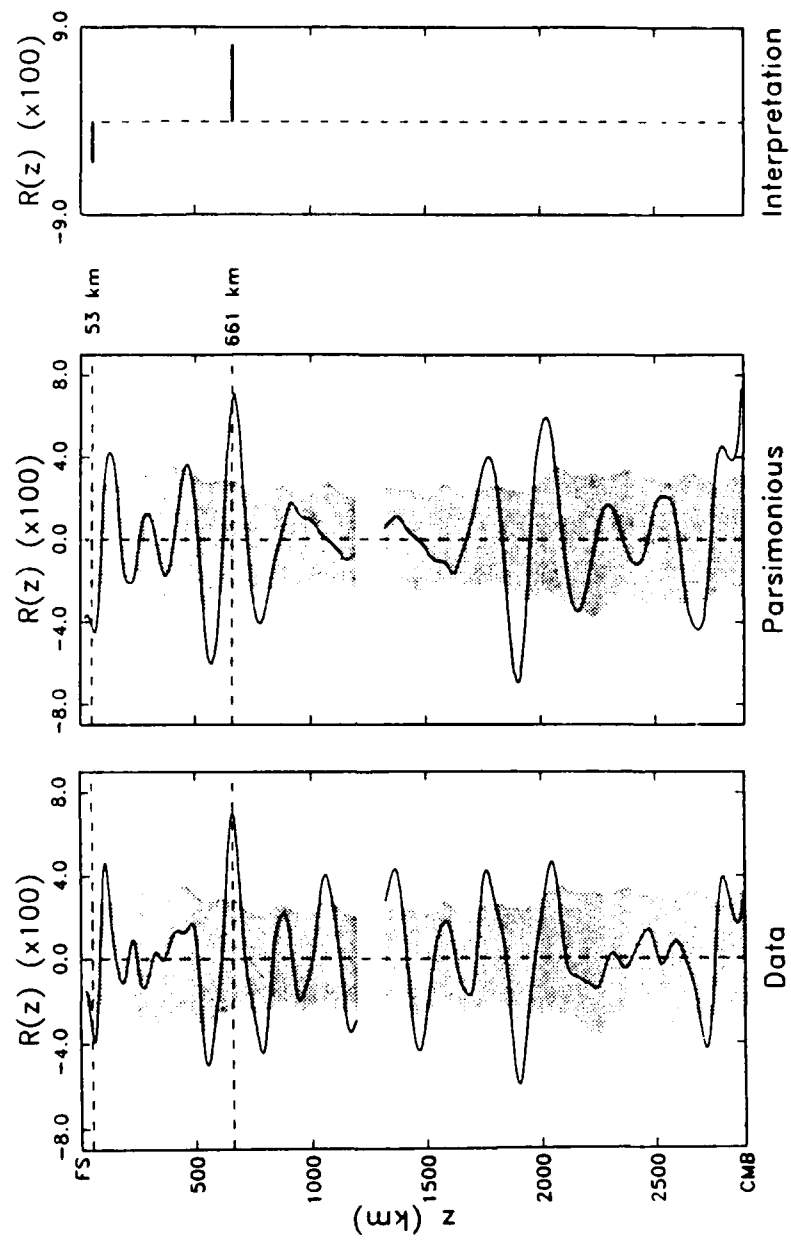Seismograms in Stack: 15

Figure 4.17

142

Figure 4.18

Figure 4.19

Source Region: Tonga, Fiji
Station: NWAO (SRO)
Low Passed Filtered (Corner at 40 mHz, truncated at 60 mHz)
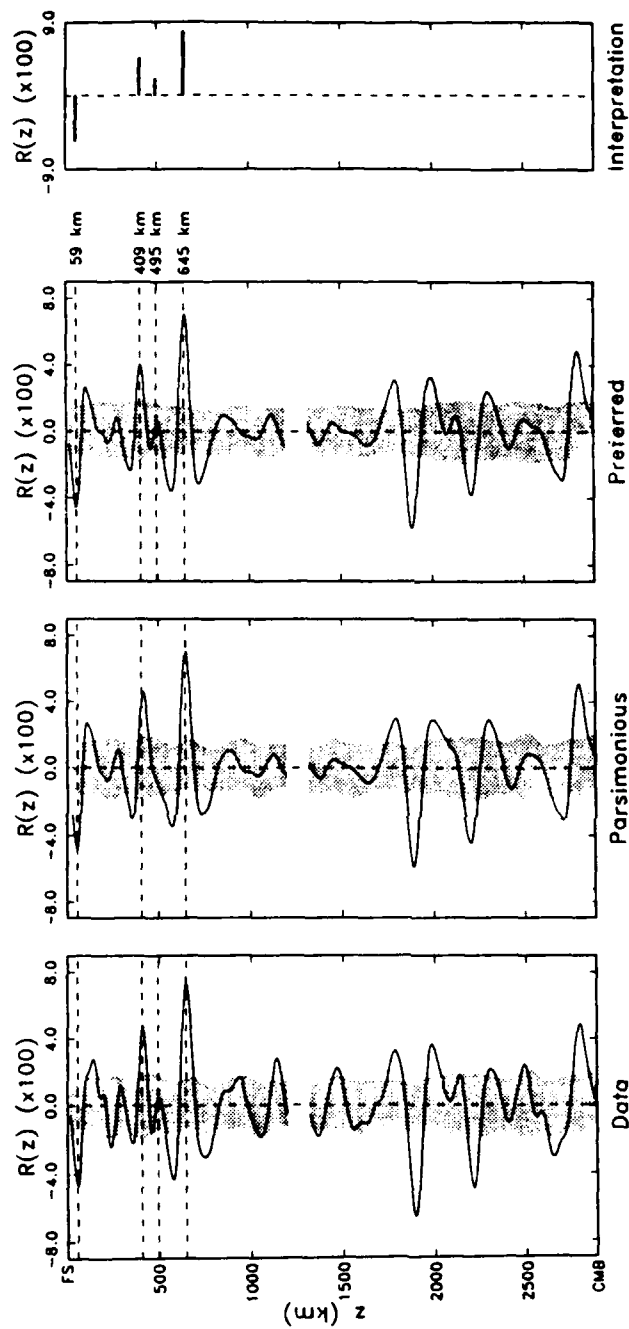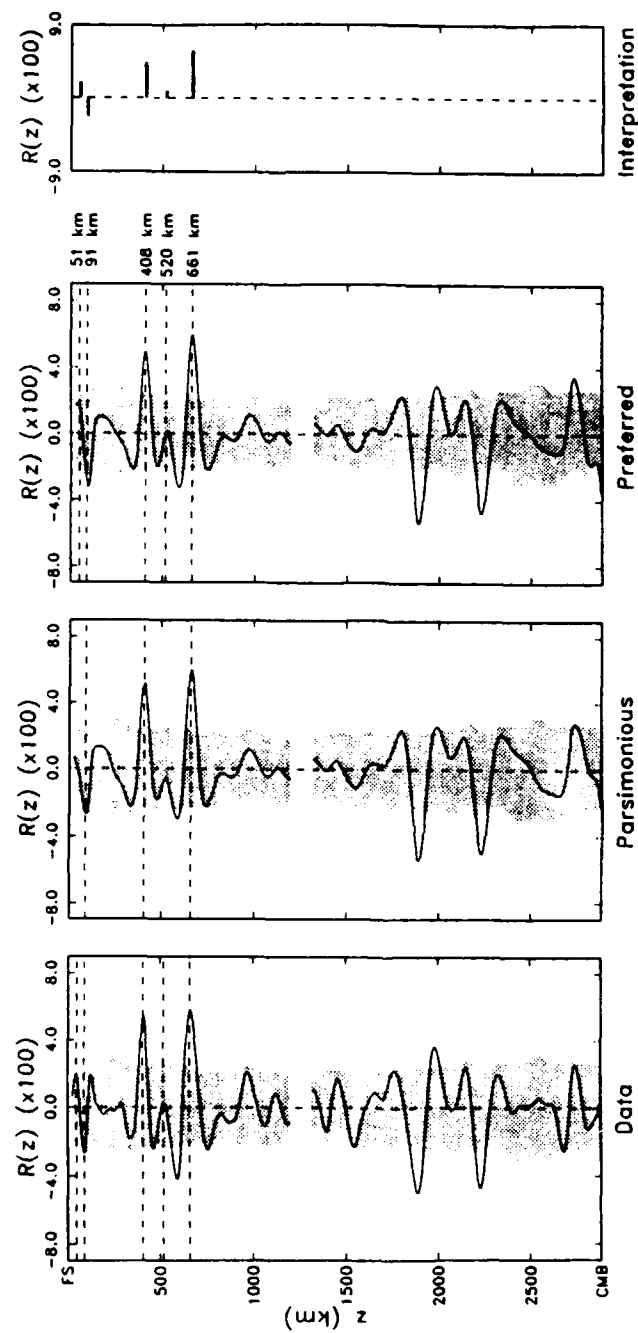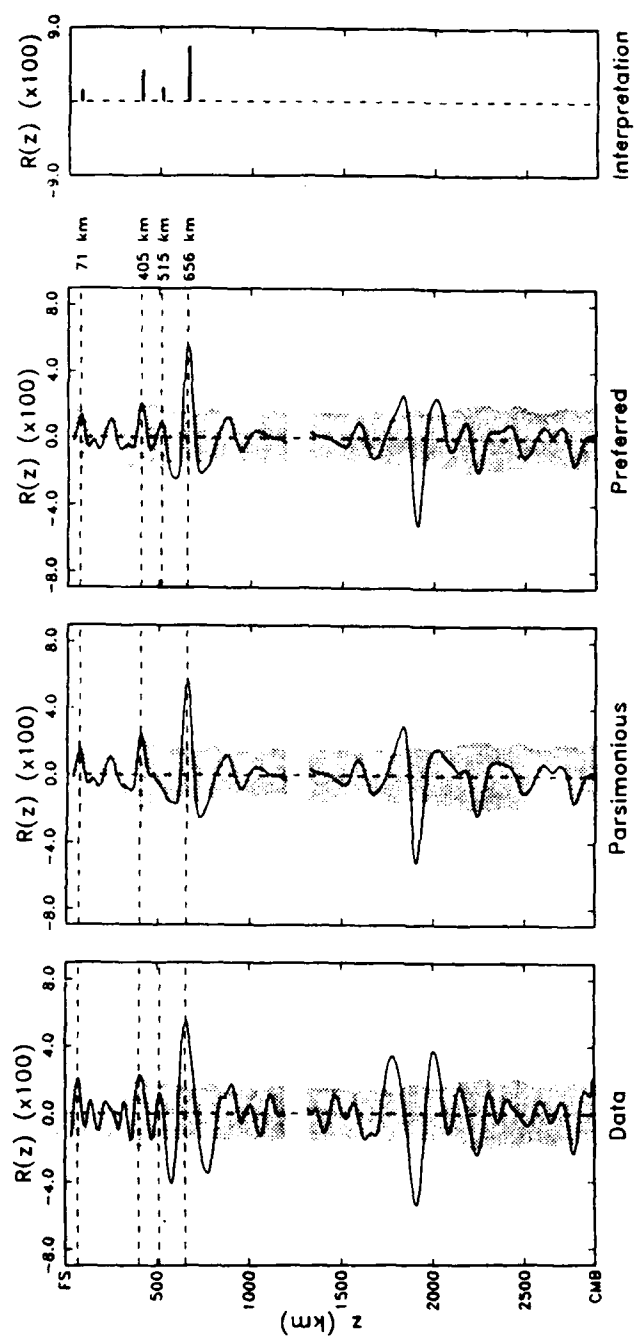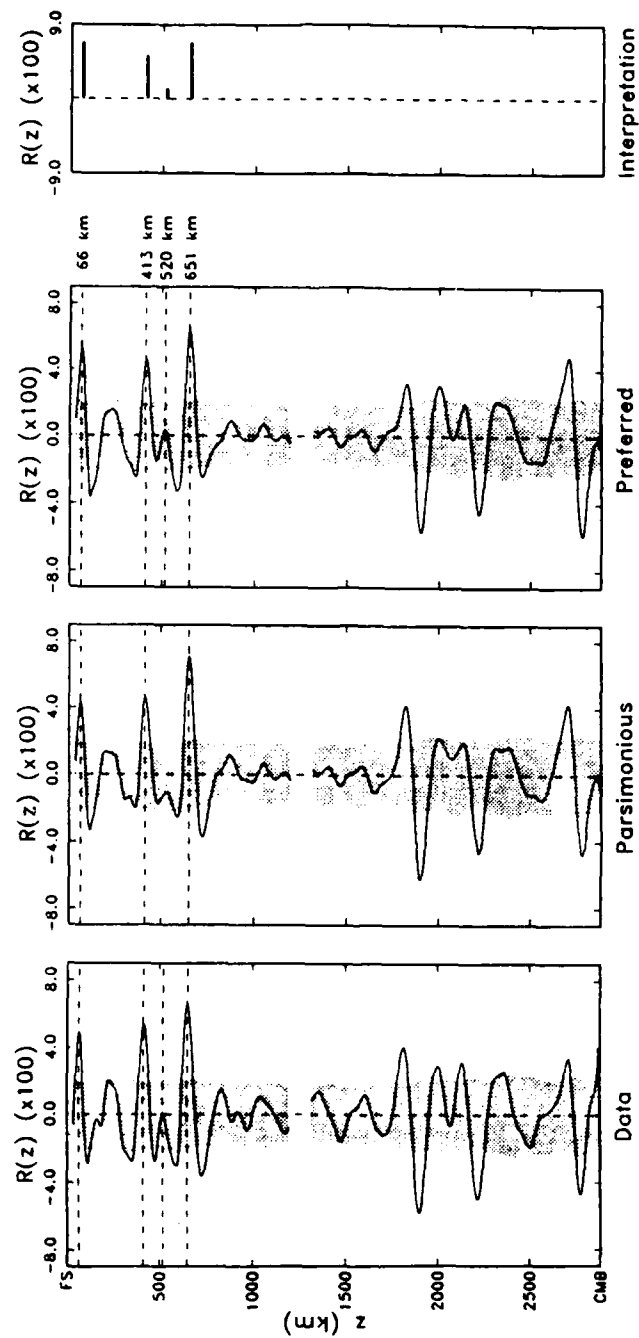Seismograms in Stack: 13

144
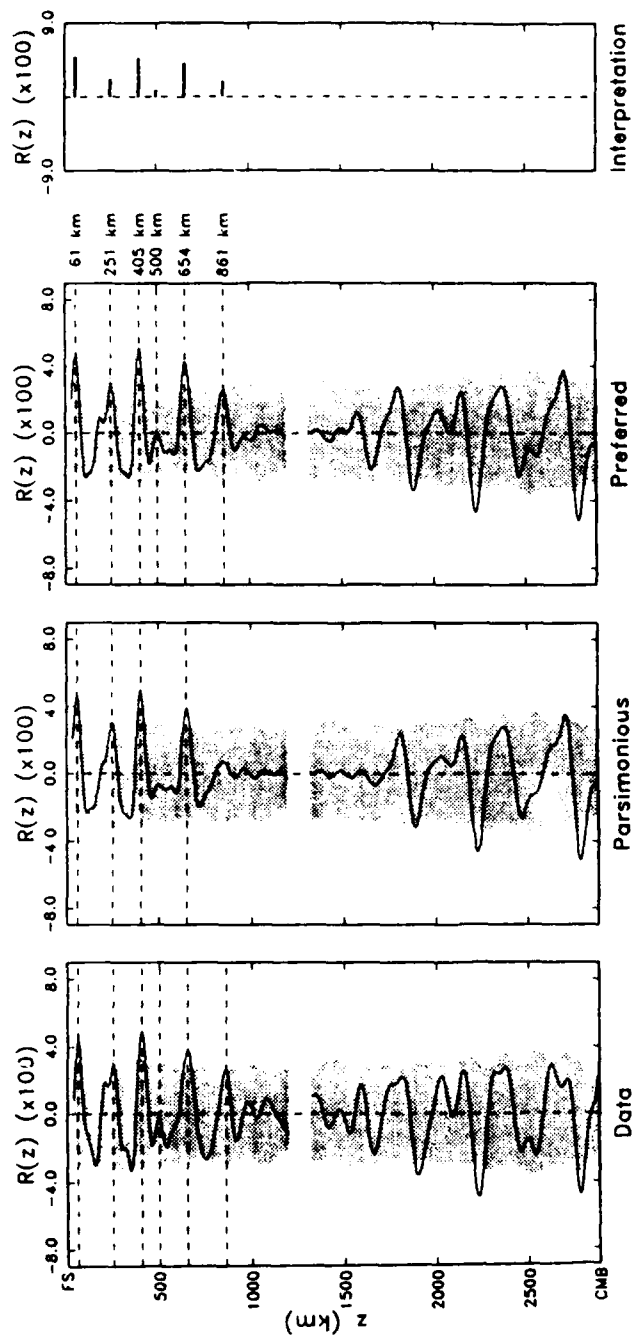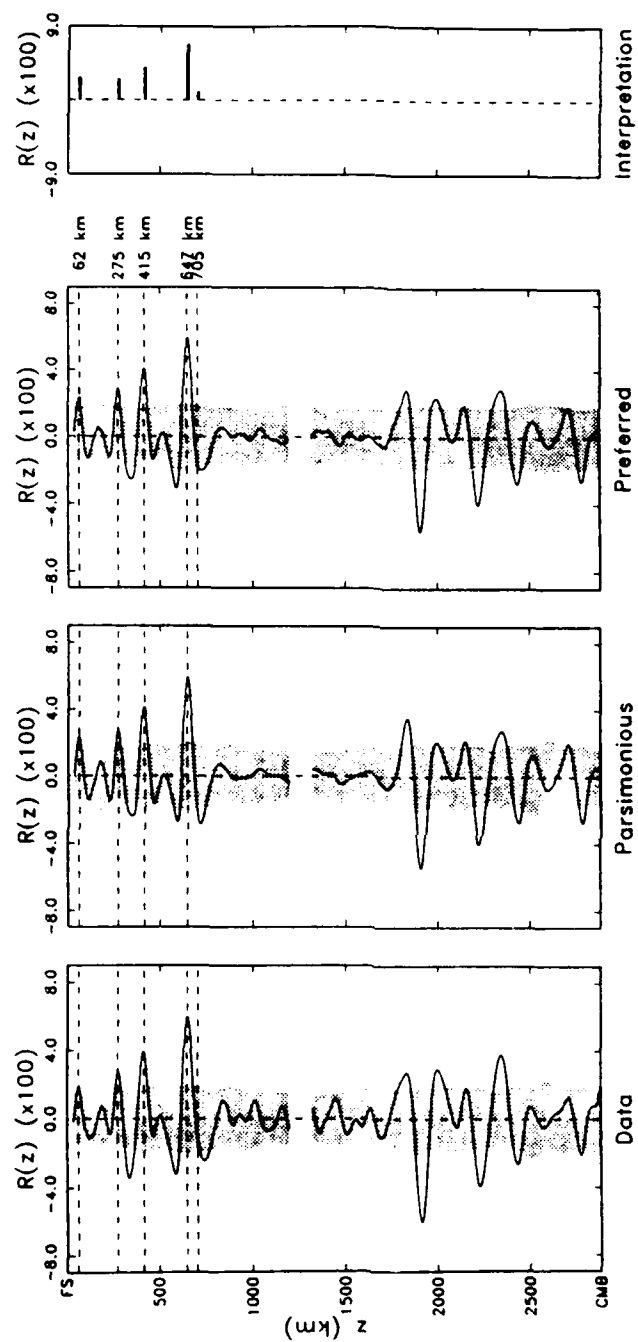
Figure 4.20

145

Figure 4.21

146

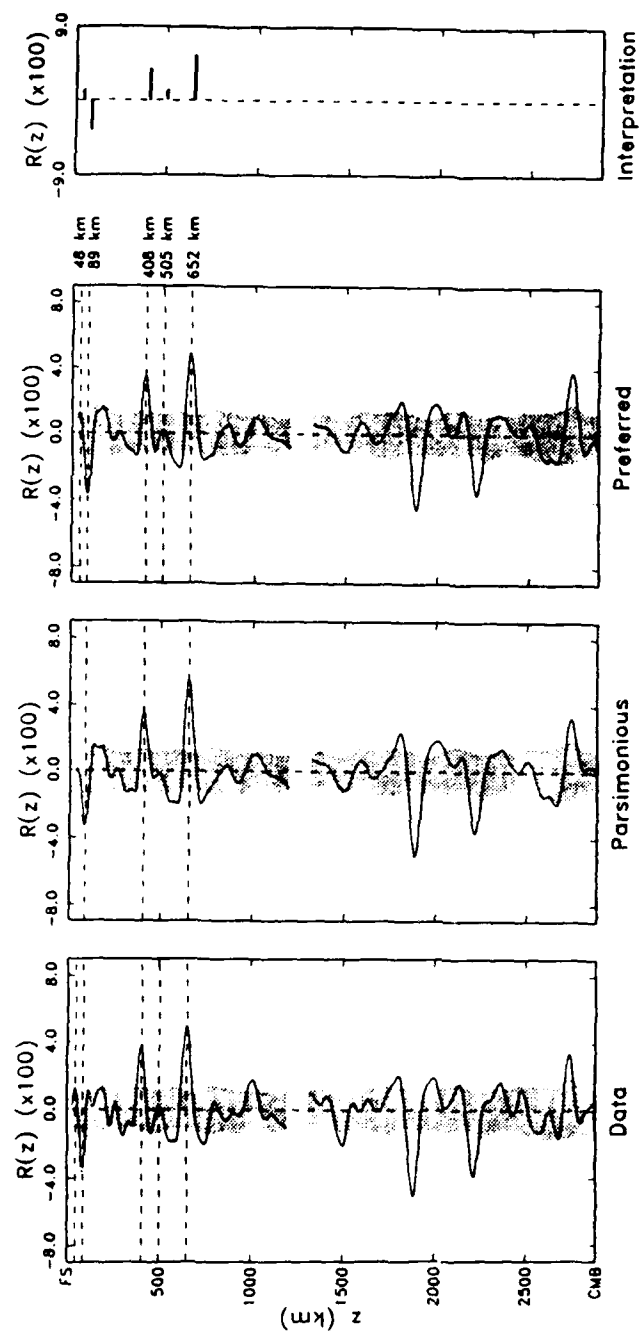Source Region: New Britain, Solomon Islands
Station: TATO (SRO)
Low Passed Filtered (Corner at 40 mHz, truncated at 60 mHz)
Seismograms in Stack: 9

Figure 4.22

147

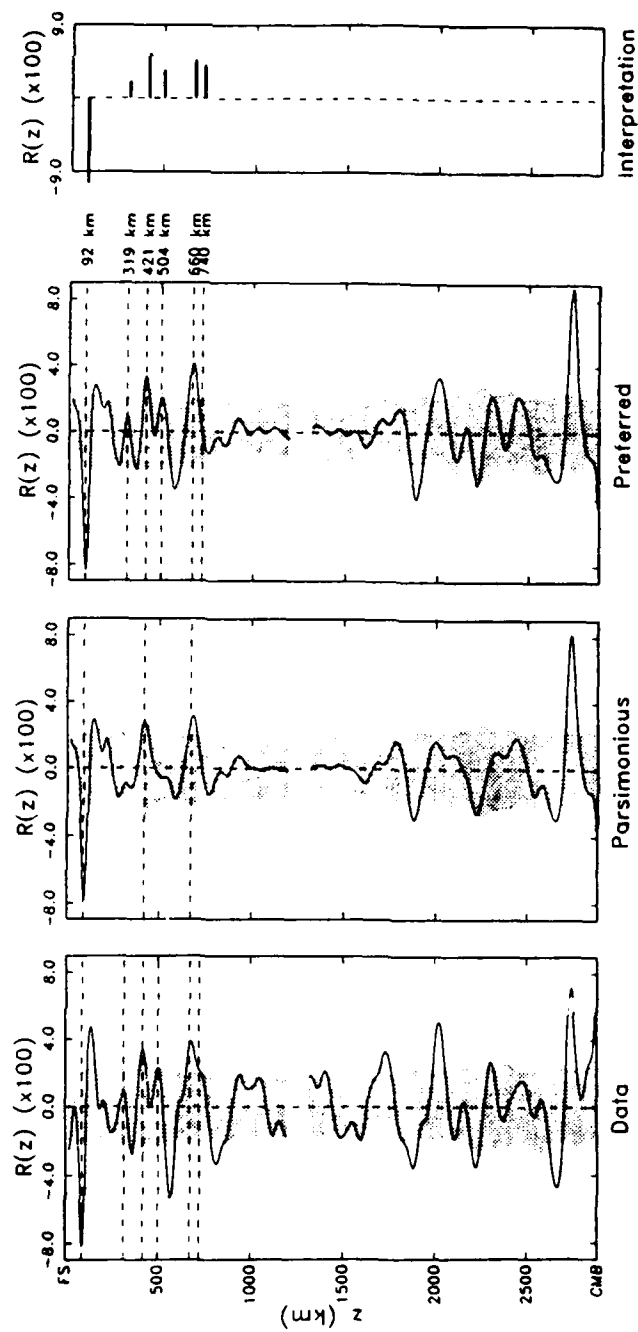Figure 4.23

148

CHAPTER 5

THE TRANSITION ZONE

INTRODUCTION

Abrupt increases in elastic wavespeed have been observed near depths of 400 km and 650 km in the Earth's mantle since the early 1960s. Unfortunately, the accumulation of 25 years of experimental and seismic data has not yet resolved a number of important questions about them: (1) Does the discontinuity at 400 km mark the transformation of the olivine component of the upper mantle to the modified-spinel structure [e.g., *Ringwood*, 1975], and/or a change in chemical composition [e.g., *Anderson and Bass*, 1986]? (2) Does the 650-km discontinuity represent a change in chemistry, the transition to perovskite structure, or both [e.g., *Liu*, 1979; *Lees et al.*, 1983]? (3) Can the 650-km discontinuity maintain a chemical boundary layer [e.g., *Ringwood*, 1982; *Ringwood and Irifune*, 1988] and does it serve as a brake to whole-mantle convective flow [e.g., *Schubert et al.*, 1975; *Richter*, 1979]? The answers to these questions have important implications for the chemical and dynamical history of the Earth.

Fundamental constraints on the nature of the transition-zone discontinuities can be obtained by measuring variations in their depth. Local velocity models derived for geographically-separated regions typically demonstrate 10–25 km variations in the depths of the 400-km and 650-km discontinuities [e.g., *Jordan*, 1979*b*]. Unfortunately, many of these studies lack significant depth resolution and few attempts have been made to measure lateral depth variations in a consistent fashion. This chapter builds upon the results of Chapter 4, utilizing mantle reverberations to detect topography on the transition-zone discontinuities. First-order reverberations are particularly amenable to this task. Their ray geometries offer uniform sampling of the transition zone, and the mantle in general, while their amplitudes are maintained for successive core reflections by the accumulation of

dynamic analogs. The latter property not only improves the SNR, but also allows us to address the statistical fluctuation of reflector depths encountered along the minor arc path.

"Migration" of first-order reverberations produces a profile of *SH* reflectivity, essentially a map of mantle reflectors. The location and amplitude of peaks in the $R(z)$ functions (Figures 4.6–4.23) provide accurate estimates of the apparent depths, z_i, and reflection coefficients, $R(z_i)$, of the major mantle discontinuities. The term "apparent" is used to denote the fact that the depth estimate is relative to the background velocity model used in migration. First-order reverberations alone are incapable of providing a direct estimate of depth, being sensitive only to the two-way, vertically-integrated travel time from the free surface (or CMB) to the discontinuity, denoted τ_z. Thus, before small variations of τ_z can be discussed in terms of discontinuity topography, it is necessary to apply corrections for heterogeneity occurring between seismic corridors. Potential sources of heterogeneity include variations in the path-averaged crustal thickness (z_M), surface bounce-point bathymetry, and lateral velocity heterogeneity in the mantle. As with τ_{ScS}, raw estimates of τ_z were adjusted to a canonical 33 km crustal thickness assuming a crustal velocity of 3.6 km/s and upper-mantle velocity of 4.5 km/s (the values assumed in crustal modeling using zeroth-order reverberations). Bounce-point bathymetry, estimated from the DBDB5 digital bathymetry database, was reduced to sea level using the same crustal velocity. The magnitude of both corrections was of order 2 s. A further correction, obtained by careful modeling of data with synthetic reflectivity profiles, was applied to account for bias in the depths of $R(z)$ peaks due to side-lobe interference and experimental geometry. The magnitude of this correction seldom exceeded 0.5 s. Estimates of $R(z)$ are also corrected for design bias via synthetic modeling. τ_z estimates for the 400-km and 650-km discontinuities (τ_{400} and τ_{650}, respectively) are compiled in Table 5.1.

TOPOGRAPHY ON THE 400-KM AND 650-KM DISCONTINUITIES

Variations in τ_{400} and τ_{650} between seismic corridors are on the order of 10 s, or 5%. From tests on synthetic data with realistic noise statistics we have estimated a 1.5-s standard error in the measurement of these times, which should not be increased dramatically by uncertainties in the crustal-thickness and bathymetry corrections. Given the assumed level of uncertainty, the dispersion of both τ_{400} and τ_{650} is significant when viewed on a path-by-path basis, implying some sort of heterogeneity between corridors, be it mantle velocity variations both above and below the discontinuities, topographic relief on the discontinuities themselves, or both. Separating these contributions is difficult, requiring us to estimate five quantities (the travel time through the upper mantle, transition zone and lower mantle, and the topography of the 400-km and 650-km discontinuities) from only three observables (τ_{ScS}, τ_{400}, and τ_{650}), a task which clearly cannot be accomplished without outside information. Some of this information can be gleaned from models of global mantle velocity heterogeneity derived by seismic tomography. There are, however, robust estimates of mantle heterogeneity which can be made from the three observables alone.

Transition Zone Travel Time

The data functional $\tau_{TZ} = \tau_{650} - \tau_{400}$ (two-way, vertical travel time through the transition zone) has the desirable property of being largely insensitive to lateral heterogeneity outside the transition zone which contaminates both τ_{650} and τ_{400} in a similar fashion. The 9.8-s variation observed in the τ_{TZ} estimates (Table 5.1) is therefore limited to the sum of transition-zone velocity variations and topography on the bounding discontinuities and is indicative of significant lateral heterogeneity. Assuming that the 400-km and 650-km discontinuities mark the transformations of olivine $\rightarrow$ β-spinel [e.g., *Ringwood*, 1975] and γ-spinel $\rightarrow$ perovskite + magnesiowüstite plus ilmenite $\rightarrow$ perovskite [e.g., *Ito and Yamada*, 1982], respectively, we can calculate the temperature

anomalies needed to generate the observed variations in τ_{TZ}. Specifically, we model the temperature derivative of τ_{TZ} as

$$\partial_T \tau_{TZ} = -2 \left[\frac{\overline{\tau}_{TZ}}{\overline{v}_s} \partial_T \overline{v}_s + \frac{\gamma_{400}}{v_s \partial_z P} \Big|_{z=400} + \frac{\gamma_{650}}{v_s \partial_z P} \Big|_{z=650} \right] \qquad (5.1)$$

where $\overline{\tau}_{TZ}$ and $\overline{v}_s$ are the mean transition-zone travel time and velocity, γ_{400} and γ_{650} the Clapeyron slopes of the 400-km and 650-km discontinuities, P is pressure and ∂ denotes the partial derivative with respect to the subscript. Estimates of the Clapeyron slopes are taken from *Suito* [1977], $\gamma_{400} = 3.5 \pm 1.5$ MPa/°C, and *Ito and Yamada* [1982], $\gamma_{650} = -2.0 \pm 1.5$ MPa/°C; the assumed temperature derivative of shear velocity is $\partial_T v_s = -0.44 \pm 0.1$ m/s°C (discussed later). Assuming that temperature anomalies are coherent in sign and magnitude across the transition zone, we calculate $\partial_T \tau_{TZ} = -0.048 \pm 0.013$ s/°C. In this model (Figure 5.1), raising the temperature of the transition zone pulls the bounding discontinuities closer together, decreasing the travel time between them. Although the reduction of ambient velocities partially counteracts this effect, $\partial_T \tau_{TZ}$ is dominated by discontinuity displacement, resulting in an overall decrease in the travel time through the transition zone for a temperature increase. The range of observed τ_{TZ} values is consistent with a long-wavelength temperature variation of 210 ± 45 °C going from the Philippines-GUMO (corridor 6 in Table 2.2) and Tonga-CTAO (5) corridors, inferred to be cold, to the Philippines-NWAO (11) and Sumba-NWAO (13) corridors, inferred to be hot, with 20 ± 7 km of thermally-induced topography on the 400-km discontinuity and 10 ± 8 km on the 650-km discontinuity. Similar temperature variations are implied by models of long-wavelength, three-dimensional mantle heterogeneity [e.g., *Woodhouse and Dziewonski*, 1984; *Nataf et al.*, 1986; *Tanimoto*, 1987, 1988], and are plausible for a mantle-wide convective flow system, so the data require no chemical inhomogeneity in the transition zone. In the next section we attempt to isolate the signatures of topography predicted by this simple model in the individual estimates of τ_{400} and τ_{650}, or equivalently τ_{LM} (two-

way, lower-mantle travel time), by applying corrections for known, long-wavelength mantle heterogeneity.

Corrections for Mantle Heterogeneity

Since detailed regional velocity models were not available for most of the seismic corridors studied, we decided to use models M84C of *Woodhouse and Dziewonski* [1984] and L02.56 of *Dziewonski* [1984] to calculate corrections for mantle heterogeneity, and the model of *Morelli and Dziewonski* [1987] to account for topography on the core-mantle boundary (CMB). In Figure 5.2 we compare crustal-corrected, whole-mantle vertical travel times, τ_{ScS}, versus the sum of delays predicted by the tomographic models. τ_{ScS} estimates are obtained by waveform inversion of zeroth-order reverberations on a corridor-by-corridor basis and are accurate to within $\pm$ 0.3 s. Since τ_{ScS} averages mantle heterogeneity along the minor arc similarly to τ_{400} and τ_{650}, but is much less sensitive to discontinuity topography, it provides an ideal test of the applicability of the mantle heterogeneity models. Because L02.56 is a *P*-wave derived model, it is necessary to assume a scaling between *P*- and *S*-wavespeed perturbations, which we take as $\delta v_s = 1.1$ δv_p, consistent with recent normal-mode splitting and tomography results [e.g., *Jordan and Lynn*, 1974; *Dziewonski and Woodhouse*, 1987; *Giardini et al.*, 1988] (q.v., *Anderson*, [1987b]). We find that the correlation between data and predicted delays is significant at greater than the 99% confidence level, but that the mantle models underestimate the extent of path-averaged heterogeneity by a factor of $m = 1.1 \pm 0.1$, where m is obtained from non-linear regression allowing for errors in both the observed and model-predicted delays (omitting corrections for CMB topography results in $m = 1.3$, but no decrease in variance reduction). A priori standard errors for τ_{ScS} were set to 0.3 s except for the Tonga-Fiji to KIP corridor (8), which was downweighted to allow for more uniform data importance (τ_{ScS} for this corridor is significantly removed from the mean). An a posteriori estimate of

1.3-s standard error for the model-predicted delays was obtained by requiring reduced χ^2 to equal the asymptotically expected value of 1 [e.g., *Jeffreys*, 1961].

That $m > 1$ is not unexpected since the tomographic models were derived by overdamped inversion and likely underestimate the amount of long-wavelength heterogeneity present in the mantle. Furthermore, because the shortest wavelengths included in these models are comparable to, or longer than, our typical epicentral ranges, a significant portion of the heterogeneity wavenumber spectrum remains unmodeled. However, the strong correlation of data and model-predicted delays suggests that the tomographic models correctly predict the geographic variation of τ_{ScS}, justifying their use in computing mantle heterogeneity corrections, and indirectly lending support to observations of large $\delta(\ln v_s)/\delta(\ln v_p)$ ratios in the lower mantle. In order to explain the full range of observed delays, all corrections are multiplied by $m = 1.1$.

Corrections for τ_{400} and τ_{650} were calculated by averaging along the minor-arc path the M84C predicted delay from the base of the crust (33 km) to the depth of the respective discontinuity. Because we are attempting to isolate the signature associated with discontinuity topography there is some concern that these corrections, which themselves include delays due to topography, will introduce bias into our results. Fortunately any such bias will be small relative to the expected signal level since travel time delays encountered by a wave propagating perpendicularly through a boundary perturbed by δz are of order $\delta z \delta v_s / v_s^2$, where δv_s is the change in velocity across the boundary, whereas the delay for a reflected wave is of order $\delta z / v_s$, a factor of $v_s / \delta v_s$ greater (≥ 10 in the Earth's mantle).

Regional Variation of τ_{400} and τ_{650}

After applying corrections, τ'_{400} and τ'_{650} (where the prime denotes a time corrected for mantle heterogeneity) were mapped to discontinuity depth using the Preliminary Reference Earth Model (PREM) of *Dziewonski and Anderson* [1981]. The geographic variation of

apparent depths is shown in Figure 5.3. We have assigned a standard error to these estimates of 10 km, due in large part to corrections for lateral heterogeneity. The inferred variation of depth is 23 km for the 400-km discontinuity and 27 km for the 650-km discontinuity (reduced to 18 km if the low-signal-quality, Philippines-TATO corridor (15) is omitted). However, due to the large uncertainties involved in the corrections for mantle heterogeneity, this evidence for discontinuity topography, taken alone, is not highly convincing. More compelling evidence of discontinuity topography comes from the correlation of τ'_{LM} (two-way travel time through the lower mantle, corrected for lower-mantle heterogeneity and CMB topography) and τ_{TZ} (coefficient of correlation $r = -0.78$), and τ'_{400} and τ_{TZ} ($r = -0.65$); see Figure 5.4. Both correlations are significant at greater than the 99% confidence level, strongly suggesting that there is an appreciable topographic component to τ_{TZ}, since neither τ'_{400} or τ'_{LM} should be affected by velocity variations within the transition zone. The topography estimated from the corrected travel times τ'_{400} and τ'_{LM} is consistent with that predicted by the model of a transition zone bounded by phase transitions (equation 5.1), although noticeably greater for the 650-km discontinuity—a point to which we return to later. Also in agreement is the correlation of τ'_{LM} and τ'_{400} ($r = 0.35$, significant at the 80% level), which, although weak, suggests that topography on the 400-km and 650-km discontinuities is anticorrelated, consistent with the assumption that the two discontinuities have Clapeyron slopes of opposite sign. A similar result was obtained by *Romanowicz and Allegre* [1979] from observations of subcontinental velocity variations in North America.

Following the analysis of τ_{ScS}, we have computed regionalized estimates of τ'_{400} and τ'_{650}. The results are consistent with little or no surface-tectonic correlations of these quantities, implying that lateral temperature variations at shallow depths, revealed by τ_{ScS} and Q_{ScS}, attenuate with depth, and are small compared to ambient heterogeneity by 400 km depth. Deep "keels," or roots, beneath stable continental blocks are observed to extend to depths at least this great. Given the lack of correlation with the depth of the 400-km

discontinuity, these keels do not appear to be primarily thermal in origin, and as such, may be indicative of deep-seated compositional heterogeneity.

Correlation of τ_{TZ} and τ'_{400}

Figure 5.4 reveals an apparent bimodal nature to the correlation of τ_{TZ} and τ'_{400}. Use of Hostelling's T^2 test [e.g., *Harris*, 1975] shows that the clustering of fast and slow transition zones is significant at greater than the 99% confidence level. Geographically, corridors in the fast transition-zone category lie on the eastern and western peripheries of the study area (Figure 5.3) and display strong spatial coherence. τ_{TZ} correlates well with low-degree, transition-zone travel-time delays calculated from model M84C (degrees 2 through 4), with the level of correlation decaying as higher degree heterogeneity is included. A strong degree 2 component of transition-zone heterogeneity has been observed by *Masters et al.* [1982] and *Romanowicz et al.* [1987], and is well modeled by M84C. That the correlation of τ_{TZ} and M84C-predicted delays decays at higher wavenumbers may be indicative of the limited resolution, both horizontal and vertical, of M84C. The model of temperature-induced transition-zone heterogeneity predicts a travel time delay for transmitted waves, such as computed from M84C, of only $\partial_T(\delta\tau_{TZ}) = 0.009$ s/°C, compared to $\partial_T\tau_{TZ} = -0.048$ s/°C predicted for transition-zone travel time as measured by first-order reverberations (i.e., as sensed by reflected phases). The 210° C temperature variation inferred from τ_{TZ} predicts less than 2 s variation in delays for transmitted waves. Although this is roughly the level of variation found for model M84C, a signal this small could easily be overprinted by other sources of heterogeneity, such as non-uniform temperature anomalies (an assumption of the phase-transition model) or small variations in composition. At present, the significance of τ_{TZ} clustering is unclear, however the geographical variation does lend support to the hypothesis of a strong degree-2 component of heterogeneity in the transition zone, a hypothesis which has met with some opposition [e.g., *Smith and Masters*, 1989].

Average τ'_{400} and τ'_{650}

τ'_{400} and τ'_{650} provide constraints on mantle structure that are difficult, if not impossible, to obtain through other means. For instance, global average values would provide an ideal means by which to constrain the depths of the transition zone discontinuities in the construction of radial Earth models. Unweighted averaging of the estimates obtained for the 18 seismic corridors of this study gives $\tau'_{400} = 185.8$ s and $\tau'_{650} = 279.5$ s, corresponding to apparent average depths of 414 km and 660 km relative to the PREM (employing a 33 km crust, $v_s = 3.6$ km/s). By way of comparison, the corresponding times for the PREM are 180.2 s and 282.9 s, respectively. Unfortunately, our sampling of the mantle is not global in extent, and the results of the previous section suggest that the averages computed from our observations of τ'_{400} and τ'_{650} may be biased from the true global averages. Although we could conceivably reduce this bias by assigning varying weights to the individual observations, we know of no satisfactory a priori way of doing so. Greater global data coverage is currently possible if shallower earthquake sources are used. Although typically associated with lower signal-to-noise ratios, the greater numbers of shallow earthqua'.es may allow them to be used in this application.

Splitting of First-Order Reverberations

Because first-order reverberations densely sample the mantle along the minor arc, τ'_{400} and τ'_{650} are estimators of the true minor-arc path average. Variations of these quantities between seismic corridors are therefore isolated samples of the long-wavelength heterogeneity of the transition zone. Lateral heterogeneity encountered along a seismic corridor by the various analogs of a first-order reverberation will result in travel-time perturbations that "split" the dynamic ray family, and introduce variations in the mean travel

times of individual ray families. Observations of reverberation splitting can provide constraints on heterogeneity with length scales shorter than the minor arc.

Because the inversion process averages over many reverberation families, a peak in the reflectivity profile should resemble the expected value of the cross correlation between split- and unsplit-reverberation multiplets, mapped into depth as discussed in conjunction with equation (3.14). Perturbations to the travel times of first-order reverberations are likely to arise from many sources of heterogeneity, leading us to expect the sum to be approximately normally distributed with standard deviation σ. Given this assumption, it can be shown that the expected value of the cross correlation of split- and unsplit-reverberation multiplets is

$$< \varphi(\tau) > \, = \frac{1}{\sigma \sqrt{2\pi}} \int_{-\infty}^{\infty} \varphi_0 (\tau - t) \exp (-t^2 / 2\sigma^2) \, dt \qquad (5.2)$$

where φ_0 is the autocorrelation of the unsplit family. Figure 5.5 depicts the increase in width and decrease in peak amplitude expected for the case where φ_0 is the autocorrelation of a pulse with a Gaussian power spectrum, characterized by a center frequency of 30 mHz and 15-mHz half width, an approximation we have found to provide a good fit to synthetic autocorrelations. The decay of the peak amplitude with increasing σ is significant, with $\varphi(0)$ reduced to 75% of $\varphi_0(0)$ for σ as low as 4 s.

The decay of peak amplitude, $\varphi(0)$, depends strongly on the characteristic width of reverberation waveforms, becoming increasingly strong as center frequency increases and the ratio of waveform width to σ decreases. Thus, by examining the low-frequency component of first-order reverberation waveforms, we can obtain an estimate of R that is largely unbiased by lateral heterogeneity, while at higher frequencies the rolloff of apparent R provides a measure of σ. By computing $R(650)$ in narrow frequency bands and comparing it to theoretical rolloff curves parameterized by σ, we have estimated the standard deviation of first-order reverberation travel times, $\sigma_{650} = 4.0 \pm 1.0$ s (Figure 5.6).

This analysis ignores variations in σ_{650} between seismic corridors, and as sampled along a single corridor by reverberations of different core-reflection number n and ray geometry. While the second effect is likely of little import owing to the extensive averaging of heterogeneity indigenous to first-order reverberations, the necessity of grouping observations from many seismic corridors to obtain a stable estimate of σ_{650} means that nonstationarity from corridor to corridor cannot be assessed. Unfortunately a similar estimate cannot be made for the 400-km discontinuity due to lower signal-to-noise ratios and interference from the side-lobes of the stronger 650-km discontinuity.

Intermediate Wavelength Topography

σ_{650} is composed of a sum of delays due to mantle heterogeneity (essentially that sampled by ScS_n) and delays due to topography on the 650-km discontinuity. The mantle component can be estimated from the standard deviation of ScS_n travel times (~2 s) obtained from waveform inversion, leaving between 2 s and 3.5 s attributable to topography, depending on whether the two sources of heterogeneity are correlated (i.e., whether they should be added linearly or quadratically). Because unmodeled complexities in crustal structure and source-time functions, and the finite transition width of the 650-km discontinuity will mimic splitting by degrading the correlation of data and synthetic waveforms, we regard the estimate of σ_{650} as an upper bound, leading to a conservative estimate of the two-standard-deviation level of peak-to-peak topography on the 650-km discontinuity of ≤ 40 km, over the wavelength interval of ~300 km (first Fresnel zone) to ~1500 km (one-half of the average epicentral distance). These results are consistent with topography estimates made from between-path variations of τ_{650} and studies of converted [e.g., *Paulssen*, 1985; *Vinnik et al.*, 1983] and reflected phases [e.g., *Kind et al.*, 1988], and imply an upper limit of ~30 km for topography on the 650-km discontinuity at wavelengths greater than 300 km–an amount easily accommodated by the model of thermally-induced topography.

159

Conversely, the amount of topography predicted for the 650-km discontinuity in a rigorously-stratified mantle is significantly greater than observed. In this scenario, the boundary between the upper and lower mantle is deflected to compensate the mass excess of downgoing slabs beneath regions of subduction. From force-balance and dynamical calculations [e.g., *Hager and Raefsky*, 1981; *Christensen and Yuen*, 1984], it is found that slab-induced topography can easily exceed 100 km. In this study we have sampled the majority of currently active deep subduction zones. Compared with regions considered free of recent subduction, the depth of the 650-km discontinuity varies by less than 30 km. While the allowances made for mantle heterogeneity are crude we would not expect them to cause us to underestimate topography by more than a factor of, say, 1.5. If greater topography is present in the regions being sampled it must be occurring on a length scale comparable with, or shorter than, the first Fresnel zone of the first-order reverberations employed (~300 km). Observations of P waves converted to S (and vice versa) by the 650-km discontinuity beneath subducting slabs provide constraints on shorter-wavelength topographic relief. The studies of *Barley et al.* [1982], *Bock and Ha* [1984] and *Richards and Wicks* [1987] imply an upper limit of 50 km of topography between the Izu-Bonin and Tonga-Fiji subduction zones, and along the strike of the Tonga slab. The seismological constraints on discontinuity topography, together covering more than a decade in wavenumber, argue persuasively against a compositional origin for the 650-km discontinuity.

REFLECTION COEFFICIENTS

Low-Frequency Estimates

Estimates of the reflection coefficients of the 400-km and 650-km discontinuities, unbiased by splitting, can be obtained by examining $R(z)$ in the limit of zero frequency. For the composite data set $R(650) = 0.072 \pm 0.01$, obtained by assuming $\sigma_{650} = 4.0$ s and extrapolating the 6.0-mHz estimate to zero frequency. Because we were unable to obtain

stable, low-frequency estimates of σ_{400}, a similar analysis for $R(400)$ is not possible. However, by assuming $\sigma_{400} = \sigma_{650}$ and extrapolating the full-bandwidth estimate of the reflection coefficient to zero frequency, we find $R(400) = 0.046 \pm 0.01$. Because the mantle component of heterogeneity is similar for first-order reverberations from the 400-km and 650-km discontinuities, as is the amount of long-wavelength topography observed between seismic corridors, the assumption that $\sigma_{400} = \sigma_{650}$ would seem to be reasonable. Our estimate of $R(400)$ falls within the range of most recent model values ($0.04 \leq R(400) \leq 0.06$) [e.g., *Gilbert and Dziewonski*, 1975; *Dziewonski and Anderson*, 1981; *Grand and Helmberger*, 1984; *Lerner-Lam and Jordan*, 1987].

$R(650)$ is also in good agreement with previously-published model estimates, which range from 0.07 to 0.09. Another direct observation of $R(650)$, in this case for P waves, is obtained from the amplitude ratio $P'650P'/P'P'$ (where $P'650P'$ is a bottomside reflection from the 650-km discontinuity; $P' = PKP$). Estimates of $R(650)$ found in this way are frequently as much as a factor of two greater than model-predicted values [e.g., *Lees et al.*, 1983]. However, these results, and the spatially-intermittent nature of $P'650P'$ observations, can be reconciled with our estimate of $R(650)$ by imposing 25 km of 300-km-wavelength topography on the 650-km discontinuity [*Kind et al.*, 1988] (see also *Paulssen* [1988])—commensurate with the amount of topography predicted by both τ'_{650} and σ_{650}.

Regional Variation of R(650)

Although individual estimates of the low-frequency asymptote of $R(650)$ are subject to considerable uncertainty, we note a curious correlation between the 6-mHz center-frequency estimate of $R(650)$ with τ'_{LM} (or equivalently τ'_{650}), a correlation nominally significant at the 97% confidence level (see Figure 5.7). This result can be explained by, but by no means requires, the presence of a cold and dense chemical boundary layer (CBL) trapped on the 650-km discontinuity. Being cold, a CBL would depress an endothermic 650-km transition and reduce the effective contrast in material properties across it by

displacing slower, more buoyant, upper mantle. This would result in smaller values of $R(650)$ being associated with deeper 650-km discontinuities, consistent with the observed correlation, and might also explain the apparently large value inferred for the Clapeyron slope of the 650-km discontinuity from observations of τ'_{400} and τ'_{650} (which imply $|\gamma_{650}| > \gamma_{400}$) by localizing strong temperature anomalies near the 650-km discontinuity–violating the assumption of uniformity throughout the transition zone. Assuming that seismic corridors with shallower apparent 650-km discontinuities are not supporting CBLs, the associated estimates of $R(650)$ provide a constraint on the intrinsic change of material properties across the phase transition. Exclusion of corridors with apparent depths to the 650-km discontinuity greater than 660 km raises the estimate of $R(650)$ to 0.084 ± 0.02, which lies nearer the upper end of model-predicted reflection coefficients.

Assuming variation of $R(650)$ is due to the thermal equilibration of a gravitationally-trapped CBL residing on the 650-km discontinuity (as in the "megalith" model of *Ringwood* [1982]), it is possible to estimate the lateral temperature anomalies existing within the layer. For normally-incident, *SH*-polarized waves

$$ R \approx \frac{1}{2}\left[\delta \ln v_s + \delta \ln \rho \right] \tag{5.3} $$

Assuming $\partial_T(\delta v_s) = \partial_T v_s$ and $\partial_T(\delta \rho) = \partial_T \rho$ (in other words, that the temperature derivatives of shear modulus and density for the two media are similar), then to first order in δv_s and $\delta \rho$

$$ \partial_T R \approx \frac{1}{2}\left[\partial_T \ln v_s + \partial_T \ln \rho \right] \tag{5.4} $$

In evaluating the effect of temperature on τ_{TZ} (equation 5.1), we assumed $\partial_T v_s = -0.44$ km/s°C, obtained from the relation

$$ \partial_T v_s = -\alpha \rho \partial_\rho v_p \frac{\delta v_s}{\delta v_p} \tag{5.5} $$

162

where α is the coefficient of thermal expansion ($2.5 \cdot 10^{-5}$/°C [*Jeanloz and Thompson*, 1983]), and $\delta v_s/\delta v_p$ the ratio of shear- and compressional-wavespeed variations (1.1, as discussed in relation to corrections for mantle heterogeneity). The remaining term, $\partial_\rho v_p = 4.0$ m^4/kgs, relating density and compressional-wavespeed perturbations, was chosen to be consistent with geoid constraints on lower-mantle density variations [*Hager et al.*, 1985]. Recent seismic evidence suggests that a similar value of $\partial_T v_s$ holds within subducted lithosphere [*Creager and Jordan*, 1986]–the most probable source of CBL material. Combining terms gives $\partial_T R(650) = 5.0 \cdot 10^{-5}$/°C. $R(650)$ is observed to vary by ~0.035, or ~40%, consistent with a total temperature variation of $\Delta T \sim 695$° C. Although the probable uncertainties in this analysis are large (on the order of ± 300° C), we note that temperature contrasts as high as 700° C may exist between the core of mature subducted lithosphere (such as the Marianas) and ambient mantle at 650 km depth [e.g., *Creager and Jordan*, 1986], thus our estimate appears reasonable. The laboratory value of $\gamma_{650} = -2.0$ MPa/°C [*Ito and Yamada*, 1982] predicts 32 km of thermally-induced topography on the 650-km discontinuity for $\Delta T = 695$° C, in reasonable agreement the total topographic relief inferred from τ'_{650}.

Although the geographic variability of depth and strength of the 650-km discontinuity can be explained by the presence of a gravitationally trapped CBL, the analysis relies heavily on uncertain estimates of low-frequency $R(650)$ and $\partial_T v_s$, and must be approached with some skepticism, especially in light of the difficulty in trapping, and maintaining, a chemical boundary layer in the midmantle [*Christensen*, 1988; *Richards and Davies*, preprint]. An alternative explanation appeals to the curvature of the 650-km discontinuity as it is thermally deflected in the vicinity of cold subducting slabs. If the inclination to the horizontal is sufficiently large, reflections produced at the discontinuity will not stack coherently, similar to out-of-plane energy in two-dimensional seismic migration. Excluding corridors whose sampling of the transition zone is most concentrated in regions of active deep subduction reduces the significance of the correlation between $R(650)$ and

163

τ_{LM} to a near-zero level. Although it is difficult to precisely gauge the amplitude reduction expected from discontinuity curvature, a simple calculation suggests that 40 km of 100-km wavelength topography would be capable of producing the observed variation in $R(z)$ (more generally, topography on the order of 40% of the horizontal wavelength is required). Given the previous observations of discontinuity topography, this would seem to be a reasonable hypothesis, suggesting that if not the sole cause, this mechanism at least contributes to the observed correlation. Unfortunately, using reverberations originating at the 650-km discontinuity alone, it is not possible to unambiguously distinguish between these two, competing, hypotheses. A potentially diagnostic observation would be evidence of reflections from the upper boundary of the CBL, should such a boundary layer exist. Unless the upper boundary is highly irregular or diffuse we would expect to see its signature in the mantle reflectivity profiles. In the following section we document the search for additional discontinuities in the transition zone.

OTHER REFLECTORS?

Modeling and Resolution

Experimental and theoretical results of high-pressure mantle petrology predict a number of minor phase transitions in the depth range of 400–1000 km, some of which may be capable of producing observable seismic discontinuities. Identification of these discontinuities in the mantle would provide valuable constraints on the composition and thermal state of the transition zone. First-order reverberations provide an ideal tool with which to search for the impedance contrasts associated these discontinuities, whose signatures in the travel times and amplitudes of direct arrivals and triplicated phases would be obscured by the much stronger 400-km and 650-km discontinuities. In this section we present evidence for three additional discontinuities, occurring at mean depths of 530 km, 730 km and 915 km, which may be present throughout the data set, and perhaps global in extent.

Evidence for these reflectors comes from two, non-independent, sources. The preferred synthetic reflectivity profiles of Figure 4.6–4.23 contain these discontinuities where apparent in data, and provide our most direct line of evidence. However, the resolution available given the small number of seismograms sampling a single seismic corridor (between 5 and 20) is limited, typically of the order of $R(z) \geq 2–3\%$. In many cases we have chosen to model features of the profiles which are nominally beneath this formal resolution threshold, justified by the consistency of the inferred reflectors from corridor to corridor. The alternative is to seek improved resolution by stacking profiles from many seismic corridors; an operation, which for the entire 18-profile suite, can produce as much as a four-fold improvement over the resolution attainable along a single corridor. Doing so, however, will damp the signature of any discontinuity with apparent topography much greater than roughly one-eight of the local seismic wavelength, analogous to the effects of splitting along a single seismic corridor. We appeal to both methods when possible, finding evidence for the three additional transition-zone discontinuities in each.

Figure 5.8 presents the results of stacking the entire 18-corridor suite of data and parsimonious synthetic profiles (Figures 4.6–4.23). While the synthetics contain a number of reflectors in the upper 300 km of the mantle, no reflectors other than the 400-km and 650-km discontinuities are included in the synthetic profiles in the depth range of 300–1000 km. The residual profile contains evidence for two additional peaks in this depth range that are nominally significant at the 95% confidence level, located near 515 km and 710 km. A third minor peak at 915 km, characterized by $R(z) = 0.45\%$, lies just below the formal 95% confidence threshold, being significantly non-zero at approximately the 90% confidence level.

The 530-Km Discontinuity

The depth and magnitude of the 515-km deep peak are robust with respect to omission of significant portions of the data set, and a similar discontinuity is observed in the majority

of individual data profiles (15 of the 18 total profiles). As modeled in the preferred synthetic profiles, the reflector appears as a greater-than-expected backswing (relative to the parsimonious profile) between the side-lobes of the 400-km and 650-km discontinuities. Although this is a minor feature of data, it is remarkably consistent from profile to profile, and unlikely to be an experimental or numerical artifact. An essentially similar discontinuity was included in 13 of the 18 profiles obtained in this study. Given the low inferred amplitude of the reflector, its presence in profiles for which we have chosen not to model it explicitly cannot be conclusively ruled out, and it may well be a ubiquitous feature of the transition zone.

There are significant trade-offs between the estimated depth and severity of this feature, making it difficult to obtain reliable estimates of either; however, the mean reflection coefficient of 0.013 ± 0.004 and depth of 525 ± 30 km are thought to be reliable. The large standard deviation in depth is the likely reason why the discontinuity does not appear as strongly in the multiple-profile stack of Figure 5.8. The apparent depths of this discontinuity do not display any tectonic correlation, nor do they correlate with the depths of the 400-km and 650-km discontinuities. Whether this is due to the large measurement uncertainty in these quantities, estimated at ± 20 km, cannot be tested directly but must be considered a distinct possibility. References to similar discontinuities in velocity, or its first derivative, can be found in the literature [e.g., *Helmberger and Wiggins*, 1971; *Helmberger and Engen*, 1974; *Fukao*, 1977; *Hales et al.*, 1980], and have been observed as precursors to $P'P'$ [*Whitcomb and Anderson*, 1970], suggesting that the transition to higher impedance is localized over a narrow depth extent.

There are several possible mineralogical explanations for this discontinuity, including: the phase transition of β-spinel $\rightarrow$ γ-spinel in olivine [e.g., *Suito*, 1977; *Weidner et al.*, 1984], the high-pressure boundary of the pyroxene-garnet solid solution [e.g., *Akaogi and Akimoto*, 1977], the aluminous garnet $\rightarrow$ ilmenite phase transition [e.g., *Liu*, 1977], or any of the numerous reactions in Al_2O_3-poor pyroxene mineralogies [e.g., *Jeanloz and*

166

Thompson, 1983; *Liu and Bassett*, 1988, and references therein]. For reasons to be detailed, none of these candidate reactions provides an entirely satisfactory match to the observations, although the first reaction appears most likely.

From measurements of single-crystal elastic properties, *Weidner et al.* [1984] concluded that the phase transition from β-spinel to γ-spinel in forsterite (Mg_2SiO_4) was both too broad, and associated with too small a change in acoustic velocity to produce an observable discontinuity. Their results are consistent with a reflection coefficient of 1.6% at STP for a zero-width discontinuity in a pure olivine mantle—commensurate with our observations. However, when corrections are made for the percentage of olivine expected in the mantle (probably less than 70 vol.%), and the 40-km width of the two-phase region [*Suito*, 1977], the predicted value is reduced to 0.8% (Figure 5.9). Allowing for the est splitting of first-order reverberations raises our estimate of $R(530)$ to 1.6%, which, although likely biased high by the omission of non-observations, is significantly greater than the predicted value. Thus unless we have consistently overestimated the strength of this reflector, or the two-phase region is narrower than determined experimentally, the inferred discontinuity may be too large to be explained entirely by the phase transition of β- to γ-spinel. In this context, we note that the experimental constraints on transition width, especially for appropriate mantle compositions, are weak.

Similar difficulties are encountered in attempting to attribute the discontinuity to solid-solution reactions in the pyroxene-garnet (majorite) system. Although there is not complete agreement on the pressure and temperature range of equilibrium, it appears that the transition of aluminous pyroxene to garnet is too broad to produce an observable discontinuity [e.g., *Bina and Wood*, 1984; *Irifune*, 1987]. In contrast to these results, *Liu* [1977] suggests that the transition of garnet to ilmenite may be as sharp as 20 km. The zero-pressure density increase of this reaction is of order 8%. If garnet constitutes some 20% of the mantle by volume near 500 km depth and assuming a Birch's-Law scaling of v_s to ρ perturbations holds [e.g., *Anderson et al*, 1968], this reaction is potentially capable of

producing a reflector as large as $R = 2\%$. While this is certainly large enough to explain our observations, it is not clear that this reaction occurs within the appropriate pressure and temperature range [e.g., *Ito and Takahashi*, 1987; *Takahashi and Ito*, 1987; *Akaogi et al.*, 1987]. Lastly, while a number of reactions are predicted for Al_2O_3-poor pyroxene, such as $2MgSiO_3 \rightarrow \beta$-$Mg_2SiO_4 + SiO_2$, they are unlikely to produce an observable discontinuity owing to extremely broad two-phase regions [e.g., *Akaogi et al.*, 1987], and may not occur at all--depending critically on the Al_2O_3 content of the mantle [*Liu*, 1977].

Recent reconnaissance determinations of the high-pressure phase transformations in diopside offer a potential resolution to this problem. At pressures on the order of 20 GPa (corresponding to depths near 550 km), $CaMgSi_2O_6$ (diopside) transforms to a mixture of Mg_2SiO_4 (spinel), SiO_2 (stishovite), and $CaSiO_3$ (perovskite), the latter characterized by an unusually-large bulk modulus [e.g., *Ito and Takahashi*, 1987; *Irifune et al.*, 1989]. Diopside may constitute up to 12 vol.% of the mantle at these depths; if the transformation occurs over a sufficiently narrow depth range, this reaction may be capable of producing, or contributing substantially to, the 530-km discontinuity--although more detailed work will need to be done to confirm this conjecture.

The 730-Km Discontinuity

The difference between data and synthetic profiles (Figure 5.8) indicates a second peak in $R(z)$, located near 710 km depth, and interpreted as an abrupt 1.5–3% increase in shear-wave impedance ($R(z) \sim 0.75$–1.5%) ~60 km beneath the 650-km discontinuity. The seismic literature contains numerous references to discontinuities near this depth [e.g., *Hart*, 1975; *Datt and Muirhead*, 1976; *Fukao*, 1977; *Muirhead and Hales*, 1980], which may be related to the slope change in the uppermost portion of the PREM lower mantle. *Sobel* [1978], using precursors to $P'P'$, also finds evidence for a second reflector separated by ~50 km from the 650-km discontinuity.

From modeling of reflectivity profiles on a corridor-by-corridor basis (Chapter 4), we have found evidence for this discontinuity in 7 of 18 profiles. As with the 530-km discontinuity, the exact placement of this reflector trades off strongly with inferred strength, with the latter being very difficult to constrain due to interaction with the strong side-lobe of the 650-km discontinuity. The mean reflection coefficient and depth are 0.015 ± 0.008, and 742 ± 15 km, respectively, close to the values obtained by stacking the entire suite of reflectivity profiles, suggesting that the discontinuity may be common to the data set as a whole (as a compromise, we have chosen to refer to this reflector as the 730-km discontinuity in what follows). Possible mineralogical explanations for this feature include: (1) the ilmenite → perovskite phase transition [e.g., *Liu*, 1977], (2) changes in the crystal symmetry system of perovskite [e.g., *Wolf and Bukowinski*, 1985], or (3) an additional, high-pressure transformation of perovskite [*Park et al.*, 1988]. (Note that we can rule out depression of the 650-km discontinuity in the slab beneath the source as a possible origin of the 730-km discontinuity. Although the results of the previous section suggest that such depression does in all likelihood occur, the transition would be inclined at too great an angle to the horizontal to stack coherently.)

Pursuing explanation (1), $R(730) = 1.5\%$ implies an intrinsic impedance increase of 15% for a mantle consisting of 20% ilmenite. Assuming $\delta(ln\rho)/\delta(lnv_s) \sim 0.7$, an approximation which holds for the 400-km and 650-km discontinuities, gives a 8.3% increase of velocity and 5.8% increase in density across the transition—a lower bound owing to heterogeneity-induced splitting, and subject to large uncertainty. *Liu* [1977] measured a 7.4% change in zero-pressure density for the transformation to perovskite structure, a value which agrees well with our estimate. The stability field of ilmenite is predicted to extend several GPa beyond that of γ-spinel [*Ito and Yamada*, 1982], in good agreement with the observed mean depth, thus this reaction seems to offer a plausible explanation of our data. On a much more speculative basis, we note that a strong positive correlation of depth to the 730-km discontinuity with the depth of the 530-km discontinuity is observed, with nearly equal

amounts of apparent topography for both discontinuities along paths where estimates overlap. Because of the difficulties encountered in isolating the signatures of these discontinuities, this correlation cannot considered reliable. Nonetheless, it would offer the intriguing possibility of topographic relief due to large-scale variations in transition-zone Al_2O_3 content, increases of which extend the stability fields of both garnet and ilmenite [e.g., *Liu*, 1977], although the required variations (on the order of 2–3 weight%) would be difficult to maintain in the presence of mantle convection.

Although changes in the crystal symmetry of perovskite have been observed in analog compounds, and predicted on the basis of quantum-mechanical equations of state for silicates [*Wolf and Bukowinski*, 1985], they are yet to be observed in $MgSiO_3$ perovskite. This is also true of the ultrahigh-pressure phase transformation tentatively proposed by *Park e al.* [1988]. One possible concern voiced in these studies is that the activation energies of these reactions may be sufficiently high that the reactions will not occur in short-duration static compression experiments, and have thus gone undetected. We will return to this question below, in our discussion of observations of an impedance increase near 915 km depth.

The alternative interpretation of the depth of the 730-km discontinuity (i.e., the alternative which arises from depth ambiguity), calling for an impedance decrease at 1830 km, would be extremely difficult to reconcile with current models of mantle mineralogy, and has no seismological precedents.

A possible structural explanation, linked to the discussion of a CBL trapped on the upper mantle-lower mantle boundary, is that the reflector observed at 730 km depth marks the "true" 650-km discontinuity, i.e., the γ-spinel $\rightarrow$ perovskite + magnesiowüstite phase transition, while the much stronger reflector at 650 km depth marks the top of a CBL supported by the large density contrast associated with the phase transition. Accumulation of cold (dense) material upon the phase transition would decrease the reflection coefficient, perhaps explaining the low magnitude observed for $R(730)$. The variation of $R(650)$ with

170

discontinuity depth would supposedly reflect thinning of the CBL with increasing distance, and age, from the source region(s). There is no a priori reason, however, to expect this layer to be spatially uniform, especially in the presence of mantle-wide convection currents [*Christensen*, 1988], in opposition to our estimates of τ'_{650} which allow for very little geographic variation. Furthermore, the depth of the discontinuity is much deeper than the experimentally-determined transition depth [*Ito and Yamada*, 1982], prompting us to reject this hypothesis.

At this point none of the remaining explanations can be decisively argued for or against, although the simplest, namely the ilmenite $\rightarrow$ perovskite phase transition, provides a quite adequate fit to observations, and, as such, is our preferred model. Accumulation of additional reverberation data will result in more robust estimates of $R(730)$ and may allow us to place useful constraints on topography of the "730-km" discontinuity.

The 915-Km Discontinuity

The residual reflectivity profile of Figure 5.8 contains evidence for an additional discontinuity, namely a 0.45% increase in impedance near 915 km depth. Being so small, however, the veracity of this observation must be questioned. The band-limited nature of the data introduces a "ringiness" to the reflectivity profiles, causing them to oscillate with a depth period proportional to the ratio of local velocity to waveform center frequency, passing through ~30 cycles over tne depth of the mantle. Because of this we would expect the residual profile to exceed the 5% false-alarm level at least once due to the correlation of random noise alone. Thus the significance of the extremely-low-magnitude reflector at 915 km depth is difficult to assess. It is, however, robust with respect to omission of significant portions of the data set, and remains in stacks of data that have been subjected to further low-pass filtering. Including a 730-km discontinuity in the synthetic stacks enhances this feature, implying its signature in the parsimonious profiles may be obscured somewhat by additional, "higher-order" structure. Clear observations in individual profiles

are limited to only two corridors, in particular, the corridor connecting shocks in the New Britain subduction zone with station CTAO (corridor 2 in Table 2.2) and the corridor linking events in the New Britain, Solomon Islands and New Hebrides seismic zones with station NWAO (corridor 12 in Table 2.2), which have in common sampling of the continental margin to the north of Australia. The magnitude of the inferred reflector along these paths is much greater than the average value obtained from the stack of Figure 5.8 (2.1% versus 0.45%, respectively), a discrepancy too large to be due to splitting alone.

The seismic literature contains numerous references to small discontinuities in velocity near 900 km depth [e.g., *Hales and Roberts*, 1970a, b; *Whitcomb and Anderson*, 1970]; including a number of observations for regions sampled in this study [e.g., *Datt and Muirhead*, 1977; *Muirhead and Hales*, 1980; *Datt*, 1981]. Thus, while the inferred strength of this reflector tests the limits of the currently available resolution, it does appear to be a real feature of data, marking possibly the fifth abrupt increase in impedance in the transition zone alone.

Mineralogical explanations for this feature are few. One possibility is related to the occurrence of symmetry changes in the crystal system of silicate perovskite, progressing from cubic to tetragonal and finally to orthorhombic symmetry with increasing depth in the mantle, as predicted by quantum-mechanical equations of state [e.g., *Wolf and Bukowinski*, 1985]. While highly speculative, this scenario is capable of explaining both the 730-km (cubic $\rightarrow$ tetragonal symmetry) and 915-km (tetragonal $\rightarrow$ orthorhombic symmetry) discontinuities simultaneously, but has difficulty explaining the "brighter" reflectors observed along corridors 2 and 12, which may require some sort of compositional heterogeneity. For the moment there does not appear to be an altogether satisfactory explanation of this feature.

172

CONCLUSIONS

The reverberation data for the western and central Pacific, the adjoining marginal basins, Indonesia and Australia are consistent with a simple model of the transition zone, bounded by phase transformations with average depths of 414 km and 660 km. Topography on the two discontinuities is negatively correlated; assuming that the temperature anomalies giving rise to topography are coherent in sign and magnitude across the transition zone, this implies that the 650-km discontinuity is endothermic. The relative magnitude of topography on the two discontinuities is generally consistent with recent Clapeyron slope estimates for the olivine $\rightarrow$ β-spinel, and γ-spinel $\rightarrow$ perovskite + magnesiowüstite systems, while the absolute topography implies ~210° C long-wavelength temperature variations in the transition zone beneath the sampled regions. Observed correlation of the depth and magnitude of the 650-km discontinuity (τ'_{LM} and $R(650)$, respectively) may be explained by, but by no means requires, a chemical boundary layer gravitationally trapped upon the discontinuity. In light of the strong geodynamical arguments against the stability of such a CBL, this hypothesis must be regarded as highly speculative. An alternative explanation, appealing to out-of-plane scattering by a locally-inclined 650-km discontinuity, may also be capable of explaining the correlation, and is more in keeping with the geodynamical constraints.

Small impedance increases located near depths of 530 km, 730 km, and 915 km are observed. The shallowest of these may be related to the phase transition of β-spinel to γ-spinel, although there are difficulties in achieving the necessary increase in impedance unless the two-phase region is narrower than experimentally determined. A second possibility is the transition to perovskite structure in diopside. The discontinuity at 730 km depth is well modeled by the transformation of ilmenite to perovskite; while changes in the crystal symmetry of silicate perovskite offer the possibility of explaining both the 730-km and 915-km discontinuities simultaneously. The constraints on these discontinuities obtainable from first-order reverberations will continue to improve with the accumulation of

173

greater stores of data, and have the potential to tell us much about the mineralogy of the midmantle.

TABLE 5.1. Transition-Zone Discontinuity Travel Times

#	Source Region	Recv.	τ'_{400}[1] sec	τ'_{650}[1] sec	τ_{TZ} sec
1	Sumba-Phil.	CHTO	188.9	283.6	93.3
2	New Britain	CTAO	184.6	280.5	96.3
3	Sumba		185.3	281.7	97.2
4	Philippines		185.9	281.2	96.3
5	Tonga-Fiji		183.6	280.5	97.0
6	Sumba-Phil.	GUMO	185.3	282.6	98.6
7	Izu-Bonin		-[2]	280.9	-
8	Tonga-Fiji	KIP	186.6	277.0	90.9
9	Sumba-Phil.	MAJO	185.4	279.8	95.9
10	Japan-Izu		181.2	277.9	95.5
11	Philippines	NWAO	189.8	278.6	89.8
12	New Britain		184.2	279.5	95.8
13	Sumba		190.4	277.1	87.4
14	Tonga-Fiji		183.3	277.1	93.5
15	Tonga-Fiji	SNZO	-[3]	-[3]	-
16	Philippines	TATO	186.5	273.9	89.1
17	New Britain		188.3	280.4	93.3
18	Japan-Izu		184.0	279.0	93.8

[1]Times corrected for crustal thickness, bounce-point bathymetry variations, and long-wavelength mantle heterogeneity.
[2]Discontinuity not observed.
[3]Discontinuity too strongly interfered with by additional structure to obtain accurate measurements of travel time.

FIGURE CAPTIONS

Fig. 5.1. Schematic illustration of the model of thermally-induced discontinuity topography used to explain the ~10-s variations in τ_{TZ} observed on a path-by-path basis. Because the discontinuities have Clapeyron slopes of opposite sign, they move together in warm regions, reducing the travel time between them. Although this is partially offset by the reduction of ambient velocity, the net result is a decrease in τ_{TZ} in locally warm regions of the transition zone. The inferred long-wavelength temperature anomaly, ΔT, is ~210° ± 45° C.

Fig. 5.2. Comparison of τ_{ScS} obtained from inversion of ScS_n and $sScS_n$ waveforms with the two-way, mean composite delay predicted by M84C and L02.56 (assuming $\delta v_s = 1.1 \delta v_p$), and the *Morelli and Dziewonski* [1987] model of CMB topography. The strong correlation suggests that geographic variations are well modeled, although the models slightly underpredict (~10%) the extent of heterogeneity encountered by multiple ScS.

Fig. 5.3. Mercator projections of study area depicting the locations of sources (triangles) and receivers (squares). Shaded regions denote the portion of the transition zone sampled along the individual seismic corridors, identified by their number from Table 5.1. Path-averaged apparent depths (relative to the PREM) of the 400-km and 650-km discontinuity are indicated for each corridor. The data are consistent with ~25 km of long-wavelength topography on both discontinuities. These results are described in the text.

Fig. 5.4. (a) Scatter plot of two-way, vertical travel time through the upper mantle, τ'_{400}, versus two-way, transition-zone travel time, τ_{TZ}. (b) Similar comparison of two-way, lower-mantle travel time, τ'_{LM}, and τ_{TZ}. (c) τ'_{400} versus τ'_{LM}. The negative correlations of the first two samples ($r = -0.65$ and -0.78) suggest variations in τ_{TZ} are due primarily to topography on the 400-km and 650-km discontinuities. Positive correlation of τ'_{400} and

τ_{LM} ($r = 0.35$) implies topography on the two discontinuities is anticorrelated, consistent with an endothermic 650-km phase transition.

Fig. 5.5. Expectation of the cross correlation of split- and unsplit-reverberation multiplets for selected values of the standard deviation of travel time σ. The unsplit autocorrelation is that expected for a pulse witn a Gaussian power spectrum (see text for details). The splitting is due to along-path variations in local first-order reverberation travel time owing to lateral heterogeneity and topography on the reflecting horizon. Increasing the variance of travel-time delays increases the width of the autocorrelation and decreases peak amplitude.

Fig. 5.6. Estimates of $R(650)$ made in three distinct frequency bands centered on the plotted symbols and each 12 mHz wide. Rates of decay for several values of the standard deviation of first-order reverberation travel times, σ_{650}, are shown. The data points are averages of 13 individual corridor estimates, and best fit by $R(650) = 0.072 \pm 0.01$ (in the limit of zero frequency) and $\sigma_{650} = 4.0 \pm 1.0$ s. With mantle heterogeneity accounted for, σ_{650} places an upper bound of 40 km of peak-to-peak topography (two standard deviation) on the 650-km discontinuity at wavelengths between 300 km and 1500 km.

Fig. 5.7. Scatter plot of the 6-mHz estimate of $R(650)$ versus two-way, vertical travel time through the lower mantle, τ_{LM}, for 13 seismic corridors where a stable estimate of low-frequency reflection coefficient could be obtained. Although the uncertainty in individual estimates of $R(650)$ is large, the correlation is nominally significant at the 97% confidence level. This result can b explained by, but does not require, the presence of a cold and dense chemical boundary layer trapped by the 650-km discontinuity, lowering the endothermic transition and decreasing the reflection coefficient by displacing slower, more buoyant, upper mantle. The PREM estimate (square) is included for comparison.

177

Fig. 5.8. Comparison of data (left) and parsimonious synthetic (center) reflectivity profiles obtained by stacking individual profiles for the 18 seismic corridors studied. Individual synthetic profiles contain model discontinuities near 400 km and 650 km depth, plus additional discontinuities in the upper 300 km of the mantle as required by the data. Residual $R(z)$ (right) exceeds the 5% false-alarm level only twice in the depth range of 300–1000 km. The peak near 515 km depth may mark the $\beta \rightarrow \gamma$-spinel transition; the peak at ~710 km may mark the ilmenite $\rightarrow$ perovskite transition. A third, minor peak at 915 km depth is discussed in the text.

Fig. 5.9. The decay of apparent reflection coefficient with increasing ratio of discontinuity transition width (δz) to wavelength (λ) is plotted for the case of a linear gradient in impedance. By the point where the width reaches one-fourth of the local seismic wavelength, the reflection coefficient is reduced by 40%, falling off rapidly for still wider transitions. The center of the passband employed in this study is approximately 30 mHz, corresponding to a 180-km wavelength in the transition zone. A discontinuity with a transition width of 40 km would thus appear ~40% weaker than a zero-width transition.
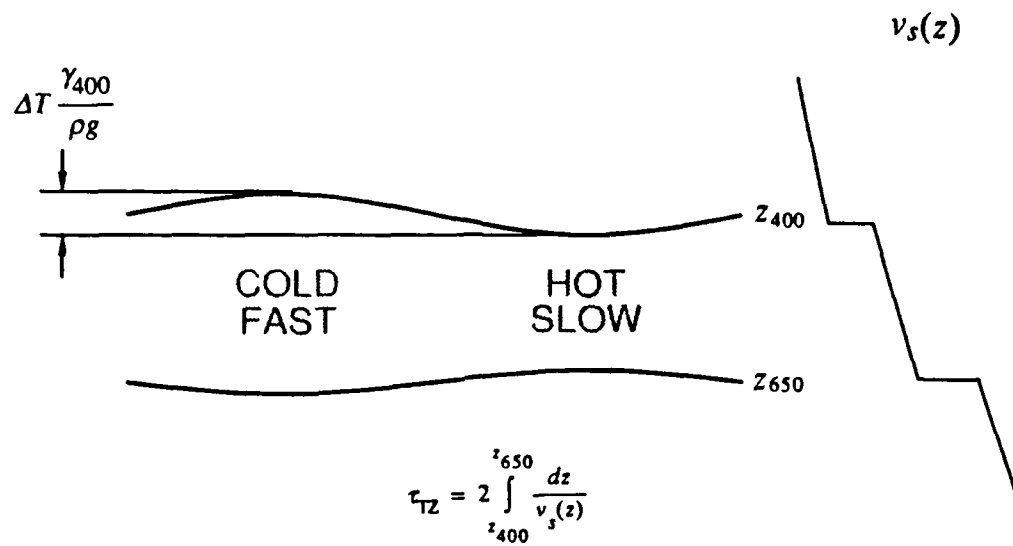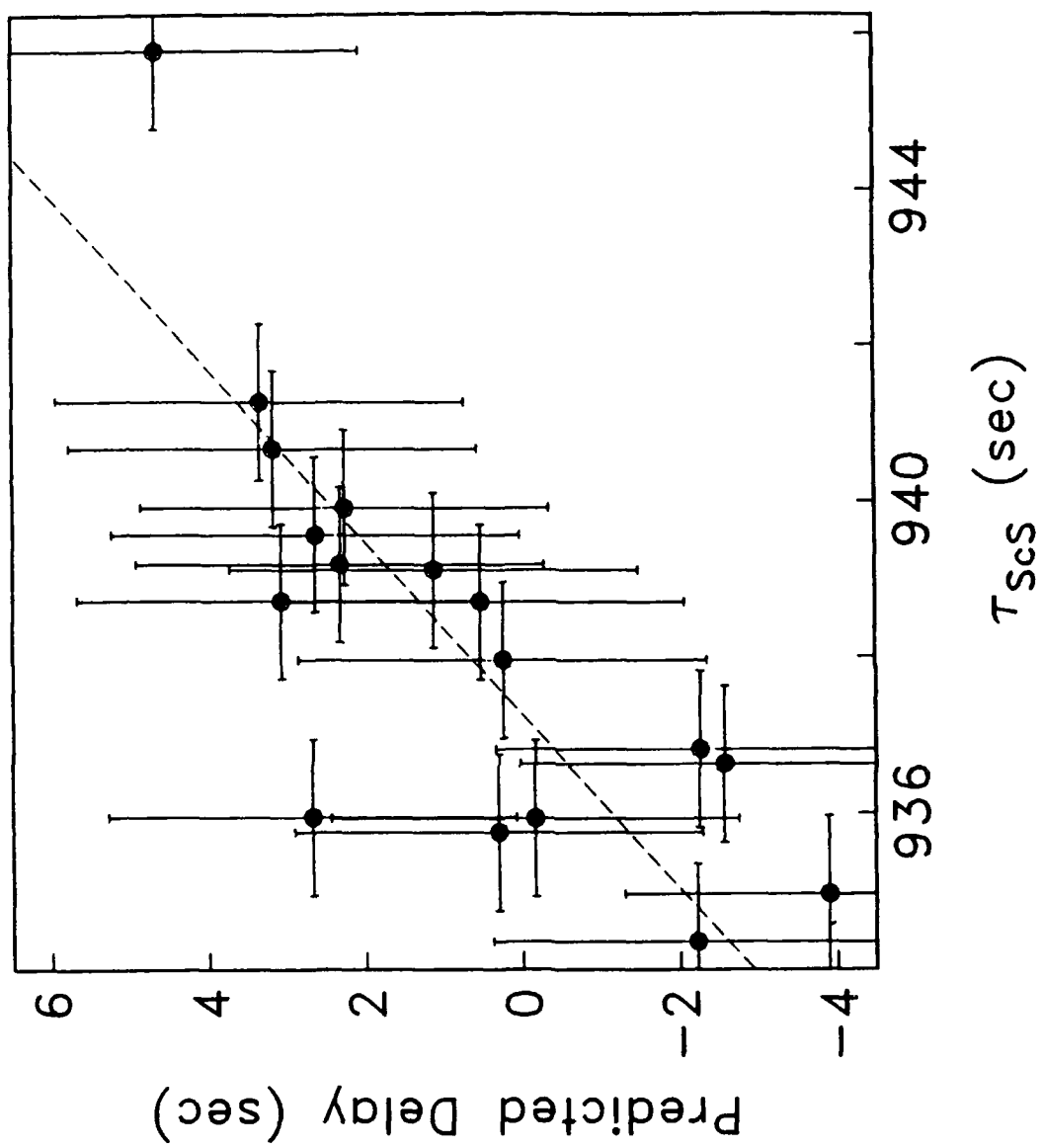
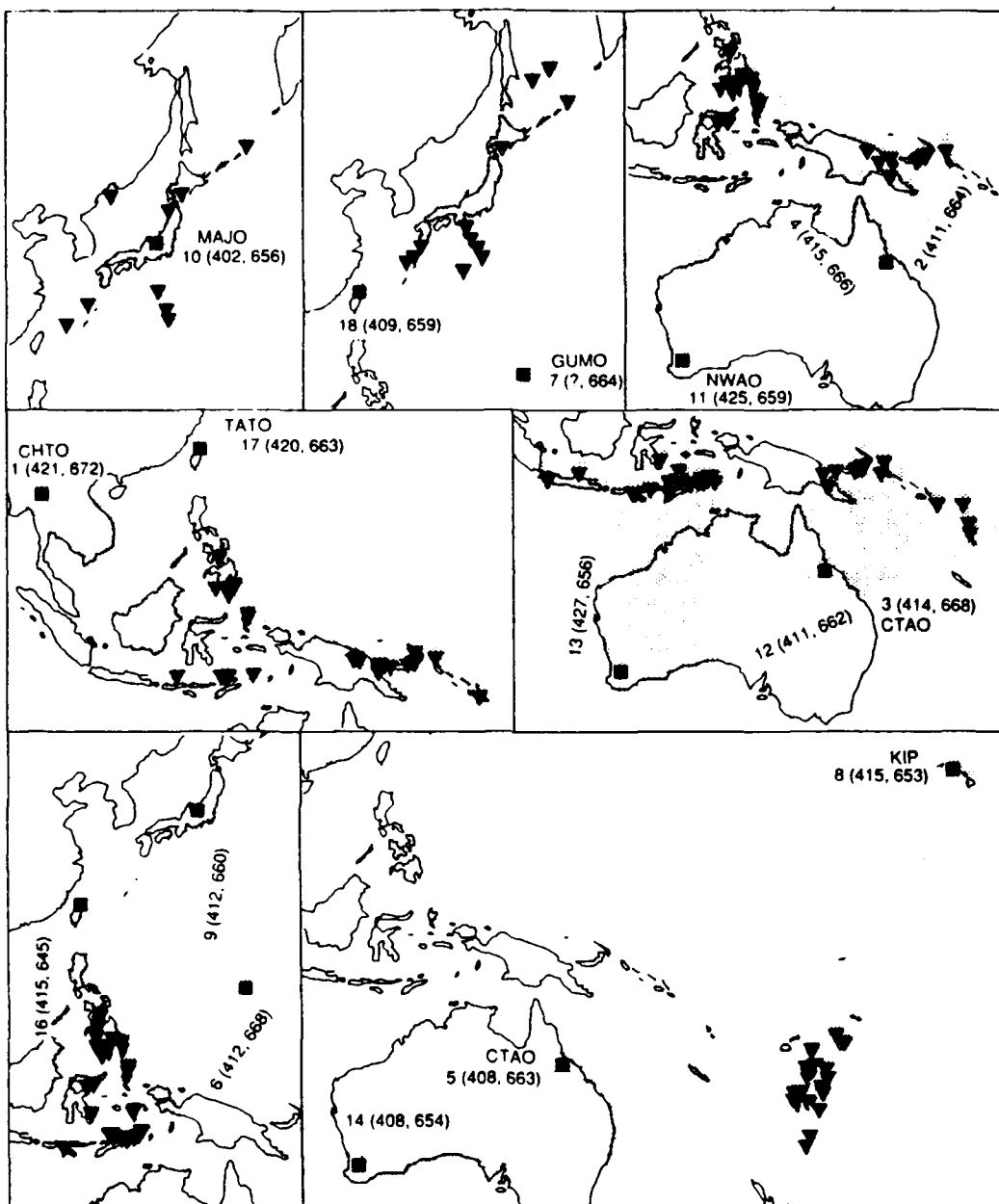$$\tau_{T2} = 2 \int_{z_{400}}^{z_{650}} \frac{dz}{v_s(z)}$$

Figure 5.1

179

Figure 5.2

180

Figure 5.3

181
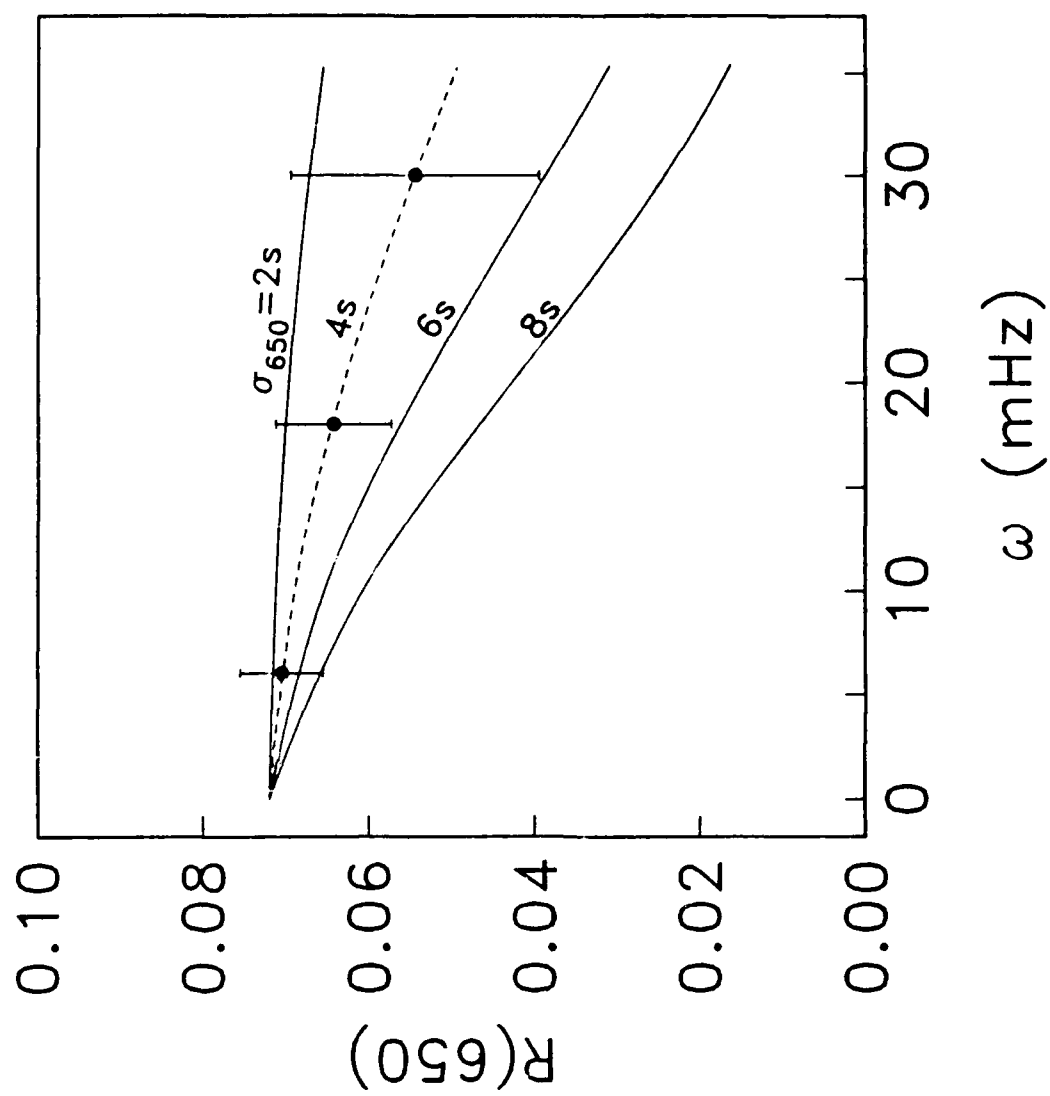
Figure 5.4

182

Figure 5.5

183

Figure 5.6

184
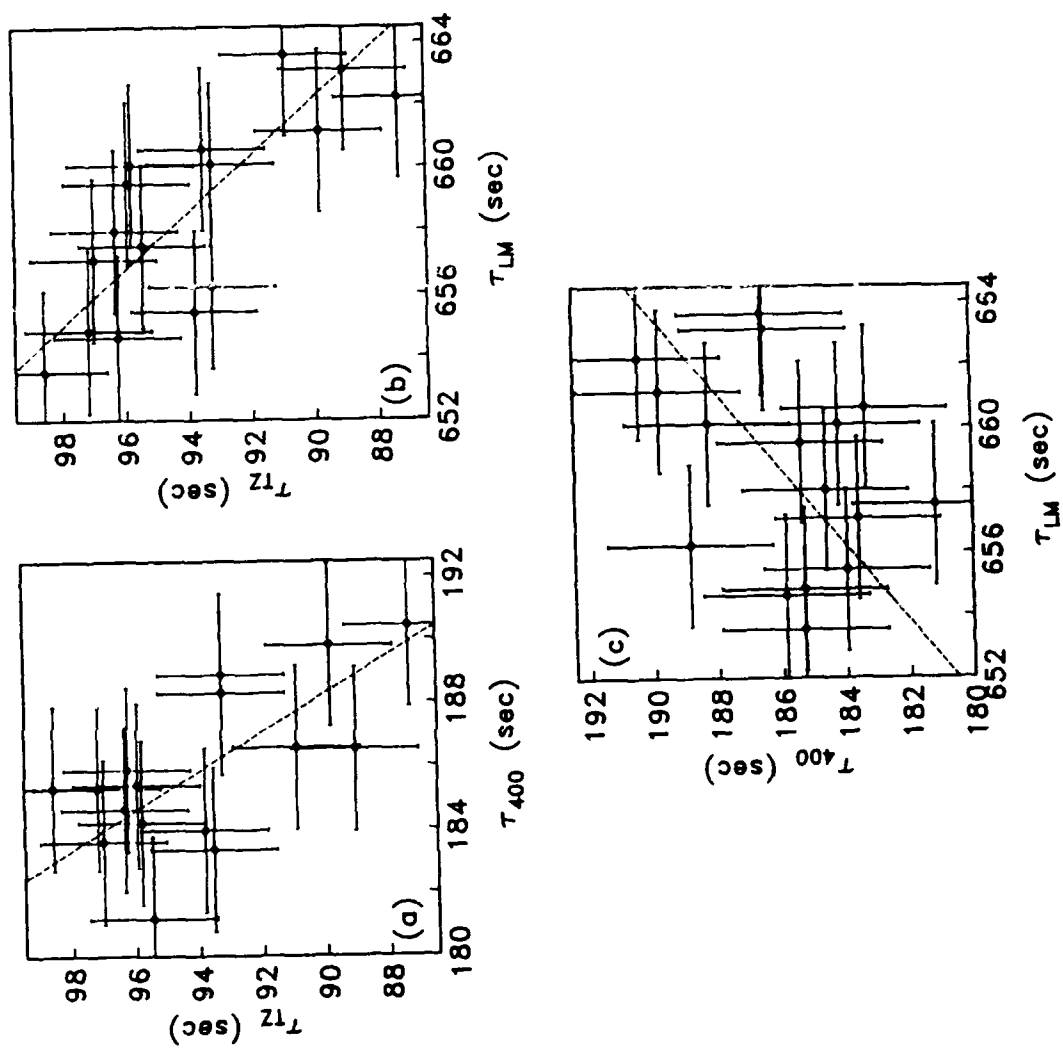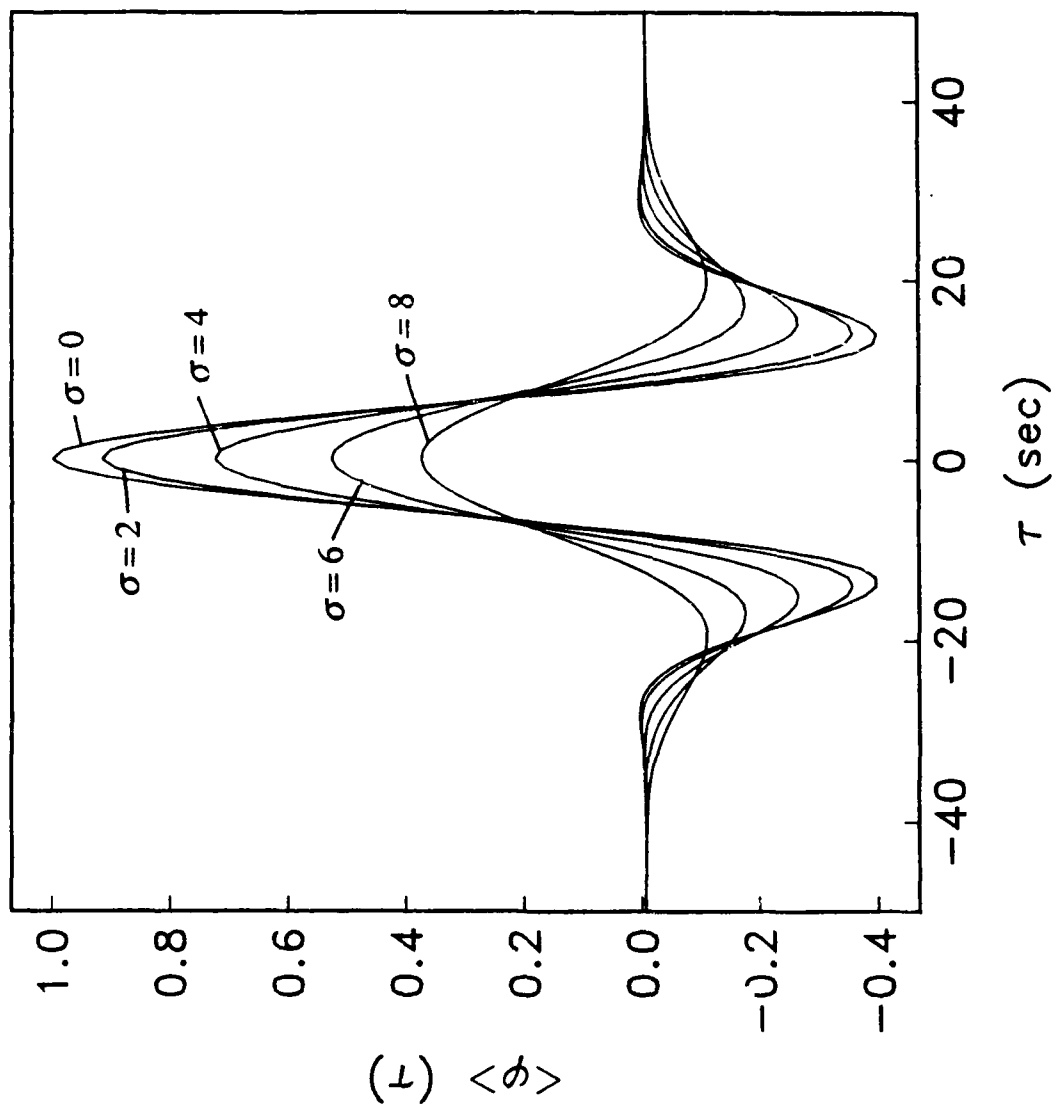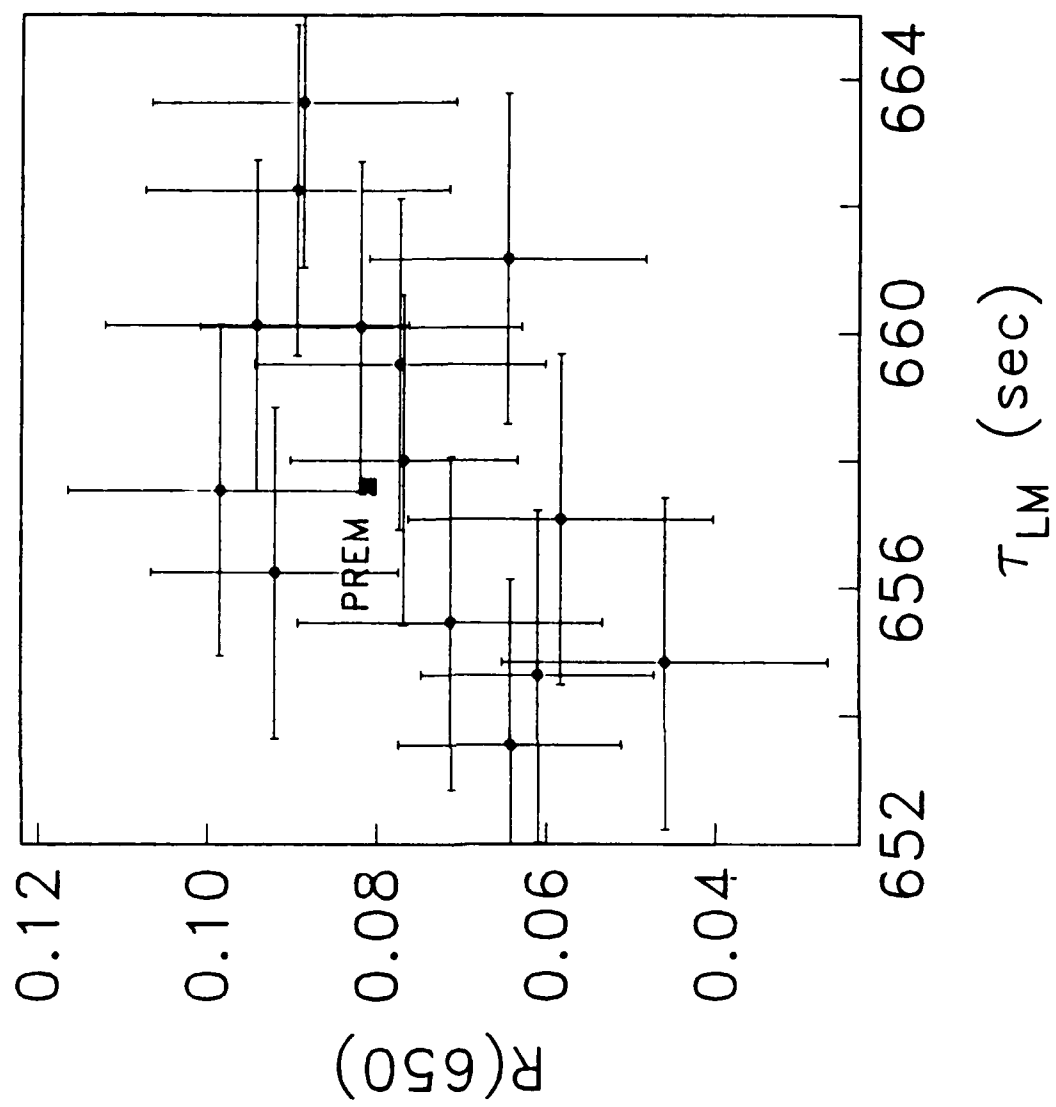
Figure 5.7

Figure 5.8

186

Figure 5.9

187
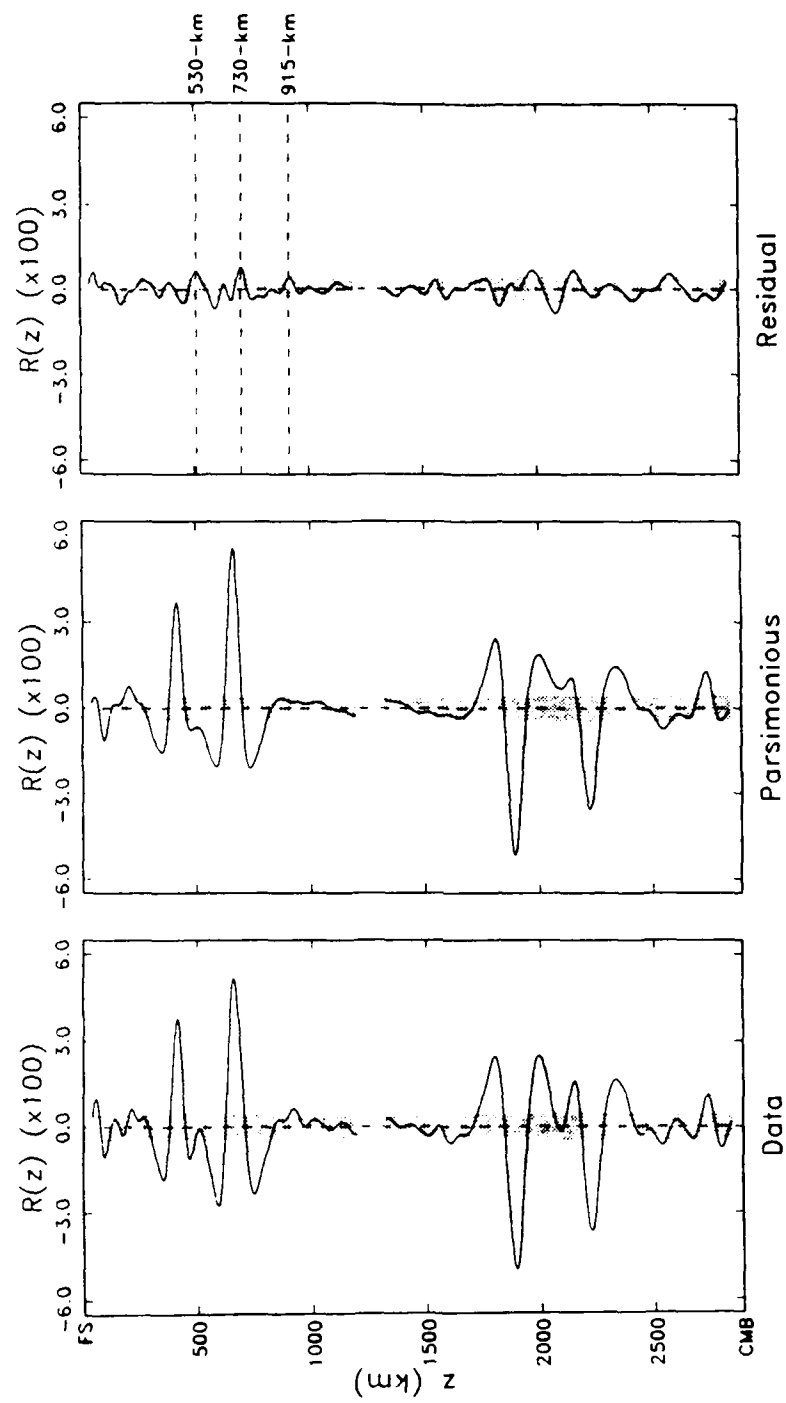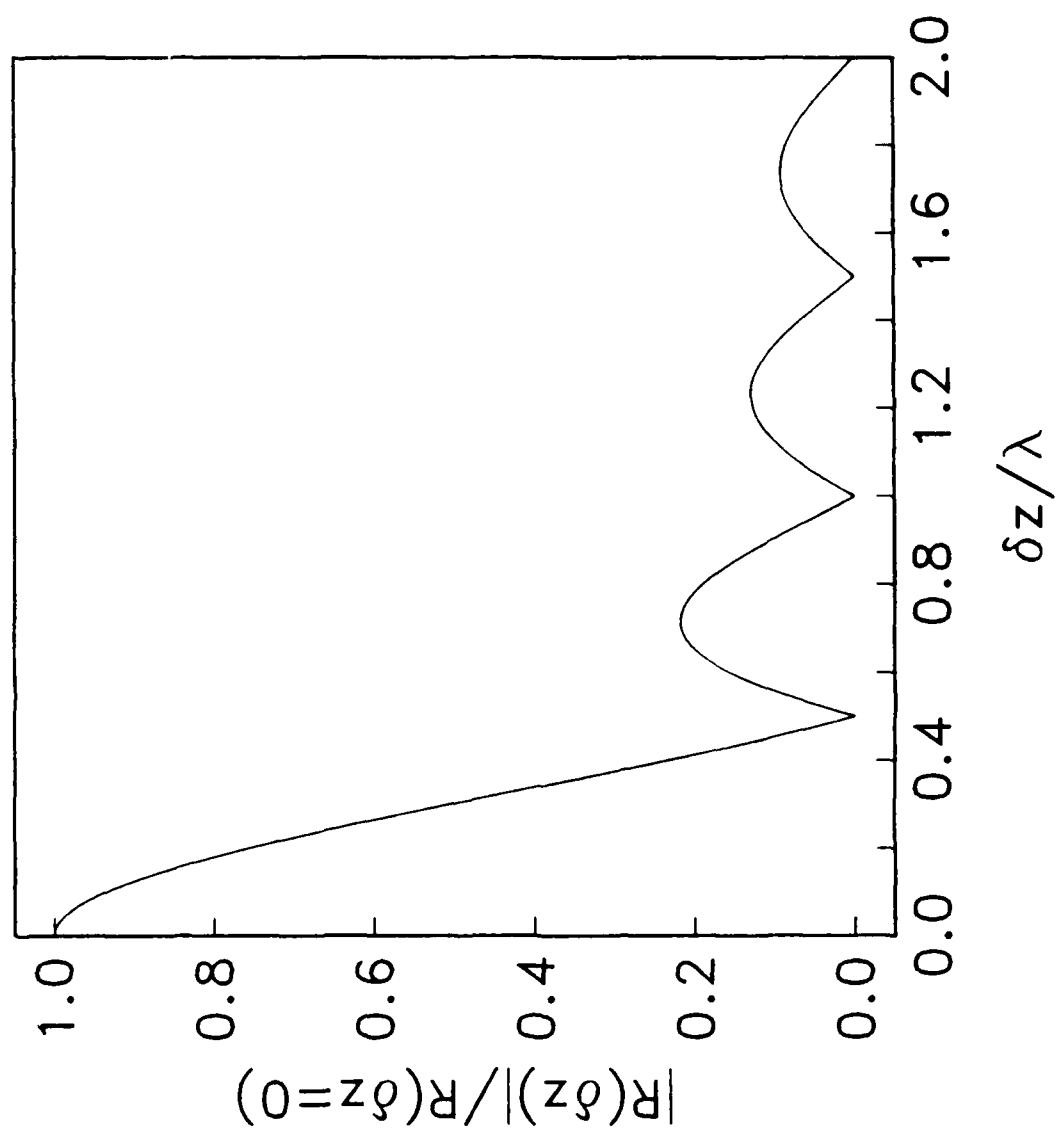
CHAPTER 6

THE UPPER MANTLE

INTRODUCTION

The Earth's upper mantle is at once tantalizingly close yet frustratingly remote. Although it rises to within a few kilometers of the surface beneath oceans, xenoliths, peridotites exposed in mountain belts and ophiolite sequences are our only direct samples of the upper mantle, forcing geoscientists to rely heavily on indirect observables of composition and state. Of the techniques employed, seismology has been arguably the most rewarding. Indeed, as early as the 1950s, seismology had provided evidence for an extensive low-velocity zone (LVZ) in the shallow upper mantle [*Gutenberg*, 1948], and detected several abrupt increases in seismic wavespeed at greater depths, most notably the Lehmann (220-km) [*Lehmann*, 1959] and 20° (400-km) [*Byerly*, 1926] discontinuities. With the advent of digital data and the refinement of interpretation techniques, modern seismology has added considerable detail to these early studies. For example, the depths and contrasts in material properties of the major mantle discontinuities are now well known [e.g., *Dziewonski and Anderson*, 1981; *Grand and Helmberger*, 1984], the systematic variations of LVZ depth and severity with lithospheric age have been mapped for the oceans [e.g., *Knopoff*, 1983], and shallow seated heterogeneity between oceanic and continental upper mantle, first detected by surface-wave dispersion studies [e.g., *Toksöz and Anderson*, 1966; *Toksöz et al.*, 1967], has been demonstrated to persist to depths as great as 400 km [e.g., *Sipkin and Jordan*, 1976; *Woodhouse and Dziewonski*, 1984; *Lerner-Lam and Jordan*, 1987]. Of course, study of the upper mantle has not been limited to seismology alone. Amongst many important results, high-pressure experimental petrology has provided the framework necessary to relate the velocity and density profiles produced by seismology to mantle composition and state [e.g., *Birch*, 1952; *Ringwood*,

1975], while the concepts of classical plate tectonics offer a convincing explanation of the global pattern of seismicity.

There remain, however, a number of outstanding questions regarding the upper mantle. While tomographic maps of the Earth's mantle have demonstrated significant deep-seated lateral heterogeneity, it is unclear whether this is primarily thermal or compositional in origin [e.g., *Anderson*, 1987a], and to what extent such heterogeneity is mirrored by radial discontinuity structure. As a case in point, the LVZ is a well documented and prominent feature of both oceanic and tectonically-active continental upper mantle, yet its existence beneath stable continental shields is still open to debate [e.g., *Hales*, 1972]. Questions concerning the sharpness and depth of the lower boundary of the LVZ remain, and there appears to be no consensus on the origin of the LVZ itself. Although commonly ascribed to the existence of a small fraction of partial melt [e.g., *Anderson and Sammis*, 1970], this is neither a necessary [*Goetz*, 1977], nor necessarily plausible explanation [e.g., *Walker et al.*, 1978].

A related concern is the often quite complicated discontinuity structure displayed by high-resolution, regional velocity models [e.g., *Hales et al.*, 1980; *Leven*, 1985]. Not seen in global Earth models such as the PREM [*Dziewonski and Anderson*, 1981], the question arises whether such structure is real–but s. .. erally variable as to be smeared out in the global models–or merely artifacts arising from u.. . eglect of lateral heterogeneity and anisotropy. Questions of this sort must be answered before we can claim to understand the role of the upper mantle in the complex dynamics and evolution of the Earth.

Of course, no one method or data set can hope to answer all the remaining questions, and we must direct our attention towards specific problems and the development of appropriate experimental techniques. In this chapter we interpret fundamentally new observations of upper mantle layering obtained from the migration of first-order reverberations. By sampling upper mantle structure over short horizontal path lengths, mantle reverberations provide constraints on the dichotomy of continents and oceans and

the characteristic length scales of heterogeneity that would be difficult to obtain by other means. As we will show, these results have important implications for the composition and state of the upper mantle.

UPPER MANTLE REFLECTIVITY STRUCTURES

As discussed in Chapter 4, the primary dictum behind synthetic modeling is to incorporate as few reflectors as necessary to adequately explain the data. In the transition zone, this requires strong discontinuities near 400 km and 650 km depth along all but one of the seismic corridors. Above 400 km, however, both the need for, and location of, additional discontinuities varies considerably from corridor to corridor. We find, however, that when corridors are grouped by their sampling of surface tectonics, the structures inferred from detailed synthetic forward modeling vary little within a group, and exhibit strong geographical coherence. These structures are discussed in detail in the following sections. For the moment, we will treat discontinuities in the upper mantle as abstract modeling artifices, postponing their interpretation until the upper mantle structures have been considered.

Continental Shields and Stable Platforms

Corridors 12 and 13 (Table 2.2), linking station NWAO in southwestern Australia with shocks in the New Britain and New Hebrides, and Sumba seismic zones, respectively, can be classified as crossing predominantly stable-shield, platform and continental-margin upper-mantle regions (Table 2.2), and are the most nearly "continental" of the 18 corridors. For these paths, an upper mantle structure featuring two abrupt impedance increases in addition to the transition-zone discontinuities provides a remarkably good fit to data. The two discontinuities occur near depths of 60 km and 260 km, respectively, with the former being the larger of the two, characterized by mean SH reflection coefficient of 0.038 (all reflection coefficients are stated at normal incidence from above). The deeper discontinuity

shows greater variation in apparent depth, and is characterized by mean $R = 0.023$. Note that although the discontinuity near 275 km appears larger than the shallower peak in the data reflectivity profile of Figure 4.18, synthetic modeling suggests that this owes to a design-induced amplification, rather than a stronger reflector per se. The upper-mantle and transition-zone structures inferred for these two corridors are shown schematically in Figure 6.1.

Continental Margins: Corridors 3 and 11 (Table 2.2), while they are primarily "continental" in their sampling of the upper mantle, feature a greater fraction of total path length in continental margins (*Jordan's* region Q) than either of the above corridors. The upper mantle structures inferred for these corridors (Figures 4.8 and 4.16) feature only one discontinuity in the upper 400 km of the mantle, specifically a moderately strong impedance increase at shallow depth (92 and 62 km, respectively); see Figure 6.1. Missing from the upper mantle is the strong signature of the 220-km discontinuity observed for the other corridors of this category. Along corridor 11, which connects shocks in the Philippines seismic zone with station NWAO in Australia, evidence for a minor impedance peak near 250 km can be seen in the data reflectivity profile (Figure 4.16). Comparing this profile with that computed for corridor 13, which samples much the same portion of the upper mantle with the exception of the region north of the Sumba seismic zone, suggests that the 220-km discontinuity is absent from the upper mantle in the Philippines region—existing only along the southern portion of the corridor, i.e., along the portion of the corridor confined to the Australia-India plate. Corridor 3 also displays an unusual level of complexity in the depth region of 150 to 300 km (Figure 4.8), which might result from interference between upper- and lower-mantle structure (see Chapter 7).

While the sources used in this study are confined exclusively to subduction zones, propagation paths for corridors in this category spend little time in the region of subduction, exiting the source region from the convex side of the island arc, opposite the subducting lithosphere. Thus it seems unlikely that structure in the region of the source has

much influence on the path-averaged estimates. Fundamentally similar velocity structures, featuring discontinuities, or velocity inflections, near 70 km and 220 km depth, have previously been obtained for western and northern Australia [*Simpson et al.*, 1974; *Goncz and Cleary*, 1976; *Hales et al.*, 1980; *Leven*, 1985].

Margins, Transitions, and Subduction Zones

Four corridors fall within this category (numbers 1, 2, 4, and 17 in Table 2.2), characterized by sampling of the tectonically complex and highly variable regions north and west of Indonesia and Australia. Like the corridors of the previous category, reflectivity profiles in this category display prominent impedance increases near 70 and 220 km depth. The mean depth and strength of these discontinuities are commensurate with estimates obtained for the more "continental" corridors (Figure 6.1). The inferred upper-mantle and transition-zone discontinuity structure for these corridors is shown schematically in Figure 6.2.

The reflectivity profile obtained for corridor 1 is a good example of the structure displayed by these corridors, with impedance increases required at 80 km and 220 km to satisfy the data (Figure 4.6). First-order reverberation bounce points for this corridor sample a number of tectonic regimes (Table 2.2, Figure 2.7) making it difficult to assign it to any one particular category, although continental and transitional upper mantle predominate. Examination of the signal-to-noise ratio estimates suggests that seismograms recorded for events in the Sumba and Java seismic zones contribute most significantly to the stack. Paths for these events encounter primarily marginal, or transitional, upper mantle. This corridor is important as it constitutes perhaps our most robust observation of the 220-km discontinuity outside the Australia-India plate (a 220-km discontinuity is also observed along corridor 17, but is not as strongly required by data).

These corridors are apparently distinguished from those of the previous category by the addition of a third upper mantle discontinuity, namely an impedance increase located at a

mean depth of 325 km, and characterized by $R = 0.019$. This reflector can be seen as a parasitic peak on the shallow side-lobe of the 400-km discontinuity, tending to drive the trough between the 220-km and 400-km discontinuities to more negative values compared to the parsimonious synthetic profiles (Figures 4.6, 4.7, 4.9, and 4.22). Although this is a relatively minor feature of data, it is remarkably well modeled by addition of a single discontinuity to the preferred synthetic profile. This fact, coupled with the apparent tectonic and geographic coherence of the observations, gives us confidence in our identification of this reflector.

There does not appear to be any evidence for well-developed LVZs (i.e., shear-wave impedance decreases) present along the corridors in this category unless the onset of velocity decrease is gradual, extending over a depth range on the order of 30 km or more. Resolution, quantified by profile variance, typical of individual corridors is of order $|R(z)|$ > 2%; discontinuities characterized by reflection coefficients significantly below this threshold could be present in the profiles and go unnoticed. Topography on the discontinuity, and lateral heterogeneity in the mantle both lead to travel-time perturbations splitting the dynamic analogs of first-order reverberation families, resulting in destructive interference and diminished resolution. Thus the stated threshold is an upper bound. The effects of splitting can be alleviated by further low-pass filtering of the data, increasing the ratio of waveform width to travel-time perturbations, thereby reducing the deteriorative effects of destructive interference. By increasing the characteristic period of the data, filtering also increases the effective seismic wavelength. Repeating the above experiments on low-passed filtered data (corner at 20 mHz, smoothly tapered to zero at 30 mHz) gives identical results. Again, no LVZ is required by data, which at these frequencies are sensitive to impedance gradients as broad as 50 km (see Figure 5.9).

Corridor 10, sampling the upper mantle beneath Japan, the Sea of Okhotsk, and Japan Sea, and corridor 6 sampling the mantle bordering the Philippine, Timor-Java, Yap and Marianas seismic zones are more difficult to classify tectonically, but may also fall into this

tectonic category, although they are deficient in sampling of continental margins relative to the other members. Both corridors can be modeled by small impedance increases at ~70 km depth, and require no other upper mantle reflectors (see Figure 6.3). Although the apparent absence of a LVZ beneath these areas--characterized by high surface heat flow-- may seem unusual, the inferred structure is similar to that found for the upper mantle beneath northeastern Japan by *Shiono et al.* [1980], although *Sacks and Snoke* [1983] note that the low subcrustal velocities of this model may imply a coincident M discontinuity and LVZ. We return to these questions later in the text. We note that corridor 10 displays a number of small reflectivity oscillations in the upper 400 km of the mantle, and a strongly distorted 400-km discontinuity (Figure 4.15). Although we have chosen not to model it explicitly, the data reflectivity profile is consistent with a low-magnitude reflector in the vicinity of 330 km.

Back-Arc Basins and Oceans

Corridors 5, 8, 9, 14 and 18 of Table 2.2 sample predominantly back-arc and oceanic regions. Corridor 8, connecting shocks in the Tonga-Fiji seismic zone with station KIP on the island of Oahu, is the most nearly pure oceanic path included in this study, with an average lithospheric age of 95 Myr. Like the other corridors in this category (see Figure 6.4), data reflectivity for this path is well modeled by an impedance decrease in the shallow upper mantle, in this case at a depth of 59 km, which most likely marks the top of the LVZ (Figure 4.13). The inferred depth of 59 km is somewhat shallower than usually predicted for ocean of this age [e.g., *Leeds*, 1975; *Knopoff*, 1983], being in better agreement with the estimate of *Regan and Anderson* [1984], which allowed for transverse isotropy in the upper 220 km of the mantle.

Corridors 8 and 14 are for events in the Tonga-Fiji seismic zone recorded at station CTAO in northeastern Australia, and station NWAO in southwestern Australia, respectively. The inferred depth to the LVZ is approximately 90 km for both of these

194

corridors, which is somewhat deep for the average age of oceanic lithosphere sampled (~50 Myr). However, the depth-age relations cited above were derived primarily from western-Pacific-crossing paths, and there is no a priori reason to assume they will hold true in Melanesia. In additional to intermediate age ocean, both paths sample some transitional regions, specifically the Lord Howe Rise (a possible continental fragment) and the eastern continental margin of Australia, where cooler upper mantle temperatures may depress the top boundary of the LVZ, and increase our estimate of path-averaged depth. Monte Carlo models of *Goncz and Cleary* [1976] derived from Rayleigh-wave observations place the top of the LVZ at a depth of ~100 km beneath eastern Australia; given the short path lengths through these regions, however, we do not expect our estimate to be biased strongly downward by the deeper LVZ beneath these regions. If the inferred depths are indeed indicative of the Melanesia region, they may be evidence of regional variability in the depth-age relation for oceanic lithosphere.

The 90 km depth estimate for corridor 5, connecting shocks in the Sumba, Java and Philippine seismic zone with the ASRO station MAJO on the island of Honshu agrees well with the results of *Seekins and Teng* [1977]. This path samples the aseismic Kyushu-Palau ridge, which appears to have a thicker lithosphere than the back-arc basins to either side. We note that a deep LVZ is also inferred for corridor 18, connecting shocks in the Sea of Japan and Izu-Bonin with station TATO on Taiwan, whose sampling of the upper mantle is more intermediate of continental-margin and back-arc regimes. The LVZ depth of 100 km derived for this corridor is the largest of the sampled regions.

Three of the five corridors with deep LVZs, specifically corridors 9, 15, and 18 show evidence of an additional reflector near 50 km depth (see Figures 4.14, 4.19, and 4.23). For these corridors, the width of the $R(z)$ peak associated with the LVZ is narrower in data than in parsimonious synthetic profiles. This runs counter to the norm found for the other major discontinuities, whose reflectivity signatures are typically wider in data owing to the splitting of first-order reverberations by mantle heterogeneity and discontinuity topography.

By superposing a smaller reflectivity peak of opposite sign (impedance increasing with depth), it is possible to reduce the apparent width of the composite peak. For the other corridors the mean depth of this reflector discontinuity coincides with the observed depth of the LVZ, precluding detection.

For the corridor connecting events in the Tonga-Fiji seismic zone with station CTAO in northeastern Australia (corridor 5 in Table 2.2), and for corridor 18 (see above), the inferred upper mantle structure contains an additional discontinuity at a depth near 280 km, interpreted as a small (R = 0.01) impedance increase. Co-existing with an impedance decrease at shallower depth (attributed to the onset of the LVZ), this reflector may mark the base of the LVZ. Of the paths featuring LVZs, however, the sampling of surface tectonic regions for these two corridors is most nearly like that of the previous category (which are void of impedance decreases in the upper mantle), complicating the straightforward interpretation of this discontinuity as the base of the LVZ. We return to this question later.

The possibility of deeper discontinuities notwithstanding, the upper mantle structures for these primarily oceanic and back-arc paths are less complex than the structures observed along more exclusively continental paths.

Subduction Zones

Corridors 7, 15 and 16 (Table 2.2) sample the upper mantle on the concave, subduction, side of the Izu-Bonin, Tonga-Fiji and Philippines seismic zones, respectively, with minor-arc paths trending subparallel to the strike of the subducting slab. For these three corridors, a quite prominent impedance decrease in the upper 95 km of the mantle is implied by synthetic modeling (inferred upper-mantle and transition-zone reflector structures are shown in Figure 6.5). For corridor 15, connecting events in the Tonga-Fiji seismic zone with station SNZO on the North Island of New Zealand, the magnitude of this reflector, $R(94)$ = −0.103, far exceeds that of either the 400-km or 650-km discontinuities (Figure 4.20), and is the single largest reflector we observe in the data set. These

observations are consistent with a extremely pronounced LVZ in the shallow upper mantle behind island arcs. All three paths all characterized by lower than average values of Q_{ScS} (Table 4.1), also consistent with a severe LVZ.

Previous models of the velocity structure of subduction zones demonstrate a great deal of variability, ranging from pronounced LVZs [e.g., *Choudhury et al.*, 1975], to models with little or no velocity variation above 300 km depth [*Shiono et al.*, 1980; *Kaila and Krishna*, 1985]. A surface-wave-derived model of the upper mantle beneath the Lau and Colville ridges, sampled by corridor 15, has neither a high-velocity lid or LVZ in the upper 250 km of the mantle [*Sundaralingham*, 1986] (it should be noted that the upper-mantle v_s ~4 km/s for this model seems unrealistically low). It is difficult to assess, however, the effect of the high-velocity slab on these results. On the other hand, our modeling should be relatively more immune to the presence of the subducting slab, which is typically at depths of 400 km or more along the propagation paths. Because we use only long-wavelength data, first-order reverberations will be sensitive primarily to the average state of the upper mantle above the subducting slab. Bearing this in mind, we are inclined to trust our analysis, and propose the existence of a strong LVZ on the concave side of these island arcs. The magnitude of the upper-boundary reflector is significantly greater in these regions than beneath old- and intermediate-age ocean, and marginal seas further removed from the arc.

Careful synthetic modeling of the low signal-to-noise ratio corridors 7 and 16 reveals no evidence for additional upper mantle reflectors. However, given the level of profile variance encountered for these corridors (Figures 4.12 and 4.21), resolution is low and the apparent absence of additional structure, such as a 320-km discontinuity, can not be considered significant. On the other hand, corridor 15 displays a very complicated upper mantle and transition zone (Figure 6.5). Apart from the extremely bright LVZ reflector, there is strong evidence for an additional discontinuity at 319 km depth, characterized by R = 0.020, similar to the discontinuity observed along corridors crossing Borneo, the South

197

China Sea, Indonesia and regions to the north of central and eastern Australia. Given the inferred severity of the LVZ along this corridor, it is logical to expect a more reflective lower boundary. If so, the deep reflector may mark the base of the LVZ.

DISCUSSION

While the structures outlined in the previous sections are often found to be quite complicated, in addition to being laterally variable, they are all assembled from the same set of building blocks. In this section we attempt to give meaning to these artifices, specifically the impedance increases at mean depths of 70 km, 230 km, and 320 km, and the shallow LVZ. From considerations of the geographic occurrence, tectonic correlation, contrast in material properties, and previous seismological observations, we propose a suite of possible mineralogical and structural explanations for these reflectors. Unfortunately, our explanations are often equivocal, and seldom unique, such that the full import of these observations in constraining the composition and state of the upper mantle cannot yet be fully realized.

The 70-Km Discontinuity

With the exception of the strong transition-zone discontinuities, the most pervasive feature of the reflectivity profiles obtained in this study is the impedance increase occurring at an average depth of 67 km, seen most clearly beneath corridors crossing continental shields, margins and transitional regions (Figure 6.6). We find compelling evidence for this discontinuity in all seismic corridors examined except those marked by LVZ reflectors. For the latter, a shallow impedance increase is inferred for paths where the LVZ is deep, facilitating detection of the shallower reflector. Although the evidence for these corridors is weaker, it is significant that the oceanic-path data are at least consistent with the possibility of a "70-km" discontinuity.

Similar observations of a velocity increase ranging from 60–90 km depth have been made by a number of authors. Perhaps the best documented of these is from data collected during the Early Rise experiment in the central U.S. and Canada, which require a ~3.2% increase in compressional-wave velocity near 90 km depth [e.g., *Green and Hales*, 1968; *Hales*, 1969]. A similar feature has been inferred for the upper mantle beneath much of Australia [*Simpson et al.*, 1974; *Muirhead, et al.*, 1977; *Hales et al.*, 1980], and in several oceanic sites [*Hales et al.*, 1970; *Shimamura and Asada*, 1976], suggesting that it may be global in extent.

Attempts have been made to explain the "70-km" discontinuity in terms of the high-pressure transition from the spinel to garnet facies in a lherzolitic or peridotitic upper mantle [e.g., *Hales*, 1969]. This transition has been observed experimentally in rocks of pyrolite composition at upper-mantle temperature and pressures [*Green and Ringwood*, 1967], and mantle xenoliths of both facies are observed frequently in kimberlites, so it seems safe to assume that the proposed reaction occurs in the Earth's uppermost mantle. Recent experimental studies, however, place the equilibrium boundary at shallower depths (45–55 km) than observed in the seismic data [*Jenkins and Newton*, 1979; *Webb and Wood*, 1986]. Unlike most upper mantle reactions, the Clapeyron slope of the spinel → garnet transition is negative at temperatures below 900° C [*Wood and Yuen*, 1983], flattening and eventually assuming positive values only at higher temperatures [*Jenkins and Newton*, 1979]. The cooler mantle beneath continental cratons and platforms could lower the reaction some 10 km, with spinel remaining stable to 55 km depth for temperatures near 600° C. The depth of the phase boundary is also critically dependent on major element composition, especially Ca, Cr, and Al content. For mantle depleted in Ca and Al and enriched in Cr, a pattern typical of basalt depletion, the reaction could be lowered an additional 10 km [e.g., *MacGregor*, 1970; *O'Neill*, 1981]. Thus it seems that, for temperatures and composition typical of subcontinental upper mantle, the transition could be lowered sufficiently to fall within the range of depths observed in this study.

Constraints on the variation of material properties observed seismically are also somewhat difficult to reconcile. If density and velocity increases associated with the transition can be assumed to follow Birch's law [*Birch*, 1952; *Anderson et al.*, 1968], our estimate of mean $R(70) = 3.5\%$ requires a 3.2% increase in density and 3.8% increase in shear velocity across the discontinuity, in agreement with the increase in compressional velocity inferred from Early Rise data. Predicted velocity and density increases at STP of <3% for the transition in a fertile pyrolite composition [e.g., *Green and Liebermann*, 1976; *Webb and Wood*, 1986] are considerably lower. Measurement uncertainties for these quantities are large, however, and while not necessarily in good agreement, the spinel → garnet transition is certainly capable of explaining the observed reflector.

An alternative explanation, due to *Forsyth* [1977], attributes the observed increase in compressional wavespeed to a corresponding increase in preferred orientation of olivine (see also *Hirn et al.* [1975]). Given that olivine constitutes some 50% to 70% of the upper mantle by volume, and is highly anisotropic, this model is capable of explaining observed compressional velocity increases without necessitating impossibly high degrees of crystal alignment. However, the constraints imposed by $R(70)$, which require a 7% increase in impedance are not as easily satisfied, and a model of anisotropy fails on several counts: (1) Although dependent on the form of anisotropy, the quasi-*SH* reflection generated at the interface of an anisotropic layer will not be greater than the reflection coefficient for an equivalent isotropic variation in velocity. Assuming that variations in apparent *SH* and *P* velocity across the discontinuity are commensurate, observations of a 3–4% increase in compressional wavespeed require greater than a 3% increase in density across the transition for $R(70) = 3.5\%$. Thus if anisotropy is to explain the increase in velocity, we must also resort to chemical layering to explain the increase in density. *Forsyth* [1977] suggests that the discontinuity may mark the limit of basalt depletion in peridotite, which could explain some of the required density increase (fertile peridotite being higher in Fe content is also 1% to 2% more dense), although this will be offset somewhat by the lower velocity of

undepleted peridotite [*Jordan*, 1979a]. Evidence from garnet-lherzolite xenoliths suggests, however, that subcontinental mantle is depleted to depths significantly in excess of 90 km [e.g., *Boyd*, 1973]. (2) Unless the anisotropy takes the form of transverse isotropy with a radial axis of symmetry, a form inconsistent with observations of shallow oceanic anisotropy, we would expect to observe large variations in $R(70)$ with azimuth. While $R(70)$ is observed to vary somewhat, the level of variation is small, and shows no apparent azimuthal dependence. Thus, while anisotropy may contribute to the discontinuity, especially beneath oceanic regions, it does not seem a likely cause of a subcontinental reflector, which we assign to the spinel → garnet transition.

The geographical distribution of observations and apparent depths for the 70-km discontinuity are shown in Figure 6.6. We find that neither the depth, or reflection coefficient of the 70-km discontinuity are strongly correlated with surface tectonics, as revealed by the inability of regionalized estimates to reconstruct the observed topography (Figure 6.7). The lack of strong correlation also argues for the spinel → garnet lherzolite transition, which is characterized by a flat Clapeyron slope over a broad range of temperatures [*Jenkins and Newton*, 1979], rather than an anisotropic horizon, which might be expected to track the base of the lithosphere.

The Low-Velocity Zone

Eight of the 18 seismic corridors treated in this study show evidence for a pronounced decrease in *SH* impedance at depths less than 100 km in the mantle (Figure 6.6). This reflector is most plausibly interpreted as the onset of the LVZ, marking the suboceanic lithosphere-asthenosphere boundary. The mean *SH* reflection coefficient for these paths is $R(LVZ) = -0.045$; excluding corridors 7, 15 and 16, whose sampling of the upper mantle is limited to the concave side of island arcs, reduces this estimate to $R(LVZ) = -0.033$. For most thermally-activated processes, partial melting included, reduction of shear velocity greatly exceeds that of density, thus $R(LVZ)$ requires a velocity decrease of ~6.6%,

201

comparable to previous estimates of 3% to 10%. The mean for paths 7, 15 and 16, $R(LVZ)$ = –0.065, is nearly twice that of the other corridors. If the LVZ is due to the presence of a small amount of partial melt [e.g., *Anderson and Sammis*, 1970], the latter value can be explained by the presence of a small degree of partial melt, presumably owing to greater H_2O pressures generated by the breakdown of hydrous phases in the subducting slab. Given the instability of even small fractions of partial melt [e.g., *Walker et al.*, 1978], the subsequent upward migration of melt (perhaps associated with marginal basin formation) may result in chemical zonation within the LVZ. Anisotropy induced by strong corner flow in the asthenosphere aboe the subducting slab [e.g., *Ribe*, 1989] may also served to accentuate the reflector.

Besides being seismically slow, the LVZ is also associated with severe attenuation, thus we might expect Q_{ScS} to be related to the depth, and possibly the reflection coefficient, of the upper boundary of the LVZ. This is indeed the case, estimates of Q_{ScS}^{-1} and z_{LVZ} are negatively correlated at greater than the 90% confidence limit. Excluding the anomalously bright reflectors observed along corridors 7, 15 and 16, estimates of Q_{ScS}^{-1} and $R(LVZ)$ are also correlated (coefficient of correlation $r = 0.73$, significant at the 85% confidence level). These correlations are important inasmuch as they confirm our interpretation of this reflector which, due to the depth ambiguity inherent to the method, could also be interpreted as an impedance increase in the D" region of the lower mantle.

Individual estimates of z_{LVZ} and z_{400} (or equivalently τ'_{400}) for the six corridors where observations overlap, are negatively correlated in excess of the 95% confidence level, further confirming the thermal origin of the inferred LVZ reflector. More important however, is the implication that temperature variations controlling the equilibrium depth of the LVZ may be persistent, and detectable, to 400 km depth in the mantle. The range of depths observed for the 400-km discontinuity for these corridors is only 8 km, near the level of resolution, so we hesitate to place too much emphasis on this result. However, assuming the Clapeyron slope of the olivine $\rightarrow$ β-spinel transition marking the 400-km

discontinuity is of order 3.5 MPa/°K [e.g., *Suito*, 1977], a temperature anomaly of ~75° C is required to produce 8 km of topography. If the top boundary of the LVZ tracks the solidus of hydrous (<4% H_2O) peridotite [e.g., *Green and Liebermann*, 1976], a temperature anomaly of this magnitude in the upper mantle could account for the entire 35 km of LVZ topography observed in this study. Assuming an anhydrous solidus requires temperature variations two to three times greater, but is not inconsistent with the observed topography. We note that this observation is speculative, and may be due wholly, or in part, to incomplete compensation of τ'_{400} for upper mantle structure.

The depth of the LVZ reflector is also strongly correlated with surface tectonic sampling (note that we have omitted corridors 7, 15 and 16 from the calculations; for these paths, the grouping of subduction zones, continental margins and Phanerzoic orogenic zones into a single tectonic region seems inappropriate). The sense of the correlation is what we would expect from the observed correlation with Q_{ScS}, specifically that the reflector migrates to greater apparent depth as the percentage of path length spent in regions B and C decreases, and sampling of cooler continental margins and platforms increases, yielding regionalized z_{LVZ} estimates of: 64 ± 10 km (oceans, primarily region B), and 122 ± 16 km (primarily region Q); see Figure 6.8.

For corridors with a shallow LVZ reflector (see Figure 6.4), we find no evidence for further discontinuities in the upper 400 km of the mantle. Although the lower boundary of the LVZ has traditionally been modeled as a sharp increase in velocity gradient, more recent mantle models have tended to depict the boundary as a gradual transition, with shear velocity returning to normal lid values at depths often as great as 400 km [e.g., *Grand and Helmberger*, 1984; *Walck*, 1984; *Lerner-Lam and Jordan*, 1987]. The structure implied in these models would be transparent to all but the lowest-frequency first-order reverberations, and therefore compatible with our results. A gradual lower boundary may imply an oceanic adiabat trending subparallel to the solidus throughout most of the upper mantle.

For two seismic corridors, specially corridors 6 and 10 (Figure 6.3), the apparent absence of a LVZ is highly anomalous, and in direct opposition to a number of previous studies. There is, however, a mechanism by which an LVZ could exist along these corridors, and yet go undetected. Because Clapeyron slopes defining the hydrous solidii of model mantle materials can be very steep [e.g., *Green and Liebermann*, 1976], only small temperature perturbations are needed to produce large offsets in equilibrium depth, the variability of which is well documented by observations of LVZ depth for other corridors. Sampling of a number of tectonic provinces along a single seismic corridor, along which the depth of the LVZ varies significantly, could introduce sufficient splitting of first-order reverberations that no LVZ would appear in the reflectivity profiles. This might explain the lack of any inferred LVZ for corridors 6 and 10, which require only a 70-km discontinuity. Examination of Figure 6.6, and Table 2.2, confirms that these paths both cross regions where large variations in z_{LVZ} are expected, offering some support for this hypothesis. In particular, the depth of the LVZ beneath the Philippine Sea is estimated to be on the order of 35 km (away from the Kyushu-Palau ridge) [e.g., *Kanamori*, 1970; *Seekins and Teng*, 1977], whereas to the north of Indonesia it may be as deep as 100 km. These two regions are both sampled along a single seismic corridor (corridor 6). Even at very low frequencies, offsets of LVZ depth this large would strongly attenuate the reflectivity profile peak.

The 220-Km Discontinuity

Observations of an abrupt increase in seismic-wave velocity near 220 km depth have been noted by a number of authors, excellent summaries of which can be found in *Nuttli* [1963] and *Anderson* [1979a]. Specific references to a 220-km discontinuity beneath the regions sampled in this study include *Simpson et al.* [1971], *Simpson et al.* [1974], *Hales et al.* [1980], *Datt* [1981], *Drummond et al.* [1982] and *Leven* [1985], all of which sample the upper mantle beneath central and northern Australia. As modeled by these authors, the

220-km discontinuity marks a sharp 1–4.5% increase in compressional velocity. Of the 18 seismic corridors examined in this study, persuasive evidence of a 220-km discontinuity is found in only 6 (Table 4.2). These corridors have in common extensive sampling of the northern Australian continental margin, and central and western continental shield (with the exceptions of corridors 1 and 17); see Figure 6.6. Our estimate of mean depth (230 km) for these corridors agrees favorably with previous studies, as do variations in the apparent depth, which are large (90 km). Assuming the increase in velocity and density across the discontinuity are linked by Birch's law, the mean value of $R(220) = 0.02$ implies a 2.2% increase in shear velocity and 1.8% increase in density. The fractional increase in shear velocity falls within the rather large range of observed compressional velocity increases.

Under oceanic regions, direct observations of a 220-km discontinuity are more rare, and are usually interpreted as marking the lower boundary of the LVZ. We do not observe a 220-km beneath any of the predominantly oceanic corridors sampled in this study. As mentioned previously this requires either a gradual transition, or depression of the high-pressure boundary of the LVZ to much greater depths. Since density probably does not decrease significantly in the LVZ, the reflectivity of the lower boundary will depend almost entirely on the contrast in shear velocity, scaling as $R \sim 1/2(\delta v_s/v_s)$. Given the resolution obtainable along a single seismic corridor, it is possible that an abrupt increase in v_s as large as 2–3% could go undetected if not accompanied by a commensurate variation in velocity. With the current data set we cannot exclude the possibility of a suboceanic 220-km discontinuity. We can, however, infer that its properties must differ from the subcontinental reflector.

Leven et al. [1981] discuss the difficulties encountered in attempting to explain this discontinuity in terms of either a phase transition or change in composition. In short, for a pyrolite mantle, the only phase transitions expected in the range of depths occupied by the 220-km discontinuity are the coesite → stishovite transition, and the formation of complex garnet solid solutions in the $Mg_4Si_4O_{12}$-$Mg_3Al_2Si_3O_{12}$ system [e.g., *Akaogi and Akimoto,*

1977]. Although the transition to stishovite is accompanied by a 60% increase in shear-wave impedance [*Akimoto*, 1972], the upper mantle abundance of free quartz is insufficient to explain the observed discontinuity. The solid solution of garnet and pyroxene in the latter reaction extends over a broad pressure range, and is also unlikely to produce a seismic discontinuity [*Bina and Wood*, 1984]. *Liu's* [1980] suggestion that the discontinuity may be associated with rapid increase in garnet content at the low-pressure boundary has not been upheld experimentally [e.g., *Irifune*, 1987], and at any rate would require temperatures exceeding 1600–1800° C in the subcontinental mantle. Compositional changes from depleted to fertile peridotite, or from garnet lherzolite to eclogite [e.g., *Anderson*, 1979*b*] are also unlikely explanations since shear velocities for these compositions are nearly indistinguishable, and are, if anything, lower in the high-density assemblage [*Jordan*, 1979*a*].

Leven et al. [1981] attribute the 220-km discontinuity to shear alignment of olivine above a subcontinental LVZ, similar to a model proposed several years earlier by *Steinmetz et al.* [1974] for the mantle beneath western Europe. In light of the inability of either mineralogical phase transformations or changes in chemical composition to adequately explain the 220-km discontinuity, we consider this model in some detail. For the moment, however, we will set aside much of the complexity of the *Leven et al.* [1981] model, focusing instead on the general viability of anisotropy in producing the observed reflections.

As mentioned in conjunction with the 70-km discontinuity, a transition in shear-wave anisotropy can produce an efficient reflector, although the amount of reflected energy will depend strongly on the form of anisotropy, and the geometry of reflector and incident wave front. If the 220-km discontinuity is to be attributed to anisotropy alone, impedance contrasts will arise solely from the variation of quasi-*SH* velocity across the boundary (for small anisotropies). To satisfy an average value of $R(220) = 0.02$ requires a minimum of 4% anisotropy, with the required anisotropy increasing as the width of the transition

between cr·stal-alignment fields increases. While this is a large anisotropy, it is not implausible assuming that roughly 50% of the intrinsic anisotropy of olivine can be realized in the mantle [e.g., *Christensen*, 1984]. We note that similar degrees of lithospheric anisotropy have recently been inferred from observations of shear-wave splitting beneath stable continental shields [*Silver and Chan*, 1988].

Unless the anisotropy takes the form of transverse isotropy with a radial axis of symmetry, we would expect to observe large variations of $R(220)$ with azimuth. For the paths where a 220-km discontinuity is confidently observed, the inferred strength of the reflector varies only slightly, with a standard deviation of 0.005, commensurate with our estimate of measurement uncertainty. Although these observations cover a large range of azimuths, they are geographically dispersed, with only limited multiple-azimuth coverage of particular geographic regions. One potentially diagnostic observation is the apparent absence of the 220-km discontinuity along the corridor connecting shocks in the Sumba seismic zone with station CTAO in northeastern Australia (corridor 3 in Table 2.2). This corridor samples the upper mantle along the northern continental margin of Australia and the Arafura Sea. Other corridors sampling these regions along more north-south-trending paths (specifically corridors 2, 4, 11, and 12; see Figure 6.6) are consistent with a 220-km discontinuity with the single exception of corridor 11. Barring geographic variability of the 220-km discontinuity within this region, the apparent absence of the 220-km along corridor 3 may be due to azimuthal variation in the reflection coefficient. Although greater geographic coverage of first-order reverberation corridors will be necessary to adequately test this hypothesis, the possibility that the 220-km discontinuity that we observe has as its origin some form of anisotropy cannot be ruled out. (Note that the anisotropy of the PREM, with $v_{SH} > v_{SV}$ above 220 km depth predicts $R(220) < 0$ in lieu of any contributions from intrinsic variation of velocity and/or density.)

Given the current status of the observations it is not possible to unambiguously constrain the nature, or the cause, of the anisotropy. It is, however, possible to compare the

observations against previous models of subcontinental anisotropy to produce a list of potential candidates. Considering the *Leven et al.* [1981] model (see also *Leven* [1985]), derived for the mantle beneath the Australian continent and northern continental margin, a potential difficulty arises, concerning the abrupt onset of low velocities beneath the 220-km discontinuity. The composite structure, essentially a 25–30 km lense of high-velocities similar to the lid-LVZ association thought to occur at shallower depths in oceanic upper mantle [*Forsyth*, 1977], should produce a complex reflectivity peak. In particular, at low frequencies, the waveforms of reflections from the top of the lense will interfere destructively with those from the bottom boundary, reducing our estimate of the reflection coefficient. We do not note any significant decrease in the estimated reflection coefficients in going from the full-bandwidth to low-frequency reflectivity profiles. In fact the estimates increase slightly, probably due to the diminishing effect of reverberation splitting at low frequencies. At higher frequencies the peak should begin to take on a bimodal appearance (approximating the derivative), which is also not observed, although it may lie below the level of vertical resolution. We note that the *Leven* [1985] model is unique, in that the onset of low velocities beneath the 220-km discontinuity is significantly more abrupt than other models of Australian upper mantle [*Hales et al.*, 1980; *Datt*, 1981]. An alternative model of subcontinental anisotropy has recently been proposed by *Silver and Chan* [1988] from observations of shear-wave splitting. In their model, most, if not all, of the lithosphere may be significantly anisotropic, owing to syntectonic recrystalization during major orogenic episodes. In this case, the 220-km discontinuity would mark the transition from random alignment of olivine in the asthenosphere to strong preferred alignment in the lithosphere, producing a simpler reflecting horizon perhaps more in keeping with the observations. Unfortunately, the *Silver and Chan* [1988] study has no data points geographically in common with the present, excluding the possibility of a direct comparison.

To examine the possibility that the 220-km discontinuity is associated with a thermally-activated process, we have computed the correlations of apparent reflector depth with Q_{ScS}, the depth of the 400-km discontinuity, and surface-tectonic classifications of the GTR1 regionalization. We find a strong, positive correlation between reflector depth and Q_{ScS} (coefficient of correlation $r = 0.87$, significant at the 95% confidence level). As true of the LVZ reflector, a correlation with tectonic province is also implied (Figure 6.9). For the 6 corridors where the 220-km discontinuity is confidently identified, regionalized estimation of the apparent depth z_{220} yields: 213 ± 13 km (primarily region Q, plus a very small amount of oceanic sampling), and 295 ± 30 km (regions P and S). Some correlation with z_{400} is found, but is not sufficiently strong to be considered significant.

The sense of these correlations are the same found for the LVZ reflector, and loosely interpreted imply that the discontinuity migrates to greater depth in colder regions of the upper mantle. If this reflector were to mark the bottom boundary of a subcontinental LVZ, we would expect precisely the opposite correlation. This also argues against a phase transitional origin, since Clapeyron slopes of most upper mantle transitions are positive. As such the sign of the correlation of discontinuity depth and Q_{ScS} is consistent with the hypothesis of *Datt* [1981] and *Leven et al.* [1981] of a LVZ beneath the 220-km discontinuity. However, in the absence of any observed impedance decreases, the data can be adequately explained by an increase in Q_β above the discontinuity, perhaps owing to colder temperatures prevailing in the stable heart of the subcontinental craton. Regardless of the precise origin of the reflector, the observed correlations of Q_{ScS}, tectonic sampling, and discontinuity depth, as well as the inference of anisotropy, all suggest that the 220-km discontinuity delimits a boundary across which significant variations in characteristic physical processes occur. Whether there is an associated change in bulk material properties cannot be ascertained from the reverberation data alone. Nonetheless, it seems logical to associate the 220-km discontinuity with the base of the subcontinental lithosphere, noting that the depth of this feature may well reach 300 km beneath the stable Australian shield.

The 320-Km Discontinuity

An additional small impedance increase in the depth range of 280–340 km is observed beneath 7 of the seismic corridors examined. The mean depth and reflection coefficient of this discontinuity are 318 ± 22 km, and 0.019 ± 0.008, respectively. As seen in the data reflectivity profiles, this discontinuity produces a parasitic peak superposed on the shallow side-lobe of the 400-km discontinuity. When accompanied by observations of a 220-km discontinuity, the two act in concert to produce a large negative trough at intermediate depths (e.g., Figure 4.9). Although the mean reflection coefficient tests the level of resolution obtainable along a single seismic corridor, the feature itself is remarkably well modeled in the preferred synthetic reflectivity profiles (see Figures 4.6 and 4.7 for examples).

This discontinuity is every bit as difficult to explain as the 220-km discontinuity. In short, no abrupt solid-solid phase transitions in any of the major mantle components are expected in this depth range, and, as discussed in relation to the 220-km discontinuity, changes in composition are unlikely to provide a satisfactory explanation. Because it often coexists with the 220-km discontinuity, anisotropy must also be considered an unlikely candidate–it being difficult to imagine a scenario capable of producing two regions of abrupt variation in preferred alignment over such a small depth interval (~100 km)–unless an alternative explanation of the 220-km discontinuity can be found.

The geographic appearance of this discontinuity demonstrates a notable affiliation with regions of subduction (see Figure 6.6), appearing along the majority of corridors with extensive sampling of the concave side of subduction zones. The exceptions are paths associated with low SNRs (corridors 7 and 16), and are not diagnostic in and of themselves. Any explanation of this discontinuity will also have to explain this affiliation. (Note that we can rule out elevation of the 400-km discontinuity in the subducting slab, as the reflector would be inclined at too great an angle to the horizontal to stack coherently.)

One possibility is that the reflector marks an impedance increase at the base of the LVZ. From the topology of the mantle solidus and geotherm, it is logical to assume that the depths of the upper and lower boundaries of the LVZ will be anticorrelated. Since for the three paths where observations of a LVZ (impedance decrease) and 320-km discontinuity overlap (corridors 5, 15, and 18) the upper boundary of the LVZ rank among the deepest observed, it is a distinct possibility that the 320-km discontinuity marks the base of the LVZ.

Given the observed affiliation with regions of active subduction, we offer the following speculative explanation of the 320-km discontinuity. Recent reconnaissance investigations of high-pressure, high-temperature phase reactions in the enstatite-forsterite-H_2O system have revealed a fascinating level of complexity [e.g., *Akaogi and Akimoto*, 1980; *Liu*, 1987], in which a number of reactions may take place depending on pressure, temperature, and the availability of H_2O. By and large these reactions are not associated with large volume changes unless the weight% of H_2O is of order of 1% or greater. Estimates of mantle H_2O content are typically lower (0.1–0.3%), however, in regions of active subduction, hydrous phases in the downgoing oceanic crust may form an efficient means of transporting H_2O to depth, resulting in locally enhanced water pressures. *Liu* [1988] proposes that the reaction: $5Mg_2SiO_4$ (forsterite) + $3H_2O$ (ice) $\rightarrow$ $3MgSiO_3$ (enstatite) + $Mg_7Si_2O_{14}H_6$ ("phase A"), may mark the bottom of the LVZ since the loss of free water will dramatically raise the mantle solidus (this in addition to the intrinsic density increase of the reaction itself). Thus this explanation is linked to the previous, relating the 320-km discontinuity to the base of the LVZ. However, the current hypothesis offers a more convincing explanation of the strong affiliation with subduction; where water is scarce, the above reaction will have a proportionately smaller effect on the solidus, producing a dim reflector whose magnitude lies below the detection threshold. This reaction also reconciles observations of a 320-km discontinuity along paths which do not display an obvious LVZ. In these cases, a gradual approach of the geotherm to the solidus may produce a broad,

211

seismically-transparent, low-pressure boundary, whereas the assimilation of free water into phase A sharply raises the solidus, producing a reflective high-pressure bound.

Akaogi and Akimoto [1980] suggest that leeching of SiO_2 by upward percolation of free water will result in a more MgO-rich mantle. If percolation occurs on a sufficiently-short time scale, leeching could further facilitate the above reaction in regions of subduction where a mechanism for continual replenishment of deep water exists.

Unlike the 220-km discontinuity, there does not appear to be any significant tectonic expression in the depth of this discontinuity (apart from its occurrence). Whether this is real, or owes to the large uncertainty in the depth estimates is uncertain. Correlations with the depths of other upper mantle reflectors, namely the 220-km and 400-km discontinuities, are likewise weak, and offer no useful diagnostics.

Comparison With Previous Studies

The models of northern Australia determined by *Hales et al.* [1980] and *Leven* [1985] are quite complicated–best described as a series of steps between which velocity is nearly constant or decreases. Apart from the 70-km, 220-km and transition-zone discontinuities, these models feature prominent velocity breaks at 325 km, 512 km, and 725 km. The mantle structure implied by these models is considerably more complicated ι ·   ˙cally assumed. Similar discontinuities are not observed in global earth models such as PREM [*Dziewonski and Anderson*, 1981], raising the question whether the structure implied by these models is real, but so laterally variable as to be smeared out in the global models, or merely artifacts owing to the neglect of lateral heterogeneity and anisotropy. Lateral heterogeneity has proven capable of introducing such artifacts into velocity models obtained from body-wave travel times and amplitudes [*Kennett*, 1981], which are especially susceptible to heterogeneity at the turning point. First-order reverberations, because they densely sample the entire minor arc, are not as sensitive to small scale heterogeneity, and provide an ideal means by which to test the validity of these complicated regional models.

The models of *Hales et al.* [1980] and *Leven* [1985] were derived for earthquake sources in the Banda Sea recorded by a temporary array of seismograph stations running approximately north-south across central Australia. The seismic corridor connecting events in the Philippines seismic zone with station CTAO in northeast Australia (corridor 4) provides a very close facsimile to their experimental geometry. Pictured in Figure 6.10 is a comparison of the data reflectivity profile obtained for this path, with two synthetic profiles mimicking the data geometry. The first synthetic profile was computed for Model 8 of *Hales et al.* [1980]. To utilize this model, which in original form describes only the variation of compressional-wave velocity of the upper 1000 km of the mantle, we were forced to make several assumptions: (1) Velocities were scaled to approximate shear-wave velocities by requiring the travel time through the upper 1000 km to match that predicted by PA2'. (2) The lower mantle was taken from model PEM. Some smoothing was required to join the two velocities profiles. (3) Density contrasts across discontinuities were required to obey Birch's Law [e.g., *Anderson et al.*, 1968], namely that $\delta v_s / v_s \approx 1.4 \, \delta \rho / \rho$. Clearly these approximations are just that, and not likely to recreate the actual shear-wave impedance profile of the Model 8 study area, nonetheless the Model 8 profile provides a good fit to data. The only differences of note between our preferred structure and that of Model 8 are Model 8's larger 325-km discontinuity, and shallower 650-km discontinuity (actually a series of three smaller impedance jumps in Model 8). Overall, the agreement of the three profiles is remarkable. Given the vastly different sampling of mantle heterogeneity characteristic of regional body-waves and mantle reverberations, it is not likely that lateral heterogeneity alone is responsible for the good agreement.

To better demonstrate the level of agreement between discontinuity structures, we have constructed a "pseudo-velocity" profile from the reflector model of Figure 6.10. Assuming a Birch's-Law scaling of velocity and density contrasts across discontinuities, constant interval velocities and $v_s = 4.5$ km/s in the lid, we arrived upon the velocity profile of Figure 6.11. Compared to Model 8, the two wavespeed profiles agree remarkably well,

especially in light of the crudity of the approximations made in constructing the pseudo-velocity profile. While largely qualitative, we take this as strong corroborative evidence of our results, which imply that most of the velocity increase in the upper mantle beneath the northern continental margin of Australia, and the Arafura Sea, occurs across a large number of small discontinuities.

CONCLUSIONS

First-order reverberations have been used to detect discontinuities over an extensive portion of the Earth's upper mantle. The results of this analysis are not always easily explained by standard models of the mantle. Evidence for a strong (SH reflection coefficient $R(70) = 0.035$) discontinuity at an average depth of 67 km is seen in all corridors which do not have shallow LVZ reflectors precluding detection. While the depth and magnitude of this feature are both greater than expected for the spinel $\rightarrow$ garnet lherzolite transition, Al and Ca depletion beneath the continents, and greater temperatures beneath the oceans, may extend the stability field of spinel to sufficient depths. The depth to this discontinuity does not correlate with any of the geothermometers at our disposal, namely Q_{ScS}, the depth of the 400-km discontinuity, or surface tectonic sampling. The lack of correlation with surface tectonics argues against *Forsyth's* [1977] hypothesis that the discontinuity marks a preferred orientation in olivine associated with lithospheric decoupling. Although not formally required to fit the data profiles, a 70-km discontinuity is an admissible feature of all the paths studied, and may global in extent.

For the six corridors whose sampling of surface tectonics was most nearly confined to the Australian shield and stable margin, as well as corridor 1, an additional impedance increase at a mean depth of 230 km is observed. *Leven et al.* [1981] ascribe this feature to a corresponding increase in the preferred orientation of olivine associated with decoupling of the continental lithosphere. Correlation of the depth of this discontinuity with surface tectonic province and Q_{ScS} indicate a thermally-activated origin, and may imply a LVZ

occurring at greater depths (though all that is required by the reverberation data is lower average upper-mantle temperatures). This observation favors the *Leven et al.* model, although we do not observe any obvious azimuthal dependence in the reflection coefficient of the 220-km, which we might expect for reflections from a gradient in preferred orientation, and which also requires a rather large anisotropy (~4%). More work needs to be done to confirm this important observation which, if correct, likely defines the base of the Australian continental lithosphere, and may reflect stress patterns imprinted on the subcontinental mantle by major orogenic events [*Silver and Chan*, 1988].

Reflections from the top of a shallow (<100 km) LVZ are detected beneath paths characterized by primarily oceanic, back-arc and transitional surface tectonic regimes. Estimates of whole-mantle quality factor, Q_{ScS}, are strongly correlated with the depth of the LVZ, as are estimates of the depth of the 400-km discontinuity. The latter may imply that the variations in temperature responsible for topography on the LVZ can still be felt at 400 km depth. The base of the LVZ, on the whole, does not appear to be a efficient reflector—probably extending over 50 km in vertical extent. This observation is compatible with recent mantle models which feature extended LVZs with velocity returning to "normal" lid values only at great depths. The upper boundary of the LVZ appears to be most severe along paths whose sampling of the upper mantle is limited to the concave side of island arcs. Partial melt, owing to greater H_2O pressures generated at the breakdown of hydrous phases in the subducting oceanic crust, may be required to explain this observation Subsequent upward migration of melt may result in the chemical zonation of the LVZ behind these island arcs, which may in turn play an accessory role in explaining the brightness of the reflector.

An additional impedance increase at a mean depth of 320 km occurs along paths characterized by extensive sampling of active subduction zones. Like the 220-km discontinuity, this reflector is difficult to explain in terms of standard models of the upper mantle. From its geographic distribution, we have speculatively assigned it to the base of

the LVZ, made locally "bright" by the sudden increase of the mantle solidus temperature owing to incorporation of free water into phase A or other high-pressure hydrous phases [*Liu*, 1988].

Upper mantle layering is seen to vary significantly over a variety of length scales, correlating with surface tectonics down to depths of at least 230 km, and perhaps as great as 320 km. Oceanic upper mantle appears relatively simple, marked by a LVZ and perhaps the 70-km discontinuity, while on the other hand, continental paths exhibit a more involved upper mantle. High-resolution regional models of the upper mantle beneath the Australian continent and northern continental-margin also contain very complex structure. Remarkably good agreement with results obtained from migration of first-order reverberations, whose sampling of mantle heterogeneity is very different from the turning-wave studies, suggests that these complicated structures are real. If lateral heterogeneity is to explain these results, it must have a characteristic length scale as long as the minor arc path lengths (1000–5000 km)–the same length scale inferred from the variability of discontinuity structures seen on a corridor-by-corridor basis. All of this implies that the upper mantle may be a very complicated place, where lateral heterogeneity, compositional layering, anisotropy, and phase transitions play important roles. Mantle reverberations provide seismology with a powerful tool to unravel the complex interactions of these phenomena.

FIGURE CAPTIONS

Fig. 6.1. Schematic depiction of the inferred upper-mantle and transition-zone structure for corridors characterized by continental sampling. Plotted are the *SH* reflection coefficients used to construct the preferred synthetic data profiles. Included is the decomposition of tectonic sampling, expressed as the percentage of horizontal path length spent in each of the six regions of *Jordan's* [1981] GTR1 tectonic regionalization: A (young oceans; < 25 Myr), B (intermediate age oceans; < 100 Myr), C (old oceans; > 100 Myr), Q (phanerozoic orogenic zone, submerged continental or transitional crust, and subduction zones), P (stable continental platforms), and S (shields).

Fig. 6.2. Schematic upper-mantle and transition-zone structure for paths in the Marginal, Transition and Subduction Zone geographic category. Conventions the same as Figure 6.1.

Fig. 6.3. Schematic upper-mantle and transition-zone structure for corridors 6 and 10 (Table 2.2), whose sampling of surface tectonics is intermediate of the Marginal, Transitional and Subduction Zone, and Back-Arc Basins and Oceans geographic categories. Conventions the same as Figure 6.1.

Fig. 6.4. Schematic upper-mantle and transition-zone structure for paths in the Back-Arc Basins and Oceans geographic category. Conventions the same as Figure 6.1.

Fig. 6.5. Schematic upper-mantle and transition-zone structure for paths whose upper mantle sampling is most nearly limited to the concave side of subduction zones. Conventions the same as Figure 6.1.

Fig. 6.6. Mercator projections of study area depicting the locations of source (triangles) and receivers (squares). Shaded regions denote the portion of the upper mantle sampled along the individual seismic corridors, identified by their number from Table 2.2. Path-averaged apparent depths of upper mantle discontinuities are indicated for each corridor; a "−" superscript is used to denote a discontinuity across which shear-wave impedance decreases with depth.

Fig. 6.7. Estimates of the depth of the 70-km discontinuity, z_{70}, versus values reconstructed from a three-parameter model of regionalized estimates: 48 ± 11 km (oceans), 77 ± 8 km (phanerozoic orogenic zones), and 58 ± 11 km (stable continental blocks). A lack of strong tectonic correlation is implied by the inability of the three parameter model to reconstruct the data.

Fig. 6.8. Estimates of the depth of the LVZ, z_{LVZ}, versus values reconstructed from a two-parameter model of regionalized estimates: 64 ± 10 km (oceans), and 122 ± 16 km (phanerozoic orogenic zones). The LVZ migrates to greater depths with increasing path length in colder continental margins.

Fig. 6.9. Estimates of the depth of the 220-km discontinuity, z_{220}, versus values reconstructed from a two-parameter model of regionalized estimates: 213 ± 13 km (phanerozoic orogenic zones), and 295 ± 30 km (stable continental blocks). The discontinuity moves to greater depths as the percentage of path length spent in stable continental regions increases. This discontinuity may mark the base of the subcontinental lithosphere.

Fig. 6.10. Data (left), Model 8 (left center), and preferred synthetic (right center) reflectivity profiles obtained for corridor 4 in Table 2.2, connecting events in the

Philippines seismic zone with station CTAO in northeastern Australia. Model of the mantle used to construct the preferred synthetic profile is shown schematically at right, consisting of discontinuities at 56, 188, 341, 409, 505, 666, and 746 km depth, depths which compare well with Model 8 of *Hales et al.* [1980].

Fig. 6.11. Comparison of the Model 8 velocity profile [*Hales et al.*, 1980], scaled to approximate *S*-wave velocities, with a "pseudo-velocity" profile (dashed) constructed from the discontinuity structure inferred from synthetic forward modeling of the data reflectivity profile shown in Figure 6.10. To construct the dashed profile, we held interval velocities constant, converted reflection coefficients to velocity contrasts by assuming a Birch's-Law scaling of velocity and density, and corrected for splitting using the value of σ_{650} (4 s) obtained in Chapter 5. While the analysis is qualitative, the similarity demonstrates the remarkable agreement obtained between discontinuity structures, and implies that most of the velocity increase in the upper mantle beneath the northern continental margin of Australia occurs across discontinuities.
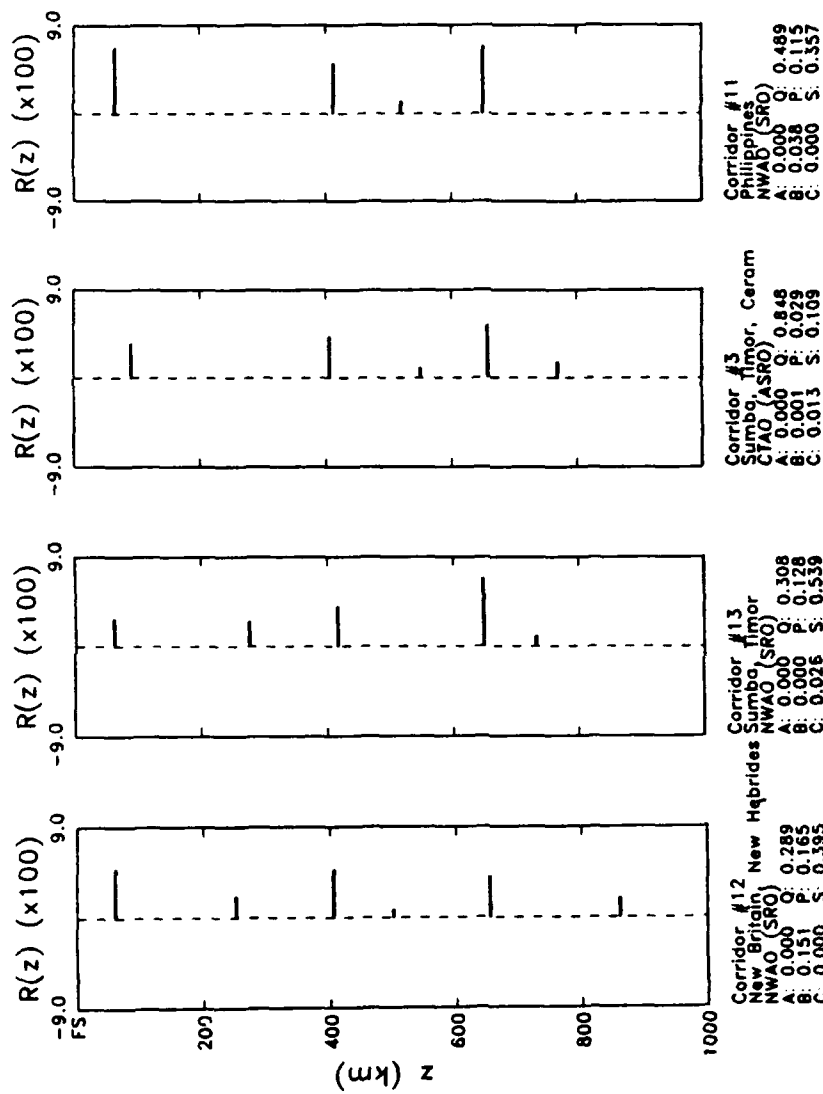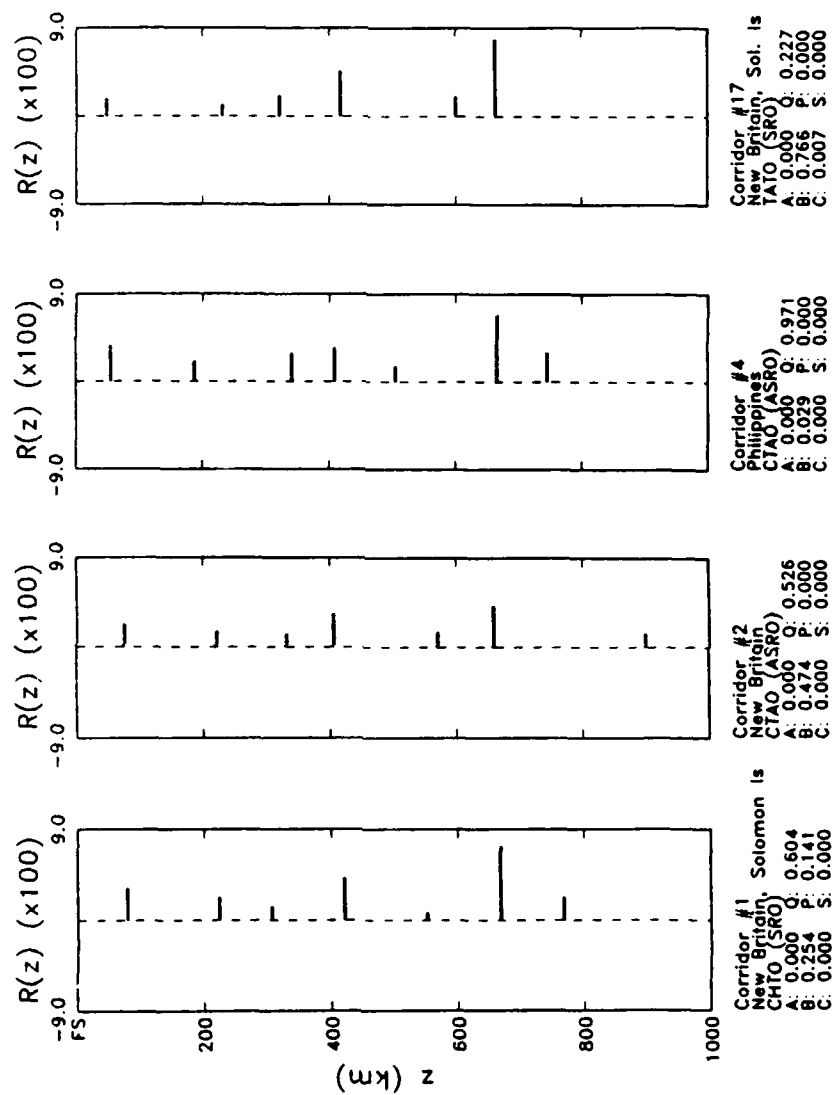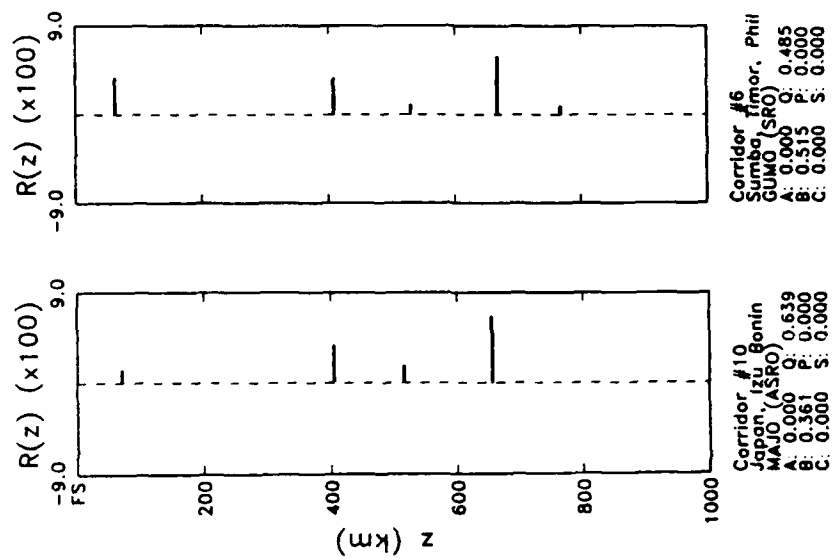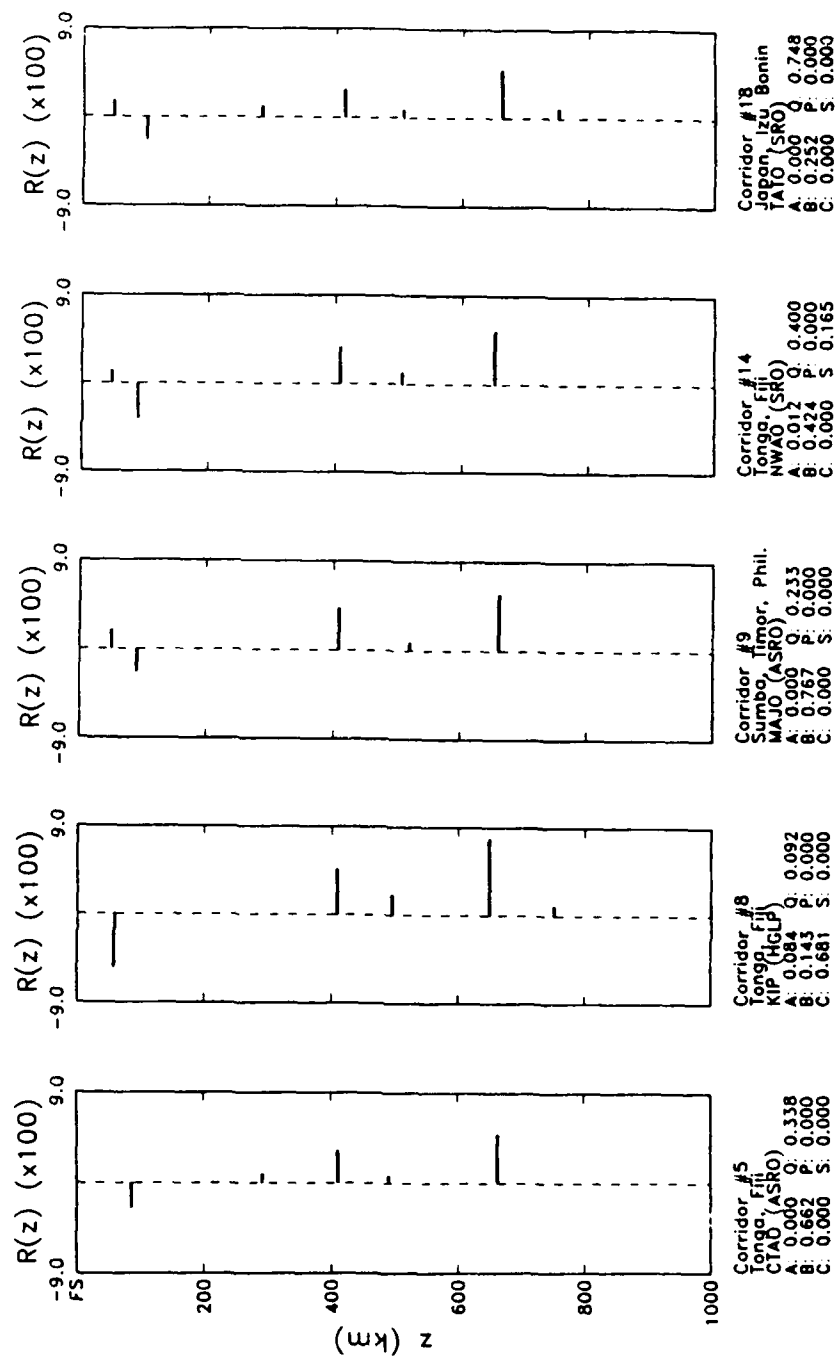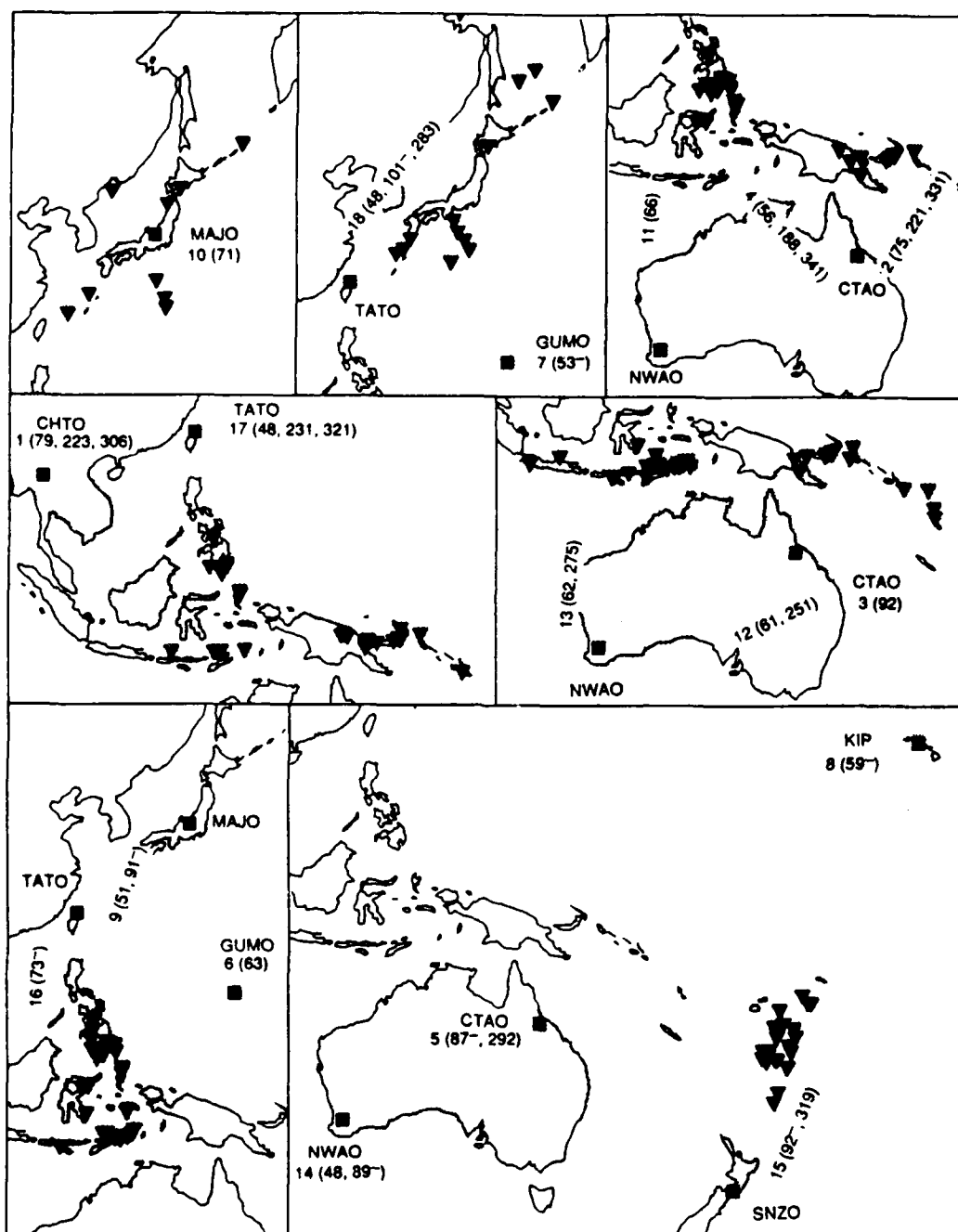
Figure 6.1

220

Figure 6.2

Figure 6.3
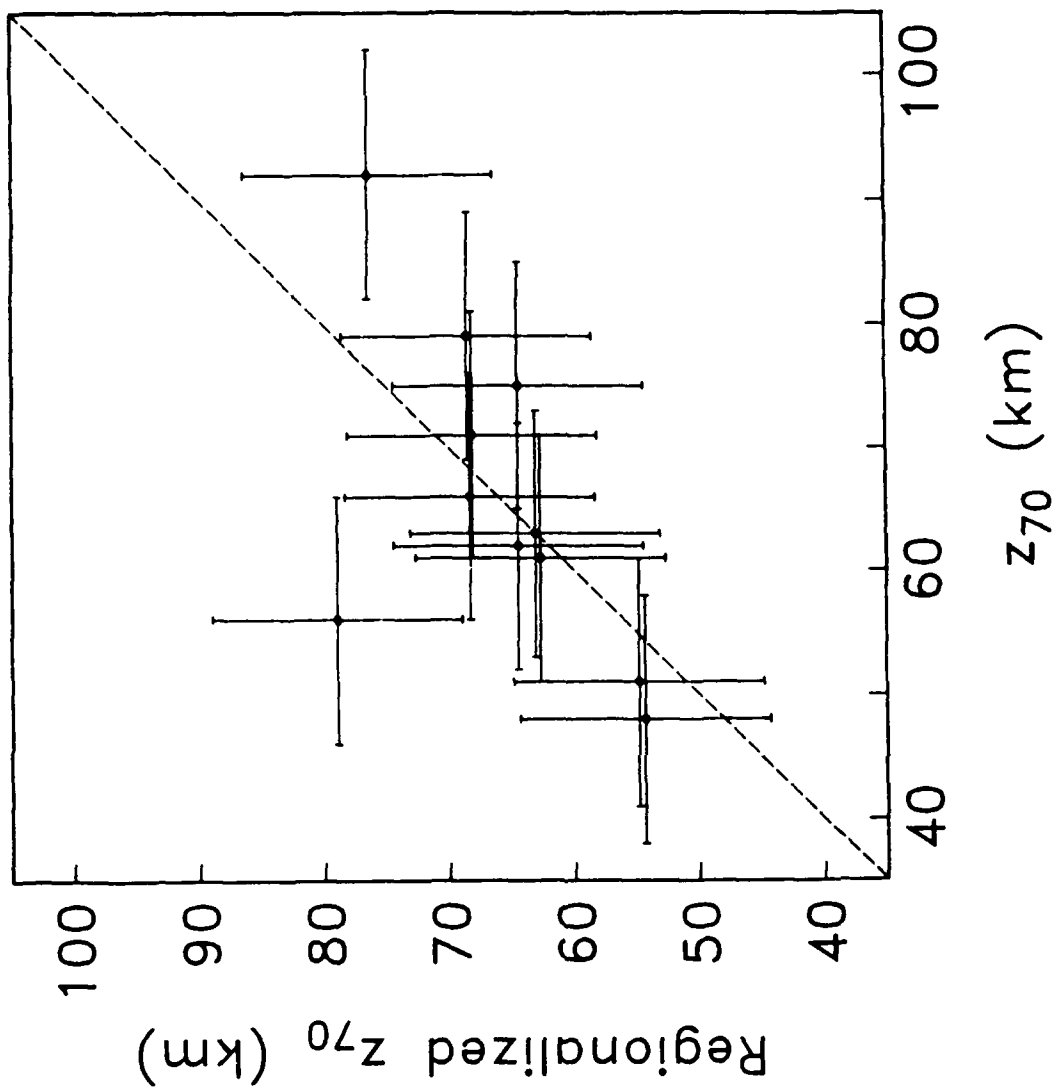
222

Figure 6.4

223

Figure 6.5

224

Figure 6.6

Figure 6.7
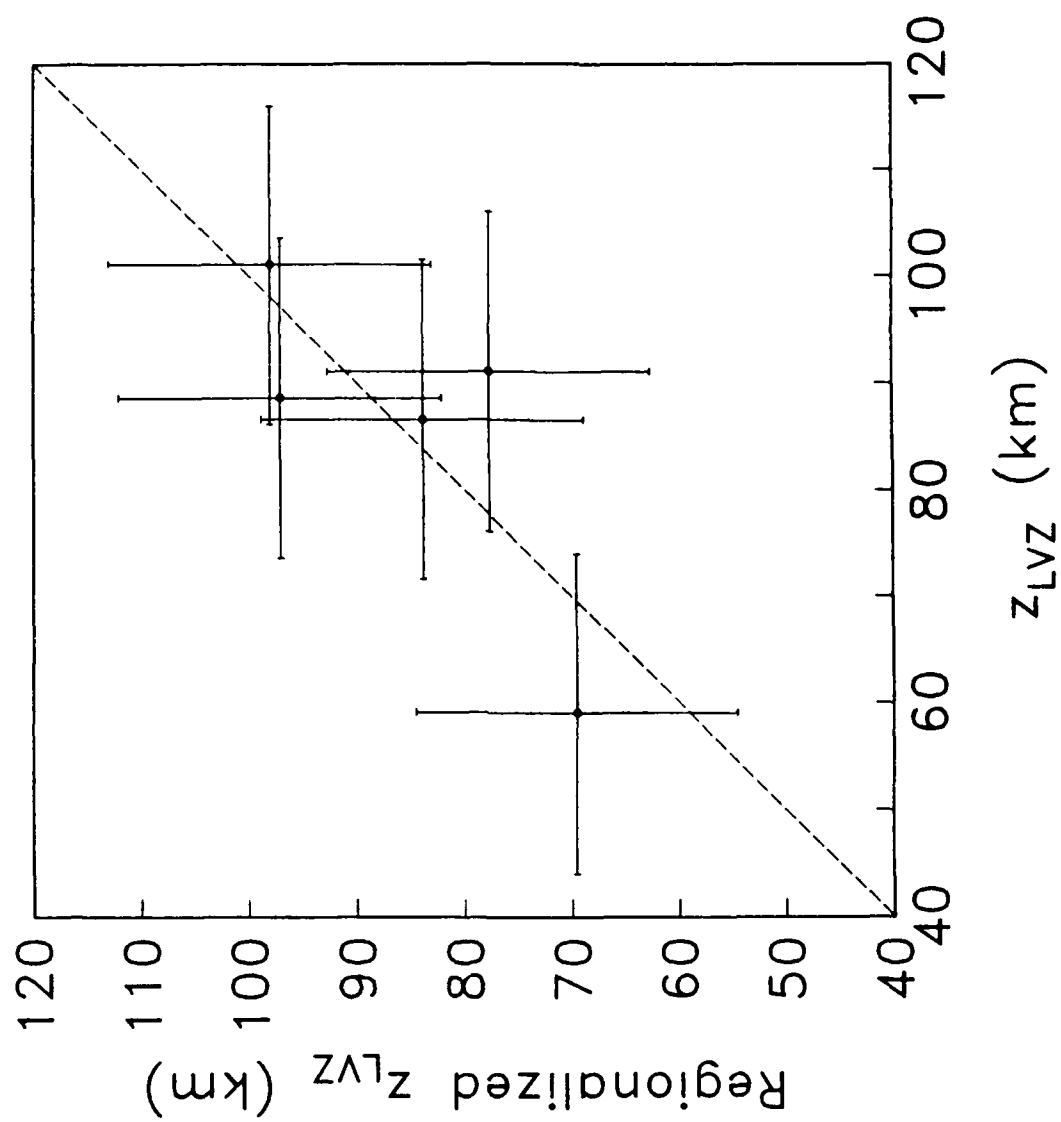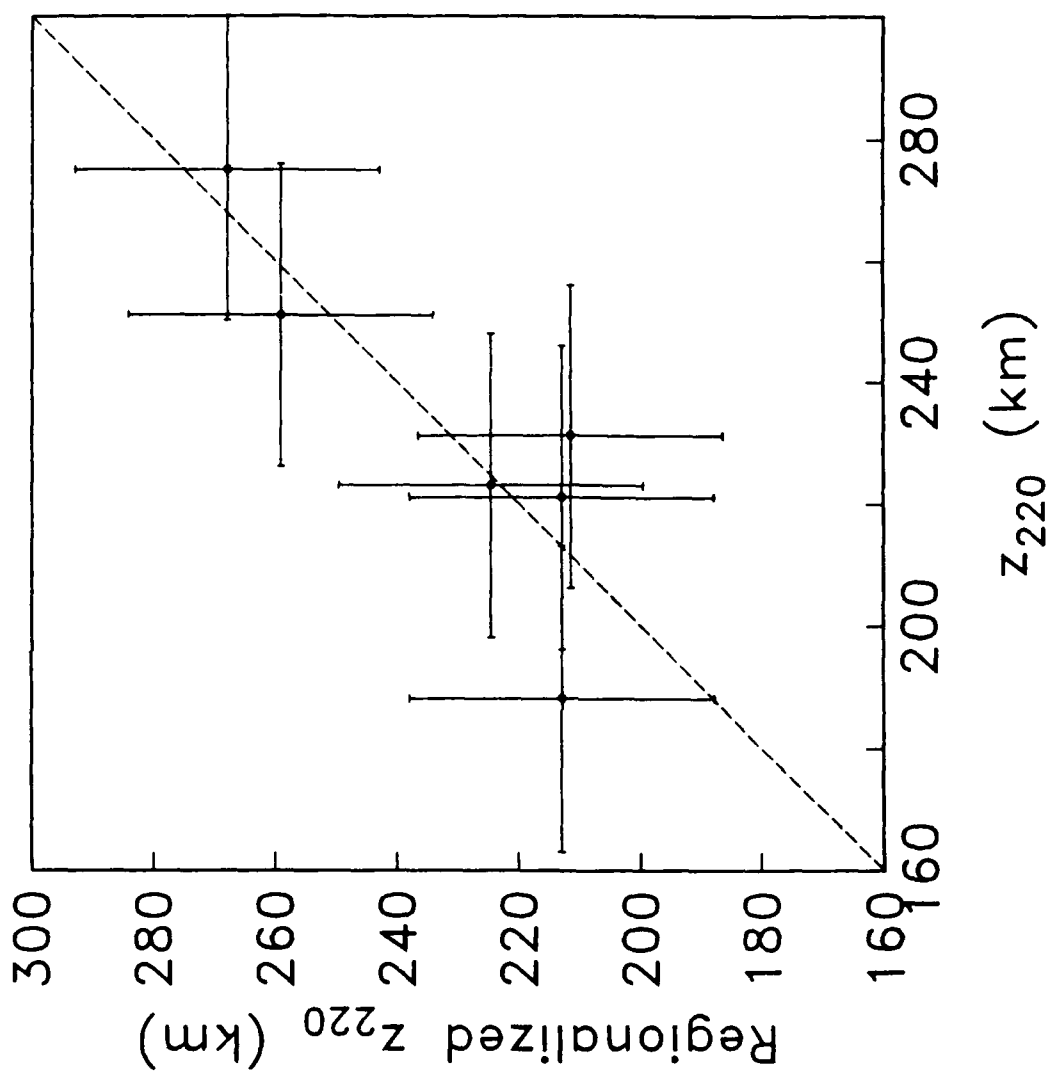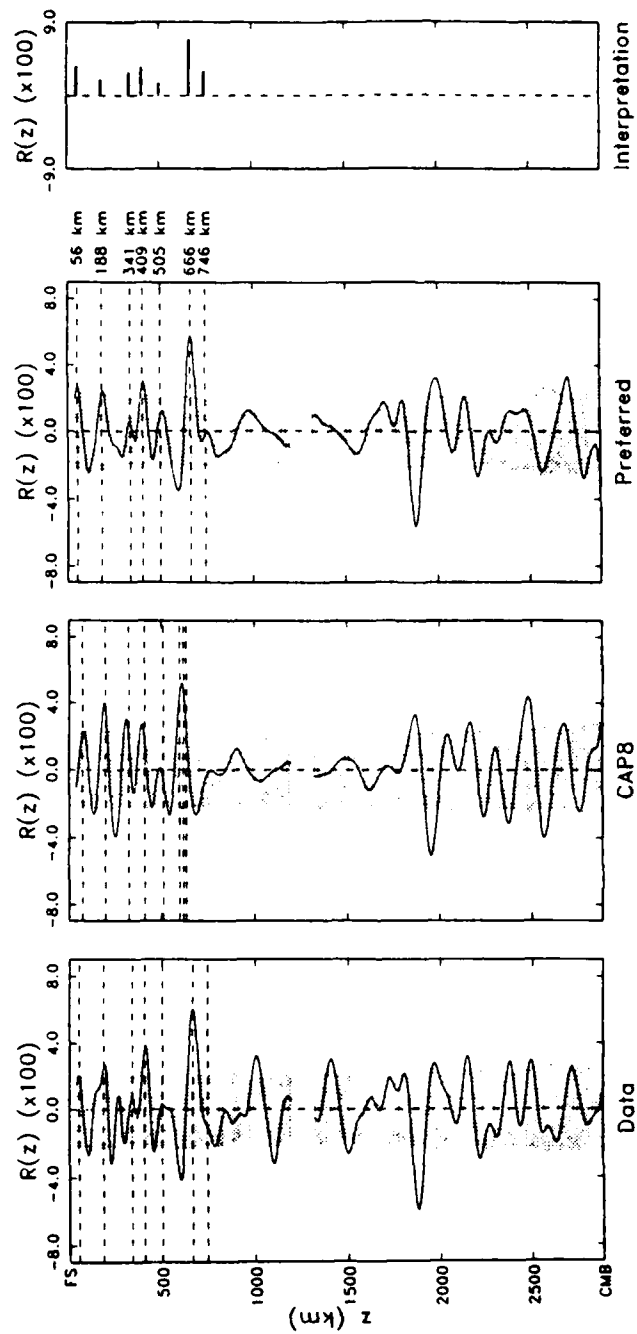
226

Figure 6.8

Figure 6.9

228

Figure 6.10

229

Figure 6.11

230

THE LOWER MANTLE AND CORE-MANTLE BOUNDARY

INTRODUCTION

The lower mantle is easily the largest distinct layer of the Earth, constituting some 55% of the Earth's total volume. As depicted in the majority of seismic models, the lower mantle appears homogeneous, with density and elastic wavespeeds increasing along an adiabat throughout most of the upper 2000 km [e.g., *Jackson*, 1983]. In the lowermost 150 km to 300 km of the mantle, identified with Bullen's D" region, seismic velocities increase only slightly with depth, perhaps even decreasing [e.g., *Doornbos and Mondt*, 1979], implying that either the assumption of adiabatic compression and/or homogeneity is being violated [e.g., *Cleary*, 1974]. Region D" has likely ties to a number of phenomena of interest to modern geophysics, including: evolution and composition of the core [e.g., *Ringwood*, 1979; 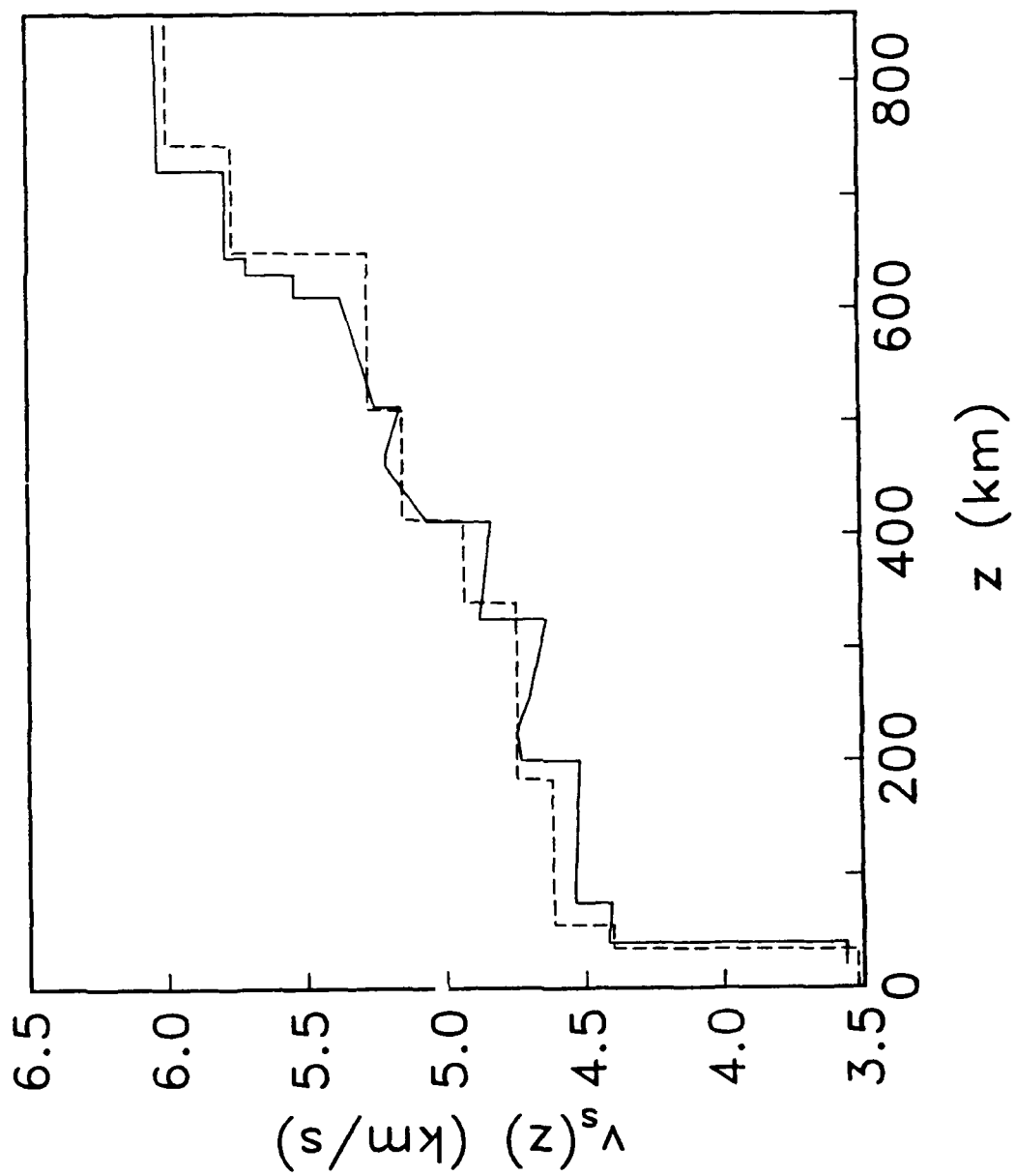*Ruff and Anderson*, 1979; *Knittle and Jeanloz*, 1986], heat flux into the mantle [e.g., *Turcotte and Oxburgh*, 1967; *Jeanloz and Richter*, 1979; *Doornbos et al.*, 1986], the fate of subducted slabs [e.g., *Dickinson and Luth*, 1971; *Ringwood*, 1975] and the source region of mantle plumes [e.g., *Yuen and Peltier*, 1980; *Hofman and White*, 1982; *Stacey and Loper*, 1983].

D" is recognized to be heterogeneous at many length scales [e.g., *Haddon*, 1982; *Dziewonski*, 1984, *Lavely and Forsyth*, 1986], making it difficult to isolate radial, or global structure, from local variations, especially when limited by geographically-sparse data sets. Furthermore, the high velocities of the lower mantle, and the necessity of "looking" through a heterogeneous upper mantle and transition zone, make the mapping of D" structure one of seismology's most difficult tasks. Nonetheless, many models of D" structure have been forwarded, perhaps the most striking of which are those of T. Lay and associates [e.g., *Lay and Helmberger*, 1983; *Young and Lay*, 1987], which feature a 2.5–3% increase of shear velocity ~275 km above the core-mantle boundary (hereafter referred

to as the CMB). If correct, such a model would have profound implications for mantle composition and evolution.

Also of interest is structure of the CMB itself–the site of the largest localized density contrast in the Earth, exceeding even that of the free surface. Tomographic inversions of large numbers of *PKP* and *PcP* travel times have provided evidence of CMB imhomogeneity variously interpreted as boundary topography [*Morelli and Dziewonski*, 1987] and/or chemical boundary layers (CBL) [*Creager and Jordan*, 1986], perhaps manifested as "continents" rafting on the liquid outer core [e.g., *Jordan*, 1979*b*].

The purpose of this chapter is to use the previously documented observations of first-order reverberations to place additional constraints on the layering of the lower mantle and CMB. First-order reverberations provide an ideal tool for probing the lower mantle. The near-vertical geometry of their ray paths offers uniform sampling of the lower mantle over short horizontal path lengths, while rendering them less sensitive to the deteriorative effects of lateral velocity heterogeneity. Because first-order reverberations are reflected at subcritical angles, their amplitudes are equally sensitive to density and velocity contrasts–an important asset in the description of mantle layering. Building upon the results of Chapter 4, we employ first-order reverberations to search for reflectors of long-period energy in the lower mantle not included in standard models. To place limits on the possible complexity of the CMB we appeal to an alternative method which, analogous to crustal modeling, utilizes the contamination of ScS_n and $sScS_n$ waveforms by reflections produced by transitional layers near the CMB should such layers exist.

Observations

Reflectivity Profiles and Depth Ambiguity

Much of the utility of first-order reverberations derives from their unique ray geometries, unfortunately, this same property admits ambiguity into the depths of discontinuities imaged by first-order reverberations, resulting in a reflectivity profile which is nearly a

232

mirror image about the midpoint of the mantle with respect to travel time. For the transition-zone discontinuities, a priori knowledge of depth is good, and ambiguity presents no real interpretive problem other than obscuring the depth region populated by false images. For the lower mantle, where structure is not nearly so well known, ambiguity proves more noisome. For instance, a reflector marking the top of the LVZ at a depth of, say, 100 km, will also be registered as an impedance increase ~170 km above the CMB, corresponding to the depth of a D" reflector proposed by *Wright et al.* [1985]. Unfortunately, using first-order reverberations alone, it is impossible to completely resolve this ambiguity.

In Chapter 6 it was found that discontinuity structure in the upper mantle was tectonically correlated, i.e., corridors with similar tectonic sampling, as quantified by the *Jordan* [1981] regionalization, displayed essentially similar patterns of upper mantle reflectors. Deeper discontinuities, in particular the transition-zone discontinuities, are apparently not tectonically correlated, and it seems logical to assume that deeper discontinuities will not be either. Given these assumptions, it is possible to partially resolve reflectivity profile ambiguity by appealing to the tectonic correlation in assigning reflectors to either the upper or lower mantle. The synthetic forward modeling experiments of Chapters 4 and 6 and comparisons with previous studies suggests that there is little reason to expect the widespread occurrence of impedance decreases beneath a depth of ~150 km in the upper mantle. On the other hand, impedance increases appear to be spread throughout most of the upper 1000 km of the mantle. We therefore feel confident in assigning to the lower mantle any feature which would otherwise mark an impedance decrease in the upper mantle beneath a depth of 150 km. Features which would appear as impedance decreases in the lower mantle will be (and have been) assigned to the upper mantle, a choice motivated not only by tectonic correlation and abundant a priori observations, but also by the probable hydrodynamic instability of density decreases in the lower mantle (although we must be careful in associating density decreases with impedance

decreases, viz a vis the effect of Fe on mantle silicates). While this analysis is necessarily somewhat subjective, we feel that the rewards of imaging lower mantle discontinuity structure justify the risk of possible misinterpretation.

Reflectivity of the Lower Mantle

To alleviate the deteriorative effects of reverberation splitting, the reflectivity profiles considered in this chapter were computed from data subjected to a second stage of low-pass filtering (corner at 20 mHz, maximum of passband at 30 mHz). Besides reducing the impact of reverberation splitting, filtering also improves the level of fit obtained between data and synthetic profiles, producing simpler waveforms and attenuating apparent structure in residual profiles arising from the inevitable slight mismatches of data and synthetic profiles. Unless otherwise stated, all data in this chapter can be assumed to have been filtered in this way.

Figure 7.1 compares data and parsimonious synthetic reflectivity profiles for the heterogeneous corridor connecting shocks in the Sumba, Philippines and New Britain seismic zones with the SRO station CHTO in Thailand (corridor 1 in Table 2.2). To model the shallow structure of this path, we have chosen to place impedance increases at 79 km and 223 km depth–a structure consistent with nearby models of the upper mantle [e.g., *Hales et al.*, 1980; *Leven*, 1985]. By comparison, the reflectivity profile for the back-arc basin corridor connecting events in the Sumba and Philippines seismic zones with the ASRO station MAJO in Japan (corridor 9 in Table 2.2), the only discontinuity necessary in the upper 300 km of the mantle is a small impedance decrease at 90 km, interpreted as the top of the low-velocity zone (Figure 7.2). Figure 7.3 depicts data and synthetic profiles for the corridor connecting the SRO station GUMO on Guam (corridor 6) with events in the Sumba and Philippine seismic zones. Again data is well modeled by a synthetic profile computed for a mantle with only a single discontinuity in the upper 300 km, in this case an impedance increase at 65 km depth. The residuals between data and synthetic profiles for

the latter two corridors (Figures 7.2 and 7.3) possess reflectivity peaks at several depths in the lower mantle, most notably in the D" region (305 km and 340 km above the CMB, respectively). Given the limited resolution attainable from events sampling a single corridor, however, the reflectivity peaks are not highly significant in either example. Similar peaks in D" are noted beneath roughly one-third of the 18 seismic corridors and display some geographical coherence, with observations limited to the lower mantle beneath western Australia and the Philippine Sea (Table 7.1, Figure 7.4). Other $R(z)$ peaks in the individual profiles display little if any consistency across the data set, suggesting they are due largely to noise processes, although we cannot rule out the possibility of laterally varying structure. As discussed in Chapter 4, our primary dictum was to be as parsimonious as possible in explaining the data, i.e., we have proposed additional discontinuities in the lower mantle only where clearly necessitated by data. If we have erred in this analysis, the bias should be toward simpler lower-mantle structure. The accumulation of more reverberation data over the next few years should allow for a more definitive statement on lower mantle reflectivity.

REGION D"

A Discontinuity in D"

As a means of improving resolution we have stacked the entire suite of 18 data and parsimonious synthetic reflectivity profiles, resulting in roughly a factor of four improvement over the resolution attainable along a typical seismic corridor (Figure 7.5). Apart from the two small impedance increases at 730 km and 915 km discussed in Chapter 5 (the false images of which appear near 1830 km and 1640 km, respectively), the only lower mantle $R(z)$ peak exceeding the 5% false-alarm level occurs 325 km above the CMB. Due to ambiguity, this reflector can also be interpreted as an impedance decrease ~200 km beneath the Earth's surface. Although it is not possible to distinguish between these two alternatives with the present data set, the agreement of the deeper interpretation with the

235

discontinuity proposed by *Lay and Helmberger* [1983] is compelling. On the other hand, there is little prior evidence for an upper-mantle impedance decrease near 200 km depth with the possible exception of the low-velocity zone, which was included in the synthetic profiles when necessitated by data (Chapters 4 and 6). (Note that the deep LVZ proposed by *Leven et al.* [1981], and discussed briefly in Chapter 6, lies below the 220-km discontinuity. Thus its lower-mantle false image would be too shallow to explain these observations, and is pertinent to only a few profiles.) Thus while largely subjective, our preferred interpretation is that of an impedance increase near the top of region D''. The mean depth inferred from Figure 7.4 agrees with individual corridor estimates (Table 1 and Figures 7.2 and 7.3). It must be noted that this feature is not strongly required by the data, with $R(2580)$ only slightly greater than the 5% false-alarm level.

Assuming the reflector corresponds to the discontinuity proposed by *Lay and Helmberger*, we can use their estimate of velocity increase ($\delta v_s/v_s = 2.75\%$) to constrain the associated contrast in density. The reflectivity estimate of Figure 7.5 ($R(2580) = 0.0085$), is consistent with a slight decrease in density, $\delta\rho/\rho = -1\%$ ($\delta\rho = -0.054$ gm/cm^3), implying long-term instability of the layer, although the probable uncertainties in this analysis are large. There are, however, several caveats which must be attached to this estimate: (1) Lateral velocity heterogeneity and topography on the discontinuity will lead to destructive interference between first-order reverberation analogs, and reduced correlation with discontinuity response functions, resulting in an estimate of $R(z)$ which is lower than the actual. (2) By stacking over the entire data set, we may have included seismic corridors along which this feature is not present. The variability of the observations may be due to signal-to-noise ratio limitations, lateral variations in the strength of the reflector, or its absence along some of the seismic corridors. In a study of Tonga-Fiji events recorded in North America, *Garnero et al.* [1988] found no evidence for a D'' discontinuity, while for a neighboring corridor, connecting deep South American events with the U.S. and Canada, they found strong evidence to support the *Lay and Helmberger* [1983] model, implying

spatial intermittency of the discontinuity at moderate length scales (~2000 km). This suggests that we should repeat the preceding analysis including only those paths where the D" discontinuity appears to be present. Doing so increases the estimate of $R(2580)$ to 0.022, which includes a multiplicative correction of 1.3 to account for the splitting of first-order reverberations. Unlike the 650-km discontinuity, it is not possible to estimate directly the standard deviation of travel times for reverberations produced at the D" reflector from the frequency spectrum of the apparent reflection coefficient. Rather, to compute the correction we assumed that topography of the magnitude observed on a corridor-by-corridor basis also exists along the individual corridors. Given that the minor-arc paths are as long as the apparent scale length of topography (Figure 7.4), this would seem to be a reasonable assumption. The correction allows for roughly 50 km (two standard deviations) of peak-to-peak discontinuity topography plus 2 s of uncorrelated mantle heterogeneity. (See Chapter 5 for a discussion of splitting, and derivation of the amplitude correction.) $R(2580) = 0.022$ implies a density increase of 1.7% ($\delta\rho = 0.09$ gm/cm^3) across the discontinuity, close to a Birch's-Law scaling: $\delta v_s/v_s \approx 1.4 \, \delta\rho/\rho$ [*Anderson et al.*, 1968]. We note that the discontinuity is also apparent in the full-bandwidth stack of Figure 5.8. Given the degree of reverberation splitting we expect, the discontinuity must appear abrupt at the seismic wavelengths of interest if it is to remain visible in that stack. The full-bandwidth estimate is peaked near 30 mHz, and somewhat narrowly banded, implying a dominate wavelength of 200 km near the CMB. Referenced to Figure 5.9, this implies that the transition width of the reflector is unlikely to exceed 40 km, and is almost certainly less (cf. *Young and Lay*, [1987]).

As a test of the uniformity of observation of this discontinuity, we have stacked the 13 seismic corridors along which the discontinuity is not clearly observed on an individual profile basis. The resulting reflectivity profile is shown in Figure 7.6. As can be seen in this figure, the D" discontinuity is attenuated relative to that of Figure 7.5, suggesting that it

is either much weaker (by nearly a factor of two) or not present among a significant fraction of the paths included in the stack.

Possible Origins of a D" Discontinuity

Because the two major components of the lower mantle, perovskite and magnesiowüstite, are predicted to be stable to pressures exceeding those at the CMB [e.g., *Vassiliou and Ahrens*, 1982; *Knittle and Jeanloz*, 1987] (but see *Park et al.* [1988] for a possible exception), it is not likely that the proposed D" discontinuity marks a phase transition in an otherwise homogeneous mantle. Although changes in the symmetry system of perovskite have been observed in analog components, and may occur in silicate perovskites [e.g., *Wolf and Bukowinski*, 1985], they are predicted to occur at fairly shallow depths in the lower mantle, suggesting that they too are unlikely candidates for a D" discontinuity. The observation of small impedance increases ~70 km and ~240 km below the 650-km discontinuity, may be evidence of such changes (Chapter 5).

Several structural interpretations of D" heterogeneity and layering have recently been forwarded. *Knittle and Jeanloz* [1986] suggest that the lower 300 km of the mantle may be a residuum layer created by oxygen dissolution into the core, with an increase in lower-mantle elastic wavespeed owing to an increase in stishovite abundance [*Knittle and Jeanloz*, 1988]. Alternatively, flow of softened lower-mantle material towards "catchments," or sites of plume-like upwelling, may locally resemble chemical inhomogeneity with vertical length scales comparable to D" thickness [e.g., *Stacey and Loper*, 1983]. Hot mantle material would be both buoyant and seismically slow relative to the surrounding mantle, however, in direct opposition to our results. Furthermore, while this model predicts horizontal heterogeneity scale lengths of 1000 km radiating out from the catchments, lengths scales perpendicular to the flow are likely to be much shorter, perhaps on the order of 10 km. It seems unlikely that our sampling of the lower mantle would be so frequently aligned with the along-grain direction of these flows. While in agreement with

observations of directionally-dependent scattering in D" [e.g., *Haddon*, 1982], this sort of structure is an unlikely explanation of our observations. A third possibility is accumulation of the crustal component of subducted slabs upon the CMB [e.g., *Ringwood*, 1975]. This model has the attractive feature of providing a long-term storage area for oceanic crust [*Hofman and White*, 1982]. Chemically denser material at the base of the mantle will be swept towards regions of upwelling [*Davies and Gurnis*, 1986; *Hansen and Yuen*, 1988], and thinned elsewhere, perhaps accounting for the geographically intermittent nature of the observations. (Note that this mechanism applies to models of chemically-distinct layers in general.)

Depth Variation

As previously noted, depths to the discontinuity at the top of D" appear to vary by ~70 km for the 5 seismic corridors where it is most confidently observed; see Table 7.1. Due to interference with false images of upper mantle structure and low signal-to-noise ratios, measurement uncertainties in the apparent depths of this reflector are large (± 25 km). Nonetheless, inferred separation from the CMB, h, is positively correlated with two-way, vertical travel time delay through region D", $\delta\tau_{D''}$, at the 95% confidence level (Figure 7.7). *Young and Lay's* [1987] estimate for the mantle region beneath India and the Indian Ocean also agrees quite well; other estimates [*Lay and Helmberger*, 1983] for regions more widely separated from ours do not correlate. $\delta\tau_{D''}$ is calculated by path-averaging the L02.56-predicted [*Dziewonski*, 1984] travel time delay through the lowermost 400 km of the mantle. In Chapter 5, tomographic models of the mantle where shown to accurately predict whole-mantle travel-time delays measured by ScS_n, and to reduce the variance of inferred depths of the 400-km and 650-km discontinuities, providing justification for their use in this application. Since model L02.56 is a P-wave-derived model it is necessary to assume a scaling between P- and S-wavespeed perturbations, which is set at $\delta v_s = 1.1\delta v_p$, consistent with recent lower-mantle tomography results [e.g., *Dziewonski and*

Woodhouse, 1987; *Giardini et al.*, 1988]. A further multiplicative correction of 1.1 was obtained from the calibration of observed and model-predicted ScS_n travel-time residuals. The resulting range of $\delta\tau_{D''}$ values is 1 s, or about 1% of total travel time. (We note that, although the correlation appears quite strong, the error bounds assigned to the individual depth estimates are appropriate. Thus, while we are confident in the basic observations, we must regard the extreme degree of correlation as somewhat fortuitous.)

The sense of the observed correlation is such that the discontinuity is furthest removed from the CMB in locally slow regions of D''. Since we would expect the increase in velocity associated with this highly mobile discontinuity to be a major contributor to D'' heterogeneity, and therefore $\delta\tau_{D''}$, the sign of the correlation is opposite to what we would predict if all other effects were held constant, suggesting an additional, perhaps thermal, contribution to heterogeneity. Assuming temperature anomalies are coherent in sign and magnitude across D'' (a reasonable assumption given the 1000–2000 km horizontal length scales under consideration) and that the only compositional contribution to heterogeneity is due to the discontinuity itself allows us to formulate a simple model of D'' heterogeneity. Let h_0 be the maximum thickness of D'' (taken to be 400 km, although the precise value is relatively unimportant in what follows), and h the observed separation of the D'' discontinuity from the CMB. For a prescribed temperature anomaly ΔT we find:

$$\Delta T \left(\partial_T \delta\tau_{D''}\right) \approx -\Delta T\, \partial_T \bar{v}_s \frac{2 h_0}{v_s^2} - \Delta T\, \partial_T h \left[\frac{2\delta v_s}{v_s^2}\right] \qquad (7.1)$$

where $\bar{v}_s$ is the mean D'' velocity and ∂_T denotes the partial derivative with respect to temperature. The first and last terms can be estimated from Figure 7.6, specifically: $\Delta T(\partial_T \delta\tau_{D''}) = 1$ s, and $\Delta T(\partial_T h) = 70$ km. Assuming $\bar{v}_s = 7.2$ km/s, $\partial_T\, \bar{v}_s = -4.4 \cdot 10^{-4}$ m/s°C, and $(\delta v_s / v_s)_h = 2.75\%$ [*Lay and Helmberger*, 1983], we find $\Delta T = 230°$ C, a not unreasonable value for long-wavelength temperature variations near the base of the mantle. (Note that here the parity of delays due to the displacement of the discontinuity and thermal

240

heterogeneity are reversed from those of the transition zone travel time τ_{TZ}. This is because $\delta\tau_{D''}$ is the travel time through a layer of constant thickness, h_0, and as such is much less sensitive to discontinuity topography.) A model consisting of a layer of intrinsically-dense mantle dregs, swept towards regions of locally hot–seismically slow–upwelling, can explain the sign of the observed correlation between discontinuity topography and velocity heterogeneity. Alternatively, assuming topography is produced by the thermal elevation of a phase transition requires a Clapeyron slope nearly an order of magnitude greater than determined for the transition-zone discontinuities ($\gamma_{D''} = -16.4$ MPa/°C). As stated earlier, there is little experimental evidence for deep mantle phase transitions, prompting us to favor the CBL interpretation, and, while the sign of the inferred Clapeyron slope is what we would expect for a lower mantle discontinuity [Navrotsky, 1980], it might be possible to rule out a phase-transitional origin solely on the basis of the magnitude of the required slope.

For a coefficient of thermal expansion, $\alpha = 2.5 \cdot 10^{-5}/°C$ [Jeanloz and Thompson, 1983], $\Delta T = 230°$ C decreases density of the dreg layer by 0.03 gm/cm^3. This is significantly less than the inferred density increase across the D'' discontinuity ($\delta\rho = 0.09$ gm/cm^3), implying a net mass excess in seismically slow regions of the lower mantle, reconciling the seemingly anomalous correlation of topographic lows (highs) on the CMB beneath seismically slow (fast) regions of D'' [Davies and Gurnis, 1986; Morelli and Dziewonski, 1987]. A 300 km accumulation of dregs is capable of depressing the CMB in excess of 5 km, consistent with the estimates of Morelli and Dziewonski [1987].

Viscous drag associated with convective flow over the dreg layer will cause accumulation of dregs beneath upwellings, and maintain topography on the interface. From simple force-balance arguments it can be shown that interface topography, δh, should scale as:

$$\delta h \sim \left[\frac{3\eta u L}{\delta \rho g d} \right]^{1/2} \tag{7.2}$$

where L is the characteristic horizontal half-width of topography, η the viscosity of the overlying fluid, d the scale height of flow (i.e., vertical extent of the boundary layer), and u the fluid velocity away from the boundary. The length scale L is inferred from the lack of correlation between discontinuity depth and velocity heterogeneity with other regions studied by *Lay and Helmberger* [1983], implying ~2000 km coagulation lengths scales for individual dreg "pools." $\delta \rho$ is assumed known (0.09 gm/cm³); adopting reasonable values for the remaining parameters ($\eta = 10^{21}$ Pa·s, $d = 300$ km, $u = 0.1$m/yr, and $L = 1000$ km) produces δh of order 200 km. While this analysis is primarily qualitative, we conclude that the inferred density contrast, topography (on both the discontinuity and CMB), and thermal anomalies associated with the proposed CBL appear to be internally consistent, and reasonable from the standpoint of mantle dynamics.

OTHER LOWER MANTLE DISCONTINUITIES

Apart from the D" reflector, and the previously noted impedance increases above 1000 km depth, no other discontinuities are found in the lower mantle. The literature contains numerous references to lower mantle discontinuities in velocity, or its first derivative, near depths of 1200 km, 1550 km, and 2300 km [e.g., *Johnson*, 1969; *Corbishley*, 1970; *Evernden and Clark*, 1970], primarily obtained from P-wave travel-time studies. The role of mantle heterogeneity was ignored in the majority of these early studies, drawing into question the identification of 1%-velocity variations in geographically-diverse data sets, although the agreement in proposed depths is intriguing. If present in the regions of the lower mantle sampled in this study, these discontinuities must be either small (less than the nominal $R(z)$ resolution of 1%) or geographically intermittent or subject to lateral depth variations well in excess of 50 km, reducing the correlation with DRFs. Our results agree

with most recent models of the lower mantle, and are consistent with the notion of smooth, adiabatic increase of lower mantle velocity and density.

BOUNDARY-INTERACTION MODELING

The method of first-order reverberation "migration" is capable of resolving discontinuities characterized by $R(z)$ as small as 1%. Unfortunately they tend to break down for discontinuities near the free surface and the CMB, which generate first-order reverberations arriving within the wave trains of the ScS_n and $sScS_n$ phases. If not completely stripped, energy from zeroth-order reverberations will map into both shallow and very-deep discontinuity structure. The large amplitudes of these phases relative to first- and higher-order reverberations suggests that their spurious contribution to the reflectivity profiles could be significant—a fact which prompted us to disregard the reflectivity profiles within 30 km of the upper and lower bounds of the mantle. It is, however, still possible to use first- and higher-order reverberations to map structure within these depth ranges.

Waveform Inversion

The inversion of zeroth-order reverberations includes the estimation of a simple, one-layer crustal model, parameterized by its thickness, z_M, and reflection coefficient $R(z_M)$. Sensitivity to the crust is not indigenous to zeroth-order reverberations per se, but rather to the superposition of first- and higher-order reverberations generated at the Mohorovicic (M) discontinuity. Figure 3.1 depicts the effect of multiple crustal transits on the composite wave train of ScS_n and higher-order reverberations. Although only long-period data are used (corner at 40 mHz tapering to zero at 60 mHz), the effect of the crust is pronounced. By analogy, the effects of similar layering near the CMB would be equally pronounced. Because the CMB resembles the free surface, both in terms of intrinsic density contrast and variation of physical processes and characteristic time scales across the interface, there is

reason to believe that it too may support a CBL—be it buoyant slag floating on the molten core and/or dense scoria settling out of the mantle.

Previous studies of CMB layering have employed *PcP* and multiple *ScS* phases with often equivocal results. *Kanamori* [1967] argues for an extremely "sharp" CMB reflector (<1 km) on the basis of high-frequency *PcP* spectra, but admits that his data cannot rule out the possibility of a smoothly-varying background component. Other studies of *PcP* require the density contrast at the CMB (defined by velocity) to be small [*Buchbinder*, 1968; *Ibrahim*, 1971], implying a density transition zone at least 30 km wide. *Ibrahim* [1971] finds evidence for two low-velocity layers straddling the CMB and finite shear velocity ($v_s = 2.2$ km/s) in the core—the latter results at odds with studies of multiple *ScS*, which impose an upper limit of $v_s \leq 0.7$ km/s in the outer portion of the outer core [e.g., *Press*, 1956; *Anderson and Kovach*, 1964; *Sato and Espinosa*, 1967]. *Anderson and Kovach* [1964] and *Kovach and Anderson* [1964] argue against a mantle-side CMB transition zone, citing the lack of extraneous frequency dependence in ScS_{n+1}/ScS_n spectral ratios. These two studies, however, impose only a very weak upper limit on CMB layering, namely that it be not much more profound than layering of the crust, effects of which were also unobserved.

To be hydrodynamically stable over long time scales, intrinsic density contrasts associated with finely stratified CMB layering would have to be large [e.g., *Sleep*, 1988], especially as the vertical extent of the boundary layer is decreased. Assuming changes in velocity are commensurate, CMB layering should produce first- and higher-order reverberations with amplitudes large enough to be detectable by their effect on composite ScS_n and $sScS_n$ waveforms. Unlike spectral ratios, sensitivity of composite ScS_n waveforms to CMB structure increases with the core-reflection number n. Use of individual waveforms rather than ratios, however, requires accurate modeling of the source and propagation effects. These are estimated during waveform inversion, but not independently of CMB structure; incorporating a priori constraints on crustal structure and

attenuation allows us to exploit boundary interactions to look for strong layering of the CMB.

Assume for the moment that the CMB is characterized simply by an abrupt discontinuity with no transition zone or mantle-side layering, then ScS_n and $sScS_n$ waveforms would be contaminated only by crustal reverberations. Presumably the modeling of the crust during waveform inversion would account for this contamination, providing estimates of the M-discontinuity depth and strength. If we add structure to the CMB, a simple, one-layer model of the crust will no longer be able to adequately describe boundary interaction, now due to interactions with both boundaries. If the CMB layering is strong enough, estimates of z_M, $R(z_M)$ and Q_{ScS} will be adversely affected, and driven away from the true values. To test these effects, three synthetic data sets were generated, mimicking the seismic corridor connecting events in the Tonga-Fiji seismic zone with the ASRO station CTAO in northeastern Australia (corridor 5 in Table 2.2). For all three, the mean crustal model employed is that which provided the best fit to data (z_M = 25 km, $R(z_M)$ = 0.12), with random variations of up to 15 km in the depth, and 30% in the reflection coefficient, applied at each surface bounce point of ScS_n and $sScS_n$. For two of the synthetic data sets, additional layering at the CMB was assumed. In these two cases the reflection coefficient of a single CMB layer was set to 12% (impedance increasing with depth across the discontinuity) with the discontinuity placed 10 km and 20 km above the CMB, respectively. Noise, modeled after the data noise spectrum, was added to all synthetic traces. Examples of the resulting synthetic seismograms are presented in Figure 7.8. As can be seen in the figure, the effect of the 10-km-thick CMB layer is difficult to detect by eye, whereas the 20-km-thick layer has a more obvious effect on the waveforms of ScS_n. and $sScS_n$.

Resolution

Inversion of these data sets led to the four panels presented in Figure 7.9, contouring the percentage of data variance explained, and Q_{ScS}, as a function of z_M and $R(z_M)$. The panel corresponding to inversion of synthetic data with no CMB layering offers a very good match to data, while models including CMB layering do not. In these cases, neither the shape of the variance reduction surface, nor the associated estimates of Q_{ScS}, resemble the data, with Q_{ScS} estimates being very strongly affected by the 20-km-thick layer (Q_{ScS} estimates greater than 3000 for reasonable crustal models). Best fitting crustal thicknesses and reflection coefficients are also biased, although not as strongly. Through a series of such experiments we have estimated the resolution attainable through this technique (Figure 7.10), which is found to decay rapidly as the discontinuity nears the CMB, with a minimum resolvable separation of 10 km (corresponding to a 5-km-thick layer at the free surface), approximating an abrupt transition at the seismic wavelengths employed in this study (~200 km at the CMB). This limit on resolution can be improved by including higher frequency data, although signal quality will decide the ultimate level of resolution. Unlike reflectivity profiling, the resolution attainable from boundary-interaction modeling is not significantly reduced by lateral variability of the depth or strength of the reflector. Reflections generated by a CMB-transition reflector will bracket the parent ScS_n pulse with the change in sign between the topside reflections preceding ScS_n and the bottomside reflections which follow ScS_n acting to bias the apparent width and, hence, apparent Q of the composite waveform. Although variations in the exact timing and amplitude of these reflected arrivals will affect the degree of bias introduced, so long as the sign of the reflection coefficient remains unchanged the bias will consistently drive estimates of Q_{ScS} obtained by waveform inversion to greater values (or lesser values for an impedance decrease). There is no provision, however, for description of CMB layering implicit in boundary-interaction modeling, the method is intended to serve as a detector only. Once observed, CMB structure can be further delineated by forward modeling or more complex inversion schemes.

Results

As in Figure 7.8, noisy synthetic data sets for all 18 seismic corridors were computed using the best-fitting crustal models obtained from data, and subsequently inverted. In all cases the synthetic grid-search panel provided a good fit to data. A data-synthetic comparison for the seismic corridor connecting shocks in the Philippines subduction zone with the SRO station NWAO in southwestern Australia (corridor 11 in Table 2.2) is given in Figure 7.11. For this experiment, the data displays a strong bimodality of lithospheric sampling (back-arc versus continental and continental-margin regimes) of two tectonically-complex regions. The crustal thickness estimated by waveform inversion is reasonable for an average of oceanic and continental crust, as is the estimate of Q_{ScS}, and even though bimodality is not explicitly included in the synthetic data set, the agreement obtained between data and synthetic panels is quite good. Data for this corridor require no mantle-side layering of the CMB at the available level of resolution (Figure 7.11). Similar levels of agreement were consistently achieved throughout the data set.

Estimates of crustal thickness obtained from waveform inversion, versus predictions garnered from the available seismic-refraction, reflection, surface-wave, and gravity literature, display very good agreement (Figure 4.4) as do prior estimates of Q_{ScS} [e.g., *Nakanishi*, 1980; *Sipkin and Jordan*, 1980b; *Chan and Der*, 1988]. Thus, within the available limits of resolution, there appears to be no strong, mantle-side layering of the CMB along any of the 18 seismic corridors sampled in this study. There are, however, several mechanisms by which layering of the CMB, perhaps associated with a thin chemical boundary layer, could be hidden from our analysis. The most obvious mechanism is that the boundary layer is either a fluid, or restricted to the core-side of the CMB, perhaps implying stable stratification of the outer portion of the outer core. In either case we would expect complete reflection of *SH*-polarized waves, with no generation of higher-order reverberations. Another plausible mechanism is chemical heterogeneity with

velocity-density systematics such that δv_s and $\delta\rho$ are anticorrelated, resulting in little or no impedance contrast. *Ruff and Anderson* [1979] propose a heterogeneous layer of CaO- and Al_2O_3-rich refractory material residing on the CMB following expulsion from the core, which, although slightly more dense than the lower mantle, may have wavespeeds 5% to 7% slower. A second possibility is the admixture of Fe in mantle silicates [e.g., *Adler*, 1966], which tends to increase density while reducing seismic wavespeed [e.g., *Birch*, 1961]. Either scenario has the potential of rendering CBL-induced layering transparent to mantle reverberations, while still producing large delays in the travel times of transmitted waves, perhaps reconciling our results with those of *Creager and Jordan* [1986].

CONCLUSIONS

An exhaustive search for radial discontinuities in the lower mantle reveals evidence for a moderately-strong reflector, located approximately 325 km off the CMB beneath western Australia and the Philippine Sea. This feature likely corresponds to the discontinuity previously proposed by *Lay and Helmberger* [1983], and is characterized by *SH* reflection coefficient $R(2580) = 0.022$, implying a 1.7% increase in density given their 2.75% increase in shear velocity. The discontinuity does not appear to be a ubiquitous feature of the D" region, showing strongly beneath roughly one-third of the seismic corridors examined. Perhaps more importantly, we find strong correlation of the depth of the D" discontinuity and lower-mantle velocity heterogeneity, consistent with a simple model of a compositionally-distinct, basal mantle layer, exceeding 300 km thickness in some regions of the lower mantle, and capable of producing up to 5 km of CMB topography.

No other deep lower-mantle reflectors, such as the discontinuities proposed by *Johnson* [1969], *Corbishley* [1970], and *Evernden and Clark* [1970], are observed. If these or other discontinuities are present in the lower mantle, they must be either small ($R(z) < 1.0\%$) or intermittent or have lateral depth variations well in excess of 50 km. Our results are in agreement with the majority of seismic models, and consistent with the hypothesis of

adiabatic compression of a compositionally-homogeneous lower mantle from ~1000 km to 2600 km depth.

Strong mantle-side layering closer to the CMB boundary, perhaps associated with the type of CBL structure proposed by *Jordan* [1979*b*] and *Jordan and Creager* [1986], is not required by the data, but could be present if it is a liquid or accompanied by small impedance contrasts or of limited vertical extent (<10 km). Extension of boundary interaction modeling to higher frequencies has the potential to place much more stringent bounds on CMB complexity.

TABLE 7.1. $R(z)$ Estimates for Region D''

#	Source Region	Recv.	h (km)[1]	Reflection Coefficient R
3	Sumba	CTAO	_2	_2
6	Sumba-Phil.	GUMO	340 ± 20	0.018
9	Sumba-Phil.	MAJO	305 ± 20	0.022
11	Philippines	NWAO	325 ± 20	0.015
13	Sumba		330 ± 20	0.012
17	New Britain	TATO	_2	_2
18	Japan-Izu		270 ± 20	0.018

[1] Height above CMB relative to model PREM of *Dziewonski and Anderson* [1981].

[2] Although a reflector is indicated in data, interference with upper mantle structure precludes accurate estimation of depth or R.

Fig. 7.1. Data (left), parsimonious synthetic (center), and residual (right) reflectivity profiles obtained from first-order reverberations sampling the seismic corridor connecting shocks in the Sumba, Philippines and New Britain seismic zones with SRO station CHTO in Thailand (corridor 1 in Table 2.2). $R(z)$ is a low-pass filtered (corner at 20 mHz, maximum of passband at 30 mHz) version of the normal-incidence, SH-polarized reflection coefficient of the mantle. The synthetic profile was computed for a mantle containing reflectors at only the four labeled upper-mantle depths. Large amplitude features in the lower mantle are false images of the upper mantle discontinuities—artifacts which arise due to poor ray-parameter coverage, resulting in a near mirror image profile. Stippled region denotes the 5% false-alarm probability level. Gap in mid-mantle is due to the destructive interference of topside and bottomside reflections which leads to instability in the inversion. While the signatures of the 320-km, 530-km and 730-km discontinuities are evident, this path displays no evidence for reflectors deeper than 1000 km.

Fig. 7.2. Data (left) and parsimonious synthetic (center) reflectivity profiles obtained from first-order reverberations sampling the seismic corridor connecting shocks in the Sumba and Philippine seismic zones with ASRO station MAJO on Honshu (corridor 6 in Table 2.2). The synthetic profile was computed for a mantle containing reflectors at only the three labeled upper-mantle depths. The difference between data and synthetic is shown at right. The peak labeled at 305 km above the CMB may be evidence of a reflector near the top of region D". Filtering and other conventions are the same as Figure 7.1.

Fig. 7.3. Data (left) and parsimonious synthetic (center) reflectivity profiles obtained from first-order reverberations sampling the seismic corridor connecting shocks in the Sumba and Philippine seismic zones with SRO station GUMO on Guam (corridor 9 in Table 2.2). The synthetic profile was computed for a mantle containing reflectors at only the three

labeled upper-mantle depths. The difference between data and synthetic is shown at right. The large negative peak near 2100 km depth is interpreted as the false image of the 530-km discontinuity, which was not included in the parsimonious synthetic profiles. Filtering and other conventions are the same as Figure 7.1.

Fig. 7.4. Mercator projections of study areas depicting the locations of sources (triangles) and receivers (squares). Shaded regions denote the portion of the lower mantle sampled by the 18 individual seismic corridors. Corridors for which a D" discontinuity is observed are numbered (Table 7.1); the apparent separation of the discontinuity from the CMB is enclosed in parenthesis

Fig. 7.5. Comparison of data (left) and parsimonious synthetic (center) reflectivity profiles obtained by stacking individual profiles for 18 seismic corridors. Profiles were computed for low-passed filtered data (corner at 20 mHz, truncated at 30 mHz) to alleviate the effects of reverberation splitting. Individual synthetic profiles contain model discontinuities near 400 km and 650 km depth, plus additional discontinuities in the upper 300 km of the mantle as required by the data. Residual $R(z)$ (right) exceeds the 5% false-alarm level only twice beneath a depth of 1000 km. The impedance increase implied at 1810 km is preferentially interpreted as an impedance increase ~70 km below the 650-km discontinuity (Chapter 5). The second peak occurs 325 km above the CMB, and may be associated with the discontinuity proposed by *Lay and Helmberger* [1983]. Filtering and other conventions are the same as Figure 7.1.

Fig. 7.6. Comparison of data (left) and parsimonious synthetic (center) reflectivity profiles obtained by stacking individual profiles for the 13 seismic corridors along which no D" discontinuity is directly observed in the individual profiles. The D" discontinuity ~305 km above the CMB is severely attenuated relative to Figure 7.5, suggesting that this

discontinuity is either weaker by almost a factor of two, or not present along a significant fraction of the paths included in the stack. Filtering and other conventions are the same as Figure 7.1.

Fig. 7.7. Scatter plot of separation of the observed D" discontinuity from the CMB, h, versus vertical, two-way, shear-wave travel-time delay through the lowermost 400 km of the mantle predicted by model L02.56 [*Dziewonski*, 1984]. (The scaling between P- and S-wavespeed perturbations is treated in Chapter 5.) The strong correlation (coefficient of correlation $r = 0.93$) suggests the discontinuity is furthest removed from the CMB in locally slow regions, consistent with sweeping of intrinsically-dense mantle dregs towards regions of locally hot–seismically slow–upwelling. Data point labelled SYL1 (triangle) is from the study of *Young and Lay* [1987], sampling D" beneath India and the Indian Ocean.

Fig. 7.8. Comparison of reverberative intervals, the window of time series used in this study, for data and three synthetic time series. Synthetic data sets feature a mean crustal thickness of 25 km with up to 15 km variations at each ScS_n and $sScS_n$ bounce point, and M-discontinuity reflection coefficient of 0.12 with 30% variation. Noise modeled after the data noise spectrum has been added to each trace. Bottom trace is data, above are synthetic with no CMB layering, 10-km CMB layer, and 20-km CMB layer, respectively. The CMB layer has a 12% impedance contrast, increasing with depth across the discontinuity.

Fig. 7.9. Comparison of four grid-search/inversion results for 10 seismograms sampling the seismic corridor connecting events in the Tonga-Fiji seismic zone with ASRO station CTAO in northeastern Australia (corridor 5 in Table 2.2). (*a*) Results of data inversion. Contours correspond to the percent of variance explained, shaded contours are the associated estimate of Q_{ScS}. The data are best fit by $z_M = 25$ km, $R(z_M) = 0.12$ and $Q_{ScS} = 210$. The other three panels are similar inversions of noisy synthetic data sets: (*b*) No

CMB structure, (c) 10-km-thick layer on the CMB, and (d) 20-km-thick layer on the CMB. The good agreement of panels (a) and (b) suggests that this path contains no strong mantle-side CMB layering.

Fig. 7.10. Resolution of mantle layering obtainable from reflectivity profiles (i.e., migration of first-order reverberations) and boundary-interaction modeling (modeling of first- and higher-order reverberation contamination of multiple ScS and $sScS$ phases). Layers thinner than 10 km (5 km at the free surface) appear as abrupt transitions to the seismic wavelengths used in this study (~200 km at the CMB). For near-normally incident SH-polarized waves $R(z) \sim 1/2(\delta v_s/v_s + \delta \rho/\rho)$.

Fig. 7.11. Comparison of grid-search and inversion results for the 14 seismograms sampling the seismic corridor connecting events in the Philippine seismic zone with SRO station NWAO (corridor 11 in Table 2.2). (a) Results of data inversion; data is best fit by $z_M = 26$ km, $R(z_M) = 0.22$ and $Q_{ScS} = 194$. (b) Similar inversion of a noisy synthetic data set with no CMB structure. Although data features strong bimodality of lithospheric sampling (back-arc versus continental and continental-margin regimes) not explicitly modeled by the synthetics, the fit is still quite good, and consistent with no resolvable CMB layering. (Note change in Q_{ScS} scale from Figure 7.9.)
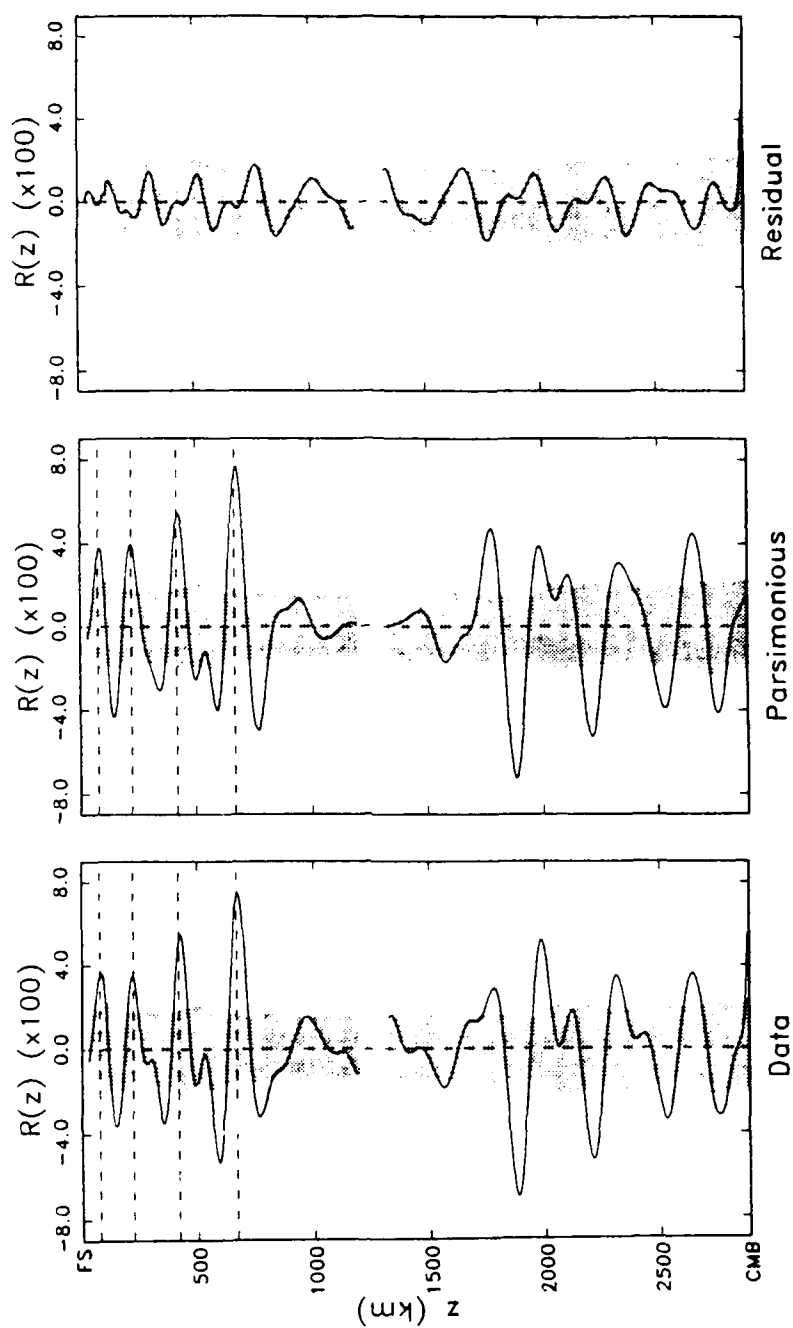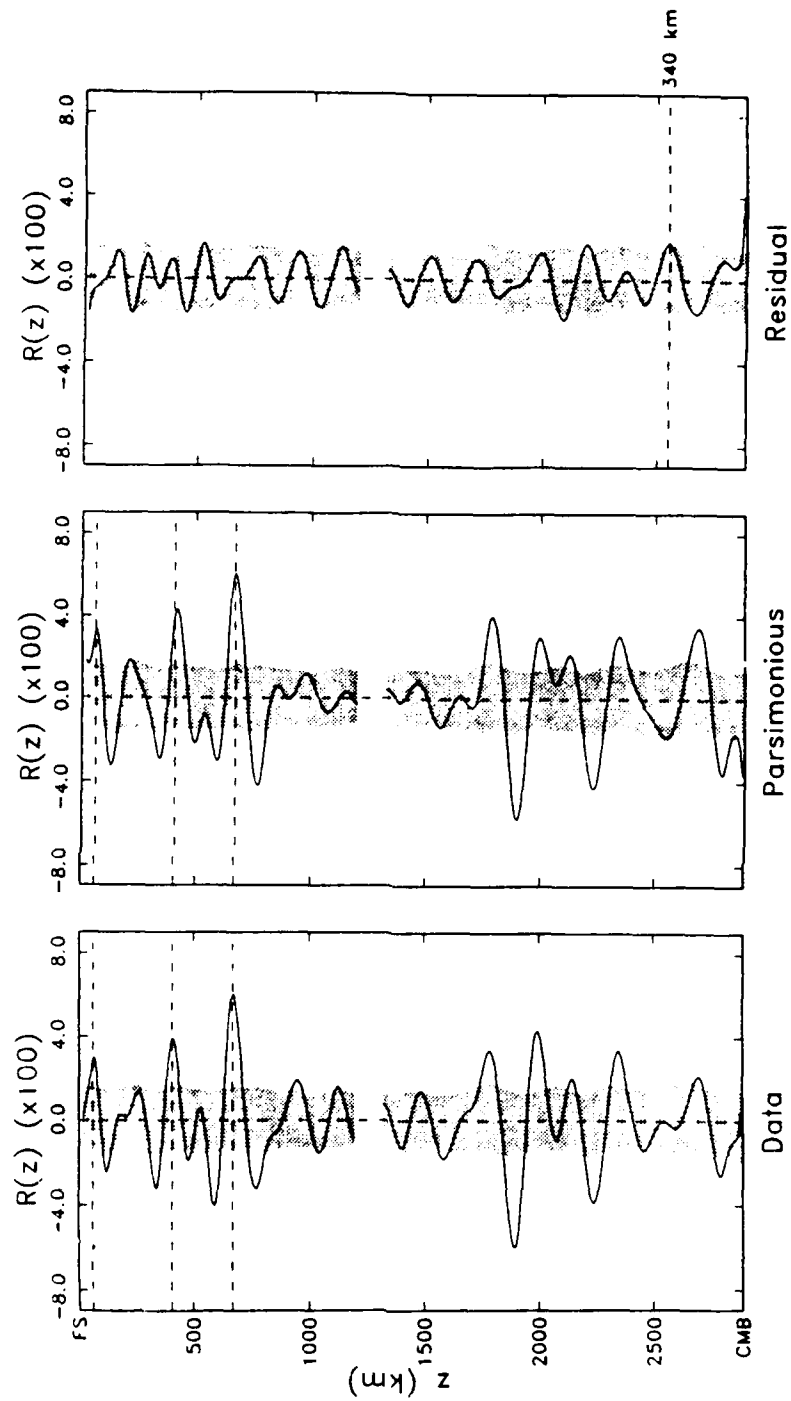
Source Region: New Britain, Solomon Islands
Station: CHTO (SRO)
Low Passed Filtered (Corner at 20 mHz, truncated at 30 mHz)
Seismograms in Stack: 17

Figure 7.1
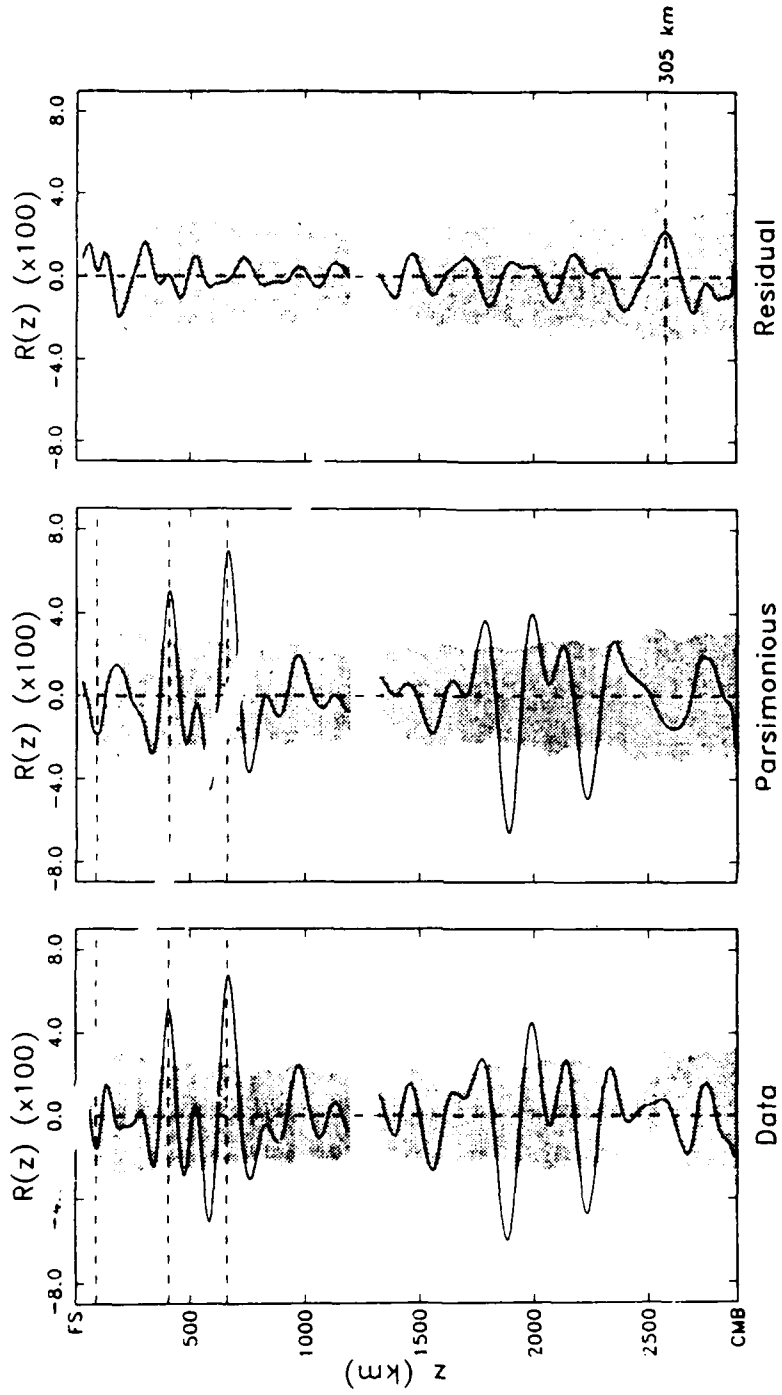
255

Source Region: Sumba, Timor, Philippines
Station: MAJO (ASRO)
Low Passed Filtered (Corner at 20 mHz, truncated at 30 mHz)
Seismograms in Stack: 14

Figure 7.2

256

R(z) (x100)

340 km

Residual

Parsimonious

R(z) (x100)

Data

z (km)

FS
500
1000
1500
2000
2500
CMB

8.0 4.0 0.0 -4.0 -8.0

Source Region: Sumba, Timor, Philippines
Station: GUMO (SRO)
Low Passed Filtered (Corner at 20 mHz, truncated at 30 mHz)
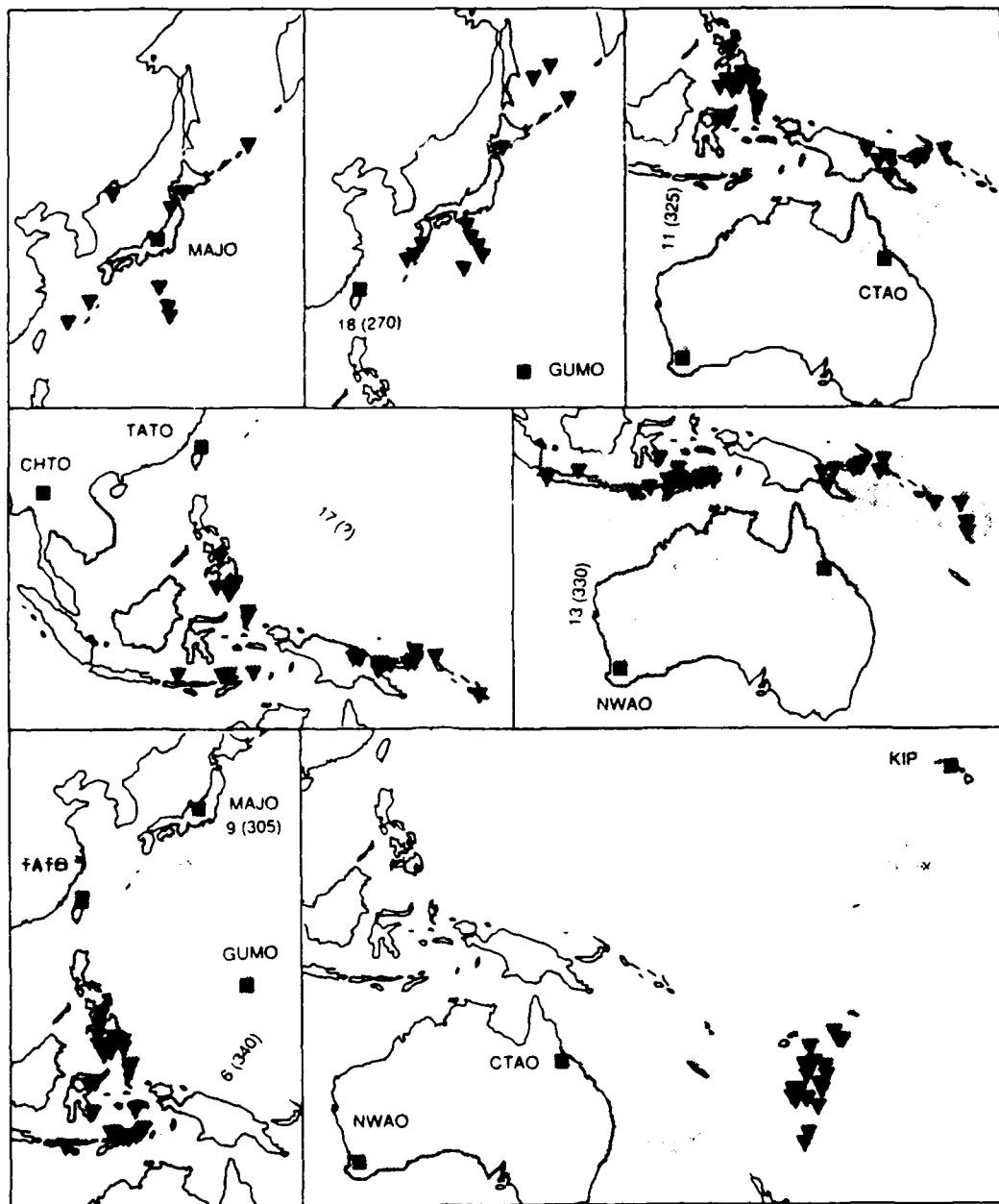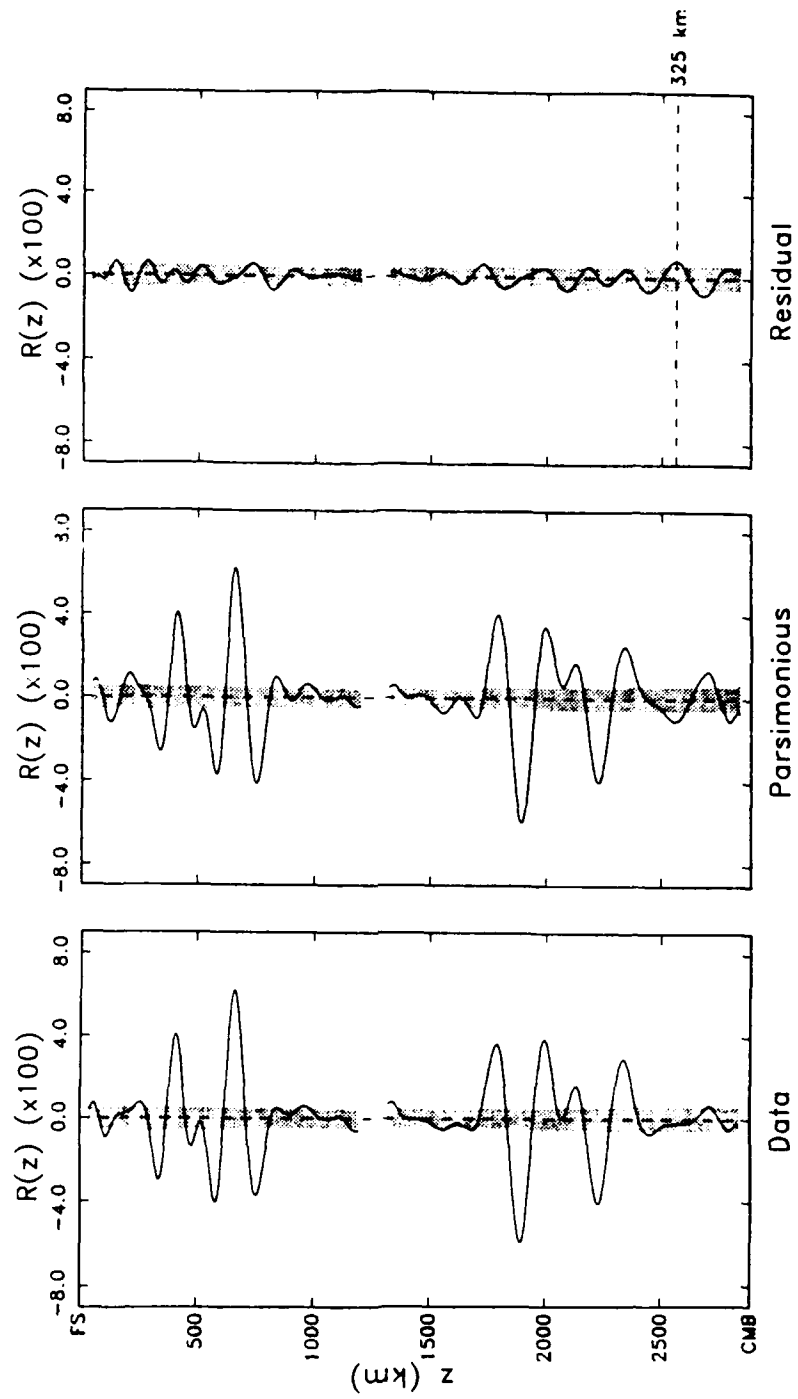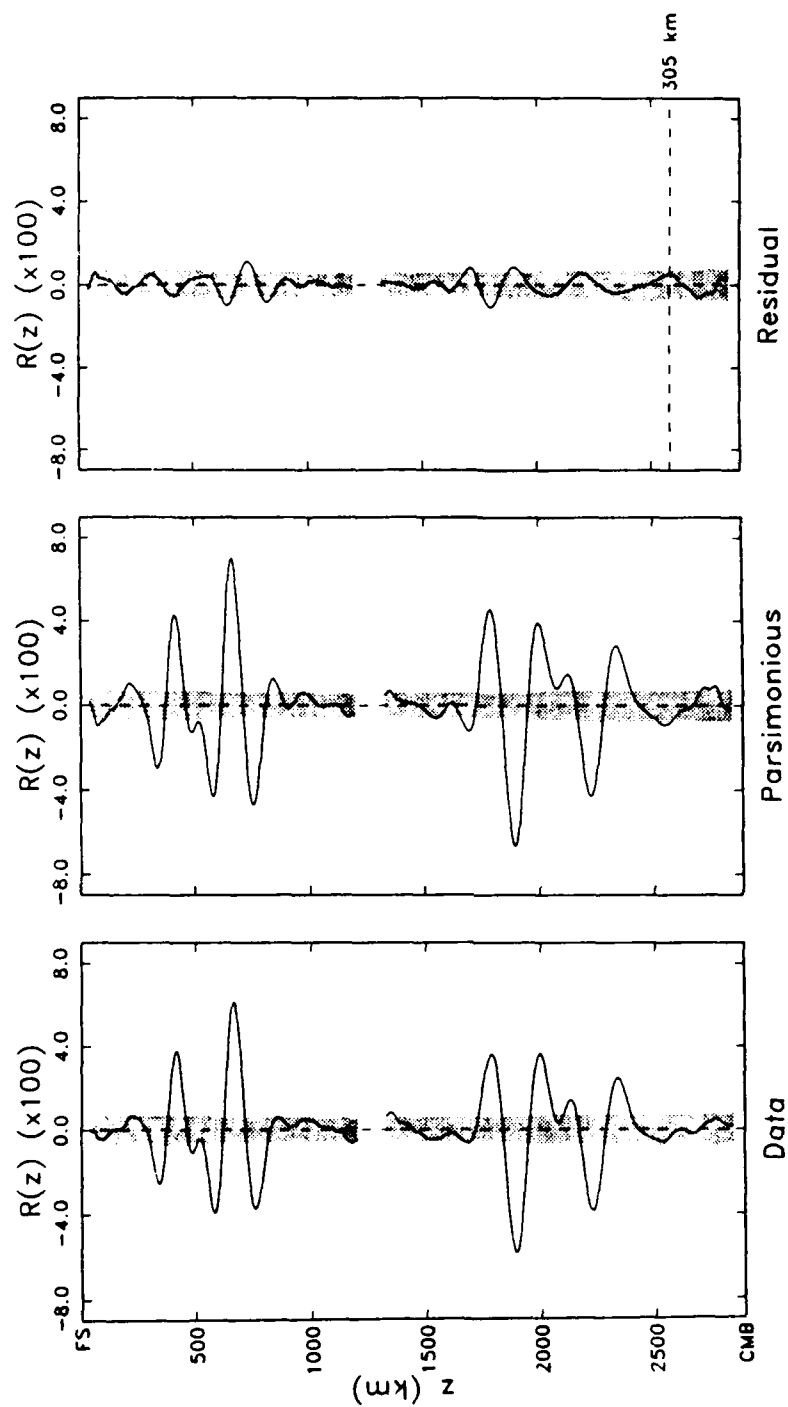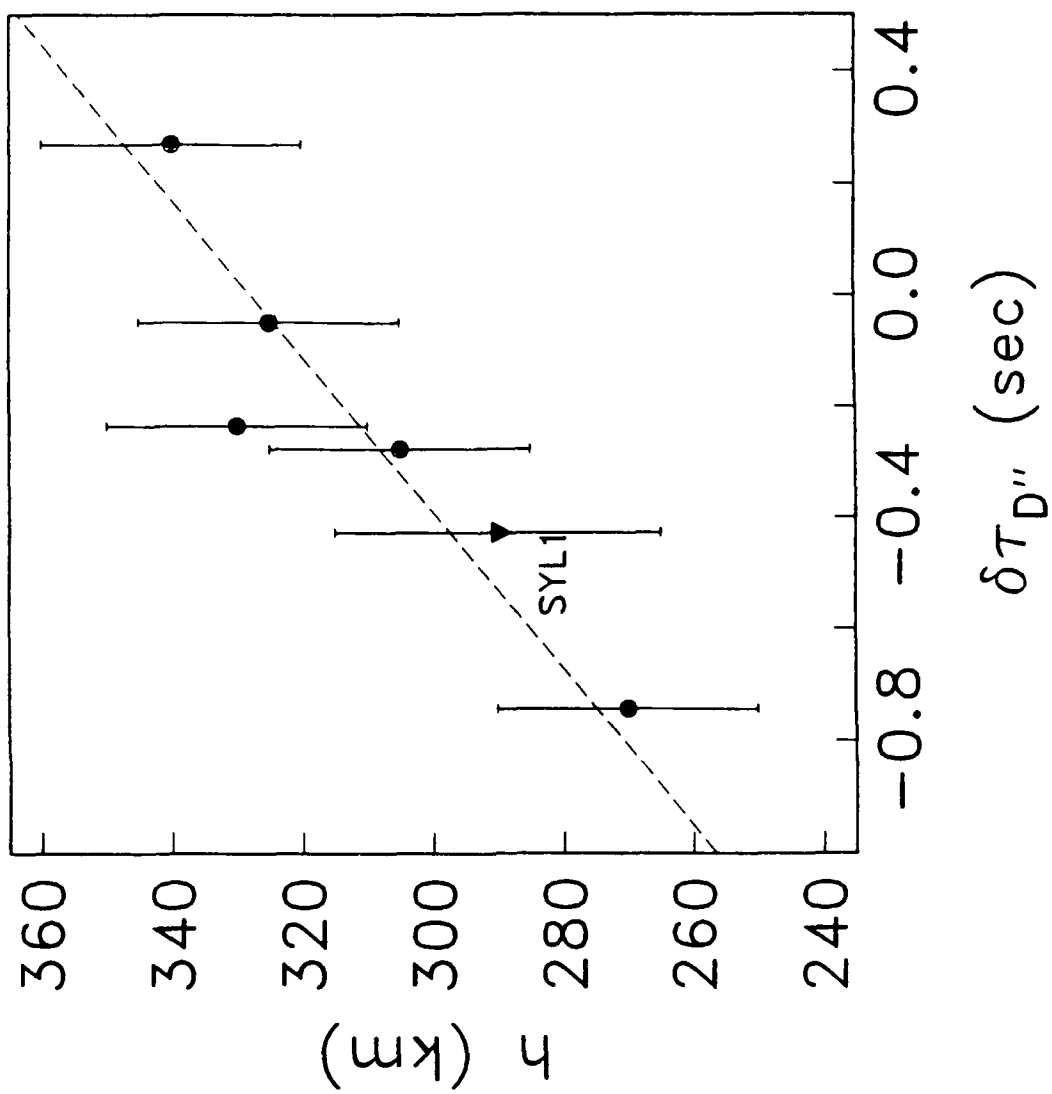Seismograms in Stack: 20

Figure 7.3

257

Figure 7.4

258

Figure 7.5
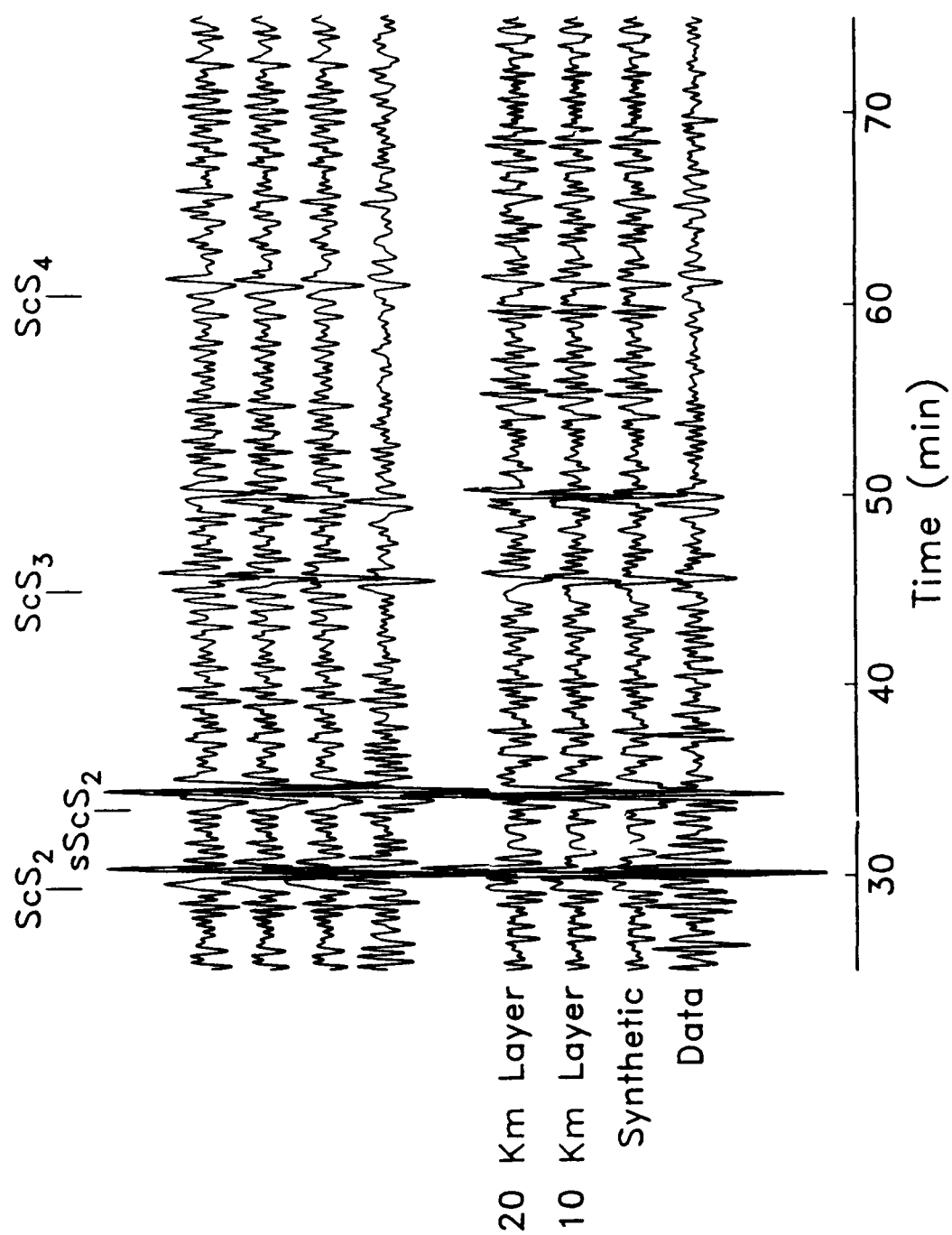
259

Figure 7.6

260

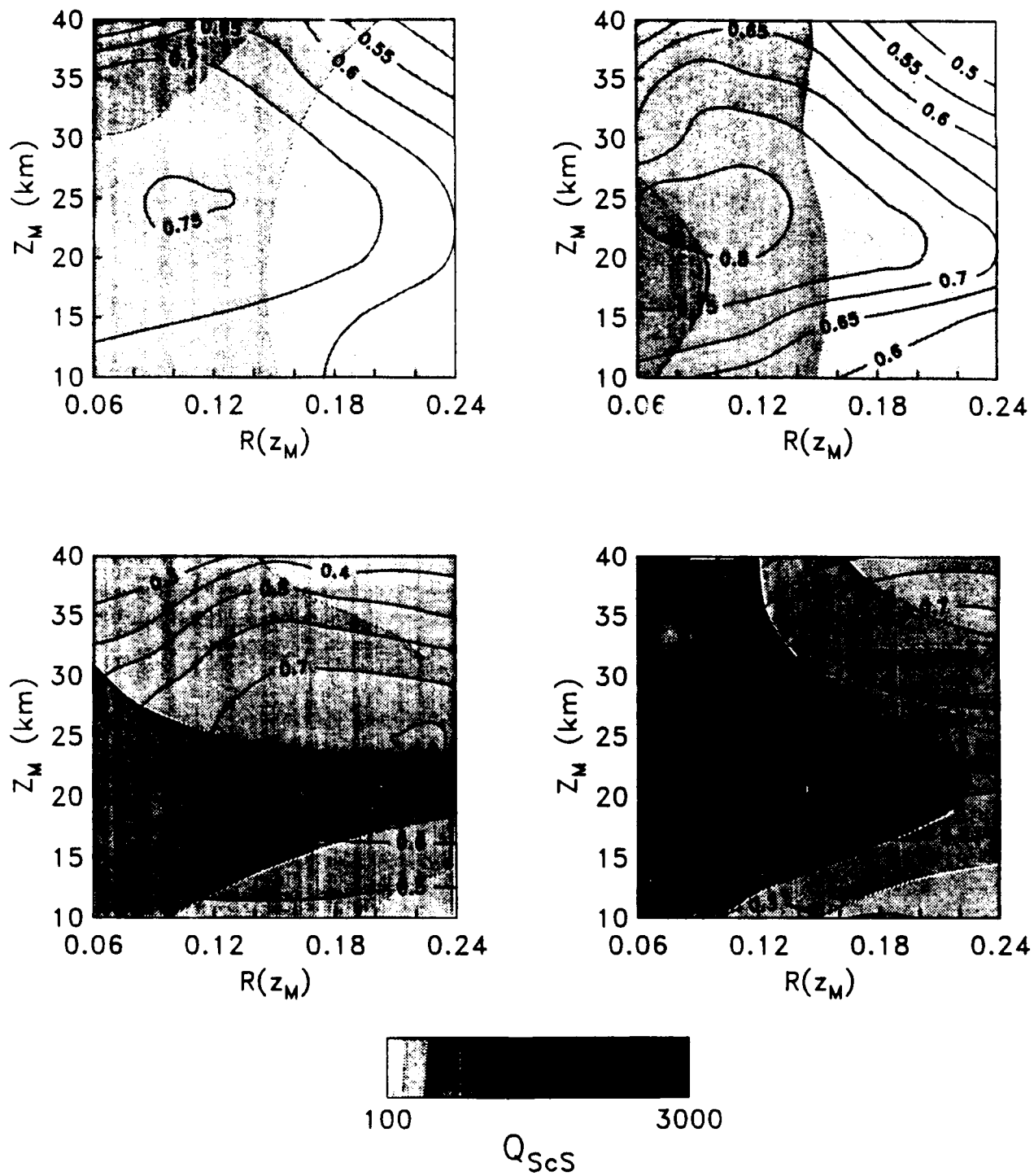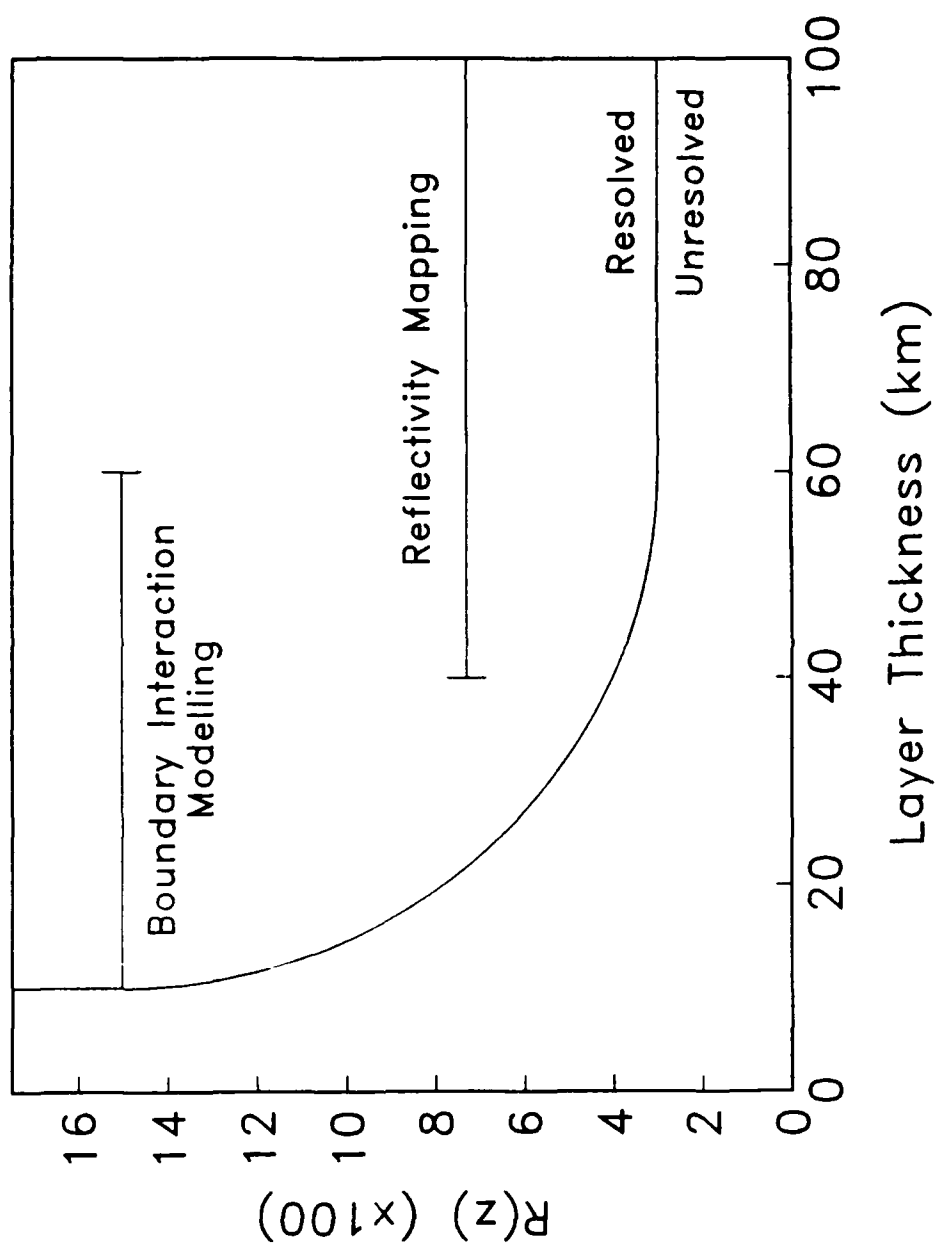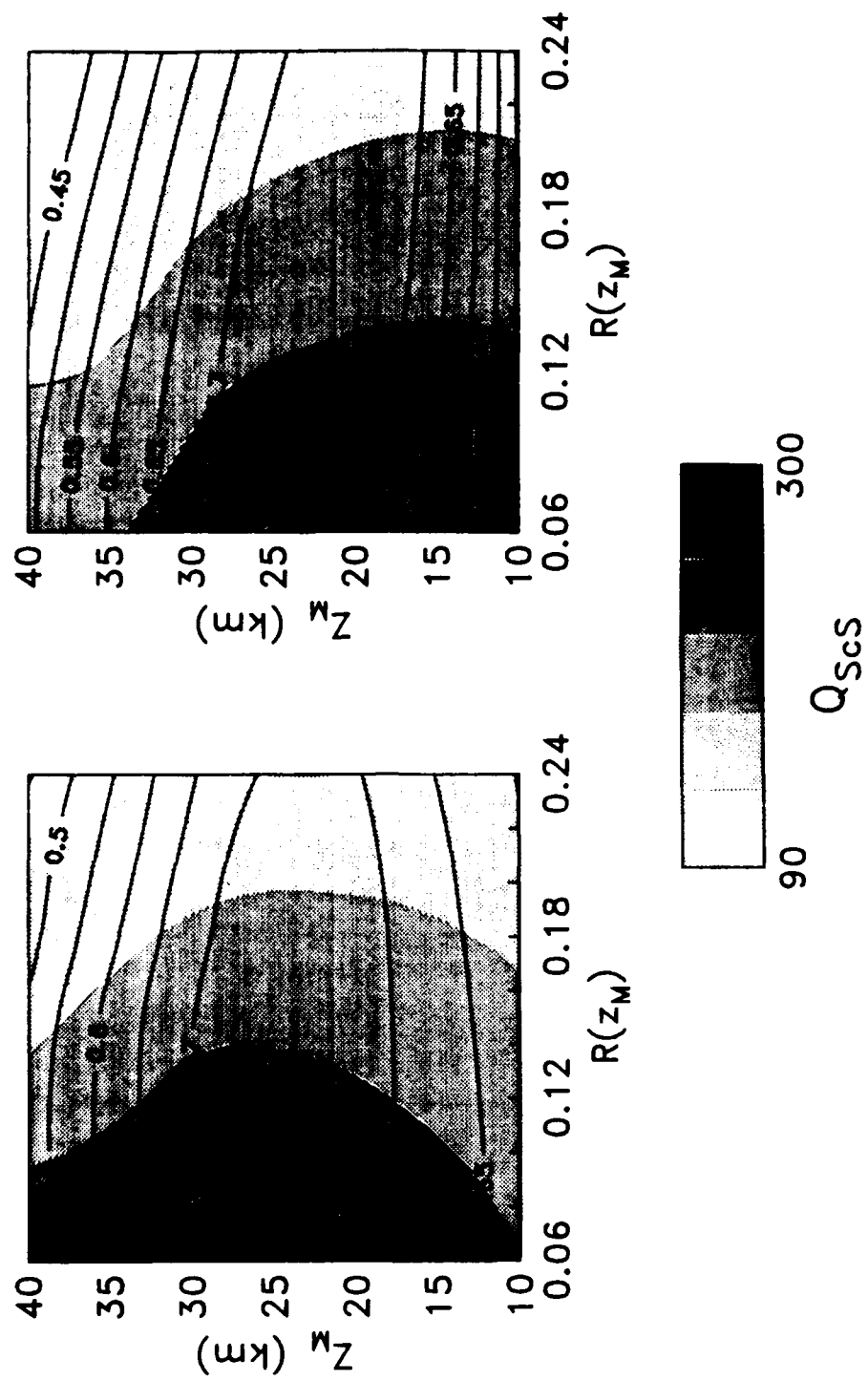Figure 7.7

Figure 7.8

262

Figure 7.9

Figure 7.10

Figure 7.11

265

CHAPTER 8

CONCLUSIONS

In this study we have developed sophisticated waveform inversion techniques and have applied them to an extensive body of long-period, reverberative-interval seismograms for paths crossing the western Pacific and adjoining marginal basins, Indonesia, and Australia. The results, namely variations in the travel times and amplitudes of zeroth- and first-order reverberations, have important implications for the composition and state of the Earth's mantle. Specifically we have found that:

(1) The impedance increases of the 400-km and 650-km discontinuities dominate the reflectivity profile of the mantle. Estimates of SH reflection coefficients for these discontinuities are consistent with prior estimates, with mean values of 0.046 ± 0.01, and 0.072 ± 0.01, respectively. Assuming a Birch's-Law scaling of velocity to density perturbations, the estimated jumps in material properties for the 400-km discontinuity are $\delta v_s = 0.27$ km/s (or approximately 5.4%) and $\delta\rho = 0.14$ gm/cm^3 (3.9%). Repeating the analysis for the 650-km discontinuity yields: $\delta v_s = 0.49$ km/s (8.5%) and $\delta\rho = 0.26$ gm/cm^3 (6.1%)–all close to recent free-oscillation solutions. Constraints on the widths of transition are weak, but require both discontinuities to be less than ~40 km in vertical extent.

(2) For horizontal wavelengths between 500 km and 5000 km we find evidence for no more than ~30 km of topography on either of these two discontinuities. For the 650-km discontinuity it is possible to statistically evaluate fluctuations at shorter wavelengths (300–1500 km), overlapping with other seismic measures of discontinuity topography; again we find less ~30 km of topography. Shorter-wavelength topography in the vicinity of subducting slabs may be greater (50 km), but only slightly so [e.g., *Barley et al.*, 1982; *Bock and Ha*, 1984; *Richards and Wicks*, 1987]. This is opposed to the predictions of topography in a compositionally-layered mantle (>100 km), where the interface between the upper and lower mantle deflects to compensate the mass excess of downgoing slabs.

The seismic data, covering more than a decade in horizontal wavelength, argue persuasively against a purely compositional origin of the 650-km discontinuity.

Unweighted averaging of estimates obtained for 18 seismic corridors gives τ'_{400} = 185.8 s and τ'_{650} = 279.5 s corresponding to average apparent depths of 414 km and 660 km relative to the PREM. By way of comparison, the corresponding times for the PREM are 180.2 s (400 km) and 282.9 s (670 km), respectively.

(3) Interpreted in terms of phase transitions, observed variations in the travel times of first-order reverberations are consistent with 210° C long-wavelength temperature variations in the transition zone. Taken at face value, the observation that topography on the two discontinuities is anticorrelated but of equal magnitude, suggests that the Clapeyron slope of the 650-km discontinuity is comparable in magnitude and opposite in sign to that of the 400-km discontinuity. The apparent depth (or equivalently τ'_{LM}) and reflection coefficient of the 650-km discontinuity, $R(650)$, appear to be negatively correlated. Although difficult to justify from the standpoint of mantle dynamics, the data are well explained by the thermal equilibration of an initially cold CBL residing on the 650-km discontinuity. If this model is allowed, the requirement of a large Clapeyron slope for the 650-km discontinuity can be relaxed, resulting in an estimate close to laboratory values (γ_{650} = −2 MPa/°C). An alternative model which appeals to slab-induced curvature of the 650-km beneath regions of subduction may also be capable of explaining the observations, and is more in keeping with the geodynamical constraints [e.g., *Christensen*, 1988; *Richards and Davies*, preprint].

(4) The impedance profile of the upper mantle appears to be punctuated by a large number of other, typically smaller, discontinuities. Specifically, we have found evidence for a moderately strong impedance increase at a mean depth of 67 km, characterized by mean *SH* reflection coefficient $R(67)$ = 0.035. This discontinuity may be present along all the corridors sampled, and is likely the seismic expression of the spinel → garnet transition, although contributions from anisotropy may play an accessory role. Beneath

267

oceans and back-arc marginal basins a strong impedance decrease is observed. On the basis of correlations with Q_{ScS} and surface tectonics, this discontinuity is interpreted as the upper boundary of the LVZ. The reflector is brightest in the upper mantle on the concave side of subduction zones, above the subducting lithosphere. Because the LVZ in these regions occupies much the same range of depths observed elsewhere, this observation may require the presence of a small amount of partial melt, presumably owing to greater H_2O pressure accompanying the breakdown of hydrous phases in the subducting oceanic crust. Subsequent upward migration of melt may result in chemical zonation of the LVZ behind these island arcs

(6) For seismic corridors with significant path length along continental shields, platforms, and margins, a discontinuity near 230 km depth is observed. Mineralogical phase transitions and compositional changes do not appear to be capable of explaining this discontinuity, which *Leven et al.* [1981] attribute to an anisotropic cap over a subcontinental LVZ. Although not required by the data, this hypothesis explains many of the observations, including the correlation of Q_{ScS} and discontinuity depth. Another small impedance is observed near 320 km depth along paths traversing regions of active subduction. The difficulties encountered in explaining the 220-km discontinuity apply to this reflector as well. A tenable hypothesis is that it marks the base of the LVZ, made "bright" through incorporation of free water into high-pressure, high-temperature hydrous phases. The observed affiliation with subduction may be due to locally-enhanced water pressures owing to advection of water into the deep upper mantle by hydrous phases in the downgoing oceanic crust.

(7) Three additional reflectors are observed in the transition zone and uppermost lower mantle at mean depths of 525 km, 742 km, and 915 km, respectively. The "530-km" discontinuity may be the seismic signature of the β-spinel $\rightarrow$ γ-spinel phase transition, although the width of the two-phase region determined experimentally may be too large to produce a sufficiently efficient reflector. The reflector near 740 km depth has several

possible explanations, including: the phase transition of ilmenite to perovskite, a change in crystal symmetry in $MgSiO_3$ perovskite, or the γ-spinel $\rightarrow$ perovskite + magnesiowüstite transition, locally depressed to greater depths by accumulation of a cold CBL upon it (although this last explanation is difficult to reconcile with laboratory estimates of equilibrium depth for the phase transition). The discontinuity at 915 km is both the most speculative of the proposed reflectors, and the most difficult to explain. Changes in perovskite crystal symmetry may be the most plausible explanation, potentially offering a simultaneous explanation of both the 730-km (cubic $\rightarrow$ tetragonal symmetry) and 915-km discontinuity (tetragonal $\rightarrow$ orthorhombic symmetry).

We are not the first to propose these discontinuities. Previous identifications, obtained by very different means, agree with our estimates of discontinuity depth and strength remarkably well, providing strong independent support. Even still, these observations, and the observations of discontinuities at depths less than 400 km, stand to be vastly improved by the accumulation of greater stores of reverberation data over the next few years.

(8) Below 1000 km depth we find evidence for only one additional discontinuity, specifically an impedance increase situated an average of 325 km above the CMB. This reflector most likely corresponds to the velocity discontinuity previously identified by *Lay and Helmberger* [1983]. Correlation of discontinuity depth, D" velocity heterogeneity, and CMB topography favor a compositional origin, namely a dense, chemically-distinct boundary layer on the CMB. The thickness of this layer exceeds 300 km beneath the Philippine Sea, but does not appear to be a ubiquitous feature of the lower mantle, perhaps occurring as "pools" swept together by lower-mantle convective flow. Results obtained from waveform inversion of zeroth-order reverberations suggest that the CMB is a relatively simple transition, where any layering or impedance transition zones are significantly less pronounced than those of the crust.

Discontinuities are perhaps the most diagnostic expression of mantle composition and state. The observations presented in this thesis represent an important new discontinuity database. While we have attempted to explain these observations in terms of currently accepted mantle compositions, phase transitions, and dynamical processes the results are sometimes equivocal, and we stress that our interpretations of these reflectors are not unique. There is a long history of profitable interplay between seismology and high-pressure petrology, geochemistry and geodynamics. It is hoped that these results will spur the search for more satisfactory explanations. In conclusion, while at first glance it might appear to be simple, a closer look reveals that the Earth's mantle is a very complicated place indeed. First-order reverberations may be seismology's best means of mapping it.

> "It is essential that the best seismological solutions be sought without reference to their physical significance; at the same time, each solution has its own meaning, in terms of materials and temperatures, and conceivably non-seismological arguments may be needed to discriminate where seismology reaches an impasse."

Francis Birch
Elasticity and Constitution of the Earth's Interior, 1952

REFERENCES

Adler, B.J., Is the mantle soluble in the core?, *J. Geophys. Res.*, *71*, 4973–4979, 1966.

Akaogi, M., and S. Akimoto, Pyroxene-garnet solid-solution equilibria in the systems $Mg_4Si_4O_{12}$- $Mg_3Al_2Si_3O_{12}$ and $Fe_4Si_4O_{12}$- $Fe_3Al_2Si_3O_{12}$ at high pressures and temperatures, *Phys. Earth Planet. Inter.*, *15*, 90–106, 1977.

Akaogi, M., and S.-I. Akimoto, High-pressure stability of a dense hydrous magnesian silicate $Mg_{23}Si_8O_{42}H_6$ and some geophysical implications, *J. Geophys. Res.*, *85*, 6944–6948, 1980.

Akaogi, M., A. Navrotsky, T. Yagi, and S.-I. Akimoto, Pyroxene-garnet transformation: thermochemistry and elasticity of garnet solid solutions, and application to a pyrolite mantle, in *High Pressure Research in Mineral Physics*, edited by M.H. Manghnani and Y. Syono, pp. 251–260, TERRAPUB/AGU, Tokyo/Washington, 1987.

Akimoto, S.I., The system $MgO\text{-}FeO\text{-}SiO_2$ at high pressures and temperatures–phase equilibria and elastic properties, *Tectonophysics*, *13*, 161–187, 1972.

Anderson, D.L., The deep structure of continents, *J. Geophys. Res.*, *84*, 7555–7560, 1979a.

Anderson, D.L., The upper mantle transition region: eclogite?, *Geophys. Res. Lett.*, *6*, 433–436, 1979b.

Anderson, D.L., Thermally induced phase changes, lateral heterogeneity of the mantle, continental roots, and deep slab anomalies, *J. Geophys. Res.*, *92*, 13,968–13,980, 1987a.

Anderson, D.L., A seismic equation of state, II, Shear properties and thermodynamics of the lower mantle, *Phys. Earth Planet. Inter.*, *45*, 307–323, 1987b.

Anderson, D.L., and R.L. Kovach, Attenuation in the mantle and rigidity of the core from multiply reflected core phases, *Proc. Nat. Acad. Sci. U.S.A.*, *51*, 168–172, 1964.

Anderson, D.L., and C. Sammis, Partial me'ting in the upper mantle, *Phys. Earth Planet. Inter.*, *3*, 41–50, 1970.

Anderson, D.L., and R.S. Hart, Attenuation models of the Earth, *Phys. Earth Planet. Inter.*, *16*, 289–306, 1978.

Anderson, D.L., and J.D. Bass, Transition region of the Earth's upper mantle, *Nature*, *320*, 321–328, 1986.

Anderson, O.L., E. Schreiber, R.C. Liebermann, and N. Soga, Some elastic constant data on minerals relevant to geophysics, *Rev. Geophys.*, *6*, 491–524, 1968.

Anderson, R.S., and J.R. Cleary, Asymptotic structure in torsional free oscillations of the Earth, I, Overtone structure, *Geophys. J..R. Astron. Soc.*, *39*, 241–268, 1974.

Bass, J.D., and D.L. Anderson, Composition of the upper mantle: Geophysical tests of two petrological models, *Geophys. Res. Lett.*, *11*, 237–240, 1984.

Barley, B.J., J.A. Hudson, and A. Douglas, *S* to *P* scattering at the 650-km discontinuity, *Geophys. J. R. Astron. Soc.*, *69*, 159–172, 1982.

Berg, E., and D.M. Chesley, Automated high-precision amplitude and phase calibration of seismic systems, *Bull. Seismol. Soc. Am.*, *66*, 1413–1424, 1976.

Billington, S., The morphology and tectonics of the subducted lithosphere in the Tonga-Fiji-Kermadec region from seismicity and focal mechanism solutions, Ph.D. dissertation, Cornell Univ., 1980.

Bina, C.R., and B.J. Wood, The eclogite to garnetite transition–experimental and thermodynamic constraints, *Geophys. Res. Lett.*, *11*, 955–958, 1984.

Birch, F., Elasticity and constitution of the Earth's interior, *J. Geophys. Res.*, *57*, 227–286, 1952.

Birch, F., Composition of the Earth's mantle, *Geophys. J. R. Astron. Soc.*, *4*, 295–311, 1961.

Bloxham, J., and D. Gubbins, Thermal core-mantle interactions, *Nature*, *325*, 511–513, 1987.

Bock, G., and J. Ha, Short-period *P-S* conversion in the mantle at a depth near 700 km, *Geophys. J. R. Astron. Soc.*, *77*, 593–615, 1984.

Bolt, B.A., *PdP* and *PKIKP* waves and diffracted *PcP* waves, *Geophys. J. R. Astron. Soc.*, *20*, 367–382, 1970.

Boyd, F.R., A pyroxene geotherm, *Geochim. Cosmochim. Acta.*, *37*, 2533–2546, 1973.

Buchbinder, G.G.R., Properties of the core-mantle boundary and observation of *PcP*, *J. Geophys. Res.*, *73*, 5901–5923, 1968.

Burdick, L.J., and D.V. Helmberger, The upper mantle *P*-velocity structure of the western United States, *J. Geophys. Res.*, *83*, 1699–1712, 1978.

Byerly, P., The Montana earthquake of June 28, 1925, *Bull. Seismol. Soc. Am.*, *16*, 209–265, 1926.

Chan, W.W., and Z.A. Der, Attenuation of multiple *ScS* in various parts of the world, *Geophys. J.*, *92*, 303–314, 1988.

Choudhury, M.A., G. Poupinet, and G. Perrier, Shear velocity from differential travel times of short-period *ScS-P* in New Hebrides, Fiji-Tonga, and Banda Sea regions, *Bull. Seismol. Soc. Am.*, *65*, 1787–1796, 1975.

Christensen, N.I., The magnitude, symmetry and origin of upper mantle anisotropy based on fabric analysis of ultramafic tectonites, *Geophys. J. R. Astron. Soc.*, *76*, 89–111, 1984.

Christensen, U., Is subducted lithosphere trapped at the 670-km discontinuity?, *Nature*, *336*, 462–463, 1988.

Christensen, U.R., and D.A. Yuen, The interaction of a subducting lithospheric slab with a chemical or phase boundary, *J. Geophys.. Res.*, *89*, 4389–4402, 1984.

Cleary, J.R., The D" region, *Phys. Earth Planet. Inter.*, *9*, 13–27, 1974.

Corbishley, D.J., Multiple array measurements of the *P*-wave travel time derivative, *Geophys. J. R. Astron. Soc*, *19*, 1–14, 1970.

Creager, K.C., and T.H. Jordan, Aspherical structure of the core-mantle boundary from *PKP* travel-times, *Geophys. Res. Lett.*, *13*, 1497–1500, 1986.

Creager, K.C., and T.H. Jordan, Slab penetration into the lower mantle beneath the Mariana and other island arcs of the northwest Pacific, *J. Geophys. Res.*, *91*, 3573–3589, 1986.

Datt, R., Seismic velocity structure using array data, *Phys. Earth Planet. Inter.*, *24*, 33–52, 1981.

Datt, R., and K.J. Muirhead, Evidence for a sharp velocity increase near 770 km depth, *Phys. Earth Planet. Inter.*, *13*, 37–46, 1976.

Datt, R., and K.J. Muirhead, Evidence of multiplicity in the *P*-travel time curve beyond 30 degrees, *Phys. Earth Planet. Inter.*, *15*, 28–38, 1977.

Davies, F.G., and M. Gurnis, Interaction of mantle dregs with convection, Lateral heterogeneity at the core-mantle boundary, *Geophys. Res. Lett.*, *13*, 1517–1520, 1986.

Dickinson, W.R., and W.C. Luth, A model for plate tectonic evolution of mantle layers, *Science*, *174*, 400–404, 1971.

Doornbos, D.J., and J.C. Mondt, *P* and *S* waves diffracted around the core and the velocity structure at the base of the mantle, *Geophys. J. R. Astron. Soc.*, *57*, 381–395, 1979.

Doornbos, D.J., S. Spiliopoulos, and F.D. Stacey, Seismological properties of D" and the structure of a thermal boundary layer, *Phys. Earth Planet. Lett.*, *41*, 225–239, 1986.

Drummond, B.J., K.J. Muirhead, and A.L. Hales, Evidence for a seismic discontinuity near 200 km depth under a continental margin, *Geophys. J. R. Astron. Soc.*, *70*, 67–77, 1982.

Duffy, T.S., and D.L. Anderson, Seismic velocities in mantle materials and the mineralogy of the upper mantle, *J. Geophys. Res.*, *94*, 1895–1912, 1989.

Dziewonski, A.M., Mapping the lower mantle: determination of lateral heterogeneity in *P*-wave velocity up to degree and order 6. *J. Geophys. Res.*, *89*, 5929–5952, 1984.

Dziewonski, A.M., and A.L. Hales, Numerical analysis of dispersed seismic waves, in *Seismology: Surface Waves and Earth Oscillations, Methods Comput. Phys., vol. 11*, edited by B.A. Bolt, pp. 39–85, Academic, San Diego, Calif., 1972.

Dziewonski, A.M., and D.L. Anderson, Preliminary reference Earth model (PREM), *Phys. Earth Planet. Inter., 25*, 297–356, 1981.

Dziewonski, A.M., and J.H. Woodhouse, Global images of the Earth's interior, *Science, 236*, 37–48, 1987.

Dziewonski, A.M., A.L. Hales, and E.R. Lapwood, Parametrically simple earth models consistent with geophysical data, *Phys. Earth Planet. Inter., 10*, 12–48, 1975.

Engdahl, E.R., and E.A. Flinn, Seismic waves reflected from discontinuities within Earth's upper mantle, *Science, 163*, 177–179, 1969.

Evernden, J.F., and D.M. Clark, Study of teleseismic P, I, Travel-time data, *Phys. Earth Planet. Inter., 4*, 1–23, 1970.

Faber, S., and G. Müller, Sp phases from the transition zone between the upper and lower mantle, *Bull. Seismol. Soc. Am., 70*, 487–508, 1980.

Faber, S., and G. Müller, Converted phases from the mantle transition observed at European stations, *J. Geophys., 54*, 183–194, 1984.

Fischer, K.M., K.C. Creager, and T.H. Jordan, Mapping the Tonga slab (abstract), *Eos Trans. AGU, 67*, 316, 1986.

Forsyth, D.W., The evolution of the upper mantle beneath mid-ocean ridges, *Tectonophysics, 38*, 89–118, 1977.

French, W.S., Two-dimensional and three-dimensional migration of model-experiment reflection profiles, *Geophysics, 39*, 265–277, 1974.

Fukao, Y., Upper mantle P structure on the ocean side of the Japan-Kurile arc, *Geophys. J. R. Astron. Soc., 50*, 621–642, 1977.

Garnero, E., D. Helmberger, and G. Engen, Lateral variations near the core-mantle boundary, *Geophys. Res. Lett., 15*, 609–612, 1988.

Giardini, D., Systematic analysis of deep seismicity, 200 centroid-moment tensor solutions for earthquakes between 1977 and 1980, *Geophys. J. R. Astron. Soc.*, *77*, 883–914, 1984.

Giardini, D., X.-D. Li, and J.H. Woodhouse, Splitting functions of long-period normal modes of the Earth, *J. Geophys. Res.*, *93*, 13,716–13,742, 1988.

Gilbert, F., and A.M. Dziewonski, An application of normal mode theory to the retrieval of structural parameters and source mechanisms from seismic spectra, *Phil. Trans. R. Soc. London, Ser. A*, *278*, 187–269, 1975.

Given, J.W., and D.V. Helmberger, Upper mantle structure of northwestern Eurasia, *J. Geophys. Res.*, *85*, 7183–7194, 1980.

Goetz, C., A brief summary of our present day understanding of the effect of volatiles and partial melt on the mechanical properties of the upper mantle, *High Pressure Research: Applications in Geophysics*, edited by M.H. Manghnani and S. Akimoto, pp. 3–23, Center for Academic Publications, Tokyo, Japan, 1977.

Goncz, J.H., and J.R. Cleary, Variations in the structure of the upper mantle beneath Australia, from Rayleigh wave observations, *Geophys. J. R. Astron. Soc.*, *44*, 507–516.

Grand, S.P., Tomographic inversion for shear velocity beneath the North American plate, *J. Geophys. Res.*, *92*, 14,065–14,090, 1987.

Grand, S.P., and D.V. Helmberger, Upper mantle shear structure beneath the northwest Atlantic ocean, *J. Geophys. Res.*, *89*, 11,465–11,475, 1984.

Green, D.H., and A.E. Ringwood, The stability fields of aluminous pyroxene peridotite and garnet peridotite and their relevance in upper mantle structure, *Earth Planet. Sci. Lett.*, *3*, 151–160, 1967.

Green, D.H., and R.C. Liebermann, Phase equilibria and elastic properties of a pyrolite model for the oceanic upper mantle, *Tectonophysics*, *32*, 61–92, 1976.

Green, R.W.E., and A.L. Hales, The travel times of P waves to 30° in the central United States and upper mantle structure, *Bull. Seismol. Soc. Am.*, *58*, 267–289, 1968.

Gutenberg, B., On the layer of relatively low wave velocity at a depth of about 80 kilometers, *Bull. Seismol. Soc. Am.*, *38*, 121–148, 1948.

Haddon, R.A.W., Evidence for imhomogeneities near the core-mantle boundary, *Phil. Trans. R. Soc. Lond., Ser. A*, *306*, 61–70, 1982.

Hagedoorn, J.G., A process of seismic reflection interpretation, *Geophys. Prospect.*, *2*, 85–127, 1954.

Hager, B.H., and A. Raefsky, Deformation of seismic discontinuities and the scale of mantle convection (abstract), *Eos Trans. AGU*, *62*, 1074, 1981.

Hager, B.H., R.W. Clayton, M.A. Richards, R.P. Comer, and A.M. Dziewonski, Lower mantle heterogeneity, dynamic topography and the geoid, *Nature*, *313*, 541–545, 1985.

Hales, A.L., A seismic discontinuity in the lithosphere, *Earth Planet. Sci. Lett.*, *7*, 44–46, 1969.

Hales, A.L., The travel times of P seismic waves and their relevance to the upper mantle velocity distribution, *Tectonophysics*, *13*, 447–482, 1972.

Hales, A.L., and J.L. Roberts, The travel times of S and SKS, *Bull. Seismol. Soc. Am.*, *60*, 461–489, 1970a.

Hales, A.L., and J.L. Roberts, Shear velocities in the lower mantle and the radius of the core, *Bull. Seismol. Soc. Am.*, *60*, 1427–1436, 1970b.

Hales, A.L., C.E. Helsley, and J.B. Nation, P travel times for an oceanic path, *J. Geophys. Res.*, *75*, 7362–7381, 1970.

Hales, A.L., K.J. Muirhead, and J.M.W. Rynn, A compressional velocity distribution for the upper mantle, *Tectonophysics*, *63*, 309–348, 1980.

Hansen, U., and D.A. Yuen, Numerical simulations of thermal-chemical instabilities at the core-mantle boundary, *Nature*, *334*, 237–240, 1988.

Harris, R.J., *A Primer of Multivariate Statistics*, 329 pp, Academic Press, New York, N.Y., 1975.

Hart, R.S., Shear velocity in the lower mantle from explosion data, *J. Geophys. Res., 80*, 4889–4894, 1975.

Haskell, N.A., Crustal reflection of plane *SH* waves, *J. Geophys. Res., 65*, 4147–4150, 1960.

Helmberger, D., and R.A. Wiggins, Upper mantle structure of midwestern United States, *J. Geophys. Res., 76*, 3229–3245, 1971.

Helmberger, D.V., and G.R. Engen, Upper mantle shear structure, *J. Geophys. Res., 79*, 4017–4028, 1974.

Helstrom, C.W., *Statistical Theory of Signal Detection*, Pergamon, Elmsford, N.Y., 1960.

Hirn, A., C. Prodehl, and L. Steinmetz, An experimental test of models of the lower lithosphere in Bretagne (France), *Ann. Géophys., 31*, 517–530, 1975.

Hofman, A.W., and W.M. White, Mantle plumes from ancient oceanic crust, *Earth Planet. Sci. Lett., 57*, 421–436, 1982.

Ibrahim, A.-B.K., The amplitude ratio *PcP/P* and the core-mantle boundary, *Pure Appl. Geophys., 91*, 114–133, 1971.

Incorporated Research Institutions for Seismology, *PASSCAL: Program for Array Seismic Studies of the Continental Lithosphere*, IRIS, Washington, D.C., 169 pp., 1984.

Ingate, S.F., J. Ha, and K.J. Muirhead, Limitations of waveform modeling of long-period seismograms, *Geophys. J. R. Astron. Soc., 86*, 57–61, 1986.

Irifune, T., An experimental investigation of the pyroxene-garnet transformation in a pyrolite composition and its bearing on the constitution of the mantle, *Phys. Earth Planet. Inter., 45*, 324–336, 1987.

Irifune, T., J.-I. Susaki, T. Yagi, and H. Sawamoto, Phase transformations in diopside $CaMgSi_2O_6$ at pressures up to 25 GPa, *Geophys. Res. Lett., 16*, 187–190, 1989.

Ito, E., and E. Takahashi, Ultrahigh-pressure phase transformations and the constitution of the deep mantle, in *High Pressure Research in Mineral Physics*, edited by M.H. Manghnani and Y. Syono, pp. 221–229, TERRAPUB/AGU, Tokyo/Washington, 1987.

Ito, E., and H. Yamada, Stability relations of silicate spinels, ilmenites, and perovskites, in *High Pressure Research in Geophysics*, edited by S. Akimoto and M.H. Manghnani, pp. 405–419, Center for Academic Publications, Tokyo, Japan, 1982.

Jackson, I., Some geophysical constraints on the chemical composition of the Earth's lower mantle, *Earth Planet. Sci. Lett., 62*, 91–103, 1983.

Jeanloz, R. and F.M. Richter, Convection, composition, and the thermal state of the lower mantle, *J. Geophys. Res., 84*, 5497–5504, 1979.

Jeanloz R., and A.B. Thompson, Phase transitions and mantle discontinuities, *Rev. Geophys., 21*, 51–74, 1983.

Jeffreys, H., *Theory of Probability*, 439 pp., Oxford University Press, Oxford, Great Britain, 1961.

Jenkins, D.M., and R.C. Newton, Experimental determination of the spinel peridotite to garnet peridotite inversion at 900° C and 1,000° C in the system $CaO-MgO-Al_2O_3-SiO_2$, and 900° C with natural garnet and olivine, *Contrib. Mineral. Petrol., 68*, 407–419, 1979.

Johnson, L.R., Array measurements of *P* velocities in the upper mantle, *J. Geophys. Res., 72*, 6309–6325, 1967.

Johnson, L.R., Array measurements of *P* velocities in the lower mantle, *Bull. Seismol. Soc. Am., 59*, 973–1008, 1969.

Jordan, T.H., Mineralogies, densities, and seismic velocities of garnet lherzolites and their geophysical importance, in *The Mantle Sample: Inclusions in Kimberlites and Other Volcanics*, edited by .'.R. Boyd and H.O.A. Meyer, pp. 1–14, American Geophysical Union, Washington, D.C., 1979a.

Jordan, T.H., Structural geology of the Earth's interior, *Proc. Natl. Acad. Sci. U.S.A.*, *76*, 4192–4200, 1979*b*.

Jordan, T.H., Global tectonic regionalization for seismological data analysis, *Bull. Seismol. Soc. Am.*, *71*, 1131–1141, 1981.

Jordan, T.H, and W.S. Lynn, A velocity anomaly in the lower mantle, *J. Geophys. Res.*, *79*, 2679–2685, 1974.

Jordan, T.H., and L.N. Frazer, Crustal and upper mantle structure from *Sp* phases, *J. Geophys. Res.*, *80*, 1504–1518, 1975.

Jordan, T.H., and S.A. Sipkin, Estimation of the attenuation operator for multiple *ScS* waves, *Geophys. Res. Lett.*, *4*, 167–170, 1977.

Jordan, T.H., and K.C. Creager, Chemical boundary layers and large-scale flow in the mantle and core (abstract), *Eos Trans. AGU*, *67*, 311, 1986.

Kaila, K.L., and V.G. Krishna, Lateral variations in the upper mantle velocity structure in the northwestern Pacific margin, *Tectonophysics*, *112*, 227–253, 1985.

Kanamori, H., Spectrum of *P* and *PcP* in relation to the mantle-core boundary and attenuation in the mantle, *J. Geophys. Res.*, *72*, 559–571, 1967.

Kanamori, H., Mantle beneath the Japanese arc, *Phys. Earth Planet. Inter.*, *3*, 475–483, 1970.

Kanamori, H., and F. Press, How thick is the lithosphere?, *Nature*, *226*, 330–331, 1970.

Karig, D.E., Origin and development of marginal basins in the western Pacific, *J. Geophys. Res.*, *76*, 2542–2561, 1971.

Kennett, B.L.N., Slowness techniques in seismic interpretation, *J. Geophys. Res.*, *86*, 11,575–11,584, 1981.

Kennett, B., and G. Nolet, The influence of upper mantle discontinuities on the toroidal free oscillations of the Earth, *Geophys. J. R. Astron. Soc.*, *56*, 283–308, 1979.

Kind, R., J.P. Davis, and I.S. Sacks, *P'P'* precursors re-examined with broadband data (abstract), *Eos Trans. AGU*, *69*, 1333, 1988.

King, D.W, and G. Calcagnile, *P*-wave velocities in the upper mantle beneath Fennoscandia and western Russia, *Geophys. J. R. Astron. Soc.*, *46*, 407–432, 1976.

Knittle, E., and R. Jeanloz, High-pressure metallization of FeO and implications for the Earth's core, *Geophys. Res. Lett.*, *13*, 1541–1544, 1986.

Knittle, E., and R. Jeanloz, Synthesis and equation of state of (Mg, Fe)SiO$_3$ perovskite to over 100 gigapascals, *Science*, *235*, 668–670, 1987.

Knittle, E., and R. Jeanloz, Mineral physics evidence for mantle layering and a fast, heterogeneous D" (abstract), *Eos Trans AGU*, *69*, 1420, 1988.

Knopoff, L., The thickness of the lithosphere from the dispersion of surface waves, *Geophys. J. R. Astron. Soc.*, *74*, 55–81, 1983.

Kovach, R.L., and D.L. Anderson, Attenuation of shear waves in the upper and lower mantle, *Bull. Seismol. Soc. Am.*, *54*, 1855–1864, 1964.

Landisman, M., S. Mueller, and B.J. Mitchell, Review of evidence for velocity inversions in the continental crust, in *The Structure and Physical Properties of the Earth's Crust*, *Geophys. Monogr. Ser.*, vol. 14, edited by J.G. Heacock, pp. 11–34, AGU Washington, D.C., 1971.

Lavely, E.M., D.W. Forsyth, and P. Friedmann, Scales of heterogeneity near the core-mantle-boundary, *Geophys. Res. Lett.*, *13*, 1505–1508, 1986.

Lay, T., and D.V. Helmberger, A lower mantle *S*-wave triplication and the shear velocity structure of D", *Geophys. J. R. Astron. Soc.*, *75*, 799–838, 1983.

Lay, T., and T.C. Wallace, Multiple *ScS* travel times and attenuation beneath Mexico and central America, *Geophys. Res. Lett.*, *10*, 301–304, 1983.

Lay, T., and T.C. Wallace, Multiple *ScS* travel times and attenuation beneath western North America (abstract), *Eos Trans. AGU*, *69*, 399, 1988.

Leeds, A.R., Lithospheric thickness in the western Pacific, *Phys. Earth Planet. Inter.*, *11*, 61–64, 1975.

Lees, A.C., M.S.T. Bukowinski, and R. Jeanloz, Reflection properties of phase transition and compositional models of the 670-km discontinuity, *J. Geophys. Res*, *88*, 8145–8159, 1983.

Lehmann, I., Velocities of longitudinal waves in the upper part of the Earth's mantle, *Ann. Géophys.*, *15*, 93–118, 1959.

Lerner-Lam, A.L., and T.H. Jordan, How thick are the continents?, *J. Geophys. Res.*, *92*, 14,007–14,026, 1987.

Leven, J.H., The application of synthetic seismograms to the interpretation of the upper mantle *P*-wave velocity structure in northern Australia, *Phys. Earth Planet. Inter.*, *38*, 9–27, 1985.

Leven, J.H., I. Jackson, and A.E. Ringwood, Upper mantle seismic anisotropy and lithospheric decoupling, *Nature*, *289*, 234–239, 1981.

Levenberg, K., A method for the solution of certain nonlinear problems in least squares, *Q. Appl. Math.*, *2*, 164–168, 1944.

Liu, L.-G., The post-spinel phase of forsterite, *Nature*, *262*, 770–772, 1976.

Liu, L.-G., The system enstatite-pyrope at high pressures and temperatures and the mineralogy of the Earth's mantle, *Earth Planet. Sci. Lett.*, *36*, 237–245, 1977.

Liu, L.-G., On the 650-km discontinuity, *Earth Planet. Sci. Lett.*, *42*, 202–208, 1979.

Liu, L.-G., The pyroxene-garnet transformation and its implication for the 200-km seismic discontinuity, *Phys. Earth Planet. Inter.*, *23*, 286–291, 1980.

Liu, L.-G., Effects of H_2O on the phase behavior of the forsterite-enstatite system at high pressures and temperatures and implications for the Earth, *Phys. Earth Planet. Inter.*, *49*, 142–167, 1987.

Liu, L.-G., W.A. Bassett, *Elements, Oxides, Silicates. High-Pressure Phases With Implications for the Earth's Interior*, pp. 250, Oxford, New York, N.Y., 1986.

MacGregor, I.D., The effect of CaO, Cr_2O_3, Fe_2O_3 and Al_2O_3 on the stability of spinel and garnet peridotites, *Phys. Earth Planet. Inter.*, *3*, 372–377, 1970.

Marquardt, D.W., An algorithm for least squares estimation of non-linear parameters, *J. Soc. Ind. Appl. Math., 11*, 431–441, 1963.

Masters, G., and F. Gilbert, Attenuation in the Earth at low frequencies, *Phil. Trans. R. Soc. Lond. A, 308*, 479–522, 1982.

Masters, G., T.H. Jordan, P.G. Silver, and F. Gilbert, Aspherical Earth structure from fundamental spheroidal-mode data, *Nature, 298*, 609–613, 1982.

Middleton, D., and J.R.B. Whittlesey, Seismic models and deterministic operators for marine reverberation, *Geophysics, 33*, 557–583, 1968.

Morelli, A., and A.M. Dziewonski, Topography of the core-mantle boundary and lateral homogeneity of the liquid core, *Nature, 325*, 678–683, 1987.

Muirhead, K.J., and A L. Hales, Evidence for *P* wave discontinuities at depths greater than 650 km in the mantle, *Phys. Earth Planet. Inter., 23*, 304–313, 1980.

Muirhead, K.J., J.R. Cleary, and D.M. Finlayson, A long-range seismic profile in southeastern Australia, *Geophys. J. R. Astron. Soc., 48*, 509–519, 1977.

Nakanishi, I., Attenuation of shear waves in the upper mantle beneath the Sea of Japan, *J. Phys. Earth , 28*, 261–272, 1980.

Nakanishi, I., Reflections of *P'P'* from upper mantle discontinuities beneath the mid-Atlantic Ridge, *Geophys. J., 93*, 335–346, 1988.

Nataf, H.C., I. Nakanishi, and D.L. Anderson, Measurements of mantle wave velocities and inversion for lateral heterogeneities and anisotropy, 3, Inversion, *J. Geophys. Res., 91*, 7261–7307, 1986.

Navrotsky, A., Lower mantle phase transitions may generally have negative pressure-temperature slopes, *Geophys. Res. Lett., 7*, 709–711, 1980.

Niazi, M., and D.L. Anderson, Upper mantle structure of western North America from apparent velocities of *P* waves, *J. Geophys. Res., 70*, 4633–4640, 1965.

Nuttli, O., Seismological evidence pertaining to the structure of the Earth's upper mantle, *Rev. Geophys., 1*, 351–400, 1963.

Okal, E.A., and D.L. Anderson, A study of lateral imhomogeneity in the upper mantle by multiple *ScS* travel-time residuals, *Geophys. Res. Lett.*, *8*, 313–316, 1975.

O'Neill, H.St.C., The transition between spinel lherzolite and garnet lherzolite, and its use as a geobarometer, *Contrib. Mineral. Petrol.*, *77*, 185–194, 1981.

Park, K.T., K. Terakura, and Y. Matsui, Theoretical evidence for a new ultra-high-pressure phase of SiO_2, *Nature*, *336*, 670–672, 1988.

Paulssen, H., Upper mantle converted waves beneath the NARS array, *Geophys. Res. Lett.*, *12*, 709–712, 1985.

Paulssen, H., Evidence for a sharp 670-km discontinuity as inferred from *P-to-S* converted waves, *J. Geophys. Res.*, *93*, 10,489–10,500, 1988.

Press, F., Rigidity of the Earth's core, *Science*, *124*, 1204, 1956.

Regan, J., and D.L. Anderson, Anisotropic models of the upper mantle, *Phys. Earth Planet. Inter.*, *35*, 227–263, 1984.

Revenaugh, J., and T.H. Jordan, Observations of first-order mantle reverberations, *Bull. Seismol. Soc. Am.*, *77*, 1704–1717, 1987.

Revenaugh, J., and T.H. Jordan, A study of mantle layering beneath the western Pacific, *J. Geophys. Res.*, in press, 1989.

Revenaugh, J., T. H. Jordan, and A. L. Lerner-Lam, The role of scattering and anelasticity in the energy budget of mantle reverberations (abstract), *Eos Trans. AGU*, *66*, 305, 1985.

Ribe, N.M., Seismic anisotropy and mantle flow, *J. Geophys. Res.*, *94*, 4213–4223, 1989.

Richards, M.A., and C.H. Wicks, Topography of the "650 km" discontinuity beneath Tonga from *S-P* conversion (abstract), *Eos Trans. AGU*, *68*, 1379, 1987.

Richards, P.G., Seismic waves reflected from velocity gradient anomalies within the Earth's upper mantle, *J. Geophys.*, *38*, 517–527, 1972.

Richards, P.G., On the adequacy of plane-wave reflection/transmission coefficients in the analysis of seismic body waves, *Bull. Seismol. Soc. Am.*, *66*, 701–717, 1976.

Richter, F.M., Focal mechanisms and seismic energy release of deep and intermediate earthquakes in the Tonga-Kermadec region and their bearing on the depth extent of mantle flow, *J. Geophys. Res.*, *84*, 6783–6795, 1979.

Ringwood, A.E., *Composition and Petrology of the Earth's Mantle*, 604 pp., McGraw-Hill, New York, N.Y., 1975.

Ringwood, A.E., *Origin of the Earth and Moon*, 295 pp., Springer-Verlag, New York, N.Y., 1979.

Ringwood, A.E., Phase transformations and differentiation in subducted lithosphere, Implications for mantle dynamics, basalt petrogenesis, and crustal evolution, *J. Geology*, *90*, 611–643, 1982.

Ringwood, A.E., and T. Irifune, Nature of the 650-km seismic discontinuity: implications for mantle dynamics and differentiation, *Nature*, *331*, 131–136, 1988.

Robinson, E.A., and S. Treitel, *Geophysical Signal Analysis*, Prentice-Hall, Englewood Cliffs, N.J., 1980.

Romanowicz, B.A., and C.J. Allegre, Deep structure of the continents; possible topography of the upper mantle phase change discontinuities (abstract), *Eos Trans. AGU*, *60*, 397, 1979.

Romanowicz, B., G. Roult, and T. Kohl, The upper mantle degree two pattern, Constraints from Geoscope fundamental spheroidal mode eigenfrequencies and attenuation measurements, *Geophys. Res. Lett.*, *14*, 1219–1222, 1987.

Ruff, L.J., and D.L. Anderson, Core formation, evolution, and convection, A geophysical model, *Phys. Earth Planet. Inter.*, *21*, 181–201, 1979.

Sacks, I.S., and J.A. Snoke, Continental and oceanic lithosphere, *Year Book Carnegie Inst. Washington*, *82*, 465–470, 1983.

Sailor, R.V., and A.M. Dziewonski, Measurements and interpretation of normal mode attenuation, *Geophys. J. R. Astron. Soc.*, *53*, 559–581, 1978.

Sato, R., and A.F. Espinosa, Dissipation in the Earth's mantle and rigidity and viscosity in the Earth's core determined from waves multiply reflected from the mantle-core boundary, *Bull. Seismol. Soc. Am.*, *57*, 829–856, 1967.

Schneider, W.A., Integral formulation for migration in two and three dimensions, *Geophysics*, *43*, 49–76, 1978.

Schubert, G., D.A. Yuen, and D.L. Turcotte, Role of phase transitions in a dynamic mantle, *Geophys. J. R. Astron. Soc.*, *42*, 705–735, 1975.

Seekins, L.C., and T.-L. Teng, Lateral variations in the structure of the Philippine Sea plate, *J. Geophys. Res.*, *82*, 317–324, 1977.

Selim, I., *Detection Theory*, Princeton University Press, Princeton, N.J., 1965.

Sengupta, M.K., and M.N. Toksöz, Three dimensional model of seismic velocity variation in the Earth's mantle, *Geophys. Res. Lett.*, *3*, 84–86, 1976.

Shimamura, H., and T. Asada, Apparent velocity measurements on an oceanic lithosphere, *Phys. Earth Planet. Inter.*, *13*, 15–22, 1976.

Shiono, K., I.S. Sacks, and A.T. Linde, Preliminary velocity structure of Japanese islands and Philippine Sea from surface wave dispersion, *Year Book Carnegie Inst. Washington*, *79*, 498–505, 1980.

Silver, P.G., and W.W. Chan, Implications for continental structure and evolution from seismic anisotropy, *Nature*, *335*, 34–39, 1988.

Simpson, D.W., C. Wright, and J.R. Cleary, Double discontinuity in the upper mantle, *Nat. Phys. Sci.*, *231*, 201–203, 1971.

Simpson, D.W., R.F. Mereu, and D.W. King, An array study of P-wave velocities in the upper mantle transition zone beneath northeastern Australia, *Bull. Seismol. Soc. Am.*, *64*, 1757–1788, 1974.

Sipkin, S.A., and T.H. Jordan, Lateral heterogeneity of the upper mantle determined from the travel times of multiple ScS, *J. Geophys. Res.*, *81*, 6307–6320, 1976.

Sipkin, S.A., and T.H. Jordan, Frequency dependence of Q_{ScS}, *Bull. Seismol. Soc. Am.*, *69*, 1055–1079, 1979.

Sipkin, S.A., and T.H. Jordan, Multiple *ScS* travel times in the western Pacific, Implications for mantle heterogeneity, *J. Geophys. Res.*, *85*, 853–861, 1980*a*.

Sipkin, S.A., and T.H. Jordan, Regional variation of Q_{ScS}, *Bull. Seismol. Soc. Am.*, *70*, 1071–1102, 1980*b*.

Sleep, N.H., Gradual entrainment of a chemical layer at the base of the mantle by overlying convection, *Geophys. J.*, *95*, 437–447, 1988.

Smith, F.B., and D.F. Shanno, An improved Marquardt procedure for nonlinear regressions, *Technometrics*, *13*, 63–75, 1971.

Smith, M.F., and G. Masters, Aspherical structure constraints from free oscillation frequency and attenuation measurements, *J. Geophys. Res.*, *94*, 1953–1976, 1989.

Sobel, P., The phase *P'P'* as a means for determining upper mantle structure, Ph.D. dissertation, Univ. of Minn., Minneapolis, 1978.

Soller, D.R., R.D. Ray, and R.D. Brown, A new global crustal thickness map, *Tectonics*, *1*, 125–149, 1982.

Souriau, A., First analysis of broadband records of the Geoscope network, potential for detailed studies of mantle discontinuities, *Geophys. Res. Lett.*, *13*, 1011–1014, 1986.

Stacey, F.D., and D.E. Loper, The thermal boundary-layer interpretation of D" and its role as a plume source, *Phys. Earth Planet. Inter.*, *33*, 45–55, 1983.

Stark, M., and D.W. Forsyth, The geoid, small-scale convection, and the differential travel time anomalies of shear waves in the Central Indian ocean, *J. Geophys. Res. 88*, 2273–2288, 1983.

Steinmetz, L., A. Hirn, and G. Perrier, Réflexions sismiques à la base de l'asthénosphere, *Ann. Géophys.*, *30*, 172–180, 1973.

Suito, K., Phase relations of pure Mg₂SiO₄, up to 200 kilobars, in *High Pressure Research , Applications in Geophysics*, edited by M.H. Manghnani and S. Akimoto, pp. 255–266, Center for Academic Publications, Tokyo, Japan, 1977.

Sundaralingham, K., Upper mantle velocity of Fiji region from surface wave dispersion, *J. Phys. Earth*, *34*, 407–426, 1986.

Takahashi, E., and E. Ito, Mineralogy of mantle peridotite along a model geotherm up to 700 km depth, in *High Pressure Research in Mineral Physics*, edited by M.H. Manghnani and Y. Syono, pp. 427–437, TERRAPUB/AGU, Tokyo/Washington, 1987.

Tanimoto, T., The three-dimensional shear wave structure in the mantle by overtone waveform inversion, I, Radial seismogram inversion, *Geophys. J. R. Astron. Soc.*, *89*, 713–740, 1987.

Tanimoto, T., The 3-D shear wave structure in the mantle by overtone waveform inversion, II, Inversion of X-waves, R-waves and G-waves, *Geophys. J.*, *93*, 321–334, 1988.

Tanimoto, T., and D.L. Anderson, Lateral heterogeneity and azimuthal anisotropy of the upper mantle: Love and Rayleigh 100–250 s, *J. Geophys. Res., 90*, 1842–1858, 1985.

Tarantola, A., Linearized inversion of seismic reflection data, *Geophys. Prospect., 32*, 998–1015, 1984*a*.

Tarantola, A., Inversion of seismic reflection data in the acoustic approximation, *Geophysics, 49*, 1259–1266, 1984*b*.

Toksöz, M.N., and D.L. Anderson, Phase velocities of long-period surface waves and structure of the upper mantle, *J. Geophys. Res., 71*, 1649–1658, 1966.

Toksöz, M.N., M.A. Chinnery, and D.L. Anderson, Imhomogeneities in the Earth's mantle, *Geophys. J. R. Astron. Soc., 13*, 31–59, 1967.

Turcotte, D.L., and E.R. Oxburgh, Finite amplitude convective cells and continental drift, *J. Fluid Mech., 28*, 24–42, 1967.

Vassiliou, M.S., and T.J. Ahrens, The equation of state of $Mg_{0.6}Fe_{0.4}O$ to 200 GPa, *Geophys. Res. Lett., 9*, 127–130, 1982.

Vinnik, L.P., Detection of waves converted from P to S in the mantle, *Phys. Earth Planet. Inter., 15*, 39–45, 1977.

Vinnik, L.P., R.A. Avetisjan, and N.G. Mikhailova, Heterogeneities in the mantle transition zone from observations of P-to-SV converted waves, *Phys. Earth Planet. Inter., 33*, 149–163, 1983.

Wajeman, N., Detection of underside P reflections at mantle discontinuities by stacking broadband data, *Geophys. Res. Lett., 15*, 669–672, 1988.

Walck, M.C., The P-wave upper mantle structure beneath an active spreading center, The Gulf of California, *Geophys. J. R. Astron. Soc., 76*, 697–723, 1984.

Walker, C., E.M. Stolper, and J.F. Hays, A numerical treatment of melt/solid segregation, Size of the eucrite parent body and stability of the terrestrial low-velocity zone, *J. Geophys. Res., 83*, 6005–6013, 1978.

Ward, S.N., Long-period reflected and converted upper-mantle phases, *Bull. Seismol. Soc. Am., 68*, 133–153, 1978.

Webb, S.A.C., and B.J. Wood, Spinel-pyroxene-garnet relationships and their dependence on Cr/Al ratio, *Contrib. Mineral. Petrol., 92*, 471–480, 1986.

Weidner, D.J., A mineral physics test of a pyrolite mantle, *Geophys. Res. Lett., 12*, 417–420, 1985.

Weidner, D.J., H. Sawamoto, and S. Sasaki, Single-crystal elastic properties of the spinel phase of Mg2SiO4, *J. Geophys. Res., 89*, 7852–7860, 1984.

Whitcomb, J.H., and D.L. Anderson, Reflection of *P'P'* seismic waves from discontinuities in the mantle, *J. Geophys. Res., 75*, 5713–5728, 1970.

White, R.E., Partial coherence matching of synthetic seismograms with seismic traces, *Geophys. Prospect.*, *28*, 333–358, 1980.

Wolf, G.H., and M.S.T. Bukowinski, Ab initio structural and thermoelastic properties of orthorhombic MgSiO$_3$ perovskite, *Geophys. Res. Lett.*, *12*, 809–812, 1985.

Wood, B.J., and D.A. Yuen, The role of lithospheric phase transitions on seafloor flattening at old ages, *Earth Planet. Sci. Lett.*, *66*, 303–314, 1983.

Woodhouse, J.H., and A.M. Dziewonski, Mapping the upper mantle: three-dimensional modeling of Earth structure by inversion of seismic waveforms, *J. Geophys. Res.*, *89*, 5953–5986, 1984.

Wright, C., K.J. Muirhead, and A.E. Dixon, The *P* wave velocity structure near the base of the mantle, *J. Geophys. Res.*, *90*, 623–634, 1985.

Young, C.J., and T. Lay, Evidence for a shear velocity discontinuity in the lower mantle beneath India and the Indian Ocean, *Phys. Earth Planet. Inter.*, *49*, 37–53, 1987.

Yuen, D.A., and W.R. Peltier, Mantle plumes and the thermal stability of the D" layer, *Geophys. Res. Lett.*, *7*, 625–628, 1980.

ACKNOWLEDGMENTS

Professor Keiiti Aki
Center for Earth Sciences
University of Southern California
University Park
Los Angeles, CA 90089-0741

Professor Thomas Ahrens
Seismological Lab, 252-21
Div. of Geological and Planetary
   Sciences
California Institute of Technology
Pasadena, CA 91125

Professor Charles B. Archambeau
Cooperative Institute for Resch
   in Environmental Sciences
University of Colorado
Boulder, CO 80309

Dr. Thomas C. Bache Jr.
Science Applications Int'l Corp.
10210 Campus Point Drive
San Diego, CA 92121   (2 copies)

Dr. Muawia Barazangi
Institute for the Study of
   of the Continent
Cornell University
Ithaca, NY 14853

Dr. Douglas R. Baumgardt
Signal Analysis & Systems Div.
ENSCO, Inc.
5400 Port Royal Road
Springfield, VA 22151-2388

Dr. Jonathan Berger
Institute of Geophysics and
   Planetary Physics
Scripps Institution of Oceanography
A-025
University of California, San Diego
La Jolla, CA 92093

Dr. S. Bratt
Science Applications Int'l Corp.
10210 Campus Point Drive
San Diego, CA 92121

Dr. Lawrence J. Burdick
Woodward-Clyde Consultants
P.O. Box 93245
Pasadena, CA 91109-3245 (2 copies)

Professor Robert W. Clayton
Seismological Laboratory/Div. of
   Geological & Planetary Sciences
California Institute of Technology
Pasadena, CA 91125

Dr Karl Coyner
New England Research, Inc.
76 Olcott Drive
White River Junction, VT 05001

Dr. Vernon F. Cormier
Department of Geology & Geophysics
U-45, Room 207
The University of Conneticut
Storrs, Connecticut 06268

Dr. Steven Day
Dept. of Geological Sciences
San Diego State U.
San Diego, CA 92182

Dr. Zoltan A. Der
ENSCO, Inc.
5400 Port Royal Road
Springfield, VA 22151-2388

Professor John Ferguson
Center for Lithospheric Studies
The University of Texas at Dallas
P.O. Box 830688
Richardson, TX 75083-0688

Professor Stanley Flatte'
Applied Sciences Building
University of California,
Santa Cruz, CA 95064

Dr. Alexander Florence
SRI International
333 Ravenswood Avenue
Menlo Park, CA 94025-3493

Professor Steven Grand
University of Texas at Austin
Dept of Geological Sciences
Austin, TX 78713-7909

Dr. Henry L. Gray
Associate Dean of Dedman College
Department of Statistical Sciences
Southern Methodist University
Dallas, TX 75275

Professor Roy Greenfield
Geosciences Department
403 Deike Building
The Pennsylvania State University
University Park, PA 16802

Professor David G. Harkrider
Seismological Laboratory
Div of Geological & Planetary Sciences
California Institute of Technology
Pasadena, CA 91125

Professor Donald V. Helmberger
Seismological Laboratory
Div of Geological & Planetary Sciences
California Institute of Technology
Pasadena, CA 91125

Professor Eugene Herrin
Institute for the Study of Earth
   and Man/Geophysical Laboratory
Southern Methodist University
Dallas, TX 75275

Professor Robert B. Herrmann
Department of Earth & Atmospheric
      Sciences
Saint Louis University
Saint Louis, MO 63156

Professor Bryan Isacks
Cornell University
Dept of Geological Sciences
SNEE Hall
Ithaca, NY 14850

Professor Lane R. Johnson
Seismographic Station
University of California
Berkeley, CA 94720

Professor Thomas H. Jordan
Department of Earth, Atmospheric
 and Planetary Sciences
Mass Institute of Technology
Cambridge, MA 02139

Dr. Alan Kafka
Department of Geology &
   Geophysics
Boston College
Chestnut Hill, MA 02167

Professor Leon Knopoff
University of California
Institute of Geophysics
   & Planetary Physics
Los Angeles, CA 90024

Professor Charles A. Langston
Geosciences Department
403 Deike Building
The Pennsylvania State University
University Park, PA 16802

Professor Thorne Lay
Department of Geological Sciences
1006 C.C. Little Building
University of Michigan
Ann Arbor, MI 48109-1063

Dr. Randolph Martin III
New England Research, Inc.
76 Olcott Drive
White River Junction, VT 05001

Dr. Gary McCartor
Mission Research Corp.
735 State Street
P.O. Drawer 719
Santa Barbara, CA 93102   (2 copies)

Professor Thomas V. McEvilly
Seismographic Station
University of California
Berkeley, CA 94720

Dr. Keith L. McLaughlin
S-CUBED,
A Division of Maxwell Laboratory
P.O. Box 1620
La Jolla, CA 92038-1620

Professor William Menke
Lamont-Doherty Geological Observatory
   of Columbia University
Palisades, NY 10964

Professor Brian J. Mitchell
Department of Earth & Atmospheric
   Sciences
Saint Louis University
Saint Louis, MO 63156

Mr. Jack Murphy
S-CUBED
A Division of Maxwell Laboratory
11800 Sunrise Valley Drive
Suite 1212
Reston, VA 22091 (2 copies)

Professor J. A. Orcutt
IGPP, A-205
Scripps Institute of Oceanography
Univ. of California, San Diego
La Jolla, CA 92093

Professor Keith Priestley
University of Nevada
Mackay School of Mines
Reno, NV 89557

Professor Paul G. Richards
Lamont-Doherty Geological
Observatory of Columbia Univ.
Palisades, NY 10964

Wilmer Rivers
Teledyne Geotech
314 Montgomery Street
Alexandria, VA 22314

Dr. Alan S. Ryall, Jr.
Center of Seismic Studies
1300 North 17th Street
Suite 1450
Arlington, VA 22209-2308   (4 copies)

Professor Charles G. Sammis
Center for Earth Sciences
University of Southern California
University Park
Los Angeles, CA 90089-0741

Professor Christopher H. Scholz
Geological Sciences
Lamont-Doherty Geological Observatory
Palisades, NY 10964

Dr. Jeffrey L. Stevens
S-CUBED,
A Division of Maxwell Laboratory
P.O. Box 1620
La Jolla, CA 92038-1620

Professor Brian Stump
Institute for the Study of Earth & Man
Geophysical Laboratory
Southern Methodist University
Dallas, TX 75275

Professor Ta-liang Teng
Center for Earth Sciences
University of Southern California
University Park
Los Angeles, CA 90089-0741

Dr. Clifford T... ber
State Univer... of New York at
   Stony Brook
Dept of Earth and Space Sciences
Stony Brook, NY ../94-2100

Professor M. Nafi Toksoz
Earth Resources Lab
Dept of Earth, Atmospheric and
   Planetary Sciences
Massachusetts Institute of Technology
42 Carleton Street
Cambridge, MA 02142

Professor Terry C. Wallace
Department of Geosciences
Building #77
University of Arizona
Tucson, AZ 85721

Weidlinger Associates
ATTN: Dr. Gregory Wojcik
4410 El Camino Real, Suite 110
Los Altos, CA 94022

Professor Francis T. Wu
Department of Geological Sciences
State University of New York
   at Binghamton
Vestal, NY 13901

OTHERS (United States)

Dr. Monem Abdel-Gawad
Rockwell Internat'l Science Center
1049 Camino Dos Rios
Thousand Oaks, CA 91360

Professor Shelton S. Alexander
Geosciences Department
403 Deike Building
The Pennsylvania State University
University Park, PA 16802

Dr. Ralph Archuleta
Department of Geological
   Sciences
Univ. of California at
   Santa Barbara
Santa Barbara, CA

J. Barker
Department of Geological Sciences
State University of New York
 at Binghamton
Vestal, NY   13901

Mr. William J. Best
907 Westwood Drive
Vienna, VA   22180

Dr. N. Biswas
Geophysical Institute
University of Alaska
Fairbanks, AK 99701

Dr. G. A. Bollinger
Department of Geological Sciences
Virginia Polytechnical Institute
21044 Derring Hall
Blacksburg, VA   24061

Mr. Roy Burger
1221 Scrry Rd.
Schenectady, NY   12309

Dr. Robert Burridge
Schlumberger-Doll Resch Ctr.
Old Quarry Road
Ridgefield, CT   06877

Science Horizons, Inc.
ATTN: Dr. Theodore Cherry
710 Encinitas Blvd., Suite 101
Encinitas, CA   92024   (2 copies)

Professor Jon F. Claerbout
Professor Amos Nur
Dept. of Geophysics
Stanford University
Stanford, CA   94305 (2 copies)

Dr. Anton W. Dainty
Earth Resources Lab
Massachusetts Institute of Technology
42 Carleton Street
Cambridge, MA   02142

Professor Adam Dziewonski
Hoffman Laboratory
Harvard University
20 Oxford St.
Cambridge, MA   02138

Professor John Ebel
Dept of Geology and Geophysics
Boston College
Chestnut Hill, MA   02167

Dr. Donald Forsyth
Dept of Geological Sciences
Brown University
Providence, RI   02912

Dr. Anthony Gangi
Texas A&M University
Department of Geophysics
College Station, TX   77843

Dr. Freeman Gilbert
Institute of Geophysics &
   Planetary Physics
University of California, San Diego
P.O. Box 109
La Jolla, CA   92037

Mr. Edward Giller
Pacific Seirra Research Corp.
1401 Wilson Boulevard
Arlington, VA   22209

Dr. Jeffrey W. Given
Sierra Geophysics
11255 Kirkland Way
Kirkland, WA 98033

Rong Song Jih
Teledyne Geotech
314 Montgomery Street
Alexandria, Virginia 22314

Professor F.K. Lamb
University of Illinois at
   Urbana-Champaign
Department of Physics
1110 West Green Street
Urbana, IL 61801

Dr. Arthur Lerner-Lam
Lamont-Doherty Geological Observatory
 of Columbia University
Palisades, NY 10964

Dr. L. Timothy Long
School of Geophysical Sciences
Georgia Institute of Technology
Atlanta, GA 30332

Dr. Peter Malin
University of California at
   Santa Barbara
Institute for Central Studies
Santa Barbara, CA 93106

Dr. George R. Mellman
Sierra Geophysics
11255 Kirkland Way
Kirkland, WA 98033

Dr. Bernard Minster
IGPP, A-205
Scripps Institute of Oceanography
Univ. of California, San Diego
La Jolla, CA 92093

Professor John Nabelek
College of Oceanography
Oregon State University
Corvallis, OR 97331

Dr. Geza Nagy
U. California, San Diego
Dept of Ames, M.S. B-010
La Jolla, CA 92093

Dr. Jack Oliver
Department of Geology
Cornell University
Ithaca, NY 14850

Dr. Robert Phinney/Dr. F. A. Dahlen
Dept of Geological
Geological Science University
Princeton University
Princeton, NJ 08540

RADIX System, Inc.
Attn: Dr. Jay Pulli
2 Taft Court, Suite 203
Rockville, Maryland 20850

Dr. Norton Rimer
S-CUBED
A Division of Maxwell Laboratory
P.O. 1620
La Jolla, CA 92038-1620

Professor Larry J. Ruff
Department of Geological Sciences
1006 C.C. Little Building
University of Michigan
Ann Arbor, MI 48109-1063

Dr. Richard Sailor
TASC Inc.
55 Walkers Brook Drive
Reading, MA 01867

Thomas J. Sereno, Jr.
Science Application Int'l Corp.
10210 Campus Point Drive
San Diego, CA 92121

Dr. David G. Simpson
Lamont-Doherty Geological Observ.
  of Columbia University
Palisades, NY 10964

Dr. Bob Smith
Department of Geophysics
University of Utah
1400 East 2nd South
Salt Lake City, UT 84112

Dr. S. W. Smith
Geophysics Program
University of Washington
Seattle, WA 98195

Dr. Stewart Smith
IRIS Inc.
1616 N. Fort Myer Drive
Suite 1440
Arlington, VA 22209

Rondout Associates
ATTN: Dr. George Sutton,
Dr. Jerry Carter, Dr. Paul Pomeroy
P.O. Box 224
Stone Ridge, NY 12484 (4 copies)

Dr. L. Sykes
Lamont Doherty Geological Observ.
Columbia University
Palisades, NY 10964

Dr. Pradeep Talwani
Department of Geological Sciences
University of South Carolina
Columbia, SC 29208

Dr. R. B. Tittmann
Rockwell International Science Center
1049 Camino Dos Rios
P.O. Box 1085
Thousand Oaks, CA 91360

Professor John H. Woodhouse
Hoffman Laboratory
Harvard University
20 Oxford St.
Cambridge, MA 02138

Dr. Gregory B. Young
ENSCO, Inc.
5400 Port Royal Road
Springfield, VA 22151-2388

Dr. Peter Basham
Earth Physics Branch
Geological Survey of Canada
1 Observatory Crescent
Ottawa, Ontario
CANADA K1A OY3

Professor Ari Ben-Menahem
Dept of Applied Mathematics
Weizman Institute of Science
Rehovot
ISRAEL 951729

Dr. Eduard Berg
Institute of Geophysics
University of Hawaii
Honolulu, HI 96822

Dr. Michel Bouchon - Universite
   Scientifique et Medicale de Grenob
Lab de Geophysique - Interne et
   Tectonophysique - I.R.I.G.M-B.P.
38402 St. Martin D'Heres
Cedex FRANCE

Dr. Hilmar Bungum/NTNF/NORSAR
P.O. Box 51
Norwegian Council of Science,
Industry and Research, NORSAR
N-2007 Kjeller, NORWAY

Dr. Michel Campillo
I.R.I.G.M.-B.P. 68
38402 St. Martin D'Heres
Cedex, FRANCE

Dr. Kin-Yip Chun
Geophysics Division
Physics Department
University of Toronto
Ontario, CANADA M5S 1A7

Dr. Alan Douglas
Ministry of Defense
Blacknest, Brimpton,
 Reading RG7-4RS
UNITED KINGDOM

Dr. Manfred Henger
Fed. Inst. For Geosciences & Nat'l Res.
Postfach 510153
D-3000 Hannover 51
FEDERAL REPUBLIC OF GERMANY

Ms. Eva Johannisson
Senior Research Officer
National Defense Research Inst.
P.O. Box 27322
S-102 54 Stockholm
SWEDEN

Tormod Kvaerna
NTNF/NORSAR
P.O. Box 51
N-2007 Kjeller, NORWAY

Mr. Peter Marshall, Procurement
 Executive, Ministry of Defense
Blacknest, Brimpton,
 Reading FG7-4RS
UNITED KINGDOM (3 copies)

Dr. Robert North
Geophysics Division
Geological Survey of Canada
1 Observatory crescent
Ottawa, Ontario
CANADA, K1A OY3

Dr. Frode Ringdal
NTNF/NORSAR
P.O. Box 51
N-2007 Kjeller, NORWAY

Dr. Jorg Schlittenhardt
Federal Inst. for Geosciences & Nat'l Res.
Postfach 510153
D-3000 Hannover 51
FEDERAL REPUBLIC OF GERMANY

University of Hawaii
Institute of Geophysics
ATTN: Dr. Daniel Walker
Honolulu, HI 96822

FOREIGN CONTRACTORS

Dr. Ramon Cabre, S.J.
Observatorio San Calixto
Casilla 5939
La Paz Bolivia

Professor Peter Harjes
Institute for Geophysik
Rhur University/Bochum
P.O. Box 102148, 4630 Bochum 1
FEDERAL REPUBLIC OF GERMANY

Dr. E. Husebye
NTNF/NORSAR
P.O. Box 51
N-2007 Kjeller, NORWAY

Professor Brian L.N. Kennett
Research School of Earth Sciences
Institute of Advanced Studies
G.P.O. Box 4
Canberra 2601
AUSTRALIA

Dr. B. Massinon
Societe Radiomana
27, Rue Claude Bernard
7,005, Paris, FRANCE   (2 copies)

Dr. Pierre Mechler
Societe Radiomana
27, Rue Claude Bernard
75005, Paris, FRANCE

Dr. Svein Mykkeltveit
NTNF/NORSAR
P.O. Box 51
N-2007 Kjeller, NORWAY   (3 copies)

Dr. Ralph Alewine III
DARPA/NMRO
1400 Wilson Boulevard
Arlington, VA 22209-2308

Dr. Robert Blandford
DARPA/NMRO
1400 Wilson Boulevard
Arlington, VA 22209-2308

Sandia National Laboratory
ATTN: Dr. H. B. Durham
Albuquerque, NM 87185

Dr. Jack Evernden
USGS-Earthquake Studies
345 Middlefield Road
Menlo Park, CA 94025

U.S. Geological Survey
ATTN: Dr. T. Hanks
Nat'l Earthquake Resch Center
345 Middlefield Road
Menlo Park, CA 94025

Dr. James Hannon
Lawrence Livermore Nat'l Lab.
P.O. Box 808
Livermore, CA 94550

Paul Johnson
ESS-4, Mail Stop J979
Los Alamos National Laboratory
Los Alamos, NM 87545

Ms. Ann Kerr
DARPA/NMRO
1400 Wilson Boulevard
Arlington, VA 22209-2308

Dr. Max Koontz
US Dept of Energy/DP 5
Forrestal Building
1000 Independence Ave.
Washington, D.C. 20585

Dr. W. H. K. Lee
USGS
Office of Earthquakes, Volcanoes,
  & Engineering
Branch of Seismology
345 Middlefield Rd
Menlo Park, CA 94025

Dr. William Leith
U.S. Geological Survey
Mail Stop 928
Reston, VA 22092

Dr. Richard Lewis
Dir. Earthquake Engineering and
  Geophysics
U.S. Army Corps of Engineers
Box 631
Vicksburg, MS 39180

Dr. Robert Masse'
Box 25046, Mail Stop 967
Denver Federal Center
Denver, Colorado 80225

Richard Morrow
ACDA/VI
Room 5741
320 21st Street N.W.
Washington, D.C. 20451

Dr. Keith K. Nakanishi
Lawrence Livermore National Laboratory
P.O. Box 808, L-205
Livermore, CA 94550 (2 copies)

Dr. Carl Newton
Los Alamos National Lab.
P.O. Box 1663
Mail Stop C335, Group ESS-3
Los Alamos, NM 87545

Dr. Kenneth H. Olsen
Los Alamos Scientific Lab.
P.O. Box 1663
Mail Stop C335, Group ESS-3
Los Alamos, NM 87545

Howard J. Patton
Lawrence Livermore National
  Laboratory
P.O. Box 808, L-205
Livermore, CA 94550

Mr. Chris Paine
Office of Senator Kennedy
SR 315
United States Senate
Washington, D.C. 20510

AFOSR/NP
ATTN: Colonel Jerry J. Perrizo
Bldg 410
Bolling AFB, Wash D.C. 20332-6448

HQ AFTAC/TT
Attn: Dr. Frank F. Pilotte
Patrick AFB, Florida 32925-6001

Mr. Jack Rachlin
USGS - Geology, Rm 3 C136
Mail Stop 928 National Center
Reston, VA 22092

Robert Reinke
AFWL/NTESG
Kirtland AFB, NM 87117-6008

Dr. Byron Ristvet
HQ DNA, Nevada Operations Office
Attn: NVCG
P.O. Box 98539
Las Vegas, NV 89193

HQ AFTAC/TGR
Attn: Dr. George H. Rothe
Patrick AFB, Florida 32925-6001

Donald L. Springer
Lawrence Livermore National Laboratory
P.O. Box 808, L-205
Livermore, CA 94550

Dr. Lawrence Turnbull
OSWR/NED
Central Intelligence Agency
CIA, Room 5G48
Washington, D.C. 20505

Dr. Thomas Weaver
Los Alamos National Laboratory
P.O. Box 1663
MS C 335
Los Alamos, NM 87545

GL/SULL
Research Library
Hanscom AFB, MA 01731-5000 (2 copies)

Secretary of the Air Force (SAFRD)
Washington, DC 20330
Office of the Secretary Defense
DDR & E
Washington, DC 20330

HQ DNA
ATTN: Technical Library
Washington, DC 20305

DARPA/RMO/RETRIEVAL
1400 Wilson Blvd.
Arlington, VA 22209

DARPA/RMO/Security Office
1400 Wilson Blvd.
Arlington, VA 22209

GL/XO
Hanscom AFB, MA 01731-5000

GL/LW
Hanscom AFB, MA 01731-5000

DARPA/PM
1400 Wilson Boulevard
Arlington, VA 22209

Defense Technical
 Information Center
Cameron Station
Alexandria, VA 22314
(5 copies)

Defense Intelligence Agency
Directorate for Scientific &
 Technical Intelligence
Washington, D.C. 20301

Defense Nuclear Agency/SPSS
ATTN: Dr. Michael Shore
6801 Telegraph Road
Alexandria, VA 22310

AFTAC/CA (STINFO)
Patrick AFB, FL 32925-6001

Dr. Gregory van der Vink
Congress of the United States
Office of Technology Assessment
Washington, D.C. 20510

Mr. Alfred Lieberman
ACDA/VI-OA'State Department Building
Room 5726
320 - 21St Street, NW
Washington, D.C. 20451

TACTEC
Battelle Memorial Institute
505 King Avenue
Columbus, OH 43201 (Final report only)